

A Thesis Submitted for the Degree of PhD at the University of Warwick

Permanent WRAP URL:

<http://wrap.warwick.ac.uk/153557>

Copyright and reuse:

This thesis is made available online and is protected by original copyright.

Please scroll down to view the document itself.

Please refer to the repository record for this item for information to help you to cite it.

Our policy information is available from the repository home page.

For more information, please contact the WRAP Team at: wrap@warwick.ac.uk

Electrochemical and Spectro- Electrochemical Investigation of Metal Electrodeposition

Alexandra Jane Borrill

Doctor of Philosophy in Chemistry

University of Warwick

Department of Chemistry

November 2020



In loving memory of my Mother

Table of Contents

TABLE OF CONTENTS	III
LIST OF FIGURES	VII
LIST OF TABLES	XVIII
ABBREVIATIONS	XIX
ACKNOWLEDGEMENTS	XXI
DECLARATIONS	XXII
ABSTRACT	1
1. INTRODUCTION	3
1.1. ELECTROCHEMISTRY	3
1.1.1. <i>Dynamic Electrochemistry</i>	4
1.1.2. <i>Electron transfer kinetics</i>	4
1.1.3. <i>Mass Transport Theory</i>	7
1.1.4. <i>Practical Systems for Mass Transport</i>	10
1.2. ELECTROCHEMICAL SET-UP	13
1.2.1. <i>Three Electrode Cell</i>	13
1.3. BORON DOPED DIAMOND	15
1.3.1. <i>Structure, Growth and Properties</i>	15
1.3.1. <i>Electrochemistry of BDD</i>	16
1.4. HEAVY METAL DETECTION	17
1.4.1. <i>Anodic Stripping Voltammetry (ASV)</i>	18
1.4.1.1. ASV Theory	19
1.4.1.2. Electrode Materials	20
1.4.1.3. ASV Parameters	26
1.4.1.4. Potential wave forms	27
1.4.1.5. Speciation and pH	29
1.4.1.6. Metallic interferences	30
1.4.1.7. Metal Electrodeposition and Stripping Theory	31
1.5. XRF	32
1.5.1. <i>EC-XRF</i>	36
1.6. ELECTROCATALYSIS	37
1.7. AIMS	38
1.8. BIBLIOGRAPHY	40
2. EXPERIMENTAL	50

2.1.	CHEMICALS.....	50
2.2.	MATERIALS.....	50
2.2.1.	<i>Boron Doped Diamond</i>	51
2.3.	FABRICATION OF ELECTRODES.....	51
2.3.1.	<i>Laser Micromachining</i>	51
2.3.2.	<i>Acid cleaning</i>	51
2.3.3.	<i>Ohmic contacting</i>	51
2.3.4.	<i>1 mm Macroelectrode Sealing</i>	52
2.3.5.	<i>Bespoke Electrodes</i>	53
2.4.	ELECTROCHEMISTRY	53
2.4.1.	<i>Characterisation of Electrodes</i>	53
2.5.	FIELD EMISSION-SCANNING ELECTRON MICROSCOPY.....	55
2.6.	TRANSMISSION ELECTRON MICROSCOPY	55
2.7.	X-RAY FLUORESCENCE SPECTROSCOPY.....	56
2.8.	ON-LINE ELECTROCHEMICAL MASS SPECTROMETRY.....	56
3.	MASS TRANSPORT INVESTIGATIONS FOR <i>EX SITU</i> EC-XRF.....	58
3.1.	OVERVIEW	58
3.2.	INTRODUCTION.....	59
3.3.	EXPERIMENTAL.....	66
3.3.1.	<i>Chemicals and Solutions</i>	66
3.3.2.	<i>Mass Transport Systems Materials and Fabrication</i>	66
3.3.2.1.	Magnetic stirrer system.....	66
3.3.2.2.	Vibrating electrode.....	67
3.3.2.3.	Wall Jet electrode.....	67
3.3.2.4.	Rotating Disk Electrodes.....	67
3.3.3.	<i>Electrochemistry</i>	68
3.3.4.	<i>ED-XRF</i>	68
3.4.	RESULTS AND DISCUSSION	69
3.4.1.	<i>Magnetic stirrer system</i>	69
3.4.2.	<i>Vibrating Diaphragm</i>	71
3.4.3.	<i>Wall-Jet Electrode</i>	77
3.4.4.	<i>EC-XRF RDE</i>	80
3.4.5.	<i>EC-XRF RDE Prototype 1</i>	84
3.4.6.	<i>EC-XRF RDE Prototype 2</i>	87
3.4.7.	<i>EC-XRF RDE Prototype 3</i>	88
3.4.8.	<i>EC-XRF of Cu with Prototype 3</i>	91
3.5.	CONCLUSION	96
3.6.	BIBLIOGRAPHY.....	98

4.	FLOW CELL EC-XRF.....	101
4.1.	OVERVIEW	101
4.2.	INTRODUCTION.....	101
4.3.	EXPERIMENTAL.....	105
4.3.1.	<i>Solutions.....</i>	<i>105</i>
4.3.2.	<i>Materials and equipment.....</i>	<i>105</i>
4.3.3.	<i>X-ray Fluorescence Spectroscopy</i>	<i>107</i>
4.3.3.1.	ED-XRF	107
4.3.3.2.	Mapping XRF.....	108
4.4.	RESULTS AND DISCUSSION	108
4.4.1.	<i>Wall Jet design</i>	<i>108</i>
4.4.2.	<i>Characterisation.....</i>	<i>113</i>
4.4.3.	<i>Copper Experiments</i>	<i>115</i>
4.4.4.	<i>Mapping XRF.....</i>	<i>122</i>
4.5.	CONCLUSIONS	126
4.6.	BIBLIOGRAPHY.....	128
5.	COPPER ELECTRODEPOSITION AND STRIPPING INVESTIGATIONS	130
5.1.	OVERVIEW	130
5.2.	INTRODUCTION.....	130
5.3.	EXPERIMENTAL.....	133
5.3.1.	<i>Solutions.....</i>	<i>133</i>
5.3.2.	<i>Electrochemistry.....</i>	<i>134</i>
5.3.3.	<i>Speciation modelling.....</i>	<i>134</i>
5.3.4.	<i>Electron Microscopy.....</i>	<i>134</i>
5.4.	RESULTS AND DISCUSSION	135
5.4.1.	<i>Model Speciation of Copper</i>	<i>135</i>
5.4.2.	<i>Electrochemistry of Cu in acetate buffer solution</i>	<i>143</i>
5.4.3.	<i>Electrochemistry of Cu in low pH electrolyte solutions</i>	<i>147</i>
5.4.4.	<i>SEM of Cu deposits formed in pH 2 sulfate, nitrate and chloride solutions.....</i>	<i>154</i>
5.4.5.	<i>Electrochemistry of Cu in pH 5 electrolyte solutions</i>	<i>159</i>
5.5.	CONCLUSIONS	169
5.6.	BIBLIOGRAPHY.....	171
6.	TRANSMISSION ELECTRON MICROSCOPY INVESTIGATION OF COPPER (I) OXIDE ELECTRODEPOSITION AND CARBON DIOXIDE ELECTROCATALYSIS	176
6.1.	OVERVIEW	176
6.2.	INTRODUCTION.....	177
6.3.	EXPERIMENTAL.....	183

6.3.1.	<i>Solutions</i>	183
6.3.2.	<i>Electrochemistry</i>	183
6.3.3.	<i>OLEMS</i>	184
6.3.4.	<i>Electron Microscopy</i>	184
6.3.4.1.	SEM.....	184
6.3.4.2.	TEM.....	185
6.3.5.	<i>Data Analysis</i>	187
6.4.	RESULTS AND DISCUSSION	187
6.4.1.	<i>Electrodeposition of Cu Cubes</i>	187
6.4.2.	<i>Identical location STEM study of growth</i>	194
6.4.3.	<i>Electrocatalysis</i>	201
6.4.4.	<i>TEM of dissolution by electrocatalysis</i>	206
6.5.	CONCLUSIONS	208
6.6.	BIBLIOGRAPHY.....	211
7.	CONCLUSIONS AND FUTURE DIRECTIONS	215
7.1.	BIBLIOGRAPHY.....	221

List of Figures

Figure 1 Reaction co-ordinate graph vs. free energy of the reaction showing the transition state.	5
Figure 2 The fermi level (E_f) of the electrode material and the HOMO and LUMO of the reactant are shown schematically.....	6
Figure 3 Reaction co-ordinate vs. potential energy graph showing overlapping curves for product and reactant, the crossover denoting the transition state.	6
Figure 4 Schematic of the double layer showing the Inner Helmholtz Plane (IHP) and the Outer Helmholtz plane (OHP). Charged molecules in the solvent line up against the charged surface of the electrode, forming a capacitor, while remaining surface charge is compensated by increased concentration of counter-ions in the diffuse layer of electrolyte, gradually giving way to bulk solution concentrations.....	9
Figure 5 Concentration diffusional profiles at a) macro electrode, b) micro electrode c) rotating disc electrode and d) wall-jet electrode (adapted from ¹¹). The arrows represent the flux of electroactive reactant whilst the purple represents the bulk concentration. Voltammogram e) is typical of a diffusion controlled system such as a macroelectrode. Voltammogram f) is typical of a system which can reach a transport limited steady state current such as microelectrodes, rotating discs and flow systems.	10
Figure 6 The three-electrode set-up showing a saturated calomel reference electrode (SCE) a working electrode and a metal coil counter electrode and their functions in the electrochemical circuit.	14
Figure 7 a) the structure of BDD showing carbon (black) and boron (blue) atoms, b) scanning electron microscopy (SEM) image of the surface of BDD showing the grain structure of a typical electrochemical grade sample.	16
Figure 8 Schematic of a) electrodeposition and b) stripping of a metal and an exemplar CV.	19
Figure 9 Comparison of stripping voltammetric current-potential curves for 100 ppb solutions of Zn, Cd and Pb in acetate buffer, pH 5.2, on a Hg coated glassy carbon electrode (Hg-GC) (top) and BDD (bottom). Figure modified from reference ¹⁰³	25

Figure 10 Schematic of a linear sweep voltammogram in the cathodic direction illustrating the different cathodic processes which could also interfere with a) metal deposition, and include b) metal catalysed ORR resulting in transformation of the metal to metal hydroxide and c) HER from proton and/or water reduction.	27
Figure 11 The change in potential over time for a digital LSV, a), with an exemplar current peak shown in b). c) is the wave form of SWV and an exemplar current peak shown in d). The peak current in d is typically larger than that of c).	28
Figure 12 Differences in stripping voltammograms of a mixture of 50 $\mu\text{g/L}$ Pb^{2+} , Cd^{2+} , and Tl^{+} on Bi and Hg thin-film electrodes. Solutions, 0.1 M acetate buffer (pH 4.5) containing 400 $\mu\text{g/L}$ Bi or 10 mg/L Hg. Deposition for 120 s at -1.2 V. Figure modified from ¹⁵⁰	31
Figure 13 Schematic of the fluorescence mechanism, a) a core electron is ejected when an x-ray photon is absorbed and b) an outer electron falls to the core shell, releasing a photon of fluorescence.	33
Figure 14 Example spectrum showing characteristic fluorescence lines from the tube material (blue) and the Bremsstrahlung (red) that make up the spectrum that irradiates the sample and which are often seen in the measured spectrum.	34
Figure 15 Schematics of a) regular, 2D geometry systems and the spectra when no filter (green) and a filter (purple) are utilised, b) 3D geometry system with spectrum showing lower backgrounds with characteristic lines from target and tube materials.	35
Figure 16 Schematic of EC-XRF showing a) preconcentration step, electrodeposition and electrochemical current-time transient and b) XRF analysis step with typical XRF spectrum of peak of interest obtained.	36
Figure 17 Schematic of the fabrication process of 1 mm macroelectrodes.	52
Figure 18 Example a) SW, b) capacitance and c) $\text{Ru}(\text{NH}_3)_6^{3+}$ data for a standard BDD macroelectrode, in a) the purple line is a good quality BDD electrode and the blue line is a BDD electrode with some observable non-diamond character.	53
Figure 19 Schematic of ASV a) an electrode in solution with no potential applied, b) electrodeposition induced by negative potential relative to E^0 and c) stripping induced by a positive potential relative to E^0	60

Figure 20 Schematic of EC-XRF a) the pre-concentration step using electrodeposition b) analysis with XRF c) comparison of XRF signal to concentration calibration to determine initial sample concentration.	62
Figure 21 Schematic a) and b) of wall-jet flow cell and c) Image of flow cell set-up over XRF optics from reference 40.	64
Figure 22 Photograph a) of BDD electrode disk top) back of disk bottom) front of disk with deposit shown and schematics b) and c) of the electrode assembly and electrode set-up respectively ref ⁴¹	64
Figure 23 CV of 0.5 mM $\text{Ru}(\text{NH}_3)_6^{3+/2+}$ with increasing rate of stirring of magnetic stirrer on a hotplate with a 14 mm diameter BDD electrode, 0.1 Vs^{-1} , 0.1 M KNO_3 . 70	
Figure 24 Increase in modulus of maximum current with increasing stirring power from CVs in 0.5 mM $\text{Ru}(\text{NH}_3)_6^{3+/2+}$ with a magnetic stirrer on a hotplate with a 14 mm diameter BDD electrode, 0.1 Vs^{-1} , 0.1 M KNO_3 n=3.	71
Figure 25 a) schematic cross-section and b) photograph of vibrating diaphragm system.	72
Figure 26 Schematic of measuring the diaphragm displacement with a dial test indicator positioned in the centre of the diaphragm to measure maximum displacement.	72
Figure 27 variation of amplitude with respect to drive voltage and drive frequency applied to the diaphragm mechanism, a resonance condition for the system is met around 10 Hz resulting in an increased amplitude.	73
Figure 28 Parameter map of the effect of drive voltage and drive frequency on peak current in 1 mM $\text{Ru}(\text{NH}_3)_6^{3+/2+}$ on a 1 mm BDD electrode, 0.1 Vs^{-1} , 0.1 M KNO_3	74
Figure 29 CVs of 1 mM $\text{Ru}(\text{NH}_3)_6^{3+/2+}$ on a 1 mm BDD electrode, drive voltage 2.0 V with varied drive frequencies, 0.1 Vs^{-1} , 0.1 M KNO_3	75
Figure 30 Modulus of the average current from n=3 CVs in 1 mM $\text{Ru}(\text{NH}_3)_6^{3+/2+}$ on a 1 mm BDD electrode at stationary and varying drive frequencies.	76
Figure 31 Schematic of wall-jet flow cell a) XRF analysis b) overall cell assembly c) photograph of cell. ⁴⁰	78
Figure 32 CVs of 1 mM $\text{Ru}(\text{NH}_3)_6^{3+/2+}$ in the O'Neil wall-jet cell, 0.1 Vs^{-1} , 0.1 M KNO_3 at flow rates from 0 to 20 ml min^{-1}	78

Figure 33 Modulus of maximum current from CVs of 1 mM $\text{Ru}(\text{NH}_3)_6^{3+/2+}$ in the O'Neil wall-jet cell, 0.1 Vs^{-1} , 0.1 M KNO_3 at flow rates from 0 to 14 ml min^{-1} , compared to wall-jet theory.	79
Figure 34 Schematic of original cap design EC-XRF RDE showing an exploded view of components.....	81
Figure 35 CVs of 0.5 mM $\text{Ru}(\text{NH}_3)_6^{3+/2+}$ with the original cap EC-XRF RDE design, stationary and with varying rotation rate, 0.1 Vs^{-1} , 0.1 M KNO_3	82
Figure 36 Modulus of maximum current from CVs of 0.5 mM $\text{Ru}(\text{NH}_3)_6^{3+/2+}$ with the original cap EC-XRF RDE design, with varying rotation rates of 5 to 25 Hz, 0.1 Vs^{-1} , 0.1 M KNO_3 , (n=1).	83
Figure 37 Prototype 1, a) schematic, b) photo, BDD disk sealed in PEEK head with Ag wire contacts screw fit to adapter which screws into RDE body which in turn screws into the rotator motor, electrocal contact kept through brass interiors of adapter and body, scale bar is 25 mm.	84
Figure 38 XRF backgrounds of the original design and prototypes 1 to 3 in the region of interest showing peaks corresponding to Fe (6.4 keV), Cu (8.05 keV), Zn (8.64 keV), Pt (9.44 keV) and Au (9.71 keV).....	85
Figure 39 CVs of 1 mM $\text{Ru}(\text{NH}_3)_6^{3+/2+}$ and 0.1 M KNO_3 with Prototype 1 at 0.1 V s^{-1} at varying rotation rates from 0 to 40 Hz.	86
Figure 40 Comparison of Levich theory with experimental peak currents from CVs of 1 mM $\text{Ru}(\text{NH}_3)_6^{3+/2+}$ and 0.1 M KNO_3 with Prototype 1 at 0.1 V s^{-1} at varying rotation rates from 0 to 40 Hz.	87
Figure 41 a) schematic b) photo of prototype 2. Dashed lines in a) show the internal brass cylinder connecting the spring pins and screw fitting at the top to enable electrocal conduction.	88
Figure 42 a) schematic b) photo of prototype 3. Dashed lines in a) show the internal brass cylinder connecting the spring pins and screw fitting at the top to enable electrocal conduction, c) is the face of the electrode inset in PEEK head and d) is the back face showing the 4 sputtered areas for the pins to make contact.	89
Figure 43 CVs of 1 mM $\text{Ru}(\text{NH}_3)_6^{3+/2+}$ and 0.1 M KNO_3 with Prototype 3 at 0.1 V s^{-1} at varying rotation rates from 0 to 42 Hz.	90

Figure 44 Comparison of Levich theory with experiment peak currents for CVs of 1 mM $\text{Ru}(\text{NH}_3)_6^{3+/2+}$ and 0.1 M KNO_3 with Prototype 3.	91
Figure 45 CVs of 100 ppm (1.6 mM) $\text{Cu}(\text{NO}_3)_2$ and 0.1 M KNO_3 on EC-XRF RDE prototype 3, at 0.1 V s^{-1} in neutral (approx. pH 5.5-7) and acidic (pH 2) solutions with and without dissolved oxygen (degassed).....	92
Figure 46 Experiment to find optimal deposition potential for Cu EC-XRF experiments in 100 ppm $\text{Cu}(\text{NO}_3)_2$ and 0.1 M KNO_3 on EC-XRF RDE prototype 3. For a neutral solution (pH 5.5-7) and a pH 2 solution, 25 Hz.	93
Figure 47 EC-XRF data, collected on Prototype 3. Concentration vs XRF signal graph, 25 Hz, two different deposition potentials in pH 6 and pH 2 solutions, aerated.	94
Figure 48 photograph of the electrode surface after a deposition in 100 ppm $(\text{NO}_3)_2$ solution at -0.5 V and 25 Hz, showing the flow profile of solution by a blueish coloured deposit. Scale bar is 10 mm.	95
Figure 49 schematic of two examples of electrochemical flow cells a) a wall-jet and b) a channel flow electrode, black surface denotes electrode surface and arrows show fluid flow profile.	102
Figure 50 schematics of two different wall-jet systems demonstrating a) a free wall-jet, adapted from ¹³ and b) confined microjet displaying channel flow. ¹⁴	102
Figure 51 Schematic of an in situ EC-XRF flow cell.	104
Figure 52 Photographs of flow cell assembled showing position of the wires for the WE, CE and RE, and the positions of the capacitor, outlets and inlet.	106
Figure 53 Photographs of the inside of the flow cell showing a) the WE and b) the CE, RE, inlet and an outlet.	106
Figure 54 Schematic cross section of the flow cell showing critical dimensions.	107
Figure 55 Schematics of a) original O'Neil cell ⁹ and b) the new cell design.	108
Figure 56 Photos of a) the original O'Neil flow cell and b) the new flow cell. WE wire is clipped to the green, RE white and red CE.	109
Figure 57 Picture of the flow cell system running, the pump system pulls solution from the reservoir beaker and into the manifold where it splits into 4 smaller tubes, these tubes are compressed using the 4 peristaltic bearings inside the 3D printed pump and passed back into the second chamber of the manifold to be combined into one tube	

that flows into the centre of the flow cell, the outlets are two thick tubes returning solution to the reservoir.....	112
Figure 58 CV of 0.1 mM $\text{Ru}(\text{NH}_3)_6^{3+}$ 0.2 M KNO_3 run at 0.1 V s^{-1} at different flow rates from stationary to 20 ml min^{-1}	114
Figure 59 Limiting current vs flow rate of 0.1 mM $\text{Ru}(\text{NH}_3)_6^{3+}$ 0.2 M KNO_3 at 0.1 V s^{-1} . Error bars are standard deviation, n=3, line resulting from fitting Equation 33 is shown in red, $R^2 = 0.990$	115
Figure 60 Cu CV in 100 μM $\text{Cu}(\text{NO}_3)_2$ and 0.2 M KNO_3 solution at 0.1 V s^{-1} , initial negative sweep direction.	116
Figure 61 XRF analysis of Cu electrodeposition from 100 μM $\text{Cu}(\text{NO}_3)_2$ and 0.2 M KNO_3 solution at a deposition potential of -0.5 V, flow rate of 20 ml min^{-1} for 900s where the test CV of 0.1 mM $\text{Ru}(\text{NH}_3)_6^{3+}$ in 0.2 M KNO_3 , 0.1 V s^{-1} prior to electrodeposition was adjusted to give different limiting currents as a proxy for electrode separation, higher limiting currents are equivalent to a closer separation.	117
Figure 62 Cu electrodeposition from 100 μM $\text{Cu}(\text{NO}_3)_2$ and 0.2 M KNO_3 solution at deposition potentials of, -0.5, -0.75, -1.0, -1.5 V at a flow rate of 20 ml min^{-1} for 900 s, error bars are standard deviation, n=3.	119
Figure 63 XRF analysis of Cu electrodeposition from 100 μM $\text{Cu}(\text{NO}_3)_2$ and 0.2 M KNO_3 solution at a deposition potential of -0.5 V at varying flow rates from stationary to 20 ml min^{-1} for 900 s, error bars are standard deviation, n=3.	120
Figure 64 XRF analysis of Cu electrodeposition from 2.5 to 100 μM $\text{Cu}(\text{NO}_3)_2$ and 0.2 M KNO_3 solution at a deposition potential of -0.5 V at a flow rate of 20 ml min^{-1} for 3600 s, error bars are standard deviation, n=3.	121
Figure 65 XRF spectra of the Cu $\text{K}\alpha$ line after deposition in 25 to 100 μM $\text{Cu}(\text{NO}_3)_2$ and 0.2 M KNO_3 solution at a deposition potential of -0.5 V at a flow rate of 20 ml min^{-1} for 3600 s, and then subsequently flushed with solution for 300 s at 20 ml min^{-1} with no applied potential.	122
Figure 66 Photographs of a) 20 ml min^{-1} and b) 5 ml min^{-1} at -0.5 V, c) -1.5 V deposition potential, 20 ml min^{-1} , all in 100 μM $\text{Cu}(\text{NO}_3)_2$ and 0.2 M KNO_3 for 900 s. Photographs have been brightened to improve visibility of deposits, a) the areas of the WE opposite the lasered hexagonal areas on the CE are highlighted, b) the area opposite the inlet on the CE and some bubbles that have disrupted deposition have been	

highlighted, c) the ring of deposit that is on the WE is highlighted and where the CE edge is relative to the WE.	123
Figure 67 a) photo of electrode surface b) XRF map for Cu, after deposition at -0.5 V, 1800 s, 100 μM $\text{Cu}(\text{NO}_3)_2$ and 0.2 M KNO_3 . In b) areas exhibiting a Cu signal are coloured red.	124
Figure 68 Summed XRF counts from 200 μm radius areas ($n=3$) at 4 different locations on the electrode surface from mapping data.....	125
Figure 69 Pourbaix diagram of 100 μM Cu a) only in water b) in 0.1 M KCl, at 25 $^\circ\text{C}$ made using Hydra Medusa. The pink shaded area indicates the acidic pHs of interest in this experiment, and the green the higher pH of interest. The green dashed lines indicate where the solvent electrolysis reactions occur in this system.	136
Figure 70 Speciation composition diagrams made using MINTEQA2 of 100 μM Cu^{2+} in 0.1 M a) acetate, b) sulfate c) nitrate and d) chloride at 25 $^\circ\text{C}$ for pH 1 to 12.	137
Figure 71 CV of 100 μM Cu^{2+} in 0.1 M acetate buffer, a) pH 3.6 , b) pH 5 with c) extended window of a), and d) extended window of b), on a 1 mm BDD macrodisk electrode, 0.1 V s^{-1} starting at 0 V in the negative direction to -2.5 V where the scan direction was reversed. All scans shown are the first scan.	145
Figure 72 Change in buffer capacity with respect to pH of a 0.1 M acetate buffer solution ($\text{pK}_a=4.76$), pink line denotes pH 3.6 and the green line denotes pH 5.....	146
Figure 73 Background CVs of pH 2 and pH 5 in 0.1 M, K_2SO_4 , KNO_3 and KCl, using a 1 mm BDD macrodisk electrode, 0.1 V s^{-1} starting at 0 V in the negative direction to -2.5 V where the scan direction was reversed.....	147
Figure 74 CVs of 100 μM Cu^{2+} in pH 2 with background electrolyte consisting of 0.1 M a) K_2SO_4 , b) KNO_3 , c) KCl, using 1 mm BDD macrodisk electrode, 0.1 V s^{-1} starting at 0 V in the negative direction to -2.5 V where the scan direction was reversed. The respective regions of interest are shown for each CV; d) K_2SO_4 , e) KNO_3 and f) KCl.	148
Figure 75 ASV stripping voltammograms of 100 μM Cu^{2+} in pH 2, 0.1 M respective background electrolyte aerated a) K_2SO_4 , b) KNO_3 , c) KCl, and deoxygenated d) K_2SO_4 , e) KNO_3 , f) KCl, 1 mm BDD macrodisk electrode, 0.1 V s^{-1} , after 300 s deposition in quiescent solution.	151

Figure 76 Raman spectra of bare BDD (background) and of deposits on BDD surface after electrodeposition at -0.4 V for 900s in 100 μM Cu^{2+} , 0.1 M K_2SO_4 pH 5 deoxygenated. Cu_2O peaks and the diamond Fano peak are seen. 100x objective lens, 488 nm laser at 10% power, 10 s acquisition time, 5 accumulations.....	155
Figure 77 FE-SEM images of BDD electrode surfaces after deposition for 300 s in 100 μM Cu^{2+} , pH 2 (0.1 M K_2SO_4), aerated solution a) and deoxygenated b) at i) -0.4 V, ii) -1 V and iii) -2 V. Scale bar 400 nm.....	156
Figure 78 FE-SEM images of BDD electrode surfaces after deposition for 300 s in 100 μM Cu^{2+} (pH 2, 0.1 M KNO_3) aerated solution a) and deoxygenated b) at i) -0.4 V, ii) -1 V and iii) -2 V. Scale bar is 400 nm.....	158
Figure 79 FE-SEM images of BDD electrode surfaces after deposition for 300 s in 100 μM Cu^{2+} (pH 2, 0.1 M KCl) aerated solution a) and deoxygenated b) at i) -0.4 V, ii) -1 V and iii) -2 V. Scale bar is 400 nm.....	159
Figure 80 CVs of 100 μM Cu^{2+} in pH 5 with background electrolyte consisting of 0.1 M a) K_2SO_4 , b) KNO_3 , c) KCl , using 1 mm BDD macrodisk electrode, 0.1 V s^{-1} starting at 0 V in the negative direction to -2.5 V where the scan direction was reversed. The respective extended window scans are shown for each CV; d) K_2SO_4 , e) KNO_3 and f) KCl	160
Figure 81 ASV stripping voltammograms of 100 μM Cu^{2+} in pH 5, 0.1 M respective background electrolyte aerated a) K_2SO_4 , b) KNO_3 , c) KCl , and deoxygenated d) K_2SO_4 , e) KNO_3 , f) KCl , 1 mm BDD macrodisk electrode, 0.1 V s^{-1} , after 300 s deposition in quiescent solution.	162
Figure 82 FE-SEM images of BDD electrode surfaces after deposition for 300 s in 100 μM Cu^{2+} , pH 5 (0.1 M K_2SO_4), aerated solution a) and deoxygenated b) at i) -0.4 V, ii) -1 V and iii) -2 V. Scale bar is 400 nm.	165
Figure 83 FE-SEM images of BDD electrode surfaces after deposition for 300 s in 100 μM Cu^{2+} , pH 5 (0.1 M KNO_3), aerated solution a) and deoxygenated b) at i) -0.4 V, ii) -1 V and iii) -2 V. Scale bar is 400 nm.	166
Figure 84 FE-SEM images of BDD electrode surfaces after deposition for 300 s in 100 μM Cu^{2+} , pH 5 (0.1 M KCl), aerated solution a) and deoxygenated b) at i) -0.4 V, ii) -1 V and iii) -2 V. Scale bar is 400 nm.....	168

Figure 85 FE-SEM images of BDD electrode surfaces after deposition for 300 s in 100 μM Cu^{2+} , pH 5 (0.1 M KCl), deoxygenated solution -0.4 V. Scale bar is 400 nm.....	169
Figure 86 Proposed mechanism for CO_2 reduction on Cu surfaces, adapted from ⁵	179
Figure 87 schematic of the electrochemical set up for the TEM samples. An SCE was the reference electrode (RE), a Pt counter electrode (CE), tweezers were used to connect to the Ti/Au contact on the BDD TEM electrode which was the working electrode.	186
Figure 88 a) chronoamperogram of electrodeposition on a 1 mm diameter BDD glass sealed electrode from 100 μM $\text{Cu}(\text{NO}_3)_2$ in 0.1 M KNO_3 for 300 s at -0.4 V b) example SEM image of the deposit formed on the BDD electrode electrodeposited by the method described above.....	188
Figure 89 Histogram of particle area from samples made by electrodeposition on a 1 mm diameter BDD glass sealed electrode from 100 μM $\text{Cu}(\text{NO}_3)_2$ in 0.1 M KNO_3 for 300s at -0.4 V.....	188
Figure 90 SEM image over two grains from a sample made by electrodeposition on a 10 x 30 mm rectangle of double sided polished BDD electrode (OLEMS electrode) from 100 μM $\text{Cu}(\text{NO}_3)_2$ in 0.1 M KNO_3 for 3 depositions of 300 s at -0.4 V.....	189
Figure 91 Histogram of particle area from SEM images from samples made by electrodeposition on a 1 mm diameter BDD glass sealed electrode from 100 μM $\text{Cu}(\text{NO}_3)_2$ in 0.1 M KNO_3 for 300s at -0.4 V. Blue shows particles from dark grains, red light grains.	190
Figure 92 Characterisation of an electrodeposited cube from 100 μM $\text{Cu}(\text{NO}_3)_2$ in 0.1 M KNO_3 for 300s at -0.4 V on a BDD TEM electrode, a) TEM image, b) EELS spectrum, c) FFT, d) simulation of Cu_2O FFT.....	191
Figure 93 FFT simulations of Cu^0 and Cu_2O along the [100], [110] and [111] directions.	193
Figure 94 Chronoamperograms of the 1, 10 and 20 s steps of electrodeposition for the IL STEM growth study on the BDD TEM electrode, deposited from 100 μM $\text{Cu}(\text{NO}_3)_2$ in 0.1 M KNO_3 at -0.4 V.	195
Figure 95 ac-ADF-STEM image of the BDD TEM electrode after a) 1 s, b) 10 s, c) 20 s of electrodeposition of Cu_2O from 100 μM $\text{Cu}(\text{NO}_3)_2$ in 0.1 M KNO_3 at -0.4 V. Red circle	

denotes particle 1, green, particle 2 and blue, particle 3. The yellow dotted line shows the edge of the hole (vacuum) in the BDD TEM electrode. The bright particles in the top right corner are Au nanoparticles that were used to help locate the area.....	195
Figure 96 Histogram of particle area of the particles in the IL STEM growth study.	197
Figure 97 High magnification ac-ADF-STEM image of particle 1 after a i) 1 s, b i) 10 s and c i) 20 s ii) respective FFTs of particle 1, deposited from 100 μM $\text{Cu}(\text{NO}_3)_2$ in 0.1 M KNO_3 at -0.4 V.	198
Figure 98 High magnification ac-ADF-STEM image of particle 2 after a i) 1 s, b i) 10 s and c i) 20 s ii) respective FFTs of particle 2, deposited from 100 μM $\text{Cu}(\text{NO}_3)_2$ in 0.1 M KNO_3 at -0.4 V.	199
Figure 99 High magnification ac-ADF-STEM image of particle 3 after a i) 10 s and b i) 20 s ii) respective FFTs of particle 3, deposited from 100 μM $\text{Cu}(\text{NO}_3)_2$ in 0.1 M KNO_3 at -0.4 V.	200
Figure 100 Intensity vs distance plots from the TEM images of a) particle 1 b) particle 2.....	200
Figure 101 a) chronoamperogram of the electrodeposition of Cu_2O for OLEMS, deposition was 3x -0.4 V for 300 s steps with 5 s intervals (OLEMS method), b) SEM of the Cu_2O modified BDD surface, from 100 μM $\text{Cu}(\text{NO}_3)_2$ in 0.1 M KNO_3	201
Figure 102 Histogram of particle areas from blue – the 1x method deposition and red – the 3x deposition.....	202
Figure 103 CV in 0.1 M K_2CO_3 solution at 0.1 V s^{-1} black line) blank BDD in CO_2 saturated solution, red line) Cu_2O modified BDD in CO_2 saturated solution and blue line) Cu_2O modified BDD in degassed solution (with Ar). BDD electrode was 1 mm diameter. All CVs are the first scan.	203
Figure 104 Photograph of the OLEMS headspace set up showing from a) above and b) side on. Showing working electrode (WE, BDD), reference electrode (RE), counter electrode (CE), CO_2 gas line in and product gas collection line out of the cell. The subaseal is making contact with the surface of solution so that the product gasses collect in the space above the BDD working electrode for collection.....	204
Figure 105 OLEMS product gas composition results in CO_2 saturated 0.1 M K_2CO_3 solution, 10x30 mm double sided BDD electrode held at -1.9 V vs NHE for 1 hour a)	

blank BDD electrode b), c) and d) 3 repeats of OLEMS on a Cu ₂ O modified BDD electrode.	205
Figure 106 SEM of Cu ₂ O modified BDD after 1 hour of electrocatalysis in CO ₂ saturated 0.1 M K ₂ CO ₃ solution at -1.9 V vs NHE.	206
Figure 107 Cu ₂ O modified BDD TEM electrode after a) 10 s and b) 3600s (1h) of CO ₂ RR electrocatalysis in CO ₂ saturated 0.1 M K ₂ CO ₃ solution at -1.9 V vs NHE.....	207
Figure 108 High magnification TEM images of nanoparticles on a Cu ₂ O modified BDD TEM electrode after a) 10 s and b) 3600 s of CO ₂ RR electrocatalysis in CO ₂ saturated 0.1 M K ₂ CO ₃ solution at -1.9 V vs NHE.....	208

List of Tables

Table 1 Table of chemicals used, purity and supplier.....	50
Table 2 Acceptable values for electrode characterisation	54
Table 3 Current increase possible relative to no induced mass transport in each system.	96
Table 4 Particle statistics summary from data in Figure 91. Median side length calculated assuming cubic particles	190
Table 5 particle size statistics for the electrodeposition IL STEM growth study. Median side length calculated assuming cubic particles.....	196
Table 6 Particle size statistics for the 1x and 3x depositions. Median side length calculated assuming cubic particles.	202

Abbreviations

ASV	Anodic stripping voltammetry
BDD	Boron doped diamond
CE	Counter electrode
CO₂RR	Carbon dioxide reduction reaction
CVD	Chemical vapor deposition
DME	Dropping mercury electrode
DPV	Differential pulse voltammetry
EC-XRF	Electrochemical x-ray fluorescence spectroscopy
EDXRF	Energy dispersive x-ray fluorescence spectroscopy
EELS	Electron energy loss spectroscopy
HER	Hydrogen evolution reaction
HMDE	Hanging mercury drop electrode
HOMO	Highest occupied molecular orbital
HPHT	High pressure high temperature
IHP	Inner Helmholtz plane
LOD	Limit of detection
LSV	Linear sweep voltammetry
LUMO	Lowest unoccupied molecular orbital
MTFE	Mercury thin film electrode
NP	Nanoparticle
NRR	Nitrate reduction reaction
OHP	Outer Helmholtz plane
ORR	Oxygen reduction reaction
RDE	Rotating disk electrode
RE	Reference electrode
SCE	Saturated calomel electrode
SEM	Scanning electron microscopy
SW	Solvent window
TEM	Transmission electron microscopy

WDXRF	Wavelength dispersive x-ray fluorescence spectroscopy
WE	Working electrode

Acknowledgements

I would like to thank the Warwick Electrochemistry and Interfaces group, Bruker, The Birmingham University Ampere group and the Diamond Science and Technology Centre for Doctoral Training for their support and knowledge. I would especially like to thank Dr Tania Read, Dr Haytham Hussein, Dr Sam Cobb, Dr Paramaconi Rodriguez, Dr James Teahan, Dr Gabriel Meloni, Georgia Wood, Nicole Reily, and Josh Tully for their help, support and friendship with science, sports, food and general sanity. I also want to thank Rod Wesson, Lee Butcher and Marcus Grant for all their help, knowledge and patience when making bespoke bits of kit.

Declarations

This thesis is my own work and has not been submitted for a degree at another university.

The work presented was carried out by myself, except in the following cases: some Introduction sections relating to heavy metal analysis and anodic stripping voltammetry were adapted from the review cited below, written with Nicole Reily. The electrochemical x-ray fluorescence data on prototype 3 in chapter 1 was collected in conjunction with Nicole Reily. The design and fabrication of the bespoke systems for electrochemical-x-ray fluorescence was done with help from Rod Wesson, Marcus Grant and Lee Butcher from electrical and mechanical workshops. TEM imaging was carried out by Dr Haytham Hussein who also aided with the electrochemical data collection and data analysis for the TEM studies. The on-line electrochemical mass spectrometry experiments were carried out in the Ampere Group labs at Birmingham University with the help of Dr Paramaconi Rodriguez.

Parts of the Introduction were published as:

Addressing the practicalities of anodic stripping voltammetry for heavy metal detection: a tutorial review. Alexandra J. Borrill, Nicole E. Reily and Julie V. Macpherson. The Analyst, 2019, 144, 6834. DOI: 10.1039/c9an01437c

Chapter 3 is in preparation for publication.

Chapter 4 is in preparation for publication.

Abstract

Metals and metal ions are of great importance to our health and environment as well as having a range of technological applications. Many metals and metal ions are toxic, some even at extremely low concentrations such as Hg, whilst others are required for biological function such as Fe and Cu. As metals in different forms are prevalent in our environment it is important to have cheap, fast and reliable methods of analysing them down to the ppb level. Electrochemistry is a powerful tool for analysis and fundamental investigations due to its flexibility, sensitivity and relatively low cost. Electrochemical methods can be easily coupled with other techniques such as spectroscopy or microscopy to add a new dimension to the analysis, such as with electrochemical x-ray fluorescence spectroscopy (EC-XRF). Here the metal is pre-concentrated on an electrode surface by electrodeposition and then chemically interrogated using XRF. Previous EC-XRF studies have suffered from cumbersome set-ups, preventing progress to commercially viable systems. In this thesis, the coupling of different mass transport systems to different more user-friendly set-ups is explored for both *in situ* and *ex situ* EC-XRF methodologies.

Metals, particularly transition metals, are especially interesting elements with potentially useful properties for electrocatalysis, but often present challenges for analysis. For example, Cu is used as an electrocatalyst for the CO₂ reduction reaction (CO₂RR) that produces feedstocks and fuels from the unwanted greenhouse gas, this is important technology for the future of the environment and sustainable chemistry. Cu catalysts are extremely well suited to this application as the materials are cheap and abundant, while favourable reductions in overpotential and improved product ratios have been observed. However, the mechanism is not fully understood, and the degradation of these catalysts leads to loss of activity. Understanding the electrodeposition and growth of Cu nanoparticles is important for their application to the CO₂RR. Herein, the electrodeposition of Cu nanoparticles was investigated in different pH and electrolyte solutions. The ability to quickly and reproducibly grow Cu nanocube electrocatalysts in a single electrochemical step without the use of any

additives other than standard electrochemical electrolytes was demonstrated. The growth mechanism and degradation of these structures during electrocatalysis was followed using Transmission Electron Microscopy (TEM) on Boron Doped Diamond (BDD) TEM electrodes, allowing multi-step experiments.

1. Introduction

1.1. Electrochemistry

Electrochemistry is the study of chemical phenomena caused by or resulting in electrical energy. It covers many areas including batteries, solar cells, corrosion, electroplating, sensing and analysis.¹ Around 1800 Volta discovered that a current was produced at the junction between two different metals, leading to the invention of the battery (Volta pile),² wherein an electrochemical equilibrium is set up that can be described by Equation 1.



where O is the oxidised species, R is the reduced species, n is the number of electrons, e^- , transferred in the reaction and k_{red} and k_{ox} are the rate constants of reduction and oxidation respectively.

Building on this, the quantitative analysis of reactions can be related to the free energy, ΔG , and the electrode potential, E , by Equation 2 and Equation 3.

$$\Delta G = \Delta G^0 + R_m T \ln Q \quad \text{Equation 2}$$

$$\Delta G = -nFE \quad \text{Equation 3}$$

where the reaction quotient Q , is the ratio of the concentration of products over reactants, the free energy change of the reaction under standard conditions is ΔG^0 , R_m being the molar gas constant and T the temperature in kelvin and F is Faraday's constant.

Equation 2 and Equation 3 can be combined to give the Nernst equation (Equation 4). The Nernst equation describes how E depends on both the standard potential for the reaction, E^0 and the concentration of products and reactants, and temperature.¹

$$E = E^0 - \frac{R_m T}{nF} \ln Q \quad \text{Equation 4}$$

1.1.1. Dynamic Electrochemistry

Applying E to an electrochemical cell causes a current, i , to flow due to either an oxidation or reductive process. In equilibrium processes both can flow (equation 1). i depends on n , the area of the electrode, A in cm^2 , and the flux, j in $\text{mol cm}^{-2} \text{s}^{-1}$, as shown in Equation 5.

$$i = nAFj \quad \text{Equation 5}$$

Dependant on whether the reaction is mass transfer or electron transfer controlled, j is described by Equation 6. For a mass transfer controlled process, k is represented by k_t a rate constant representing mass transfer in the system, whilst for a kinetically controlled process, k represents an electron transfer rate constant e.g. $k_{red/ox}$ in Equation 6 or k_0 (the intrinsic rate constant at E_0). C describes the concentration of the electroactive species at the electrode surface.

$$j = kC \quad \text{Equation 6}$$

1.1.2. Electron transfer kinetics

Many reactions operate under conditions of electron transfer controlled kinetics i.e. where the rate of mass transfer is higher than the rate of electron transfer between e.g. O being reduced to R . This electron transfer process, as for other chemical reactions, can be represented on a free energy vs reaction coordinate plot, illustrated in Figure 1.

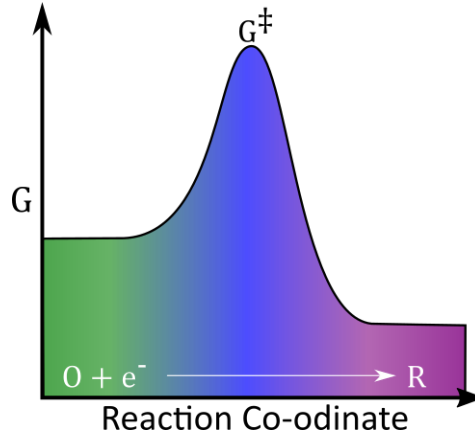


Figure 1 Reaction co-ordinate graph vs. free energy of the reaction showing the transition state.

Transition state theory gives us a predicted rate of this reaction in the Arrhenius form in Equation 7.

$$k_{red} = \mathcal{A} \exp\left(\frac{-\Delta G_{red}^{\ddagger}}{RT}\right) \quad \text{Equation 7}$$

Where $\Delta G_{red}^{\ddagger}$ is the free energy of activation, \mathcal{A} is a factor to include collision frequency rates of O with the electrode surface. The activation free energy for the reverse reaction (ΔG_{ox}^{\ddagger}) is simply the energy difference between R and the transition state (G^{\ddagger}). The transfer coefficient, α , is a descriptor of how closely the transition state behaves like reactants (approaches 0) or products (approaches 1). A value of $\alpha = 0.5$) is often assumed, and considered appropriate for many reactions.³ The reduction (and oxidation) rate constants as a function of electrode overpotential ($E - E^0$), η , can be written as Equation 8 and Equation 9.

$$k_{red} = k_{red}^0 \exp\left(\frac{-\alpha F \eta}{RT}\right) \quad \text{Equation 8}$$

$$k_{ox} = k_{ox}^0 \exp\left(\frac{(1 - \alpha) F \eta}{RT}\right) \quad \text{Equation 9}$$

Where k_{red}^0 and k_{ox}^0 are constants that are independent of η . A simplification can be used if no current flows when $C_{ox} = C_{red}$ and $\eta = 0$, as this means that these two rates are equal and can be written as k^0 . These rate equations can be combined to form an overall expression for the current at the working electrode, under conditions where both oxidation and or reduction is happening (Equation 1). This is a form of

the Butler-Volmer equation, Equation 10.¹ Under conditions of high η , the equation can be simplified to just either the reductive or oxidative branch of the equation.

$$i = F A k^0 \left(\exp \left\{ \frac{(1 - \alpha) F \eta}{RT} \right\} [R]_o - \exp \left\{ \frac{-\alpha F \eta}{RT} \right\} [O]_o \right) \quad \text{Equation 10}$$

The effect of η can also be illustrated by relating the position of the Fermi level of electrode surface to that of the highest occupied molecular orbital (HOMO) and the lowest unoccupied molecular orbital (LUMO) of the reactant molecule, Figure 2. For e.g. a reduction process, when the Fermi level is below the LUMO no electron transfer occurs. Upon the application of a negative potential the Fermi level is raised, when its energy exceeds that of the LUMO of the reactant, electron transfer occurs from the electrode to the reactant molecule, the more the level is raised the greater the rate constant for electron transfer, k_{red} .

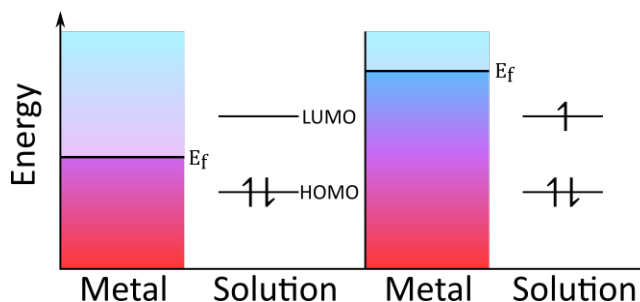


Figure 2 The fermi level (E_f) of the electrode material and the HOMO and LUMO of the reactant are shown schematically.

This, however, does not explain why rate constants are different for different electron transfer reactions, ranging from 'reversible' (fast kinetics) to 'irreversible' (slow kinetics). Marcus theory,⁴ Figure 3, provides a more in depth understanding.

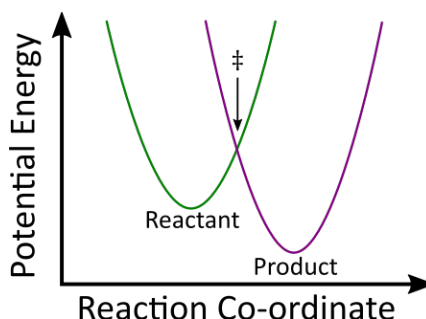


Figure 3 Reaction co-ordinate vs. potential energy graph showing overlapping curves for product and reactant, the crossover denoting the transition state.

Figure 3 shows the potential energy curves for products and reactants, e.g. *O* and *R*. The relative positions of the curves on the reaction co-ordinate correspond to the solvated geometries of the molecule or complex in solution. Electron transfer occurs orders of magnitude faster than nuclear vibrations and so bond lengths are essentially fixed on the timescale of electron transfer and it can only occur where the nuclear coordinates of the reactants and products overlap, this is known as the Franck-Condon principle.⁵⁻⁷ It can be observed that for greater differences in geometries of the solvated products and reactants, the intersection of the curves representing the transition state is at a much higher energy, meaning a higher energy barrier needs to be overcome to progress the reaction.

Inner-sphere reactions proceed through specific adsorption of the reactant, intermediate or ligand on the electrode surface, within the double layer and are therefore extremely surface dependent.⁸ This adsorbed state requires disruption to the solvation shell. In contrast, outer-sphere reactions do not require adsorption or reorganisation of the solvation shell for electron transfer, they must only be close enough to the surface for electron transfer (tunnelling) to be possible.^{8,9} Many outer sphere reactions involve very fast electron transfer, which is made possible by retaining the same geometry and solvation shell structure in products and reactants, while changing only the charge state of the metal. Reactions that are inner-sphere and require extensive solvation shell reorganisation, tend to have much slower kinetics,⁴ which in turn are influenced by the nature of the analyte-electrode interaction. There are, of course, many scenarios which lie in between these two extremes.

1.1.3. Mass Transport Theory

Calculation of the theoretical currents for a system requires understanding of both the electron transfer kinetics and the rate of transport of electroactive species to the surface of the electrode. There are three main forms of mass transport: (i) diffusion; (ii) migration and (iii) convection. Diffusive flux occurs when there is a concentration gradient, in this case when the electroactive species is being consumed at the

electrode surface. Fick described the diffusional flux, j_d , down a linear gradient to a planar surface in Equation 11. Equations are displayed only in one-dimension for simplicity.

$$j_d = -D \frac{\partial C}{\partial x} \quad \text{Equation 11}$$

D is the diffusion coefficient of electroactive species, in $\text{cm}^2 \text{s}^{-1}$. Equation 11 can be extended to include the change in concentration at the electrode surface with respect to time, t , to give Equation 12, Fick's second law.

$$\frac{\partial [O]}{\partial t} = -D \frac{\partial^2 C}{\partial x^2} \quad \text{Equation 12}$$

Equation 13, the Cottrell equation, can be derived from Equation 11 and Equation 5, and used to calculate the diffusion controlled current on a planar electrode as a function of time. The bulk concentration of electroactive species is given by C_{bulk} .

$$i = \frac{nFA\sqrt{D}C_{\text{bulk}}}{\sqrt{\pi t}} \quad \text{Equation 13}$$

Migration occurs when an electrostatic force is applied to ions in solution, moving them to or from the source. In electrochemistry the potential drop between the electrode and solution can cause migration of charged electroactive species in addition to diffusion. The migratory flux is related to the charge on the species z_i , the concentration, diffusion coefficient and the potential gradient.

$$j_m = -Dz_iC \frac{F}{RT} \frac{\partial \phi}{\partial x} \quad \text{Equation 14}$$

Migration can be eliminated experimentally by the addition of an inert background salt (supporting electrolyte) typically at least two orders of magnitude higher in concentration than the electroactive species, resulting in a much-reduced double layer thickness. The added electrolyte also constitutes the majority migratory ions in solution. Ions in solution act to balance the charge on the electrode by forming an electrical double layer with the electrode surface that extends into solution, Figure 4. More advanced models of the double layer exist, such as the Gouy-Chapman model which defines the placement of ions according to the energy of the system due to Maxwell-Boltzmann statistics.^{1,10}

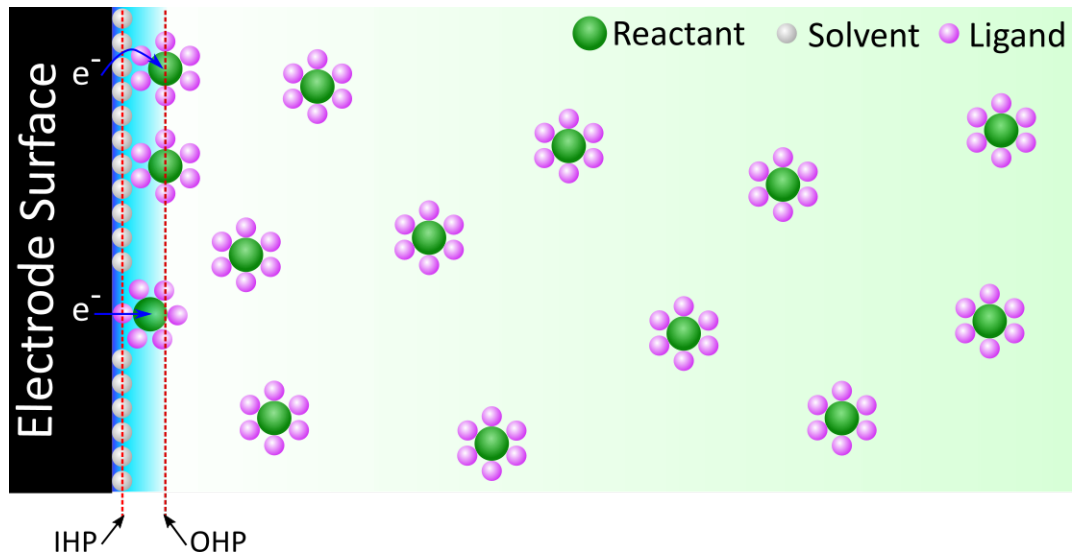


Figure 4 Schematic of the double layer showing the Inner Helmholtz Plane (IHP) and the Outer Helmholtz plane (OHP). Charged molecules in the solvent line up against the charged surface of the electrode, forming a capacitor, while remaining surface charge is compensated by increased concentration of counter-ions in the diffuse layer of electrolyte, gradually giving way to bulk solution concentrations.

The double layer shields the bulk solution from the charge on the electrode, so that analyte ions only feel the effect of the electrode potential when very close to its surface. Therefore, migration effects are largely ignored unless low conductivity solutions or thin layer cell electrodes are being used.

Convection describes any mass transport that occurs due to a pressure gradient, such as temperature gradients or forced solution flow by mechanical means. Deliberately induced convection is often used to reduce experimental times, or provide quantitative, predictable hydrodynamics for analytical applications. The flow in a system can be described by the incompressible Navier-Stokes equation, Equation 15.

$$u \frac{\partial u}{\partial x} = \frac{1}{\rho} \left(-\frac{\partial p}{\partial x} + \mu \frac{\partial^2 u}{\partial x^2} + g \right) \quad \text{Equation 15}$$

Where u is solution velocity, ρ is the density, p is the pressure, μ is the viscosity and g is used to couple the Navier-Stokes to transport from the electric field. Convective flux, j_c is given by Equation 16.

$$j_c = uC \quad \text{Equation 16}$$

Diffusion, migration and convection can be combined to give the Nernst-Planck equation, Equation 17, for total flux of species along one dimension.¹

$$j = -D \frac{\partial C}{\partial x} - Dz_i C \frac{F}{RT} \frac{\partial \phi}{\partial x} + uC$$

Equation 17

1.1.4. Practical Systems for Mass Transport

Experimentally mass transport can be controlled in many ways. For quantitative applications such as electroanalysis or the determination of electron transfer kinetics, it is important that mass transport of analyte to the electrode is known, reproducible and high. To illustrate the enhancements achieved with different mass transport systems we first consider a macroelectrode operating under diffusion-controlled stationary conditions for oxidation of a fast electron transfer electroactive species Figure 5 a), and the corresponding example current-voltage response (voltammogram) in e).

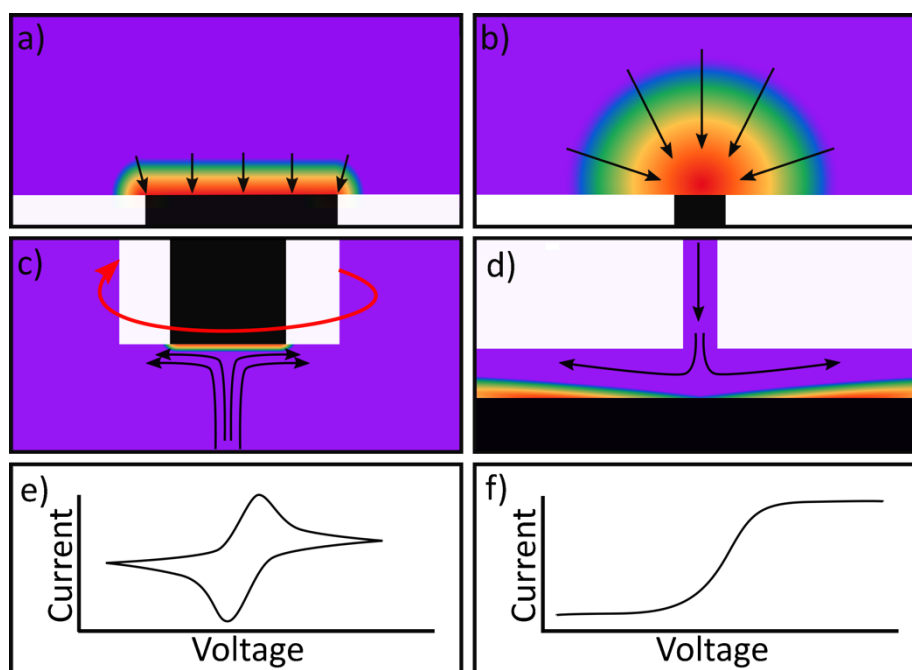


Figure 5 Concentration diffusional profiles at a) macro electrode, b) micro electrode c) rotating disc electrode and d) wall-jet electrode (adapted from ¹¹). The arrows represent the flux of electroactive reactant whilst the purple represents the bulk concentration. Voltammogram e) is typical of a diffusion controlled system such as a macroelectrode. Voltammogram f) is typical of a system which can reach a transport limited steady state current such as microelectrodes, rotating discs and flow systems.

The peak current under planar diffusion-controlled conditions is described empirically by the Randles-Sevcik equation (Equation 18).¹

$$i_p = 0.4463nFAC\left(\frac{nFvD}{RT}\right)^{\frac{1}{2}} \quad \text{Equation 18}$$

Where i_p is peak current and v is scan rate. The mass transport limited flux in the system is related to the current passed by Equation 5 where j is equal to $k_t C$. Electron transfer is omitted here as mass transport is the rate limiting step. Thus under stationary conditions, $k_t = 269000n^{1/2}D^{1/2}v^{1/2}F^{-1}$ (for $T = 298$ K) and for the exemplary case of a 1 mm planar disk electrode (assuming $n = 1$, $D = 1 \times 10^{-5} \text{ cm}^2 \text{ s}^{-1}$ and $v = 0.1 \text{ V s}^{-1}$), is 0.0028 cm s^{-1} . As the electron transfer process is initiated the current begins to flow and the electroactive species is depleted at the surface, setting up a diffusion gradient. As the potential is increased the concentration at the electrode surface approaches zero and planar diffusion limitations dominate, resulting in current that peaks then falls.

One way of increasing mass transfer is by decreasing the size of the electrode such that the diffusional flux profile changes from linear to hemispherical (Figure 5 b)),¹² such electrodes are referred to as micro or nanoelectrodes. Equation 19 describes the theoretical steady-state current at an inlaid planar disk micro (and smaller) electrode in stationary solution, see CV in Figure 5 f).

$$i_{lim} = 4nrFDC \quad \text{Equation 19}$$

where i_{lim} is the limiting current and r is the electrode radius. Under these conditions $k_t = 4D/\pi r$. Hence by shrinking the electrode diameter by three orders of magnitude, from 1 mm to 1 μm , k_t is now nearly two orders of magnitude bigger, 0.25 cm s^{-1} (for $D = 1 \times 10^{-5} \text{ cm}^2 \text{ s}^{-1}$). Voltammograms for microelectrodes reach a steady state limiting current because hemispherical diffusion is very fast and they become limited by electron transfer kinetics. Although microelectrodes generate much less current, they suffer less from capacitive charging (the area is much smaller), and can be used at fast scan rates, in low conductivity and high resistivity solutions (ohmic drop effects are not significant).¹³ The main drawback of the smaller current can be overcome by moving to microelectrode arrays.¹⁴

Many systems couple convective flow to diffusion as a means of increasing mass transport in the system (referred to as hydrodynamics). A popular choice is the

rotating disk electrode (RDE)^{15,16} which provides well defined hydrodynamics and results in the concentration gradient being confined to a much smaller distance from the electrode surface compared to the stationary macrodisk electrode, Figure 5 c). The hydrodynamics for an RDE are very well understood, being first characterised by Levich and Landau in 1942.¹⁷ As the RDE rotates, solution moves towards the outside of the electrode due to centrifugal force and fresh solution is drawn towards the electrode face. The Levich equation (Equation 20) describes the relationship between limiting current (i_{lim}) and rotation frequency, ω (Hz);

$$i_{lim} = 1.554nFAD^{\frac{2}{3}}\omega^{\frac{1}{2}}\nu^{\frac{-1}{6}}c \quad \text{Equation 20}$$

where ν is kinematic viscosity. By rotating at 50 Hz (for $D = 1 \times 10^{-5} \text{ cm}^2 \text{ s}^{-1}$ and $\nu = 0.01 \text{ cm}^2 \text{ s}^{-1}$ for water at room temperature) k_t is almost an order of magnitude larger than that of the same diameter (= 1 mm) stationary disk electrode = 0.011 cm s^{-1} . The RDE voltammogram is also at steady state as the convective flux means transport to the electrode surface is fast.

Other examples of well-defined hydrodynamic systems include the wall-jet electrode, depicted in Figure 5 d),^{18,19} the wall-jet is described by Equation 21.

$$i_{lim} = 1.597k_{mj}r^{\frac{3}{4}}\nu^{\frac{-5}{12}}D^{\frac{2}{3}}a^{\frac{-1}{2}}V_f^{\frac{3}{4}}C \quad \text{Equation 21}$$

k_{mj} , is a unitless constant describing the momentum flux (0.90), a is the jet diameter in cm, V_f is the volume flow rate of solution in $\text{cm}^3 \text{ s}^{-1}$.²⁰ Other well defined flow systems exist such as channel flow electrodes and tubular flow electrodes (current is proportional to $V_f^{1/3}$ for both).^{21–23}

Less well-defined mass transport systems are also found such as sonication, vibration and even magnetic stirring,^{24,25} however, these are less prevalent in the literature. Sonication uses an ultrasonic tip, either placed close to the electrode face or acting as the electrode (sonotrode). The smaller the electrode tip separation, the greater the current increases (over an order of magnitude).²⁶ Although giving large solution velocities, sonication can be difficult to use practically; it is very dependent on maintaining exact cell geometries and separations. There is also an issue of

ultrasound induced surface effects. These can be individual cavitation events, erosion of the electrode surface or the increase in faradaic processes such as gas evolution or solvent splitting. All result in variability in the currents which increase as electrode – tip separation is decreased. Mechanical damage to electrodes is also possible caused by heating of components and mechanical wear due to the high frequencies employed (10s of kHz).^{27,28}

Vibration, being a similar mode, but using lower frequencies (1-10s Hz), also shows useful but lower increases in currents (doubling) compared to sonication and has generally been applied to small electrodes (1 mm or less). It is generally the electrode itself that is vibrated rather than having a tip vibrate, as in sonication. The lower frequencies, although gaining only a modest increase in currents, do not have ultrasound induced surface effects. Vibration is much less damaging and causes less heating, but again, the practicalities of this set-up are challenging and cell dependent.^{29,30} It has been found that the main factor for increasing the current is vibration frequency with an $f^{\frac{1}{2}}$ relationship. The amplitude of oscillation has been shown to have little effect.^{25,31}

1.2. Electrochemical set-up

1.2.1. Three Electrode Cell

A typical experimental electrochemical cell requires a working electrode (WE), a reference electrode (RE), and a counter electrode (CE), Figure 6.

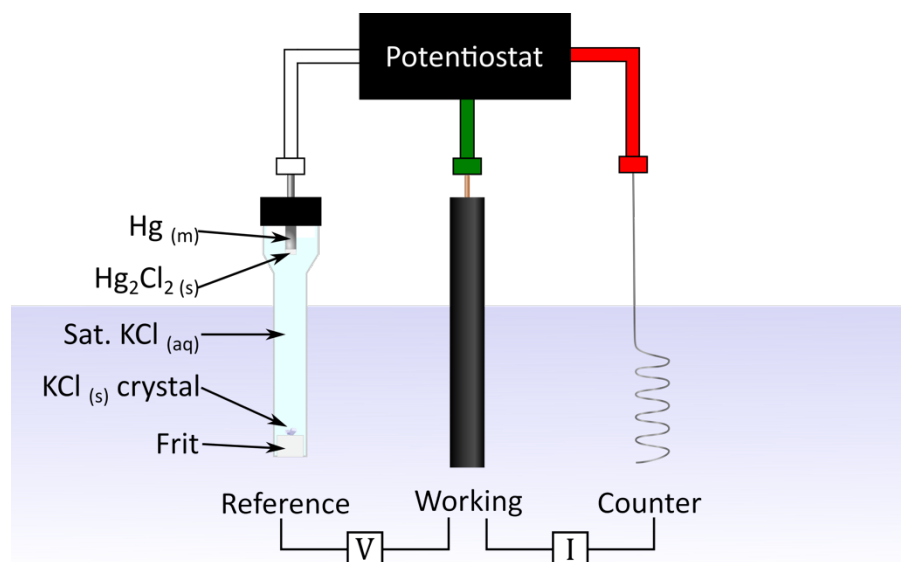


Figure 6 The three-electrode set-up showing a saturated calomel reference electrode (SCE) a working electrode and a metal coil counter electrode and their functions in the electrochemical circuit.

The WE, where the reaction of interest occurs, must be well defined and understood to enable useful analysis of the results. The WE is typically made from highly conductive materials such as metals, some inorganic semiconductors and carbon materials. The voltage is applied between the WE and the RE, which is used to define a reference potential. REs, such as the Saturated Calomel Electrode (SCE), are used as they maintain a constant, known potential inside the electrode and are in contact with the solution through a frit. They only maintain a constant potential if their equilibrium is not disturbed, for example by being forced to pass a current.

This is why the third electrode, the CE is required for most macroelectrode set-ups. They are generally high surface area inert metals such as a Pt coil or mesh and are present to make sure no current flows through the RE, instead it moves from CE to WE. The CE will swing out to a voltage necessary to produce an equal but opposite current to that of the WE, most often due to solvent electrolysis. To prevent the products of CE electrolysis interfering with the reaction of interest, it is advised to not situate the CE too close to the WE. However symmetrical placement of the CE is advised such that a uniform current flow is experienced. If placed too close, there is also the issue of mass transport around the WE being affected. Ohmic drop (Equation

22), where \mathcal{R} is resistance, is an important consideration when considering placement of the WE and RE, as solution resistance between these two electrodes is not compensated for by a standard potentiostat.

$$E = i\mathcal{R} \quad \text{Equation 22}$$

Background electrolyte helps to mitigate ohmic drop by decreasing the solution resistance. Often a Luggin capillary is recommended to locate the RE as close to the WE as possible. However, disturbances in the mass transfer profile to the WE must also be considered.

1.3. Boron Doped Diamond

Diamond is well known as a gemstone of exceptional strength, it is also an extremely useful material for several scientific and technological applications including grits, drill bits, speaker domes, lenses, waveguides, heatsinks, x-ray detection and quantum computing.^{32,33} For these applications synthetic intrinsic diamond is used. Electrochemical applications require highly conducting materials, and when doped with boron (BDD) diamond becomes semiconducting and blue in colour. At high B concentrations BDD appears black and exhibits conductivity comparable to metallic materials, enabling use as an electrode material whilst maintaining most of its exceptional properties, the obvious exception being its visible light transmission.³⁴

1.3.1. Structure, Growth and Properties

Diamond is a lattice of sp^3 bonded carbon but by replacing a carbon with a boron atom a hole is introduced as boron has one less electron than carbon, see Figure 7 a). These holes are created just above the valence band, which enables conduction, via variable-range hopping of holes.³⁵ An increase in doping results in higher conductivities making BDD a p-type semiconductor where thermal activation is not required to pass a current. Doping concentrations of about 10^{20} atoms cm^{-3} are used for electrochemistry.^{32,34} The quality of BDD can be determined using Raman spectroscopy as the signatures for sp^2 and sp^3 bonded carbon differ; the extent of

boron doping can be assessed by the shift of the sp^3 peak and the existence of a Fano resonance displaying asymmetry which arises due to metallic levels of doping.³⁶

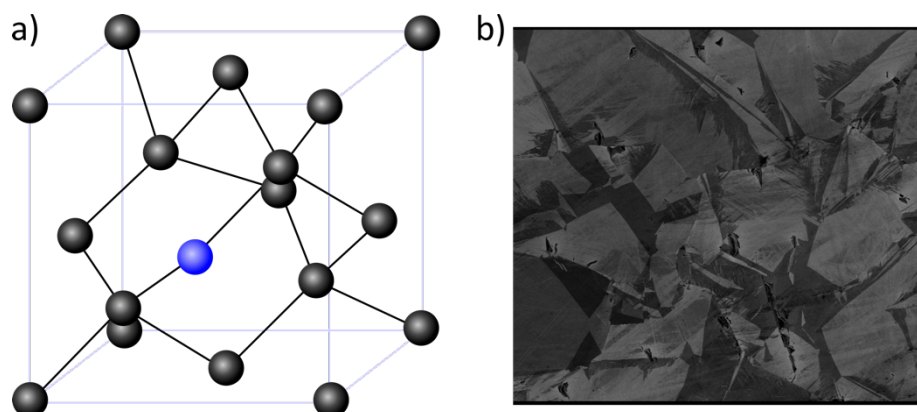


Figure 7 a) the structure of BDD showing carbon (black) and boron (blue) atoms, b) scanning electron microscopy (SEM) image of the surface of BDD showing the grain structure of a typical electrochemical grade sample.

The BDD used for electrochemistry is grown synthetically using chemical vapour deposition (CVD). This process uses a substrate and seed crystals in a vacuum chamber with a controlled flow of a gas mixture. A plasma from a hot filament or microwave energy creates radicals and induces growth on the seeds. The BDD used here is polycrystalline as it is much faster and cheaper to grow large area wafers, making it commercially viable. These wafers are removed from the substrate, polished on the growth face and lapped on the nucleation face after synthesis, see Figure 7 b). Other methods of synthetic diamond growth are used in industry such as high temperature, high pressure (HPHT),³⁷ but CVD is most popular for scientific applications.^{32,33}

1.3.1. Electrochemistry of BDD

BDD has excellent electrochemical properties, it has a wide solvent window (SW) due to the electrocatalytically inert surface, low capacitance and is insensitive to dissolved oxygen.³⁸ Depending on the CVD growth method adopted BDD electrodes can have small amounts of non-diamond sp^2 bonded carbon material present at (most likely) the grain boundaries between crystals from the growth. These regions are more electrocatalytic and can reduce the size of the SW, make the surface more active towards oxygen reduction and be responsible for larger observed capacitances. Using microwave-CVD is it possible to produce high quality BDD with

negligible sp^2 bonded carbon.^{32,33} BDD also displays excellent signal to noise ratios, resistance to corrosion in extreme conditions, resistance to biofouling and high stability.^{34,38–41}

1.4. Heavy Metal Detection

Heavy metals are defined as naturally occurring elements with a high atomic weight and density.⁴² A number of heavy metals are found on the Environmental Quality Standards Directive List including As, Cd, Cu, Cr, Fe, Pb, Hg, Ni and Zn, which are highlighted as priority substances for assessment of water quality.⁴³ Whilst some heavy metals are essential to life in trace quantities, they can be toxic at higher concentrations.^{44,45} Others, in comparison, are toxic even in small quantities.^{46–48} Identification and detection is thus essential, down to very low concentrations, sub-ppb. Although heavy metals occur naturally within the environment, anthropogenic activities have led to an increase in their abundance within the natural system,⁴² with water bodies and sediments often acting as sinks for pollutants. Some heavy metals bioaccumulate up the food chain, so analysis of primary sources is necessary for entire ecosystem health.⁴⁹ Quantitative heavy metal analysis is not only important in environmental systems but in pharmaceuticals,^{50–52} food stuffs,^{53,54} and biological samples such as blood, urine and human hair.^{55–59}

Importantly, the speciation of a metal controls its bioavailability and therefore toxicity. Compounds only pose a biological risk if they are able to cross membranes, which is the case for free (hydrated) metal ions and lipid soluble complexes.^{60–63} Metals that are strongly bound to ligands or inorganic particles (and are not lipid soluble) are often considered non-toxic or inert. Labile metal complexes have weakly coordinating ligands; the more labile the metal the higher the rate of ligand exchange.

Inductively Coupled Plasma–Mass Spectrometry (ICP-MS) and ICP-Optical Emission Spectrometry (OES) are the main techniques used for heavy metal detection. Whilst both can detect ppb concentrations, ICP-MS instruments are capable of ppt detection

limits.^{64–66} For analysis, these techniques require samples to be processed and analysed in a laboratory. The instrumentation is large, expensive and requires a trained operative. Such methods are not easily adaptable to “at the source” measurements. Prior to analysis, the solution is typically strongly acidified (< pH 2), forcing all metal ions, whether strongly bound or not, into the free state. Solid samples are acid digested to form acidic solutions prior to analysis. In contrast Anodic Stripping Voltammetry (ASV) offers less complex, lower cost and smaller footprint instrumentation with similar sub-ppb limits of detection (LOD).^{67,68} It has thus long been proposed as a viable technique for at the source or on-line heavy metal detection.^{63,69–71}

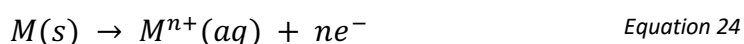
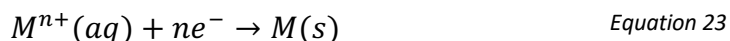
1.4.1. Anodic Stripping Voltammetry (ASV)

ASV has been shown to be capable of detecting up to thirty different elements,^{72,73} although some, e.g. As, require more involved detection protocols than others.⁷⁴ Whilst the bulk of analysable species for ASV are metals, cathodic stripping voltammetry and adsorptive stripping voltammetry (not discussed herein) can be used to determine concentrations of organic and inorganic compounds such as sulfides, thiols, halides,^{16,72} pesticides and pharmaceuticals.^{75,76} In contrast to ICP techniques, unless the solution is deliberately acidified, ASV provides information on the concentration of free/labile metal at the measurement pH of the solution. Interestingly, despite substantial literature on the subject little commercial activity using ASV has emerged, suggesting the methodology is challenging to implement. This section aims to address why this is by developing an understanding of the factors involved and the challenges associated with ASV.

Historically, Hg was the WE of choice for ASV in a dropping mercury electrode (DME) or thin film format.^{73,77} However, as Hg now features in the top ten chemicals of major public health concern⁷⁸ it is no longer a commercially viable electrode material and all existing Hg-based products are being phased out in accordance with the 2013 Minamata Convention.⁷⁹ Thus there is a need to find alternative electrode materials for ASV with many papers dedicated to attempts to find electrode materials that rival liquid Hg.^{16,80}

1.4.1.1. ASV Theory

ASV involves a two-step process. First cathodic reduction of a labile or free metal ion to its zero-valence metallic state on the electrode surface, a process known as electrodeposition, Equation 23, which is a widely researched area.^{81–83} Deposition is often carried out at a potential more negative than the formal standard potential of the M^{n+}/M redox couple, $E^{0'}$, for a suitable time period (seconds to hours), under controlled and known mass transfer conditions. This is the pre-concentration step.



To improve the limit of detection (LOD) the pre-concentration time is typically extended or the rate of deposition increased; the latter achieved by increasing the mass transfer rate to the electrode, or the applied overpotential.^{63,73} Pre-concentration is followed by anodic oxidation (known as stripping or dissolution), of the metal back to metal ions, Equation 24; the stripping step. Figure 8 illustrates these processes. Hence electrode material, deposition potential (E_{dep}) and mass transfer are all important factors for consideration.⁸⁴

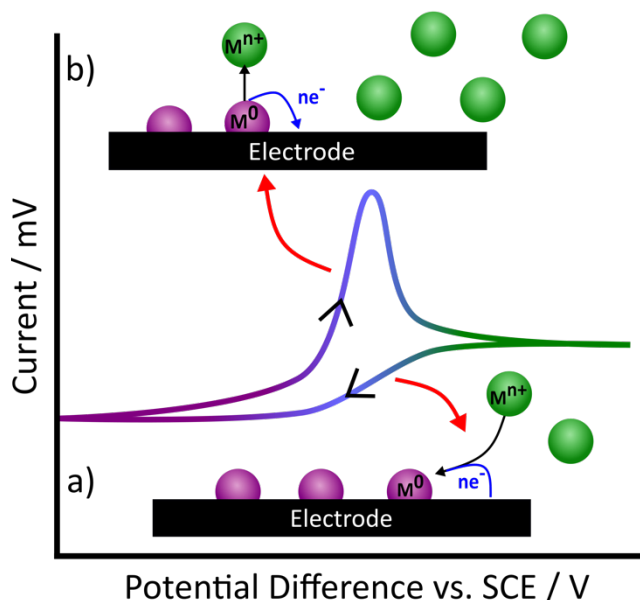


Figure 8 Schematic of a) electrodeposition and b) stripping of a metal and an exemplar CV.

Experimentally, analysis of oxidative stripping peaks in the current-potential trace is used to determine metal concentration. The simplest method of performing the stripping step is by linearly sweeping the current in the anodic direction, although to

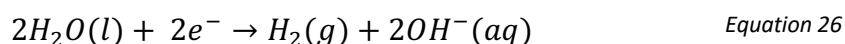
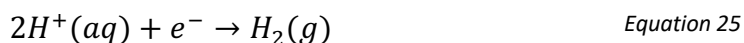
help further increase sensitivity, more complex potential waveforms can be adopted.⁸⁵ The potential at which the stripping peak occurs depends on the chemical identity of the species and the area under the peak (for a standard linear sweep voltammogram (LSV), this equates to charge^{15,77}) depends on the amount of metal deposited. In particular, the stripping peak potential can be thermodynamically related to a specific metal through consideration of $E^{0'}$, for the specific M^{n+}/M redox couple,⁸⁶ although this can be more challenging for non-Hg based electrodes. Experimentally peak current/area is related to the original concentration of the species in solution by means of a calibration plot.

Calibrations are determined either by plotting peak height (current) or peak area (charge) vs. known concentration. The calibration mode chosen depends on the application. There are exceptions, and some literature use both.^{19,87,88} If background processes are present, peaks require background subtraction or baseline subtraction.⁸⁹ Commonly peak height is employed, partially from the historical use of Hg electrodes, where the peaks are usually well-defined and symmetrical.¹⁵ However, in situations where more than one metal is present, peak shape varies or overlap occurs, the use of peak area can provide better calibration linearity.^{77,90,91} Knowledge of the solution matrix composition is key when it comes to calibrating for multi metal solutions, as metal-metal interactions can cause variations in observed signal (*vide infra*); individual and mixed calibrations, standard additions, or spiking methods are commonly employed in these cases.

1.4.1.2. Electrode Materials

Hg served as an ideal electrode for ASV as it forms homogenous liquid metal amalgams (mercurous alloys) upon metal deposition, leading to well defined stripping peaks. Using Hg, a wide range of metals could be detected,⁷² limited only by anodic dissolution of Hg; Hg cannot be used to analyse Hg or metals with more positive $E^{0'}$ than its own, e.g. Ag.⁹² Whilst recent use in the literature is very limited, due to environmental concerns, the electrochemical characteristics which make Hg ideal for ASV are very briefly discussed in order to understand the favourable attributes required for alternative electrode development.

Hg has the advantages of relatively low capacitance compared to other metals, minimal non-faradaic contributions (from surface oxidation) and a wide cathodic window, due to both the hydrogen evolution reaction (HER; Equation 25),⁹ and solvent electrolysis (Equation 26)⁹³ being kinetically less facile compared to other metal surfaces.



Even as an Hg-metal amalgam, electrode characteristics in ASV are typically dominated by Hg, rather than that of the dissolved metals.^{72,94} Given the well-behaved characteristics of Hg electrodes, theoretical models to predict peak shape, position and height i.e. peak current, i_p have been published and corroborated experimentally.^{95–97} The two most popular types of Hg electrodes used in stripping analysis were the hanging Hg drop electrode (HMDE) and the Hg thin film electrode (MTFE).^{15,80}

With a need to find an alternative to Hg-based electrodes, and as no other metal exists which is liquid at room temperature, solid electrodes have been sought which possess as many of the favourable attributes of Hg as possible, including; retarded HER, low background currents, reproducible surface and narrow stripping peaks whilst also exhibiting low toxicity. Several recent reviews cover the many different types of solid electrodes and chemically modified solid electrodes that have been applied to heavy metal detection by ASV and related techniques.^{69,98,99} Biological molecules such as DNA, enzymes and bacteria are also increasingly being used as modifiers due to their high specificity.^{99,100} Examples of metallic electrodes such as Au,⁵⁴ Ag,¹⁰¹ Pt,⁹⁶ Ir,¹⁴ Bi⁶⁷ and the more recent, Te,¹⁰² can all be found in the literature. In the case of metal electrodes, the possible formation of alloys between deposit and electrode during the metal deposition process, should also be considered as is the case for Bi, which alloys with a variety of metals including Pb, Cd, Sb, Tl, Ga.⁶⁷ Surface modified or C based electrodes have become increasingly popular in ASV.^{69,103–105}

Under the conditions of ASV measurements, C electrodes do not alloy with deposited metals.

Metal deposition and stripping are more complicated on a solid electrode for a variety of reasons. Firstly, unlike Hg, as soon as the metal is deposited there is a change in surface properties. The surface characteristics are now the combination of the deposit plus the underlying solid electrode, and potentials of deposition, onset potentials for HER and water reduction will change to reflect this (in addition to solution pH). This effect is often overlooked in the literature, but it will affect how metals deposit and the resulting analysis. Moreover, on a solid surface, it is impossible to provide defect free, pristine surfaces, so deposition is likely to be heterogeneous, with a range of different morphologies present.¹⁰⁶ This leads to different energies being required to strip the metal (or alloy) from the surface and hence broader stripping peak and changeable peak positions are often observed.¹⁰⁷ For example, nanoparticles (NPs) of different sizes, but the same composition, have been observed to strip at different potentials.^{108,109} It is thus important that the deposition parameters, preparation of the electrode surface etc. are optimised as much as possible to try and move towards a homogeneous, monodisperse distribution of deposited structures on the electrode surface. However, this can be challenging.

Also important for consideration is if too much metal is deposited on the surface it may not be possible to remove all the metal during the stripping step. This becomes an issue when comparing charge passed to predictions from theory,¹¹⁰ and when using the same electrode for repeat deposition/stripping measurements. Incomplete stripping may also arise from conversion of the deposited metal to a less electrochemically active form, such as a metal oxide/hydroxide. This can occur due to reaction with another species, such as oxygen in the solution or electrochemically generated hydroxide ions (OH^-).¹¹¹ Furthermore, when depositing multiple metals, a variety of scenarios could occur; metals may form independently, one metal may plate preferentially on another, intermetallic deposits between the multiple metals

could form, or one metal may inhibit or block the deposition of another. In reality several of these could occur at once, again complicating the analysis.

Information on the interaction between a solid electrode and a depositing metal can be inferred by observing the potential at which deposition occurs. The situation is obviously slightly more complicated in the presence of an alloy. For a metal, deposition and stripping theoretically occurs at E^0 , but when depositing onto a foreign material, there are three possibilities; underpotential deposition (UPD), overpotential deposition (OPD) and alloy formation. UPD occurs at a potential lower than E^0 when the interaction between the electrode and the metal is stronger, hence more favourable than the metal-metal interaction. OPD requires an overpotential E^0 , to induce deposition. The higher the overpotential required, the more difficult metal deposition is for that system.¹¹² Theoretical equations do exist for metal stripping on solid electrodes, but with limited success, compared to Hg, for fitting theory to experiment and is explored further in Section 1.4.1.7. Most papers acknowledge that the complex and stochastic nature of metal deposition on solid electrodes makes prediction both complicated and flawed.^{113,114} So despite decades of research, no general theory for metal stripping on a solid electrode system has yet been found.

The Bi based electrode is one of the most popular metal electrode materials used in ASV. Bi is typically used in thin film format, the Bi film electrode (BiFE), and is considered to be very similar in electrode characteristics to Hg, but importantly with lower toxicity. Similar results have been seen for Sb films.¹¹⁵ Bi (and Sb) films electrodeposited or co-deposited on C substrates have been suggested as a promising alternative as they produce narrow, well resolved, reproducible stripping peaks due to their ability to form solid-metal alloys with a range of metals.^{67,116}

A popular alternative is C, materials such as glassy carbon, carbon nanotubes, graphite (highly ordered pyrolytic graphite, edge plane pyrolytic graphite, graphene and even pencil lead) and carbon paste are also good electrode materials for ASV.^{103,105,117,118} C electrodes are more inert than metals and have low background

currents, allowing them to also achieve lower LODs.^{80,119} They are non-toxic so again are attractive for *in-vivo* or general environmental and biological studies. Their surfaces are easy to covalently modify by synthetic chemistry methods, opening up further possible applications.^{93,120} Modification of carbon electrodes to improve sensitivity or selectivity in ASV is commonplace.^{80,92} For example, conducting polymer layers containing surface molecules that chemically complex metal ions have enabled the simultaneous detection of Pb, Cu and Hg in the range 10^{-7} to *ca.* 10^{-10} M.^{121,122} Useful ASV metal electrodes, such as Bi and Au have also been added to the C surface, typically in NP form by either electrodeposition¹²³ or chemical reduction methods.¹²⁴ The density of NPs is often such that individual diffusion fields to each NP overlap, reducing the spectacular mass transfer enhancements expected from very small NP electrodes (Section 1.1.4). However, the background signals will be reduced as a result of a reduced amount of active metal on the surface leading to improved signal to noise ratios. The use of modified C electrodes for ASV applications has been extensively reviewed elsewhere.^{103,117}

BDD has been used widely in ASV analysis as it offers the widest potential window of any electrode material in aqueous solution due to the kinetics of water oxidation and reduction being very slow. This is thought to be due to a lack of available catalytic sites on the sp^3 surface.^{119,125} Studies have shown that the stripping potentials for the metals Zn, Cd and Pb, Figure 9, were not significantly shifted on BDD relative to Hg. Both electrodes were capable of metal detection over a concentration range of 3-4 orders of magnitude, with LODs in the low ppb range.¹⁰⁴

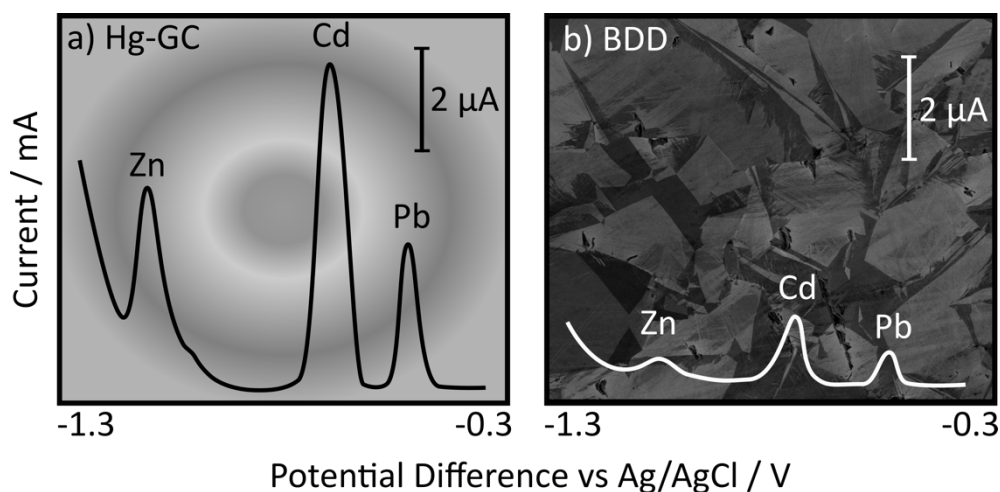


Figure 9 Comparison of stripping voltammetric current-potential curves for 100 ppb solutions of Zn, Cd and Pb in acetate buffer, pH 5.2, on an Hg coated glassy carbon electrode (Hg-GC) (top) and BDD (bottom). Figure modified from reference ¹⁰⁴.

In recent years there has been a greater rise in the use of cheap, disposable and/or multiplexed electrodes for heavy metal detection. The disposable nature means long term issues with electrode fouling due to placement in the real environment can be negated. However, batch reproducibility does need to be assured in order to have confidence in the results. The use of multiplexed electrodes on the same platform, means that different electrodes can be employed to extend the range of detectable species.¹²⁶ Such electrodes are well suited for on-site analysis as they are small and when integrated with appropriate instrumentation, portable. Often, these are screen printed electrodes, where the RE and CE electrodes can be printed alongside WE, producing a compact sensor system. Alternatively, microfabrication procedures can be used to print arrays of metal electrodes.¹²⁶ Screen printed electrodes can be made from many different materials such as C or metal oxide, printed as an ink and integrated into a support. The surface can be further functionalised if required, through the addition of e.g. metal NPs, metal ion complexing groups, depending on the application of interest.^{127,128,129} In some cases the support can be made flexible enabling the electrode device to be worn, for example, on the wrist, as is the case for the detection of heavy metals in sweat.¹²⁶

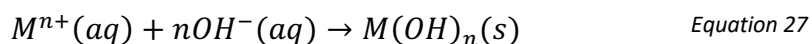
Additionally, the emergence of 3D printing technologies, for the high throughput production of bespoke devices, has also impacted ASV, along with other areas of

electrochemical analysis.¹³⁰ 3D printing provides an opportunity to design and print electrodes in non-conventional geometries, and has been used with nanocarbon composite filaments^{131,132} and metals.¹³³ It has also been used to produce bespoke flow cells to house a more traditional electrode format, e.g. screen printed carbon.¹³⁰

1.4.1.3. ASV Parameters

For solutions containing a mixture of metals, in order to ensure deposition of all metals, the potential must be made more negative than the most negative E^0 metal. For solid electrodes, it is important to understand the voltammetric behaviour of the metals of interest on the solid electrode of choice before choosing the deposition potential, E_{dep} . Furthermore, η is also likely to strongly influence the morphology of the metal deposits formed on the surface. The situation is further complicated when the heterogeneity of the surface is taken into account, be that morphology or surface electroactivity. For example, on BDD which contains heterogeneously doped grains, at moderate overpotentials different morphologies for a single metal can be obtained on differently doped regions of the surface when the grains are significantly large.¹⁹ This can result in broadened stripping peaks,^{19,104,119} compared to e.g. the BiFE or Hg electrode.

However, there are limits to the maximum overpotential that can be employed, for example, if E_{dep} is close to the cathodic window, HER (Equation 25) results. Bubble formation from HER may block electrode accessibility, changing effective electrode area. Production of OH^- due to water, acid or oxygen reduction will result in local pH rises, which in turn can affect metal speciation or lead to the formation of insoluble metal (hydro)oxides (Equation 27).^{134,135}



If oxygen is present in solution, the oxygen reduction reaction (ORR) is also possible¹¹¹ (Equation 28 and Equation 29, written for the four electron pathway), catalysed via the metal electrodeposits which are invariably more active than the support electrode. Whether ORR goes via a two or four electron pathway,¹¹¹ it also results in either proton depletion or hydroxide ion formation (pH dependant). Given it occurs

at potentials less negative than those described by Equation 25 and Equation 26, ORR is definitely a cause for concern. Equation 25 to Equation 29 are illustrated schematically in Figure 10.

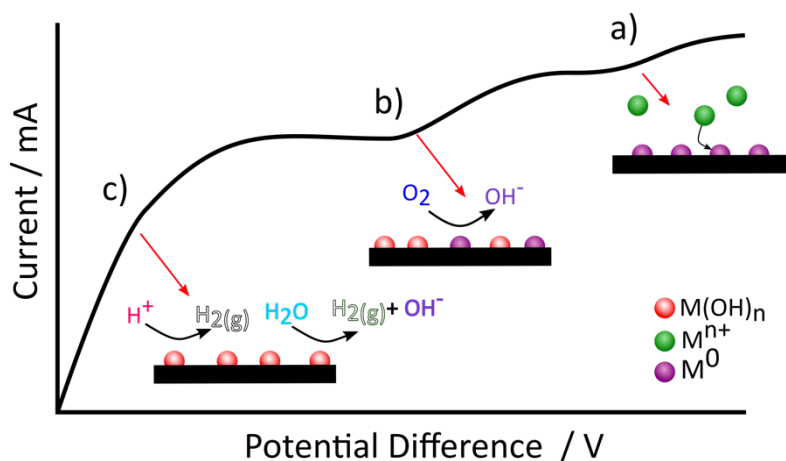
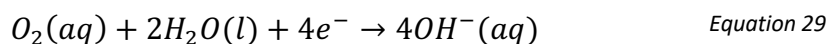
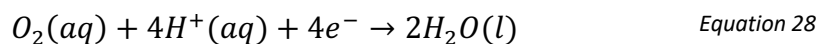


Figure 10 Schematic of a linear sweep voltammogram in the cathodic direction illustrating the different cathodic processes which could also interfere with a) metal deposition, and include b) metal catalysed ORR resulting in transformation of the metal to metal hydroxide and c) HER from proton and/or water reduction.

Overall, metal hydroxide/oxide formation means the electrodeposited species are no longer in the metallic form. Even though some may remain electrochemically active, the characteristics have changed drastically. This can result in less metal being detected via the M/M^{n+} stripping response, leading to an underestimation of the concentration of heavy metal in the original solution.

1.4.1.4. Potential wave forms

One of the simplest voltammetric experiments is linear sweep voltammetry (LSV), where the potential is swept (more accurately “stepped” with digital potentiostats) from one voltage to another at a specified rate (scan rate; Figure 11 a) and b)). Whilst this is useful for assessing the voltammetric behaviour of metal deposition and stripping on an electrode surface, it contains both the faradaic (from metal stripping) and non-faradaic (background currents such as a capacitance) components of the current in the voltammetric window.

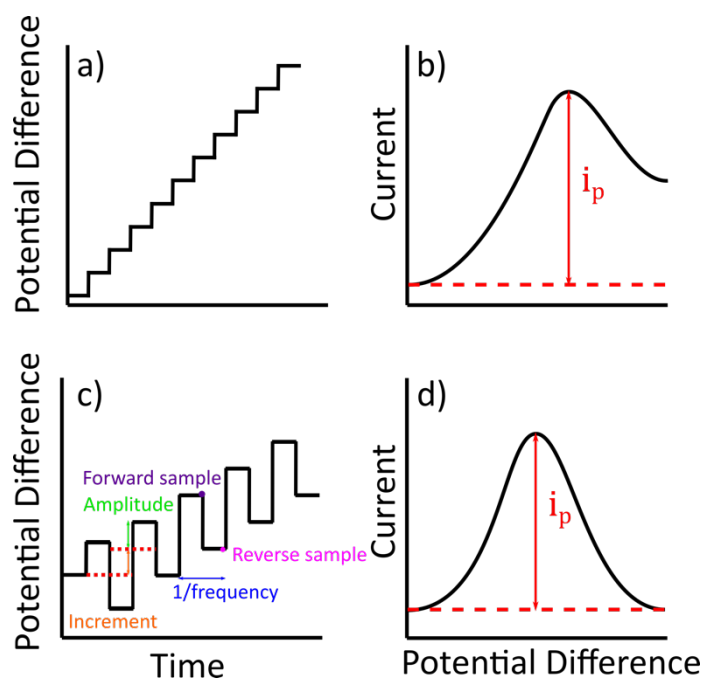


Figure 11 The change in potential over time for a digital LSV, a), with an exemplar current peak shown in b). c) is the wave form of SWV and an exemplar current peak shown in d). The peak current in d is typically larger than that of c).

To increase sensitivity other wave forms, which use a series of potential pulses e.g. as shown in Figure 11 c), to generate current-time decay curves per pulse, are typically adopted in ASV analysis. Ideally, the current is sampled at a time in each pulse when the non-faradaic currents have decayed to zero i.e. the remaining current is faradaic only. Text books will say the current is sampled at the last point in the current-time decay curve, however commercial potentiostats will sample over a manufacturer-defined percentage of the pulse.¹³⁶ The resulting SWV current should therefore be free of background contributions from non-faradaic currents, enhancing the signal of interest and improving LODs. One example of a voltammetric technique with a pulsed waveform is square wave voltammetry (SWV) (Figure 11 c) and d)), first introduced by Barker in 1952⁸⁵ and later made popular through the work of the Osteryoungs.^{137–139} Others include Normal Pulse and Differential Pulse (DPV). DPV and SWV are the most popular, with SWV typically taking less time to run than DPV, due to the use of shorter current pulses.¹³⁷

Voltammetry is not the only electrochemical method used for heavy metal detection, other potentiostatic, galvanostatic and impedance based methods have been successfully implemented, but are not discussed within the scope of this thesis.⁹⁹

1.4.1.5. Speciation and pH

As the pH of the system decreases, speciation changes, the degree of metal-ligand complexation changes and, for example, metal hydroxide species can exist as hydrated metal ions and adsorbed metal cations are released into solution. The overall result is an increase in the number of free metal ions in solution as pH decreases, which directly translates to increasing stripping peak currents. Thus, for ASV in real samples it is very important to recognise the role pH plays in the results observed. This concept has been illustrated experimentally using a dual electrode arrangement consisting of a closely placed pH generating electrode and ASV detector electrode in a ring-disk geometry. Via the generation of protons through electrolysis of water at the ring, it was possible to quantifiably decrease the pH of the disk electrode measurement environment.^{140,141} For both Hg and Cu detection on BDD ring-disk electrodes, the stripping currents were shown experimentally to increase as the local pH decreased.^{140,141}

For many ASV measurements reported in the literature some form of pH adjustment is often included as part of the solution preparation process. pH adjustments are typically made by addition of an acid (e.g. HNO₃, HCl) or buffer.^{22,63,73} As discussed, it is important to then reflect how closely the ASV measurement of the free/labile metal ions represents the original solution at the source. Local pH increases at the electrode surface during electrodeposition, due to Equation 25, Equation 26, Equation 28 and Equation 29 should not be neglected and is one reason why buffers are added. Acetate (pH \approx 4-5.6) buffers are most commonly used for ASV,^{29,57,59,62,73,80,142,143} although phosphate¹⁴⁴ (pH \approx 7) and citrate⁶³ (pH \approx 6) have also been employed. Buffer ions should weakly bind to the metal ions to ensure they remain labile in solution.^{145,146} If speciation is an important consideration minimal change to the sample solution is preferred.

1.4.1.6. Metallic interferences

ASV is most easily analysed when only single metals are considered, however, in reality several metals are likely to be present. Multi metal analysis is especially difficult as there are several ways metals can interfere with one another. Possible intermetallic formation and stripping peak overlap are important considerations, but these can be difficult to account for with an unknown sample. Researchers have combined ASV with independent secondary analytical techniques which provide characteristic elemental signatures, to help with multi metal identification in unknown systems e.g. electrochemical-localised surface plasmon resonance,^{22,147} and electrochemical x-ray fluorescence spectroscopy (EC-XRF).^{148–150}

The stripping potentials for two metals that have deposited independently (not as an intermetallic compound) can also sometimes overlap (e.g. Cd/Tl), making quantification difficult.^{80,151} However, there are several combinations of multi metals that can be simultaneously detected without issue, but this depends on factors such as electrode material, relative concentrations of the metals, deposit morphologies, etc.^{23,152} This is illustrated by Figure 12 where Bi can both act in an analogous way to Hg for some metals, and form binary intermetallic complexes with others. In the example given Bi forms an intermetallic compound with Cd, making its stripping potential more negative and enabling resolution from the Tl peak.^{116,153}

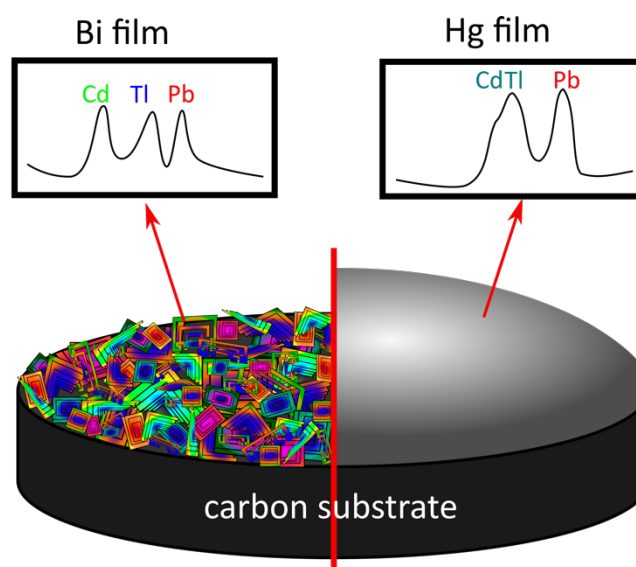


Figure 12 Differences in stripping voltammograms of a mixture of 50 µg/L Pb^{2+} , Cd^{2+} , and Tl^+ on Bi and Hg thin-film electrodes. Solutions, 0.1 M acetate buffer (pH 4.5) containing 400 µg/L Bi or 10 mg/L Hg. Deposition for 120 s at -1.2 V. Figure modified from ¹⁵¹.

Interfering metals can also be removed prior to ASV analysis using pre-treatment processes or methods such as ion exchange resins.¹⁵⁴ The interference of Cu-Cd and Cu-Pb intermetallics can be mitigated by the addition of ferrocyanide to form an inert Cu complex in solution, but renders the Cu unquantifiable.¹⁵⁵ Ion exchange resins have been used to remove interfering Mn, Fe, Cu and Ni from solution, prior to the detection of inorganic As¹⁵⁶ and determine labilities of soluble metals.¹⁵⁷

Finally, detecting fewer metals at a time can help reduce possible metal-metal interference effects. This can be achieved using e.g. a chemically modified electrode that selectively accumulates specific metals due to strong interactions of the metal of interest with specific groups on the modifying material leading to improved resolution,¹⁵⁸ or by varying the deposition potential to plate only metals with the more positive E^0 's.¹⁵⁹

1.4.1.7. Metal Electrodeposition and Stripping Theory

Theoretical equations do exist for metal stripping on solid electrodes, but have been applied with limited success compared to those for Hg, when comparing theory to experiment. Many papers come with assumptions and admissions that the stochastic nature of metal deposition on solid electrodes makes stripping predictions both complicated and flawed.¹¹⁴ Berzins and Delahay describe the theoretical peak current

for a reversible system on a solid electrode,¹¹³ whilst Nicholson developed a theory for a reversible fractional monolayer system where the activity of the deposit was proportional to the fraction of electrode covered.^{160,161} Ward Jones *et al.* proposed a general theory for cathodic and anodic stripping that considered monolayer, thin multi-layer and thick films for both reversible and irreversible regimes. The premise of this theory was based on changes to the diffusion field rather than the activity of the deposit.^{106,162}

In 2011, Brainina published on the comparison of theory and experiment for the stripping of Au nanoparticles and showed that thermodynamic and kinetic information could be obtained.¹⁶³ In the same year Gileadi published “The Enigma of Metal Deposition” highlighting there has been no previous proof of the mechanism of charge transfer during deposition (and stripping) and that assumptions of α being equal to 0.5 are unfounded. This was based on the effect of the energy difference between a hydrated (or complexed) metal ion and one on the metal surface being non-negligible.¹⁶⁴

This is by no means an exhaustive list of examples but illustrates the point that, despite decades of research and advances in analytical and computational modelling, our understanding of deposition and stripping on solid metal surfaces is not complete. This is not surprising given the many factors that must be considered (described above).⁹⁶ Furthermore, even after many decades of research dedicated to unravelling the complexities involved with just the metal deposition and stripping process, new understanding continues to be revealed.^{81,165–167}

1.5. XRF

X-ray techniques are widely used for the analysis of materials and elemental identification, XRF especially is routinely used for the analysis of metals in industries such as mining, metallurgy, petrochemical and cement.^{168–170} Many other areas also use forms of XRF; including environmental monitoring, medical applications, compost and fertilizer, drinking water monitoring and geology.¹⁶⁹

XRF works by irradiating a sample with x-rays generated in the x-ray tube, x-ray photons are absorbed and core electrons from the atoms of the sample are ejected. Electrons from higher energy levels (outer shells) relax into the hole left from the core electron and emit a photon by fluorescence (also an x-ray, generally between 1 and 25 keV) in the process; this is known as the photoelectric effect. Several transitions are possible as there are usually several different shells that electrons can transition from. As each shell has a characteristic energy, each transition also has a characteristic energy, which is the difference in energy between the two shells, and corresponds to the wavelength of the emitted photon that is detected.^{171,172}

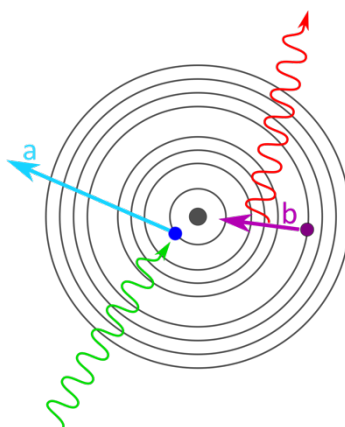


Figure 13 Schematic of the fluorescence mechanism, a) a core electron is ejected when an x-ray photon is absorbed and b) an outer electron falls to the core shell, releasing a photon of fluorescence.

X-ray tubes contain a heated filament (cathode) and a metallic plate (anode, usually elemental Mo, Rh, W for example) in a vacuum. When a potential is applied between the electrodes, electrons are emitted from the cathode and hit the anode resulting in x-ray emission from the anode. These x-rays leave the tube through a small window. The x-rays generated (tube spectrum) are a mixture of the element lines from the target/tube material and a broad continuum of wavelengths known as Bremsstrahlung which are the photons emitted from the electrons decelerating as they hit the anode, Figure 14. The Bremsstrahlung is largely responsible for the backgrounds in XRF.

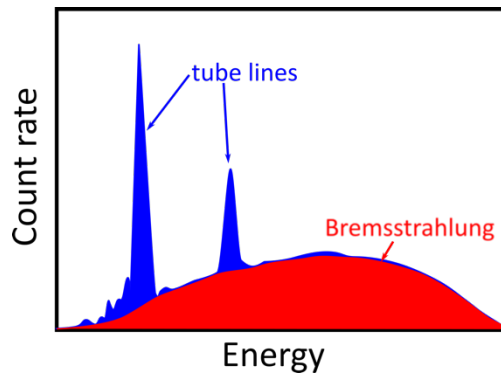


Figure 14 Example spectrum showing characteristic fluorescence lines from the tube material (blue) and the Bremsstrahlung (red) that make up the spectrum that irradiates the sample and which are often seen in the measured spectrum.

The sensitivity of XRF depends on the combination of the elements of interest and the composition of the spectrum used to excite the sample. Efficient excitation is achieved by having a good match between the intense lines in the tube spectrum and the adsorption edge energy of the element of interest in the sample. X-rays are likely to interact with the k shell as the concentration of electrons is highest there. Similarly XRF is very sensitive to high atomic number elements as they have more electrons to interact with.¹⁷³ XRF must be carefully optimised if light element analysis is required, this often involves specialist instrument modifications.

The two major variations on XRF are energy dispersive XRF (ED-XRF) and wavelength dispersive XRF (WD-XRF). WD-XRF irradiates the sample directly, the resulting fluorescence passes through a collimator and hits a diffraction crystal. The fluorescence is diffracted, and a detector mounted on a goniometer is moved to measure the intensity of each wavelength sequentially. WD-XRF provides excellent sensitivity and resolution but instrumentation is larger, more powerful, more expensive and can require cooling systems making running more expensive and complicated than ED-XRF.¹⁷⁰

ED-XRF often uses filters between the x-ray tube and the sample to remove some of the background or characteristic elemental lines (from the x-ray tube material) from the tube spectrum, whilst making sure useful excitation lines are present. The whole fluorescence spectrum is then measured simultaneously on a detector. Silicon drift

detectors are often used in ED-XRF instruments, these are well suited to the range of energies in XRF and give high count rates. The signal is then analysed by a multi-channel analyser and a spectrum constructed. The main modifications to ED-XRF are the secondary target and polarising target instruments, known as 3D geometry. In basic secondary target systems, a secondary target is between the x-ray tube and sample, placed orthogonally to one another (Figure 15). The secondary target is irradiated and in turn irradiates the sample with x-rays characteristic of the element it is made of. This leads to lower backgrounds (less scatter) and better excitation (if optimised for the element of interest), but it requires more primary x-ray intensity. If the secondary target is a polarising target then only reflected, hence polarised, x-rays from the x-ray source reach the sample. These modifications improve signal to noise ratios.¹⁷⁰

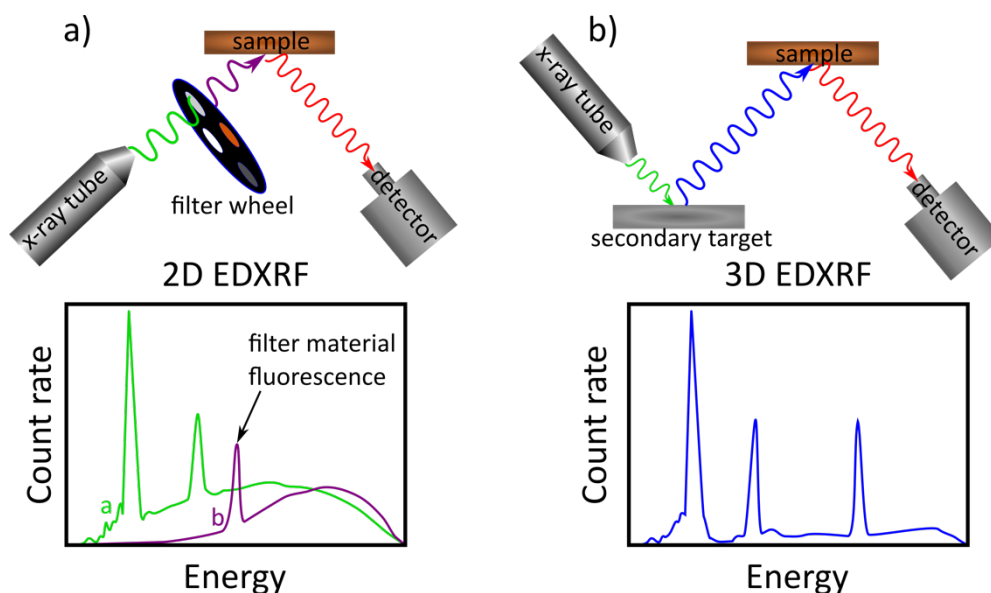


Figure 15 Schematics of a) regular, 2D geometry systems and the spectra when no filter (green) and a filter (purple) are utilised, b) 3D geometry system with spectrum showing lower backgrounds with characteristic lines from target and tube materials.

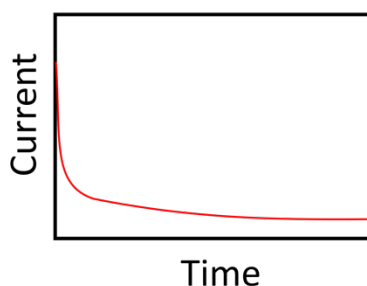
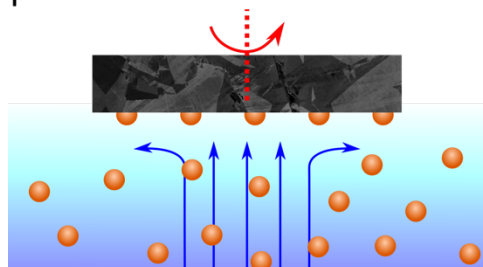
ED-XRF is very versatile and fast, also relatively cheap but resolution and sensitivity suffer compared to WD-XRF. Benchtop ED-XRF systems are common and handheld ED-XRF analysers have grown in popularity for applications such as geology,¹⁷⁴ art and archeology¹⁷⁵ as fast compositions of metals in rock, paint and artefact samples can be obtained.

1.5.1. EC-XRF

XRF has been used in industry extensively for metal analysis and is most effective for solid samples. Typical detection limits are around the 1-10s ppm with a strong dependence on sample and instrument. There are several liquid applications, for example the analysis of petrochemicals and oils.¹⁷² The sensitivity in liquid samples is similar, which is not sufficient for most liquid applications but can be improved through the use of a sample pre-concentration step. Different commercial examples of pre-concentration exist, one of the most common is repeatedly drying aliquots (to pre-concentrate) of solution on a specially designed sample plate, this can achieve LODs of around 0.2 ppm.¹⁴⁸ This is effective but requires a lot of time and a skilled technician.

A new method, first described in the 2014 paper by Hutton *et al.*¹⁴⁸ explored the possibility of using electrochemistry to pre-concentrate metal ions from solution onto the surface on a BDD electrode by electrochemical reduction to the metal (electrodeposition) and then analysing the electrode surface with XRF, Figure 16.

a) Electrochemical pre-concentration



b) XRF analysis

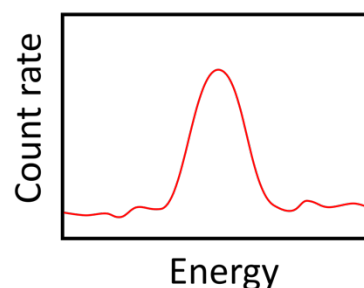
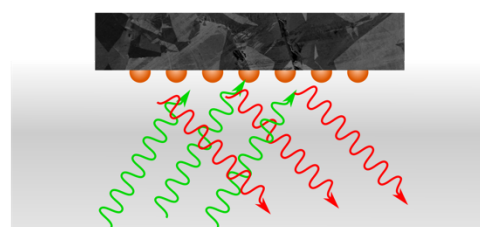


Figure 16 Schematic of EC-XRF showing a) pre-concentration step, electrodeposition and electrochemical current-time transient and b) XRF analysis step with typical XRF spectrum of peak of interest obtained.

The method was possible for both *ex situ*¹⁴⁸ and *in situ* applications.¹⁴⁹ BDD was used as the electrode material as XRF is very insensitive to light elements such as C and B allowing easy analysis of deposits on its surface.¹⁷² Other forms of C would not be suitable as they are not as mechanically robust and materials such as graphite have a layered structure which scatters the x-rays strongly resulting in high backgrounds.¹⁷⁶ BDD, despite being crystalline, is made up of very small randomly oriented crystals so diffraction effects are minimal.

In proof of concept *ex situ* measurements, a home built RDE system was employed using a cap to hold the BDD electrode in place. The electrode was 250 μm in thickness, thicker disks result in higher backgrounds. After pre-concentration via electrodeposition the BDD electrode was removed and placed in the instrument for analysis. Whilst showing promising results for Pd, Cu and Pb detection, the transferral of the BDD to the instrument and reattachment often resulted in breakages (fractures) of the thin BDD.^{148,150} An *in situ* flow cell was also produced whereby deposition and XRF analysis were carried out simultaneously in the XRF system for the simultaneous monitoring of the deposition of five metals, Cu, Pb, Hg, Zn and Ni.¹⁴⁹

1.6. Electrocatalysis

The area of electrocatalysis is huge, with electrochemical splitting of water, oxygen reduction and CO_2 reduction being some of the biggest areas of activity. There are many reviews which cover the work done in these areas, a few are highlighted below. Of importance to the metals deposited in this thesis, is the electrochemical conversion of CO_2 into a range of useful products that can be used as fuels or chemical feedstocks. This is doubly advantageous as CO_2 from the atmosphere can be removed and used to create products that would otherwise require fossil fuels for their synthesis. CO_2 is a greenhouse gas whose concentration in the atmosphere has been increasing due to anthropogenic factors such as the burning of fossil fuels, thereby contributing to global warming.^{177,178}

The electrocatalysis of the CO₂ reduction reaction (CO₂RR) mainly produces C1 and C2 products including ethanol, methane and formate, the products and ratios produced depend on what conditions and catalysts were used in the reaction.¹⁷⁹ There is a huge range of catalysts in literature, they can be enzymes, molecular catalysts, inorganic structures, carbon based materials, transition metals, alloys or oxides.¹⁷⁹ Most of these catalysts involve a metal surface as the proposed active site for the reduction.^{180,181} Transition metals are particularly prevalent due to their ability to exist in multiple oxidation states which is advantageous for a catalyst.

One of the most promising metals for this application is Cu, which appears in literature in many forms from metallic to oxide to layered and in morphology from surfaces to nanoparticles.¹⁸² The advantage of Cu is that it decreases the overpotential of the reaction, and therefore energy usage. Cu also has desirable products and ratios, being particularly good at C-C bond formation, additionally it is also an extremely cheap, available and safe metal compared to alternatives such as Au or Pb.^{183–185} The reaction mechanisms for Cu catalysts are still not fully understood but many modelling and deactivation studies appear in literature attempting to glean further understanding to enable the design of improved catalysts.^{186–188} Cubic nanoparticle Cu catalysts have shown improved selectivity for multi-carbon products such as ethylene^{189,190} and provide a practical route for catalyst tailoring by changing cube size by electrodeposition or solution phase synthesis.^{191–193}

1.7. Aims

This thesis aims to develop improved methods for the analysis of metals and their deposits using BDD electrodes. By learning from existing methods such as ASV and EC-XRF, better understanding of the factors involved in analysis will be gained in order to design improved systems. In chapter 3, a BDD electrode that is easy to handle and reuse, which is optimised for both electrochemistry and XRF, is developed. Several different mass transport systems are explored and the RDE found to be the best system for *ex situ* EC-XRF due to the high and well-defined

hydrodynamics. This electrode is then tested on a Cu system to investigate its analytical capabilities.

Chapter 4 aims to develop an *in situ* EC-XRF flow cell system, a bespoke wall jet flow cell is designed, optimised for analysis by XRF. The electrochemical characteristics of the flow cell are analysed and tested on a Cu system for EC-XRF. The effect of deposition potential, flow rate and concentration on XRF signal are investigated and the distribution of Cu deposit is mapped by XRF to show how deposition occurs in such a system.

Chapter 5 demonstrates the effect of pH, electrolyte and dissolved oxygen on the stripping characteristics of Cu on a BDD electrode. The ability to measure heavy metal concentrations in environmental waters in environmental conditions speeds up analysis as well as providing additional information of the state of the system. The deposits created during pre-concentration are imaged and their morphologies related to the ASV and speciation where possible. This chapter aims to elucidate the factors involved in designing an effective methodology for ASV and demonstrates the range of possible morphologies that can be electrodeposited from simple solutions.

Finally, Chapter 6 uses BDD TEM electrodes to track the growth of Cu₂O cubes with identical location TEM, elucidating the formation mechanism of the electrocatalyst. The electrocatalytic activity for the CO₂ reduction reaction is assessed using on-line electrochemical mass spectrometry and then the deactivation of these catalysts is addressed. Optimising the electrocatalytic reduction of CO₂ is a very relevant challenge for the future of the environmental and energy science, as it simultaneously uses up an unwanted resource and converts it into important feedstocks that would otherwise be produced from fossil fuels. The use of bespoke BDD electrodes enables the interrogation of the electrode surface and electrodeposits in a way that would not be possible with other electrode materials. These BDD TEM electrodes allow insight not only through electrochemistry but also through spectroscopy and microscopy of this important electrocatalytic reaction.

1.8. Bibliography

- 1 A. J. Bard and L. R. Faulkner, *Electrochemical Methods: Fundamentals and Applications*, Wiley, New York, 2 edition., 2000.
- 2 J. L. Sheean, *J. Chem. Educ.*, 1930, **7**, 33–42.
- 3 J. O. Bockris and Z. Nagy, *J. Chem. Educ.*, 1973, **50**, 839.
- 4 R. A. Marcus, *Angew. Chemie Int. Ed. English*, 1993, **32**, 1111–1121.
- 5 E. U. Condon, *Phys. Rev.*, 1928, **32**, 858–872.
- 6 J. Franck, *Trans. Faraday Soc.*, 1926, **21**, 536–542.
- 7 S. E. Schwartz, *J. Chem. Educ.*, 1973, **50**, 608–610.
- 8 A. J. Bard, *J. Am. Chem. Soc.*, 2010, **132**, 7559–7567.
- 9 R. G. Compton and C. E. Banks, *Understanding Voltammetry*, IMPERIAL COLLEGE PRESS, 2010.
- 10 O. Stern, *Zeitschrift für Elektrochemie und Angew. Phys. Chemie*, 1924, **30**, 508–516.
- 11 H. G. Lee, H. S. Yoon and M. Y. Ha, *Int. J. Heat Mass Transf.*, 2008, **51**, 4055–4068.
- 12 R. J. Forster, *Chem. Soc. Rev.*, 1994, **23**, 289–297.
- 13 J. Heinze, *Angew. Chemie Int. Ed. English*, 1993, **32**, 1268–1288.
- 14 M. A. Nolan and S. P. Kounaves, *Anal. Chem.*, 1999, **71**, 3567–3573.
- 15 T. R. Copeland and R. K. Skogerboe, *Anal. Chem.*, 1974, **46**, 1257A-1268a.
- 16 M. L. Tercier and J. Buffle, *Electroanalysis*, 1993, **5**, 187–200.
- 17 L. Landau and B. Levich, *Acta Physicochim. URSS*, 1942, **17**, 141–153.
- 18 H. Gunasingham and B. Fleet, *Anal. Chem.*, 1983, **55**, 1409–1414.
- 19 L. A. Hutton, M. E. Newton, P. R. Unwin and J. V. Macpherson, *Anal. Chem.*, 2011, **83**, 735–745.
- 20 C. M. A. Brett, A. M. C. F. Oliveira Brett, A. C. Fisher and R. G. Compton, *J. Electroanal. Chem.*, 1992, **318**, 53–59.
- 21 A. J. Bard, M. Stratmann, E. Gileadi and M. Urbakh, *Encyclopedia of Electrochemistry, Thermodynamics*, Wiley-VCH, 2002.
- 22 S. Wang, E. S. Forzani and N. Tao, *Anal. Chem.*, 2007, **79**, 4427–4432.
- 23 J. F. Van Staden and M. C. Matoetoe, *Anal. Chim. Acta*, 2000, **411**, 201–207.

- 24 H. W. Webb, *Analyst*, 1945, **70**, 301–304.
- 25 D. E. Williams, K. Ellis, A. Colville, S. J. Dennison, G. Laguillo and J. Larsen, *J. Electroanal. Chem.*, 1997, **432**, 159–169.
- 26 H. D. Dewald and B. A. Peterson, *Anal. Chem.*, 1990, **62**, 779–782.
- 27 C. R. S. Hagan and L. A. Coury, *Anal. Chem.*, 1994, **66**, 399–405.
- 28 G. C. Richard, C. E. John and M. Frank, *Electroanalysis*, 1997, **9**, 509–522.
- 29 Z. Bi, C. S. Chapman, P. Salaün and C. M. G. Van Den Berg, *Electroanalysis*, 2010, **22**, 2897–2907.
- 30 C. S. Chapman and C. M. G. Van Den Berg, *Electroanalysis*, 2007, **19**, 1347–1355.
- 31 B. C. Towe, *IEEE Trans. Biomed. circuits Syst.*, 1987, **34**, 657–663.
- 32 R. S. Balmer, J. R. Brandon, S. L. Clewes, H. K. Dhillon, J. M. Dodson, I. Friel, P. N. Inglis, T. D. Madgwick, M. L. Markham, T. P. Mollart, N. Perkins, G. A. Scarsbrook, D. J. Twitchen, A. J. Whitehead, J. J. Wilman and S. M. Woollard, *J. Phys. Condens. Matter*, 2009, **21**, 364221.
- 33 A. Gicquel, K. Hassouni, F. Silva and J. Achard, *Curr. Appl. Phys.*, 2001, **1**, 479–496.
- 34 J. V. Macpherson, *Phys. Chem. Chem. Phys.*, 2015, **17**, 2935–2949.
- 35 S. Koizumi, H. Umezawa, J. Pernot and M. Suzuki, *Power Electronics Device Applications of Diamond Semiconductors*, Elsevier, 2018.
- 36 F. Pruvost and A. Deneuve, *Diam. Relat. Mater.*, 2001, **10**, 531–535.
- 37 G. Wood, M. Newton, V. Shkirskiy, P. R. Unwin, J. Macpherson, M. Munday and C. Walters, *ChemRxiv*, , DOI:10.26434/chemrxiv.12619697.v1.
- 38 Y. V. Pleskov, *Russ. J. Electrochem.*, 2002, **38**, 1275–1291.
- 39 R. Trouillon and D. O’Hare, *Electrochim. Acta*, 2010, **55**, 6586–6595.
- 40 L. J. Simcox, R. P. A. Pereira, E. M. H. Wellington and J. V. Macpherson, *ACS Appl. Mater. Interfaces*, 2019, **11**, 25024–25033.
- 41 R. E. Wilson, I. Stoianov and D. O’Hare, *Electrochem. commun.*, 2016, **71**, 79–83.
- 42 P. B. Tchounwou, C. G. Yedjou, A. K. Patlolla and D. J. Sutton, *Mol. Clin. Environ. Toxicol.*, 2012, **101**, 133–164.
- 43 Council Directive 2008/105/EC on environmental quality standards in the field

- of water policy, *Off. J. Eur. Union*, 2008, **L348/84**, 84–97.
- 44 M. Olivares and R. Uauy, *Am. J. Clin. Nutr.*, 1996, **63**, 791–796.
- 45 H. A. Schroeder, A. P. Nason, I. H. Tipton and J. J. Balassa, *J. Chronic Dis.*, 1967, **20**, 179–210.
- 46 H. Needleman, *Annu. Re. Med.*, 2004, **55**, 209–222.
- 47 A. Martelli, E. Rousselet, C. Dycke, A. Bouron and J. M. Moulis, *Biochimie*, 2006, **88**, 1807–1814.
- 48 J. Godt, F. Scheidig, C. Grosse-Siestrup, V. Esche, P. Brandenburg, A. Reich and D. A. Groneberg, *J. Occup. Med. Toxicol.*, 2006, **1**, 1–6.
- 49 P. M. Chapmann, H. E. Allen, K. Godtfredsen and M. N. Z'Graggen, *Environ. Sci. Technol.*, 1996, **30**, 448A-452A.
- 50 M. Kazemipour, M. Ansari, A. Mohammadi, H. Beitollahi and R. Ahmadi, *J. Anal. Chem.*, 2009, **64**, 65–70.
- 51 S. M. Rosolina, J. Q. Chambers, C. W. Lee and Z. L. Xue, *Anal. Chim. Acta*, 2015, **893**, 25–33.
- 52 S. M. Rosolina, J. Q. Chambers and Z. L. Xue, *Anal. Chim. Acta*, 2016, **914**, 47–52.
- 53 G. Hughes, K. Westmacott, K. C. Honeychurch, A. Crew, R. M. Pemberton and J. P. Hart, *Biosensors*, 2016, **6**, 1–39.
- 54 A. Giacomino, A. Ruocco, S. Squadrone, M. Rizzi, M. C. Abete, C. La Gioia, R. Toniolo, O. Abollino and M. Malandrino, *Food Chem.*, 2017, **221**, 737–745.
- 55 G. Hughes, K. Westmacott, K. C. Honeychurch, A. Crew, R. M. Pemberton and J. P. Hart, *Biosensors*, 2016, **6**, 50–89.
- 56 A. Sani and I. L. Abdullahi, *Toxicol. Reports*, 2017, **4**, 72–76.
- 57 A. K. Jaiswal, S. Das, V. Kumar, M. Gupta and N. Singh, *Int. J. Eng. Res.*, 2015, **4**, 235–239.
- 58 G. Liang, L. Pan and X. Liu, *Int. J. Environ. Res. Public Health*, 2017, **14**, 1–10.
- 59 G. Kefala, A. Economou, A. Voulgaropoulos and M. Sofoniou, *Talanta*, 2003, **61**, 603–610.
- 60 G. E. Batley and T. M. Florence, *Anal. Lett.*, 1976, **9**, 379–388.
- 61 T. M. Florence, G. E. Batley and P. Benes, *C R C Crit. Rev. Anal. Chem.*, 1980, **9**, 219–296.

- 62 T. M. Florence, *Water Res.*, 1977, **11**, 681–687.
- 63 T. M. Florence, *Talanta*, 1982, **29**, 345–364.
- 64 J. W. Olesik, *Anal. Chem.*, 1991, **63**, 12A-21A.
- 65 C. Reimann, U. Siewers, H. Skarphagen and D. Banks, *Sci. Total Environ.*, 1999, **239**, 111–130.
- 66 A. B. M. Helaluddin, R. S. Khalid, M. Alaama and S. A. Abbas, *Trop. J. Pharm. Res.*, 2016, **15**, 427–434.
- 67 J. Wang, *Electroanalysis*, 2005, **17**, 1341–1346.
- 68 G. Gillain, G. Duyckaerts and A. Disteche, *Anal. Chim. Acta*, 1979, **106**, 23–37.
- 69 Y. Lu, X. Liang, C. Niyungeko, J. Zhou, J. Xu and G. Tian, *Talanta*, 2018, **178**, 324–338.
- 70 M. G. Tamba and N. Vantini, *J. Electroanal. Chem.*, 1970, **25**, 235–244.
- 71 G. M. S. Alves, L. S. Rocha and H. M. V. M. Soares, *Talanta*, 2017, **175**, 53–68.
- 72 J. Wang, *Stripping analysis : principles, instrumentation, and applications*, VCH, Weinheim, 1985.
- 73 T. M. Florence, *Analyst*, 1986, **111**, 489–505.
- 74 H. Greschonig and K. J. Irgolic, *Appl. Organomet. Chem.*, 1992, **6**, 565–577.
- 75 K. Pecková, J. Musilová and J. Barek, *Crit. Rev. Anal. Chem.*, 2009, **39**, 148–172.
- 76 P. Manisankar, G. Selvanathan, S. Viswanathan and H. Gurumalles Prabu, *Electroanalysis*, 2002, **14**, 1722–1727.
- 77 W. D. Ellis, *J. Chem. Educ.*, 1973, **50**, A131.
- 78 World Health Organisation, *Trace elements in human nutrition and health*, 1996.
- 79 United Nations Environment Programme, *Minimata Convention on Mercury*, 2017.
- 80 J. Wang, *Analytical Electrochemistry*, 2006.
- 81 H. E. M. Hussein, R. J. Maurer, H. Amari, J. J. P. Peters, L. Meng, R. Beanland, M. E. Newton and J. V. Macpherson, *ACS Nano*, 2018, **12**, 7388–7396.
- 82 Y. Z. Su, Y. C. Fu, Y. M. Wei, J. W. Yan and B. W. Mao, *ChemPhysChem*, 2010, **11**, 2764–2778.
- 83 S. C. S. Lai, R. A. Lazenby, P. M. Kirkman and P. R. Unwin, *Chem. Sci.*, 2015, **6**, 1126–1138.

- 84 R. D. DeMars and I. Shain, *Anal. Chem.*, 1957, **29**, 1825.
- 85 G. C. Barker and I. L. Jenkins, *Analyst*, 1952, **77**, 685–696.
- 86 R. G. Compton and C. E. Banks, *Understanding Voltammetry*, IMPERIAL COLLEGE PRESS, 2010.
- 87 Z. Stojek and Z. Kublik, *J. Electroanal. Chem.*, 1979, **105**, 247–259.
- 88 J. Duay, J. E. Ortiz-Santiago and T. N. Lambert, *Electroanalysis*, 2017, **29**, 2685–2688.
- 89 A. J. Bard, *Electroanalytical Chemistry, A Series of Advances*, M. Dekker, 1966.
- 90 R. G. Clem, G. Litton and L. D. Ornelas, *Anal. Chem.*, 1973, **45**, 1306–1317.
- 91 J. Wang, X. Cai, C. Jonsson and M. Balakrishnan, *Electroanalysis*, 1996, **8**, 20–24.
- 92 D. W. M. Arrigan, *Analyst*, 1994, **119**, 1953–1966.
- 93 F. Scholz, *Electroanalytical Methods*, 2nd edn., 2010.
- 94 O. Mikkelsen and K. H. Schroder, *Electroanalysis*, 2003, **15**, 679–687.
- 95 C. M. A. Brett and A. M. C. F. Oliveira Brett, *J. Electroanal. Chem.*, 1989, **262**, 83–95.
- 96 K. Z. Brainina, *Talanta*, 1971, **18**, 513–539.
- 97 R. S. Nicholson and I. Shain, *Anal. Chem.*, 1964, **36**, 706–723.
- 98 M. B. Gumpu, S. Sethuraman, U. M. Krishnan and J. B. B. Rayappan, *Sensors Actuators, B Chem.*, 2015, **213**, 515–533.
- 99 B. K. Bansod, T. Kumar, R. Thakur, S. Rana and I. Singh, *Biosens. Bioelectron.*, 2017, **94**, 443–455.
- 100 L. Cui, J. Wu and H. Ju, *Biosens. Bioelectron.*, 2015, **63**, 276–286.
- 101 M. Brand, I. Eshkenazi and E. Kirowa-Eisner, *Anal. Chem.*, 1997, **69**, 4660–4664.
- 102 A. Bobrowski, A. Królicka, J. Śliwa and J. Zarębski, *Electrochim. Acta*, 2017, **252**, 453–460.
- 103 N. Y. Stozhko, N. A. Malakhova, M. V. Fyodorov and K. Z. Brainina, *J. Solid State Electrochem.*, 2008, **12**, 1185–1204.
- 104 E. A. McGaw and G. M. Swain, *Anal. Chim. Acta*, 2006, **575**, 180–189.
- 105 M. Hersey, S. N. Berger, J. Holmes, A. West and P. Hashemi, *Anal. Chem.*, 2019, **91**, 27–43.
- 106 S. E. Ward Jones, F. G. Chevallier, C. A. Paddon and R. G. Compton, *Anal. Chem.*,

- 2007, **79**, 4110–4119.
- 107 D. Menshykau and R. G. Compton, *J. Phys. Chem. C*, 2009, **113**, 15602–15620.
 - 108 O. S. Ivanova and F. P. Zamborini, *Anal. Chem.*, 2010, **82**, 5844–5850.
 - 109 D. K. Pattadar, J. N. Sharma, B. P. Mainali and F. P. Zamborini, *Curr. Opin. Electrochem.*, 2019, **13**, 147–156.
 - 110 M. E. Hyde, C. E. Banks and R. G. Compton, *Electroanalysis*, 2004, **16**, 345–354.
 - 111 E. Yeager, *Electrochim. Acta*, 1984, **29**, 1527–1537.
 - 112 A. J. Bard and L. R. Faulkner, *Electrochemical Methods: Fundamentals and Applications*, Wiley, New York, 2 edition., 2000.
 - 113 T. Berzins and P. Delahay, *J. Am. Chem. Soc.*, 1953, **75**, 555–559.
 - 114 S. P. Perone and H. E. Stapelfeldt, *Anal. Chem.*, 1966, **38**, 796–799.
 - 115 E. Tesarova, L. Baldrianova, S. B. Hocevar, I. Svancara, K. Vytras and B. Ogorevc, *Electrochim. Acta*, 2009, **54**, 1506–1510.
 - 116 J. Wang, J. Lu, Ü. A. Kirgöz, S. B. Hocevar and B. Ogorevc, *Anal. Chim. Acta*, 2001, **434**, 29–34.
 - 117 W. Zhang, S. Zhu, R. Luque, S. Han, L. Hu and G. Xu, *Chem. Soc. Rev.*, 2016, **45**, 715–752.
 - 118 S. Sharma, *J. Electrochem. Soc.*, 2020, **167**, 037501.
 - 119 J. V. Macpherson, *Phys. Chem. Chem. Phys.*, 2015, **17**, 2935–2949.
 - 120 W. E. Van der Linden and J. W. Dieker, *Anal. Chim. Acta*, 1980, **119**, 1–24.
 - 121 A. Mandil, L. Idrissi and A. Amine, *Microchim. Acta*, 2010, **170**, 299–305.
 - 122 M. A. Rahman, M.-S. Won and Y.-B. Shim, *Anal. Chem.*, 2003, **75**, 1123–1129.
 - 123 A. Economou, *Sensors (Switzerland)*, 2018, **18**, 1–23.
 - 124 L. Cui, J. Wu and H. Ju, *Chem. - A Eur. J.*, 2015, **21**, 11525–11530.
 - 125 S. Alehashem, F. Chambers, J. W. Strojek, G. M. Swain and R. Ramesham, *Anal. Chem.*, 1995, **67**, 2812–2821.
 - 126 W. Gao, H. Y. Y. Nyein, Z. Shahpar, H. M. Fahad, K. Chen, S. Emaminejad, Y. Gao, L. C. Tai, H. Ota, E. Wu, J. Bullock, Y. Zeng, D. H. Lien and A. Javey, *ACS Sensors*, 2016, **1**, 866–874.
 - 127 A. Hayat and J. L. Marty, *Sensors (Switzerland)*, 2014, **14**, 10432–10453.
 - 128 M. Li, Y. T. Li, D. W. Li and Y. T. Long, *Anal. Chim. Acta*, 2012, **734**, 31–44.
 - 129 B. Molinero-Abad, D. Izquierdo, L. Pérez, I. Escudero and M. J. Arcos-Martínez,

- Talanta*, 2018, **182**, 549–557.
- 130 Q. Sun, J. Wang, M. Tang, L. Huang, Z. Zhang, C. Liu, X. Lu, K. W. Hunter and G. Chen, *Anal. Chem.*, 2017, **89**, 5024–5029.
 - 131 K. C. Honeychurch, Z. Rymansaib and P. Iravani, *Sensors Actuators, B Chem.*, 2018, **267**, 476–482.
 - 132 Z. Rymansaib, P. Iravani, E. Emslie, M. Medvidović-Kosanović, M. Sak-Bosnar, R. Verdejo and F. Marken, *Electroanalysis*, 2016, **28**, 1517–1523.
 - 133 K. Y. Lee, A. Ambrosi and M. Pumera, *Electroanalysis*, 2017, **29**, 2444–2453.
 - 134 P. Veluchamy and H. Minoura, *J. Mater. Sci. Lett.*, 1996, **15**, 1705–1707.
 - 135 G. H. A. Therese and P. V. Kamath, *Chem. Mater.*, 2000, **12**, 1195–1204.
 - 136 S. J. Cobb and J. V. Macpherson, *Anal. Chem.*, 2019, **91**, 7935–7942.
 - 137 J. G. Osteryoung and R. A. Osteryoung, *Anal. Chem.*, 1985, **57**, 101A–110A.
 - 138 G. C. Barker and A. W. Gardner, *Analyst*, 1992, **117**, 1811–1828.
 - 139 R. A. Osteryoung and J. Osteryoung, *Phil. Trans. R. Lond. A*, 1981, **302**, 315–326.
 - 140 T. L. Read, E. Bitziou, M. B. Joseph and J. V. Macpherson, *Anal. Chem.*, 2014, **86**, 367–371.
 - 141 T. L. Read, M. B. Joseph and J. V. Macpherson, *Chem. Commun.*, 2016, **52**, 1863–1866.
 - 142 H. R. Badiei, J. McEnaney and V. Karanassios, *Spectrochim. Acta - Part B*, 2012, **78**, 42–49.
 - 143 L. Pinto and S. G. Lemos, *Electroanalysis*, 2014, **26**, 299–305.
 - 144 A. Kawde, A. Ismail, A. R. Al-Betar and O. Muraza, *Microporous Mesoporous Mater.*, 2017, **243**, 1–8.
 - 145 I. Šinko and J. Doleal, *J. Electroanal. Chem.*, 1970, **25**, 299–306.
 - 146 Y. K. Chau and K. Lum-Shue-Chan, *Water Res.*, 1974, **8**, 383–388.
 - 147 N. Li, D. Zhang, Q. Zhang, Y. Lu, J. Jiang, G. L. Liu and Q. Liu, *Sensors Actuators, B Chem.*, 2016, **231**, 349–356.
 - 148 L. A. Hutton, G. D. O’Neil, T. L. Read, Z. J. Ayres, M. E. Newton and J. V. Macpherson, *Anal. Chem.*, 2014, **86**, 4566–4572.
 - 149 G. D. O’Neil, M. E. Newton and J. V. Macpherson, *Anal. Chem.*, 2015, **87**, 4933–4940.

- 150 Z. J. Ayres, M. E. Newton and J. V. Macpherson, *Analyst*, 2016, **141**, 3349–3357.
- 151 J. Wang, J. Lu, S. B. Hocevar, P. A. M. Farias and B. Ogorevc, *Anal. Chem.*, 2000, **72**, 3218–3222.
- 152 G. E. Batley, *Mar. Chem.*, 1983, **12**, 107–117.
- 153 I. Švancara, C. Prior, S. B. Hočevár and J. Wang, *Electroanalysis*, 2010, **22**, 1405–1420.
- 154 H. W. Nurnberg, *Fresenius Z Anal Chem*, 1983, **316**, 557–565.
- 155 G. Zhao and G. Liu, *IEEE Sens. J.*, 2018, **18**, 5645–5655.
- 156 L. Skvortsova, A. Tyo, E. Zakharova and V. Shelkovnikov, in *AIP Conference Proceedings*, 2016, vol. 1772, pp. 1–9.
- 157 P. Figura and B. McDuffie, *Anal. Chem.*, 1980, **52**, 1433–1439.
- 158 H. Bagheri, A. Afkhami, H. Khoshsafar, M. Rezaei and A. Shirzadmehr, *Sensors Actuators, B Chem.*, 2013, **186**, 451–460.
- 159 T. M. Florence and G. E. Batley, *Determination of copper in seawater by anodic stripping voltammetry*, 1977, vol. 75.
- 160 M. M. Nicholson, *J. Am. Chem. Soc.*, 1957, **79**, 7–12.
- 161 A. Milchev and T. Zapryanova, *Electrochim. Acta*, 2006, **51**, 2926–2933.
- 162 S. E. Ward Jones, F. W. Campbell, R. Baron, L. Xiao and R. G. Compton, *J. Phys. Chem. C*, 2008, **112**, 17820–17827.
- 163 K. Z. Brainina, L. G. Galperin, E. V. Vikulova, N. Y. Stozhko, A. M. Murzakaev, O. R. Timoshenkova and Y. A. Kotov, *J. Solid State Electrochem.*, 2011, **15**, 1049–1056.
- 164 E. Gileadi, *J. Electroanal. Chem.*, 2011, **660**, 247–253.
- 165 I. Atek, S. Maye, H. H. Girault, A. M. Affoune and P. Peljo, *J. Electroanal. Chem.*, 2018, **818**, 35–43.
- 166 J. Ustarroz, T. Altantzis, J. A. Hammons, A. Hubin, S. Bals and H. Terry, *Chem. Mater.*, 2014, **26**, 2396–2406.
- 167 M. H. Mamme, J. Deconinck and J. Ustarroz, *Electrochim. Acta*, 2017, **258**, 662–668.
- 168 A. M. T. Pereira and P. R. G. Brandao, *Miner. Eng.*, 2001, **14**, 1659–1670.
- 169 C. Vanhoof, J. R. Bacon, A. T. Ellis, U. E. A. Fittschen and L. Vincze, *J. Anal. At. Spectrom.*, 2019, **34**, 1750–1767.

- 170 R. Jenkins and C. O. J. Wiley, 1999, 23–25.
- 171 R. Jenkins, *X-ray Fluoresc. Spectrom.*, 1999, 75–88.
- 172 B. Beckhoff, habil. B. Kanngießner, N. Langhoff, R. Wedell and H. Wolff, *Handbook of Practical X-Ray Fluorescence Analysis*, Springer Berlin Heidelberg, Berlin, Heidelberg, 1st edn., 2006.
- 173 E. M. A. Hussein, *Radiation Mechanics*, Elsevier Science, 2007.
- 174 H. Rowe, N. Hughes and K. Robinson, *Chem. Geol.*, 2012, **324–325**, 122–131.
- 175 V. Orfanou and T. Rehren, *Archaeol. Anthropol. Sci.*, 2015, **7**, 387–397.
- 176 M. K. Tiwari and K. J. S. Sawhney, *J. Phys. Condens. Matter*, 2010, **22**, 175003.
- 177 D. W. Keith, *Science*, 2009, **325**, 1654–5.
- 178 L. D. Danny Harvey, *Climate and global environmental change*, Routledge, 2018.
- 179 G. O. Larrazábal, A. J. Martín and J. Pérez-Ramírez, *J. Phys. Chem. Lett.*, 2017, **8**, 3933–3944.
- 180 W. Yang, K. Dastafkan, C. Jia and C. Zhao, *Adv. Mater. Technol.*, 2018, **3**, 1–20.
- 181 D. J. Fermin and F. Marken, in *Electrochemical reduction of carbon dioxide: overcoming the limitations of photosynthesis.*, eds. D. J. Fermin and F. Marken, Royal Society of Chemistry, Cambridge, 1st edn., 2018, pp. 1–16.
- 182 P. Sebastián-Pascual, S. Mezzavilla, I. E. L. Stephens and M. Escudero-Escribano, *ChemCatChem*, 2019, cctc.201900552.
- 183 J. Gao, D. Ren, X. Guo, S. M. Zakeeruddin and M. Grätzel, *Faraday Discuss.*, 2019, **215**, 282–296.
- 184 J. Gong, X. Chang, T. Wang, Z. Zhao, P. Yang, J. Greeley, R. Mu, G. Zhang, Z. Gong, Z. Luo, J. Chen, Y. Cui and G. Ozin, *Angew. Chemie Int. Ed.*, 2018, 15415–15419.
- 185 H. Jung, S. Y. Lee, C. W. Lee, M. K. Cho, D. H. Won, C. Kim, H. S. Oh, B. K. Min and Y. J. Hwang, *J. Am. Chem. Soc.*, 2019, **141**, 4624–4633.
- 186 S. Popović, M. Smiljanić, P. Jovanović, J. Vavra, R. Buonsanti, N. Hodnik, I. Edition, S. Popović, M. Smiljanić, P. Jovanović, J. Vavra, R. Buonsanti and N. Hodnik, *Angew. Chemie Int. Ed.*, 2020, 2–13.
- 187 D. Ren, J. Gao and M. Grätzel, *ACS Symp. Ser.*, 2019, **1331**, 209–223.
- 188 Y. Zheng, A. Vasileff, X. Zhou, Y. Jiao, M. Jaroniec and S. Z. Qiao, *J. Am. Chem.*

- Soc., 2019, **141**, 7646–7659.
- 189 F. S. Roberts, K. P. Kuhl and A. Nilsson, *Angew. Chemie - Int. Ed.*, 2015, **54**, 5179–5182.
- 190 P. Grosse, D. Gao, F. Scholten, I. Sinev, H. Mistry and B. Roldan Cuenya, *Angew. Chemie - Int. Ed.*, 2018, **57**, 6192–6197.
- 191 X. Guo, W. Lv and X.-Y. Li, *J. Phys. Chem. C*, 2014, **118**, 11062–11077.
- 192 A. Loiudice, P. Lobaccaro, E. A. Kamali, T. Thao, B. H. Huang, J. W. Ager and R. Buonsanti, *Angew. Chemie - Int. Ed.*, 2016, **55**, 5789–5792.
- 193 I. C. Chang, P. C. Chen, M. C. Tsai, T. T. Chen, M. H. Yang, H. T. Chiu and C. Y. Lee, *CrystEngComm*, 2013, **15**, 2363–2366.

2. Experimental

2.1. Chemicals

All solutions were prepared using Milli-Q water (Millipore, deionised), with resistivity of 18.2 MΩ cm at 25 °C. All chemicals used as received without further purification.

Table 1 is a list of chemicals used.

Table 1 Table of chemicals used, purity and supplier.

Chemical	Formula	Purity	Supplier
Hexaamineruthenium(III) chloride	$\text{Ru}(\text{NH}_3)_6 \text{Cl}_3$	>99%	Strem chemicals
Potassium nitrate	KNO_3	>99%	Sigma Aldrich
Potassium sulfate	K_2SO_4	>99%	Sigma Aldrich
Copper (II) nitrate	$\text{Cu}(\text{NO}_3)_2$	99.99%	Sigma Aldrich
Nitric acid	HNO_3	70%	Fisher Scientific
Lead (II) nitrate	$\text{Pb}(\text{NO}_3)_2$	99.99%	Sigma Aldrich
Potassium chloride	KCl	>99%	Sigma Aldrich
Copper (II) sulfate	CuSO_4	99.99%	Sigma Aldrich
Copper (II) chloride	CuCl_2	99.99%	Sigma Aldrich
Sulfuric acid	H_2SO_4	>95%	Sigma Aldrich
Hydrochloric acid	HCl	38%	Fluka
Acetic acid	CH_3COOH	>99%	Sigma Aldrich
Sodium acetate	CH_3COONa	>99%	Sigma Aldrich
Potassium carbonate	K_2CO_3	>99%	Sigma Aldrich

pH measurements were made using a commercial pH probe (Mettler Toledo) and adjustments were made using the respective acid to the electrolyte used, e.g. solutions of $\text{Cu}(\text{NO}_3)_2$ in KNO_3 are adjusted with HNO_3 .

2.2. Materials

2.2.1. Boron Doped Diamond

All boron doped diamond (BDD) was procured from Element Six™ and grown in free-standing wafer form via microwave assisted chemical vapor deposition with a boron doping concentration $>10^{20}$ atoms cm^{-3} . BDD for glass sealed macro electrodes and all other non-XRF electrodes was a free-standing electroanalytical grade wafer (7/1), ≈ 600 μm thick and polished to $\approx \text{nm}$ roughness on the growth face. BDD for EC-XRF was electro processing grade and was supplied as 20 and 25 mm diameter disks ≈ 250 μm thick and polished to $\approx \text{nm}$ roughness on the growth face.

2.3. Fabrication of electrodes

2.3.1. Laser Micromachining

The cutting out of 1 mm macros and any modifications to size or shape of BDD samples was done using a laser micro-machiner (Oxford Lasers, UK, E-355H-ATHI-O, 355 nm, 34 ns, Nd:YAG approx. 1200 J cm^{-2} 10 KHz repetition rate, 1 mm s^{-1} milling speed). Due to the formation of graphitic carbon during the laser micromachining process all samples were acid cleaned (see Section 2.3.2) prior to use to remove the non-diamond carbon.

2.3.2. Acid cleaning

Acid cleaning was carried out by boiling BDD samples in concentrated sulfuric acid saturated with potassium nitrate for 30 minutes, then boiling them in sulfuric acid for a further 30 minutes followed by a thorough rinse in DI water. This process ensures the BDD surface is clean and oxygen terminated.¹

2.3.3. Ohmic contacting

Electrical contacts to BDD samples were made by sputtering (Moorfield minilab 060 platform sputter/evaporator, UK) a 10 nm layer of titanium onto the lapped (nucleation face) of the diamond followed by a layer of gold (or Pt for EC-XRF electrodes at 400 nm thickness) to prevent oxidation of the titanium. The shape (0.5 mm diameter circle for 1 mm macroelectrodes) and position of the contacts was controlled using a kapton (RS, UK) mask made by laser micromachining. The contacts

were annealed to form the titanium carbide bonds (400 °C, 5 hours) required for an ohmic contact between C and Ti.

2.3.4. 1 mm Macroelectrode Sealing

Borosilicate glass capillaries (I.D. 1.16 mm, O.D. 2 mm, Harvard Apparatus Ltd., Kent, UK) were held at both ends, heated in the centre via a heated coil and pulled apart via gravity to create tapered ends, these ends were sealed over a blue Bunsen burner flame. 1 mm BDD rounds are placed into the tapered glass with the polished face towards the taper (contacted face away) and placed under vacuum for approx. 30 minutes, this is to prevent oxygen reacting with the BDD during heating. While still under vacuum these are heated around the BDD to melt the glass and create a seal between the glass and the BDD. The BDD containing capillaries are removed from vacuum and the taper is then polished away to expose the BDD polished face using carbimet grit papers (Buehler, Germany) of decreasing roughness. Silver epoxy (RD, UK) is syringed into the capillary and a copper wire pushed into the epoxy until it touched the contact on the back of the BDD, when the silver epoxy is cured Araldite (RS, UK) is used to seal off the top of the electrode where the copper wire protrudes from the capillary. This process can be seen as a schematic in Figure 17.

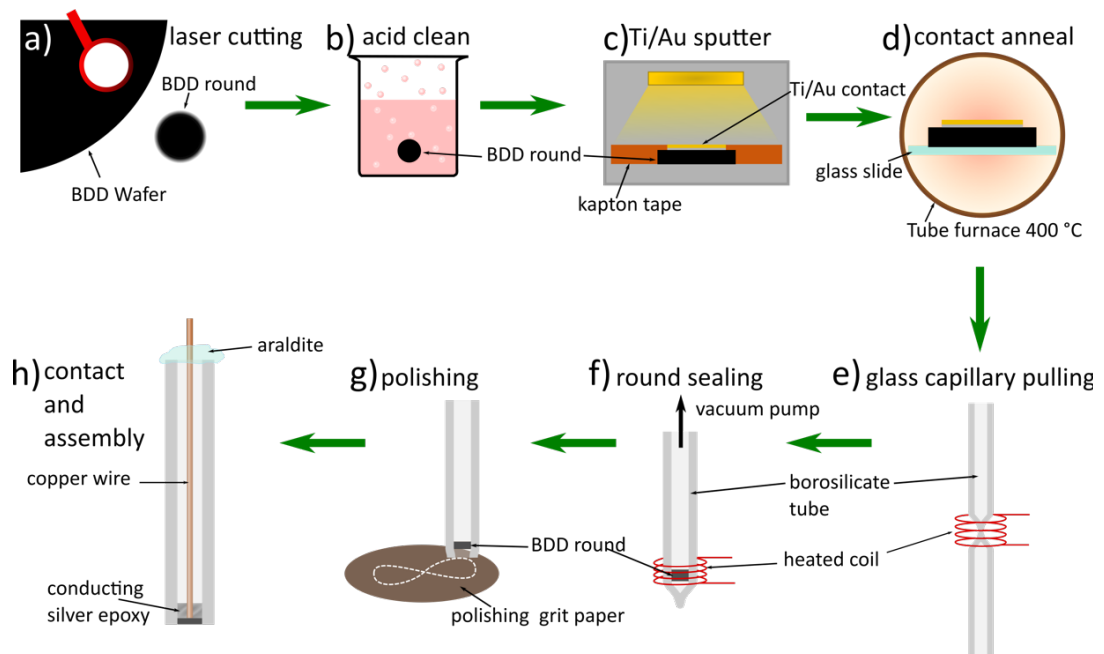


Figure 17 Schematic of the fabrication process of 1 mm macroelectrodes.

2.3.5. Bespoke Electrodes

Materials for the fabrication of bespoke electrodes and accessories in this work included polyetheretherketone (PEEK, Ensinger, UK), Araldite (RS, UK), silver epoxy (Chemitronics, RS, UK), silver wire (99.9% Strem chemicals, UK), copper wire (99.9% Strem chemicals, UK), epoxy overcoat (Chemitronics, RS, UK), 3D printed plastic (high impact polystyrene and acrylonitrile butadiene styrene, CEL), O-rings (polymax, UK). Materials used for each electrode are described in the chapters they appear in. EC-XRF and other bespoke electrodes were mostly made using similar methods to 1 mm macroelectrodes which are described further in the experimental of the chapters in which they appear.

2.4. Electrochemistry

All electrochemistry was done in a three-electrode set up with a saturated calomel reference electrode (SCE) and Pt coil counter electrode in stationary conditions at a scan rate of 0.1 Vs^{-1} , at 25°C unless otherwise stated. The potentiostats used varied between different work and are specified in the relevant chapter experimental sections.

2.4.1. Characterisation of Electrodes

Characterisation of electrodes was done by assessing the size of the solvent window (SW), capacitance and reversibility by peak separation, Figure 18 and follow the methods and advice in reference 1.

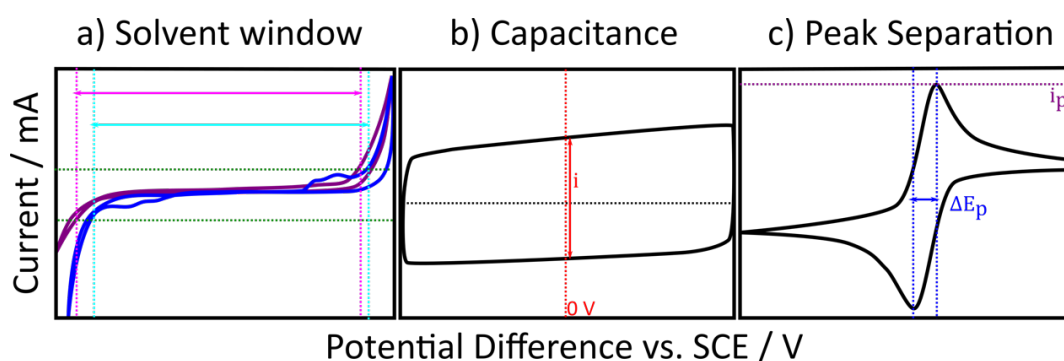


Figure 18 Example a) SW, b) capacitance and c) $\text{Ru}(\text{NH}_3)_6^{3+}$ data for a standard BDD macroelectrode, in a) the purple line is a good quality BDD electrode and the blue line is a BDD electrode with some observable non-diamond character.

For BDD the SW was measured as the potential window between where the current reaches $\pm 0.4 \text{ mA cm}^{-2}$ in 0.1 M KNO_3 at 0.1 V s^{-1} . The current increases quickly after the onset of the SW due to solvent splitting, this is kinetically slow on BDD which is why it has such a wide SW compared to other materials, however impurities such as sp^2 in the grain boundaries or left over from laser micromachining can be sites for solvent splitting or the oxygen reduction reaction and act to reduce the SW. If these are present in sufficient quantities the SW will demonstrate the poor quality of the electrode as denoted in Table 2.

The capacitance measurement in the same solution was the average current density at 0 V divided by the scan rate. The capacitance is related to the capacitance of the double layer and consists of currents from non-faradaic reactions, making up the background of the electrochemical solvent window.

Peak separation experiments to test reversibility were done using an outer-sphere redox couple, hexamine-ruthenium (III) chloride, $\text{Ru}(\text{NH}_3)_6^{3+/2+}$, and analysing the CVs. The peak separation should be 59 mV for a one electron process, as predicted by the Nernst equation, and peak currents should be similar to those predicted by Randles-Sevcik.¹ Increased peak to peak separations can occur due to poor electrical contacts, poor quality material or other resistances in the solution/circuit. Acceptable values are tabulated in Table 2.

Table 2 Acceptable values for electrode characterisation

Property	Acceptable ranges standard 1 mm macro	Acceptable Range – bespoke electrodes (EC-XRF etc.)
SW	3+ V	2+ V
Capacitance	6-10 $\mu\text{F cm}^{-2}$	6-12 $\mu\text{F cm}^{-2}$
Peak separation	59-80 mV	59-90 mV

These ranges are larger for bespoke electrodes as they are generally much larger with relatively much smaller contact areas as well as being a lower grade BDD. These factors made it extremely difficult to make bespoke electrodes that met the generally

accepted values, and so different ranges were required. These were decided upon after making up and testing several electrode versions and accepting the values of the ones that gave reproducible electrochemistry where redox features could still clearly be seen.

2.5. Field Emission-Scanning Electron Microscopy

Field Emission-Scanning Electron Microscopy (SEM) is a technique used to image features and probe composition of surfaces down to the nm scale by scanning a focused beam of electrons accelerated to between 0.1 and 30 kV across the surface. The electrons interact with the surface, are detected and used to build up an image. In this thesis In-lens and SE2 (secondary electron collection modes) were the modes used. A Zeiss Gemini (SEM), Warwick Microscopy RTP, was used to collect data. This instrument had energy dispersive spectroscopy (EDS) capability which uses the electron beam to irradiate the sample, causing fluorescence, which is then collected to make spectra of points or maps of the sample composition by element, in a very similar way to mapping XRF.

2.6. Transmission Electron Microscopy

Transmission electron microscopy (TEM) can be used to probe surfaces and features to the sub nm level. In this technique the electron beam is focussed and manipulated in several stages before being passed through the sample (sample must be thin, less than 100 nm) and then enlarged and projected onto a fluorescent screen. For imaging this screen is lifted and a charge coupled device is used to collect the electrons which are processed into a digital image. Maintaining a high vacuum is critical for successful TEM imaging, so is quality and cleanliness of sample. In this work a JEOL 2100 LaB6, Warwick Microscopy RTP, was used for TEM imaging and a JEOL ARM200F was used for TEM and scanning TEM (STEM) where resolution is ≈ 80 pm, allowing atomic resolution. The fabrication and electrochemical set-up of the TEM BDD electrode is described in Chapter 6.

2.7. X-Ray Fluorescence Spectroscopy

The system used in this thesis was a Rigaku NEX-CG: 50 kV Pd X-ray tube secondary target carousel system with Cu, Mo, Al and RX9 targets (RX9 is a polarising target) with an irradiated spot size of 24 x 22 mm (oval) and a Zr collimator. Unless otherwise stated the following measurement parameters were used for XRF analysis: vacuum, Mo target, 300 s live time, automatic current, 1.6 μ s shaping time. Mo target was selected as this has the most efficient overlap of irradiating spectrum and absorbance by sample out of available targets for Cu and Pb, the main metals of interest.

2.8. On-Line Electrochemical Mass spectrometry

Electrochemical measurements were performed with an Autolab PGSTAT12, multi ion mass detection as a function of time was used, this measures a maximum of 6 channels and a time difference of 50 ms between the detection on each channel. One of the channels was used to follow the changes in the total pressure and the other five channels were used to measure the following fragments: H₂, CH₄, C₂H₂, CO and H₂O. A secondary electron multiplier voltage of 1340 V was used for the samples of H₂O, CO, CO₂, C₂H₄ and CH₄ and 2100 for H₂. Several electrochemical set-ups were used and are described in detail in Chapter 6. This work was carried out in the labs of the Ampere group at Birmingham University.

2.9. Bibliography

- 1 J. V. Macpherson, *Phys. Chem. Chem. Phys.*, 2015, **17**, 2935–2949.

3. Mass transport investigations for

Ex Situ EC-XRF

3.1. Overview

In this chapter the increase in mass transport due to stirring, agitation by vibration, a wall-jet electrode and rotating disk electrode (RDE) are investigated relative to a stationary system. These systems are assessed on their mass transport characteristics as well as suitability of the instrumentation and electrodes for electrochemical x-ray fluorescence spectroscopy (EC-XRF). This application requires the system to not just simply maximise the mass transport, but also ideally to be simple, cheap, reproducible, portable with low XRF background electrodes and be useable for an untrained end user. The usability and reliability of an analytical system is extremely important for acceptance and uptake of the system, and so high priority was assigned to developing an electrode optimised for EC-XRF in combination with a simple and reliable system. Although direct competition with inductively coupled plasma mass spectrometry (ICP-MS) type systems is unlikely, EC-XRF is a promising candidate for on-site analysis of heavy metals, without the requirement for a wet lab or highly skilled user due to the portability of electrochemical and energy dispersive XRF instrumentation. This will allow fast analysis of environmental waters, the quality of which is of critical importance to environmental and human health. Many heavy metals are toxic at high concentrations so fast identification of contamination events from mine drainage or industrial incidents is crucial as well as regular routine testing for monitoring.

Boron doped diamond (BDD) is ideal for this application as it is essentially x-ray transparent, non-metallic and has excellent electrochemical properties as previously discussed. Previous work on EC-XRF has demonstrated both the potential for low limits of detection (LODs) and the difficulty of using the system due to the fragility of

thin BDD disks. Therefore, packaging of the BDD as an electrode was a major consideration in electrode development alongside retaining low XRF backgrounds.

A magnetic stirrer system was investigated as an extreme example of cheap and simple instrumentation, requiring only small readily available instrumentation and a stationary working electrode. The flow was not well defined and so was irreproducible, mass transport improvements were also poor, so this system was deemed unsuitable for further development. A similar issue was found with the vibrating diaphragm system, except it produced several extra practical complications despite the modest improvements in mass transport. The wall-jet electrode required challenging fluidics and reproducibility and mass transport in this particular system were poor as well as being variable with reassembly after cleaning. It was found that the RDE was the most effective at increasing mass transport and the most practical system for *ex situ* XRF analysis, despite the slightly larger and more expensive instrumentation. Therefore, several iterations of RDEs were made to achieve a system optimised for both electrodeposition and XRF analysis.

3.2. Introduction

Mass transport is a critical consideration in electrochemistry and even if not controlled, its impact on the resulting electrochemical system must be understood. In traditional electrochemical systems, stable temperatures and stationary set-ups are employed to prevent convective flow and background electrolyte is added to prevent migration. These act to reduce mass transport to diffusion only.^{1,2} However, electroanalytical applications generally require low limits of detection (LODs) which may require a higher transport than is provided by a simple stationary system. One way of increasing the mass transport is to use microelectrodes which have hemispherical diffusion, as described in Chapter 1, section 1.1.4, this results in higher diffusive flux to the electrode surface. The downside is that the small currents produced by microelectrodes can be challenging to measure on standard instrumentation. If small currents are problematic, an array of microelectrodes can be used to provide easily measurable currents whilst maintaining the advantages of

high diffusion and low background currents. A diffusion only solution isn't always viable, for some applications larger electrodes are required (EC-XRF) or are simpler to fabricate and integrate into systems (on-line analysis). The other method of increasing mass transport is by introducing solution flow to the system, this can be achieved in many ways such as introducing convection by forced solution flow,^{3,4} or induced temperature gradients⁵ as previously discussed in Chapter 1, section 1.1.4.

For quantitative analysis it is important that mass transport of the analyte to the electrode is reproducible, well defined and high so that errors and analysis times can be kept to a minimum while achieving low LODs. Anodic stripping voltammetry (ASV) (Figure 19) is a special case as it involves a phase change (electrodeposition and stripping, see Chapter 1, section 1.4.1) rather than purely solution phase redox reactions, for example in electrochemical nitrate and oxygen sensors.⁶ Mass transport is critical for the pre-concentration step in which a potential is applied to the working electrode to force electrodeposition (usually of metals) from solution onto the surface. The higher the mass transport rate or the longer the deposition time, the more the electrochemical deposit builds up on the surface. This is essential when dealing with trace analyte concentrations in order to obtain a detectable, quantifiable signal during the stripping step.^{7,8}

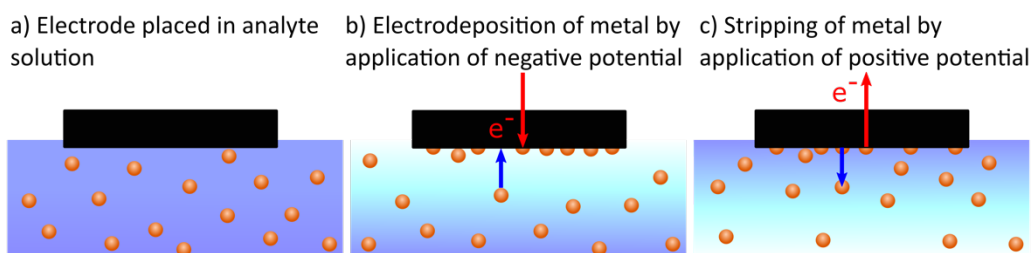


Figure 19 Schematic of ASV a) an electrode in solution with no potential applied, b) electrodeposition induced by negative potential relative to E^0 and c) stripping induced by a positive potential relative to E^0

Cheap, fast and reliable analysis of metal ions in aqueous solution is important in several fields, from monitoring of environmental systems to mining to pharmaceutical processes.^{9–13} These applications typically require detection limits of around ppb-ppm as many heavy metals are toxic even at these low concentrations.^{14,15} However at low concentrations some are safe and several are

even essential to life.^{16,17} In the field methods are highly desired, enabling a time and cost effective alternative to analysis at a centralised facility.

For heavy metal analysis, the major technique currently used is ICP-MS, which can detect down to ppt levels on some advanced instruments.¹⁸ The disadvantages of ICP-MS are that high purity chemicals and trained technicians are required for reliable analysis.^{18–20} In addition, the cost of instrumentation is high, and analysis must be done in a laboratory meaning samples must be transported. ASV is an alternative, which can detect around 30 different elements to low ppb level, this is heavily dependent on the sample and system used.^{21,22} ASV equipment is relatively cheap and portable with fast analysis times making it suitable for *in situ* analysis, but an experienced user is required and sometimes additional sample processing. Interferences such as intermetallic compounds (Cu-Zn, Cu-Ni *etc.*) and surface fouling can be very problematic, making analysis complicated and requiring optimisation for each application. This often requires the employment of a highly skilled user who can analyse results and adapt methods.^{23–28}

Energy dispersive x-ray fluorescence spectroscopy (ED-XRF) is an extremely good detection system for metals in solids and is used widely across mining, metal and cement industries.^{29,30} Instrumentation is reliable, easy to use and portable.³¹ However, many common forms of XRF have poor detection limits for liquid samples, typically in the range of 1-10 ppm, some types such as total reflection XRF are better, but some form of pre-concentration is still required for low concentration liquid analysis.^{32,33} An example of a simple commercial pre-concentration method for liquid analysis is the Rigaku Ultra-Carry system. This is a hydrophobic plastic disk with a small area of an adsorbent material in the centre onto which a small aliquot of analyte solution (200 µL) is pipetted. The solution is dried on a hotplate and the procedure repeated to increase detection limits, by depositing more material. After drying the disk is analysed as usual with XRF and the results compared to a calibration plot. This method, although simple and effective, Rigaku claims LODs down to ppb,³⁴ requires approximately an hour for the drying step (which can be repeated to increase LOD). Other pre-concentration methods for XRF include activated thin layers

(ion-exchange extractant), nanomaterials (as adsorbents) and liquid phase microextraction and EC-XRF.³³

Electrochemical-XRF (EC-XRF) is a hybrid method of electrochemistry and ED-XRF, it uses electrochemical pre-concentration onto an electrode in the same way as ASV, the difference is the analysis step is done with ED-XRF and not stripping voltammetry (Figure 20). In EC-XRF a boron doped diamond (BDD) electrode is used as the substrate, this is an ideal material for this application as it possesses metallic like conductivity without containing metallic elements that would increase the XRF backgrounds. XRF is very insensitive to light elements such as C and B and so the BDD acts like an x-ray transparent window allowing analysis of deposits on the surface.³⁵ Despite being crystalline, BDD is made up of many small crystals and is thin enough (approx. 250 μm) to only negligibly increase backgrounds. To ensure the backgrounds are low the BDD electrode is removed from the electrochemical set-up and analysed in XRF as a freestanding disk to avoid putting metallic parts of the electrochemical apparatus in the XRF. BDD is extremely chemically resistant with a wide solvent window and a reproducible surface from mechanical polishing (an alumina slurry polish is sufficient and a standard procedure in electrochemistry), making it ideal for reusable sensing applications.³⁶ Other forms of carbon would not be suitable as they are not as mechanically robust so are more prone to mechanical wear which limits their lifetime, and materials such as graphite have a layered structure which scatters the x-rays strongly resulting in peaks and high backgrounds.³⁷

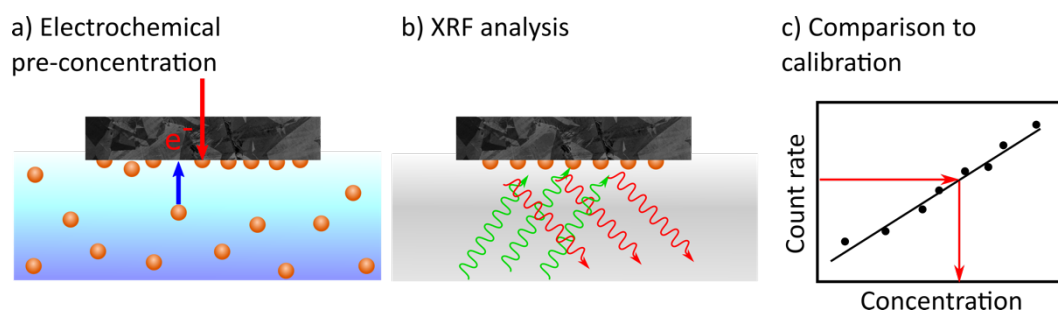


Figure 20 Schematic of EC-XRF a) the pre-concentration step using electrodeposition b) analysis with XRF c) comparison of XRF signal to concentration calibration to determine initial sample concentration.

Electrochemical pre-concentration is extremely effective, instrumentation is cheap and portable, analysis of solid samples by XRF is fast, simple and prone to few interferences, compared to methods such as ICP-MS which require a lot of preparation and measure elements sequentially. EC-XRF provides the best of both worlds by eliminating the use of stripping voltammetry which, as mentioned above, suffers from many sample variables and interferences.^{38–40}

Previous work on EC-XRF have used the electrode in either an RDE or wall-jet electrode configuration in order to increase mass transport and aid pre-concentration of the metal.^{38–40} Choosing a method for inducing mass transport depends heavily on the application. For EC-XRF, large electrodes are required (> 1 cm diameter) to maximise the area over which electrodeposition can occur and make full use of the analysable area in XRF. Previously *in situ* EC-XRF used a wall-jet system to flow solution over the working electrode, which was placed in the XRF chamber, for continuous analysis, Figure 21.⁴⁰ With the electrode component sitting directly over the x-ray unit any leakage in the system is catastrophic, hence extreme care must be taken to produce a water tight system.

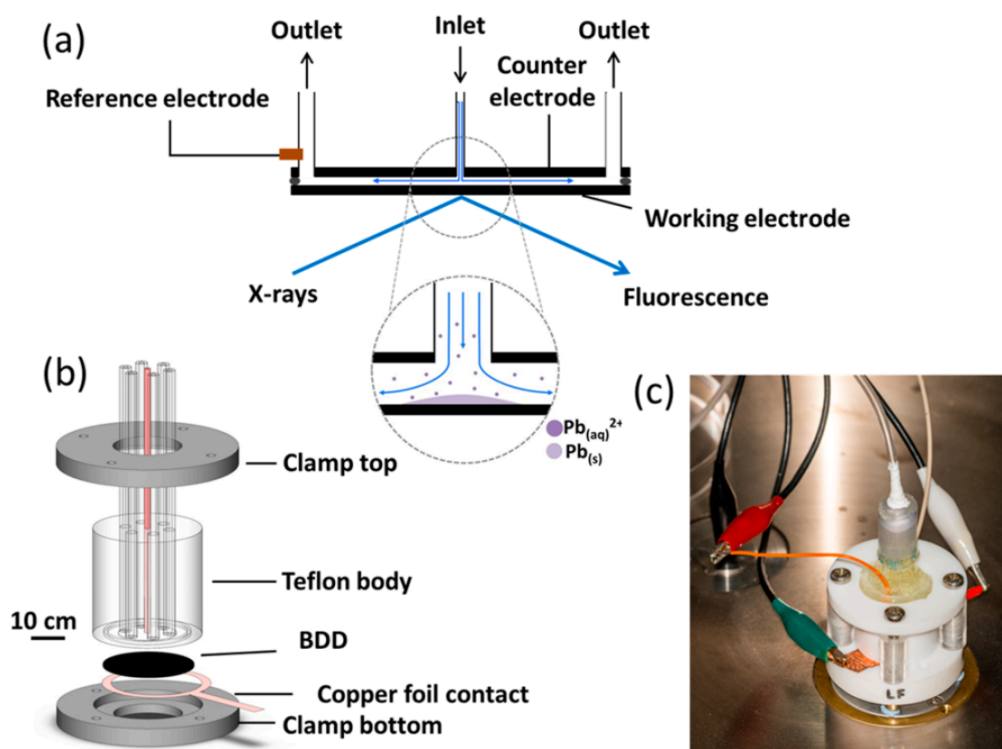


Figure 21 Schematic a) and b) of wall-jet flow cell and c) Image of flow cell set-up over XRF optics from reference 40.

Brett *et al.* have empirically determined the wall-jet equation for calculating the theoretical current and its dependence on other factors, Equation 30.³

$$i_{lim} = 1.597k_m j r^{\frac{3}{4}} v^{\frac{-5}{12}} D^{\frac{2}{3}} a^{\frac{-1}{2}} V_f^{\frac{3}{4}} C \quad \text{Equation 30}$$

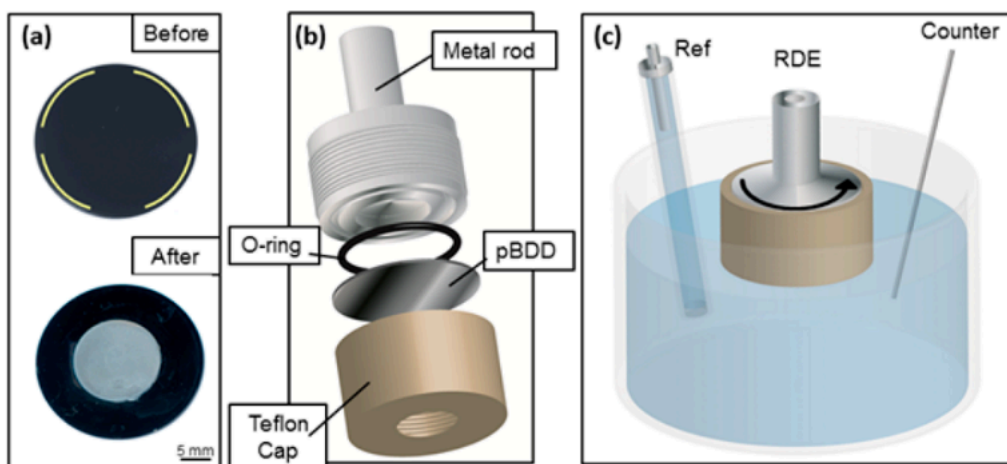


Figure 22 Photograph a) of BDD electrode disk top) back of disk bottom) front of disk with deposit shown and schematics b) and c) of the electrode assembly and electrode set-up respectively reference 41.

A bespoke RDE was utilised for *ex situ* EC-XRF, such that the electrode could be removed from the set-up and analysed stand-alone in the XRF, see Figure 22. This system achieved a 2.6 fold increase in current from stationary peak currents at 20 Hz.

The RDE is a relatively simple set-up, however rotator motors and electrodes need to be of high quality to prevent wobble, RDE motors are also fairly large compared to other systems. This work was proof of concept, and this early design of the RDE head meant the system was very difficult to use and often resulted in breakages of the BDD. Development of a BDD-RDE rotator head that is easy to handle and reuse and well as being well suited to both electrochemistry and XRF is important.³⁸ The Levich equation (Equation 31) can be used to calculate theoretical currents for RDE systems.⁴²

$$i_{lim} = 1.554nFAD^{\frac{2}{3}}\omega^{\frac{1}{2}}v^{\frac{-1}{6}}C \quad \text{Equation 31}$$

Stirring can be thought of as the simplest way of introducing mass transport but no theoretical equations have been developed due to the complexity of mass transport in the system. As such, stirring has never competed with controlled mass transfer methods such as RDEs for quantitative analytical applications.⁴³ Other less well-defined mass transport systems are also found such as sonication and vibration, however, these are less prevalent than RDE in the literature. Sonication, although giving large solution velocities and over an order of magnitude current increase, can be difficult to use practically, it can either be used with a sonication horn tip or with the electrode being on the tip itself, called a sonotrode. Due to the high frequencies used, cavitation events are induced where small bubbles form then collapse quickly causing high speed microjets, this can cause heating and damage to materials close by.⁴⁴ Sonication is very dependent on maintaining exact cell geometries and electrode-tip separations, it can cause damage to electrodes and other components so would not be suitable for EC-XRF.⁴⁵

Vibration is usually implemented by oscillating the electrode, the main difference between vibration and sonication is vibration works around the Hz frequencies whereas sonication is kHz. Because of this cavitation events are not induced in vibration but current increases relative to stationary are modest, around double, and it is much less destructive to components.^{46,47} It has generally been applied to small electrodes, less than 1 mm, and the practicalities of this set-up can be challenging and are cell dependent.^{46,47} It is reported that the max current is proportional to oscillation frequency, $f^{\frac{1}{2}}$, and that the amplitude of oscillation has little effect.^{48,49} All of these techniques increase the rate of analyte ions reaching the electrode surface and hence decrease the pre-concentration time compared to a stationary set-up.

So far, no other methods of mass transport than RDE and flow cell have been investigated for EC-XRF and the focus in this work is on the development of a simple, reliable system that prioritises ease of use by an end user. Several methods of mass transport are investigated in this chapter, methods were chosen based on their

simplicity and ease of implementation to an EC-XRF optimised electrode. The best mode of mass transport was then used to develop an improved EC-XRF electrode and set-up.

3.3. Experimental

3.3.1. Chemicals and Solutions

All solutions were prepared using Milli-Q water (18.2 MΩ cm at 25 °C). All mass transport systems were assessed using a 1 mM solution of hexamine-ruthenium (III) chloride, $\text{Ru}(\text{NH}_3)_6^{3+/2+}$ (98%, Aldrich), in 0.1 M potassium nitrate (KNO_3) (99% Aldrich), as described in Chapter 2, unless otherwise stated. EC-XRF experiments used copper (II) nitrate, copper (II) sulphate (99.99% Aldrich) and nitric acid (70% Fischer).

3.3.2. Mass Transport Systems Materials and Fabrication

All BDD for electrodes in this chapter was supplied and processed as described in Chapter 2, ohmic contacts are Ti/Pt as the initial metals of interest for this project were Pb and Cu, the fluorescence of Au is close to that of Pb and so Pt was used as its fluorescence peak is further away, therefore less likely to overlap and cause an interference in XRF analysis. 1 mm macroelectrodes used were made as previously described. All bespoke electrodes here are electroprocessing grade BDD. The vibrating diaphragm system and RDE prototype casings were fabricated by Rod Wesson, Lee Butcher and Marcus Grant in the electrical and mechanical workshops (Department of Chemistry), from my designs.

3.3.2.1. Magnetic stirrer system

A standard 2 cm long magnetic flea and a hotplate stirrer (RCT basic, IKA) were used for this set up. The working electrode used is 14 mm diameter BDD. The controls on the hotplate stirrer unit had no numbers, only a dial and so 0% is taken as the dial turned off and the percentage quoted is between this and 100% where the dial is

turned as far as it will go, as judged by eye. The manufacturer states the RPM range as 50-1500 rpm.

3.3.2.2. Vibrating electrode

A bespoke vessel made from a PEEK cylinder with a diaphragm (KNF part #022460 for a N86KT.18 vacuum pump and is 41 mm in diameter) connected to the circumference. The centre of the diaphragm was moved by an electromagnet system (the coil is 550 turns of double (Bi-filar) 0.25 mm enamelled copper wire on an ETD29 bobbin that required forced air cooling so it does not heat the solution, this drives the magnet which is a 7.5 mm diameter x 27 mm long bar of Aluminium-Nickel-Cobalt, Onecall 1079493). The electromagnet is controlled by an input voltage – the drive voltage, and a frequency. The drive voltage approximated to a control of oscillation amplitude. Most of the remaining parts and casing are made from Aluminium. In this system a 1 mm glass sealed BDD electrode was used for characterisation. A watch dial meter was employed to measure the amplitude.

3.3.2.3. Wall-Jet electrode

The design employed here was identical to that used in reference ⁴⁰ by O’Neil. The flow cell consisted of a BDD counter electrode (16 mm diameter) with 6 arrays of outflow holes sealed in a Teflon case with an O-ring that held a 25 mm diameter BDD back contacted electrode in place against a Teflon holder and copper foil, to which the working electrode cable is clipped. In the outflow a chloridised silver wire was inserted into the cell as a reference. The flow was controlled by a HPLC pump (Gilson Model 305, France) with a max flow rate of 14 ml min⁻¹.

3.3.2.4. Rotating Disk Electrodes

The “original design” electrode used the original Al threaded rod used by Hutton,³⁸ the rotator unit, BDD disk and cap were all made to the same design as those used by Hutton with the exception of the cap which was made from PEEK instead of Teflon, this was to increase the stiffness to prevent cap breakage, which was an issue with the original design.

Materials used for RDE electrode prototypes included polyetheretherketone (PEEK, Ensinger, UK), Araldite (RS, UK), silver epoxy and epoxy overcoat (Chemtronics, RS, UK), silver wire, copper wire (99.9% Strem chemicals, UK), brass rod.

All Prototypes are made of PEEK and brass bodies and consist of a removable head, which houses the BDD disk in the PEEK with overcoat epoxy to seal. The body is designed to fix the head to the shaft of the rotating motor and provide a continuous electrical contact between them through the brass inner, whilst the O-ring prevents solution ingress.

Prototype 1 used silver wire to contact to the BDD and was exposed on the back face of the head so that when screwed to the body it made electrical contact with the metal exposed on the body.

Prototype 2 and 3 used Au coated brass springs (RS, UK) to make a temporary connection to the contacts on the back of the BDD.

3.3.3. Electrochemistry

Experiments were run with a CH Instruments 730 A potentiostat, as a 3-electrode cell, with an SCE reference (CH Instruments) and Pt coil counter electrode with a scan rate of 0.1 V s^{-1} unless otherwise stated. Characterisation of the systems was carried out and all reached acceptable values of solvent window, capacitance and comparable $\text{Ru}(\text{NH}_3)_6^{3+/2+}$ peak currents to theory as previously described in Chapter 2. Polishing pads and alumina polish ($0.05 \text{ }\mu\text{m}$ Micropolish, Buehler) were used to mechanically clean the electrodes between experiments.

3.3.4. ED-XRF

A Rigaku NEX-CG: 50 kV Pd x-ray tube secondary target carousel system with Cu, Mo, Al and RX9 targets (RX9 is a polarising target) was used with an irradiated spot size of $24 \times 22 \text{ mm}$ (oval), and a Zr collimator. Unless otherwise stated the following

measurement parameters were used for all XRF analysis: vacuum, Mo target, 300 s live time, automatic current, 1.6 μ s shaping time. The molybdenum secondary target was used as this was most appropriate for the metals of interest (Cu) as it caused the most efficient excitation of Cu out of the available targets, thereby giving the best signal to noise ratio.

3.4. Results and Discussion

3.4.1. Magnetic stirrer system

The simplest way of introducing mass transport is through the use of a standard magnetic stirrer. The electrochemical cell, containing a solution of $\text{Ru}(\text{NH}_3)_6^{3+/2+}$ and the 3 electrodes, the original design EC-XRF RDE electrode (1.54 cm^2 area) as the working electrode, was placed on a modified hot plate stirrer and a magnetic stirrer added to the solution. Efforts were made for the working electrode and the magnetic bar to be kept in the centre of the cell. There are no theoretical equations for currents when stirring in such a system as flow in the system is turbulent. Figure 23 shows the CV response of the BDD electrode for $\text{Ru}(\text{NH}_3)_6^{3+}$ reduction, in both stationary solution (black line) and as the stirring rate was increased from 0 – 100 %, by measure of the extent of rotation of the dial as no quantifiable value was present on the dial.

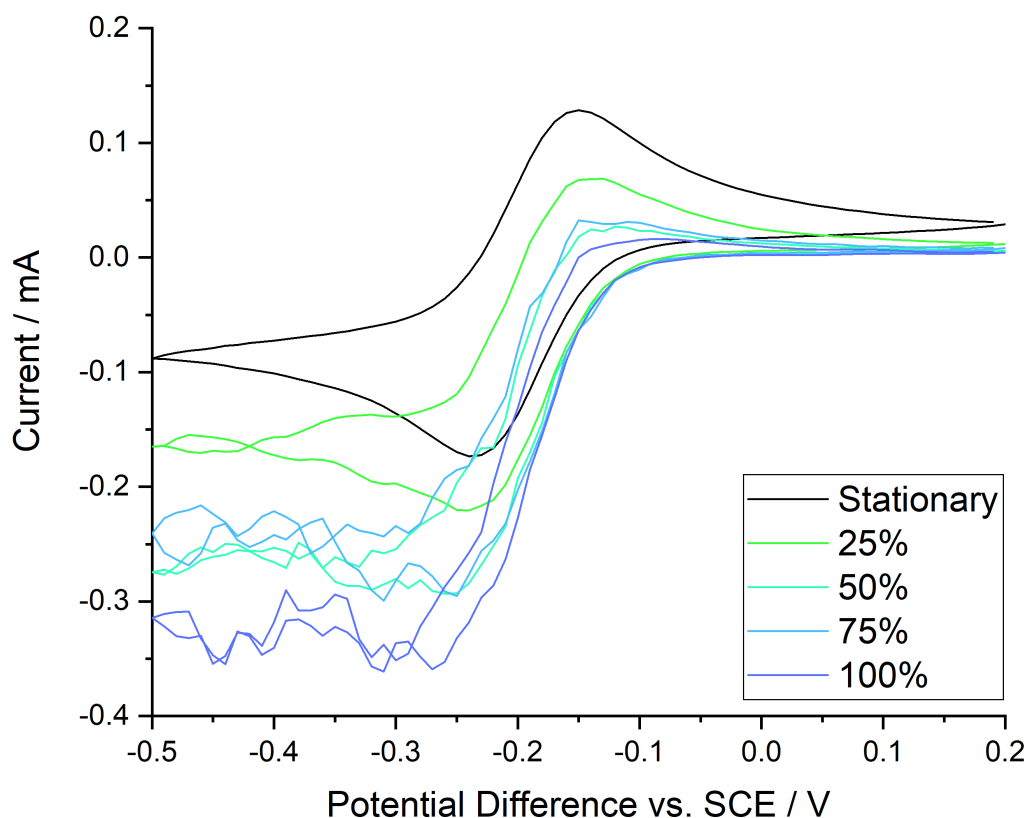


Figure 23 CV of 0.5 mM $\text{Ru}(\text{NH}_3)_6^{3+/2+}$ with increasing rate of stirring of magnetic stirrer on a hotplate with a 14 mm diameter BDD electrode, 0.1 Vs^{-1} , 0.1 M KNO_3 .

The stationary CV had a peak current of -0.17 mA, close to the theoretical value of -0.19 mA. The current was increased to a limiting current of $\approx 0.35 \text{ mA}$ with the maximum stirring rate. These currents give k_t values, with the use of Equation 30, of 2.56 and 4.71 cm s^{-1} respectively. The stirred CVs show current fluctuations due to fluctuations in mass transport caused by the magnetic stirrer moving around in the beaker, causing turbulence.

Figure 24 shows the average maximum current (modulus, $n=3$, error bars are standard deviation) for the 5 different rates of stirring tested. The variability in maximum current at 100% is very large, due to increased turbulence, whereas the stationary CVs are very reproducible, the error bars are contained within the point symbol.

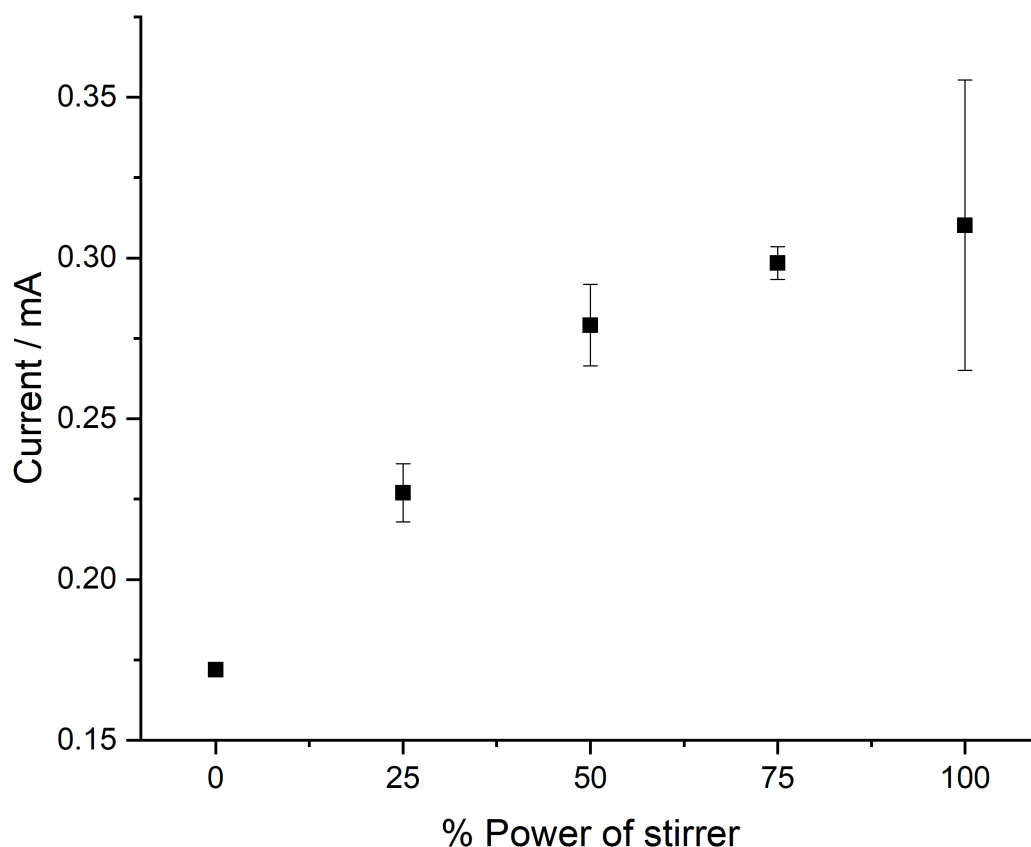


Figure 24 Increase in modulus of maximum current with increasing stirring power from CVs in 0.5 mM $Ru(NH_3)_6^{3+/2+}$ with a magnetic stirrer on a hotplate with a 14 mm diameter BDD electrode, 0.1 Vs^{-1} , 0.1 M KNO_3 $n=3$.

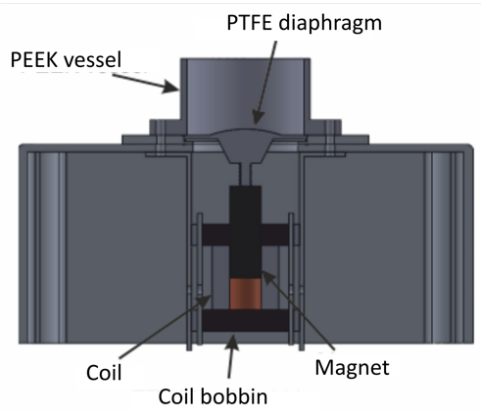
Figure 23 and Figure 24 show that the stirrer increased mass transport and a limiting current was reached, however there was considerable variability, generally increasing with stirring rate as turbulence also increased. This is likely due to the tendency for the magnetic stirrer bar to move around the bottom of the cell, several beakers were trialled, but the magnetic stirrer would always move randomly around the bottom. As maximum current improvements were modest (1.8 fold) compared to the original RDE (2.6 fold),³⁸ and variable, it was decided that this system was unsuitable for an analytical method and not worth further development.

3.4.2. Vibrating Diaphragm

Vibration in a system will increase mass transport and there are two ways this can be achieved, vibrate the electrode or vibrate the solution, as discussed in Chapter 1, section 1.1.4, it is more common for the electrode to be vibrated. However, as the

electrode for this system needed to be large and have a temporary electrical contact (so it could be removed from the system for XRF analysis), vibration could cause parts or contacts that are not permanently affixed to move or separate. Due to this it was decided that having a component for vibration separate to the electrode was less prone to these issues and so a bespoke cylindrical vessel with a vibrating diaphragm at its base was made. This was controlled using a drive voltage and a drive frequency that caused the centre of the flexible diaphragm to oscillate by way of an electromagnet, Figure 25.

a) Schematic of Vibrating Diaphragm



b) Photo

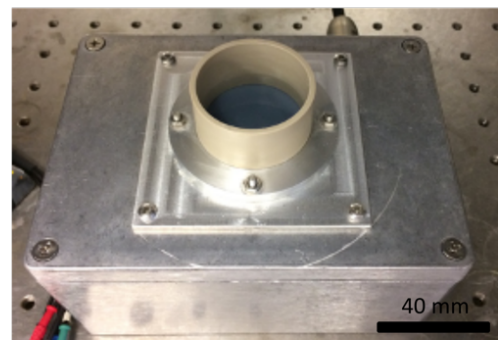


Figure 25 a) schematic cross-section and b) photograph of vibrating diaphragm system.

To understand how drive voltage and drive frequency affect the amplitude of the displacement of the diaphragm, a dial indicator placed on the surface of the centre of the diaphragm and used to measure the displacement, shown in Figure 26.

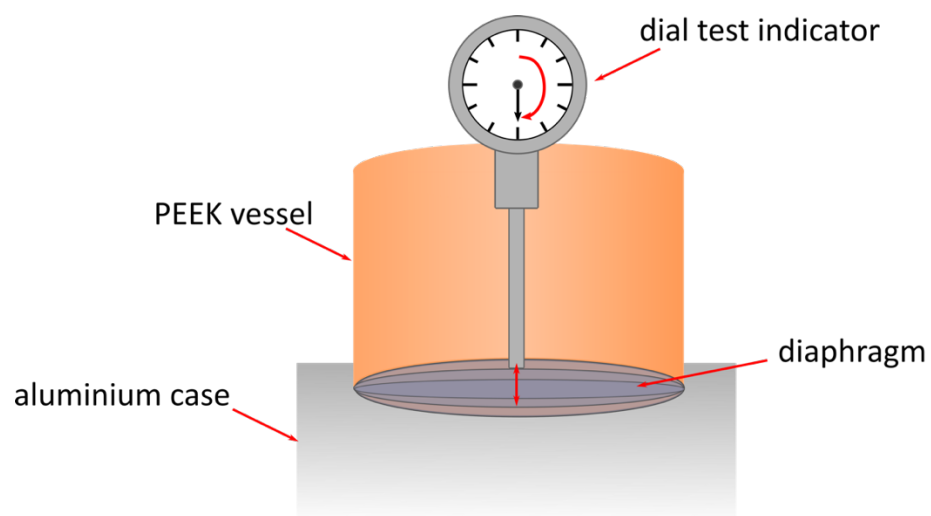


Figure 26 Schematic of measuring the diaphragm displacement with a dial test indicator positioned in the centre of the diaphragm to measure maximum displacement.

This shows that amplitudes varied between 2.5 and 29.5 μm for the parameters used. Increasing drive voltage for a fixed frequency resulted in a larger amplitude but there also appears to be some dependence of the amplitude on drive frequency, this is due to the electromagnetic system hitting a resonance condition at approximately 10 Hz.

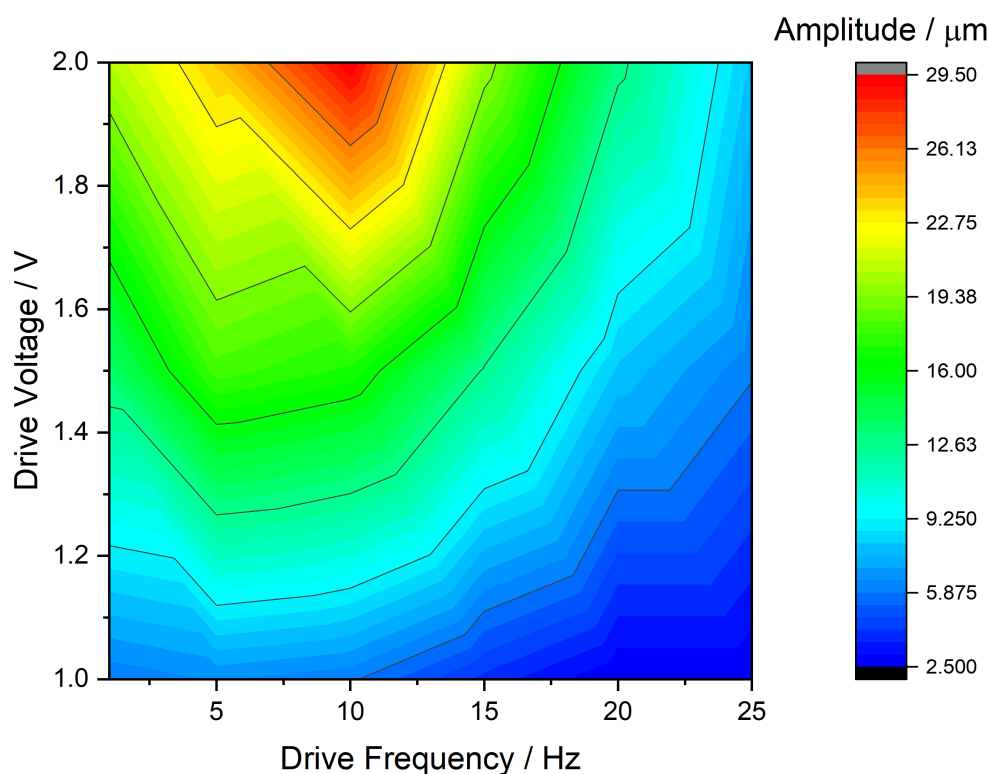


Figure 27 variation of amplitude with respect to drive voltage and drive frequency applied to the diaphragm mechanism, a resonance condition for the system is met around 10 Hz resulting in an increased amplitude.

The electrochemical cell was set-up within this vessel. The characterisation of this system was initially done using a 1 mm BDD macroelectrode and 1 mM $\text{Ru}(\text{NH}_3)_6^{3+}$. The positioning of the electrode was challenging, a micro positioner and clamp were used to hold the electrode. To position the electrode, it was placed in the centre of the vessel, as judged by eye and held lightly in the clamp, it was then lowered to touch the surface of the diaphragm (same as dial test indicator). The mechanism was then turned on so the diaphragm would move, hit the electrode and, as the electrode was held only lightly, it was moved to the position of maximum displacement of the diaphragm and then the clamp was tightened. Positioning the electrode in this way meant it was always as close as possible to the diaphragm. Moving the electrode to a measured distance away from the diaphragm was not feasible as the diaphragm

was very flexible and moved if pressure was applied (e.g. if an electrode was lowered onto it) and so a reliable zero point could not be fixed.

The effects of drive voltage and drive frequency on maximum current were investigated and the results are shown in Figure 28. This shows that the amplitude variation seen in Figure 27 did not affect the maximum current as may have been expected. It seems that when the cell is full of liquid the oscillations may be damped and the resonance condition is not hit as when it was empty. Unfortunately, this means the amplitudes are unlikely to be the same as when empty, but it was not possible to test the amplitude with the cell full of solution as this would have damaged the dial indicator. It is probably safe to assume that increasing the drive voltage increases the amplitude and this is the reason for the higher currents at higher drive voltages. A drive voltage of 2 V was chosen for further experiments as it gave the largest currents.

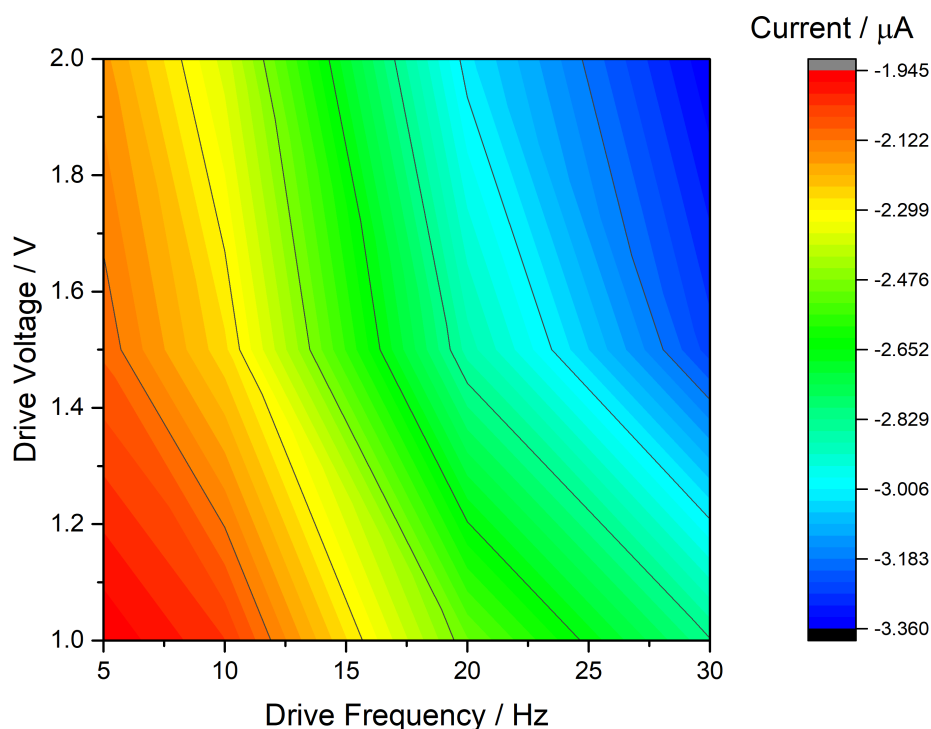


Figure 28 Parameter map of the effect of drive voltage and drive frequency on peak current in 1 mM $\text{Ru}(\text{NH}_3)_6^{3+/2+}$ on a 1 mm BDD electrode, 0.1 Vs^{-1} , 0.1 M KNO_3 .

The characterisation CVs for the purposes of addressing mass transport increases were done with a fixed 2 V drive voltage and varied frequency and are shown in Figure 29.

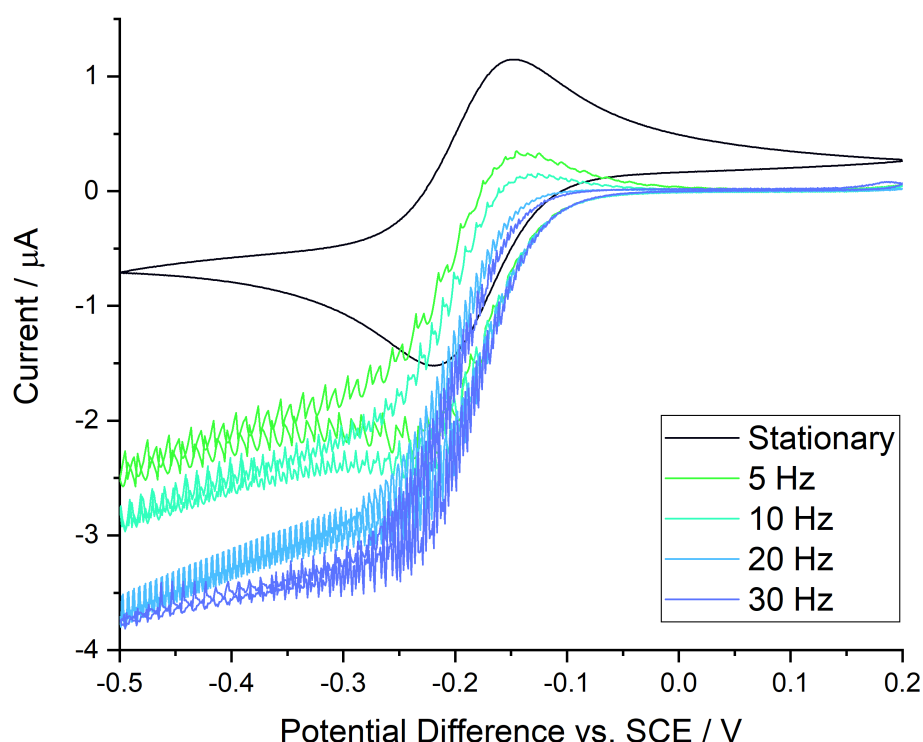


Figure 29 CVs of 1 mM $\text{Ru}(\text{NH}_3)_6^{3+/2+}$ on a 1 mm BDD electrode, drive voltage 2.0 V with varied drive frequencies, 0.1 Vs^{-1} , 0.1 M KNO_3 .

The peak current of the stationary electrode was $-1.52 \mu\text{A}$ while the theoretical current was $-1.97 \mu\text{A}$. This difference could be caused by an error in concentration or active electrode area, but the difference is small and other characteristics met the criteria in Chapter 2. Figure 29 shows that as vibration is applied the shape changes from a peak current to an apparent limiting current regime, as frequency increases the maximum current increases. The oscillations of the diaphragm can be seen as periodic peaks in the CVs, the frequency of these agree well with the quoted frequencies applied. The faster the oscillation frequency of the diaphragm, the faster solution is moved, meaning replenishment of the active species is going to be faster at higher frequencies. The maximum current here represents a 2.4 fold increase, which is better than stirring but still not as high as the original RDE. If higher frequencies were run, significant surface turbulence lead to solution losses and so higher frequencies were not run. This was expected to be the maximum current

increase possible for this particular system, but it is hard to judge the effects of amplitude as they are coupled to frequency, although literature claims that amplitude has little effect.⁴⁸ The modulus of the average maximum currents for each frequency and of stationary are shown in Figure 30. The error is small and appears to be fairly consistent, not increasing with increasing rates as the stirring system, suggesting that the mass transport to the electrode face is well-defined and not turbulent. The max current varies with respect to frequency approximately by the factor $f^{\frac{3}{5}}$. In literature current was found to vary with $f^{\frac{1}{2}}$, which is close to the value obtained from these data.

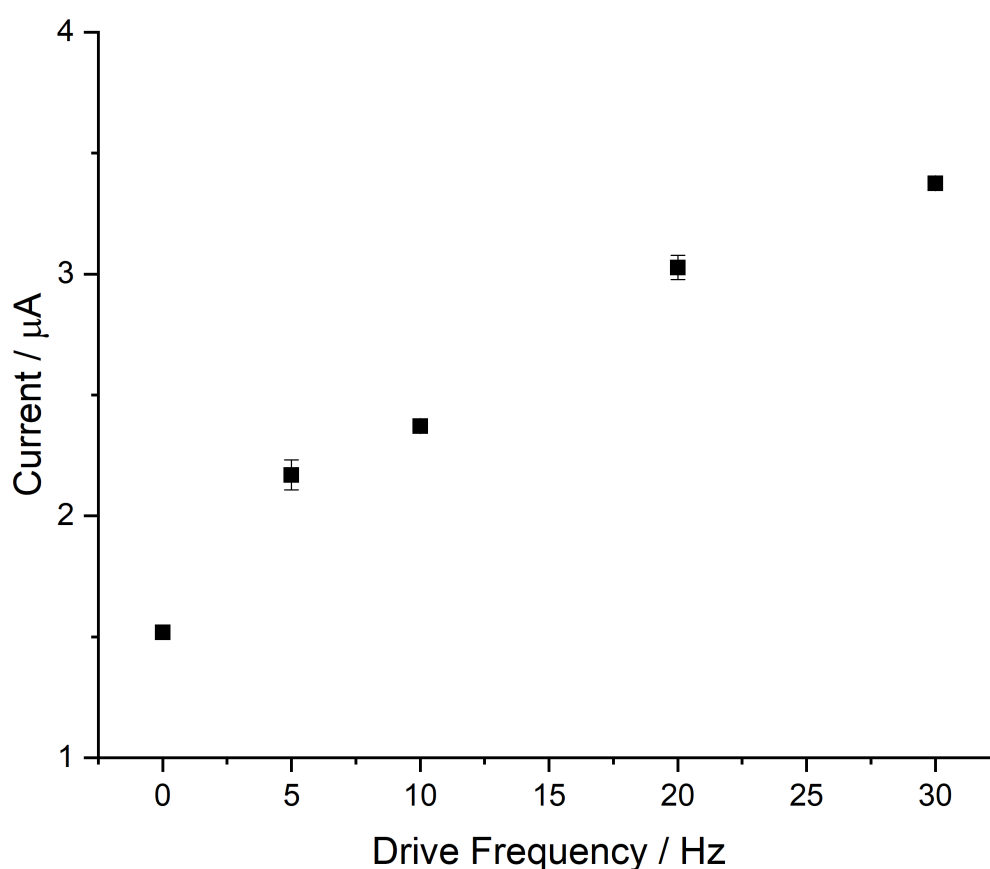


Figure 30 Modulus of the average current from $n=3$ CVs in 1 mM $\text{Ru}(\text{NH}_3)_6^{3+/2+}$ on a 1 mm BDD electrode at stationary and varying drive frequencies.

Initial trial work looked at implementation of an EC-XRF RDE electrode (Original RDE, BDD disk diameter = 25 mm), into the cell, which was held in place with a clamp and stand. However, difficulties emerged which made this methodology impractical for continued use in its current format. (i) It was too difficult to achieve a known electrode-diaphragm separation as the RDE could not be mounted on a micro

positioner and so could not be positioned in the same manner as the 1 mm BDD electrode (i) Due to the large electrode size, only 5 mm less than the vessel diameter, for all frequencies higher than approximately 5 Hz (and 2 V drive voltage) the solution tended to be propelled through the small gap between electrode and wall and come out of the cell, thereby changing the volume and resulting in loss of electrode-solution connection. These factors render this particular system irreproducible with feasible mass current increases of less than 2.4 fold compared to the original RDE so no further optimisation was carried out.

3.4.3. Wall-Jet Electrode

The cell employed here was the same as that used in reference 40 by O'Neil (Figure 31). The flow cell consisted of a BDD counter electrode (with 6 x 3 mm diameter hexagonal array of 60 μm diameter holes as the outflow) sealed in a Teflon case with an O-ring that held a 25 mm diameter BDD back contacted electrode in place against a Teflon base and copper foil to make a contact. In the outflow, a chloridised silver wire was inserted into the cell as a reference electrode. The flow was controlled by a HPLC pump with a max flow rate of 14 ml min^{-1} .

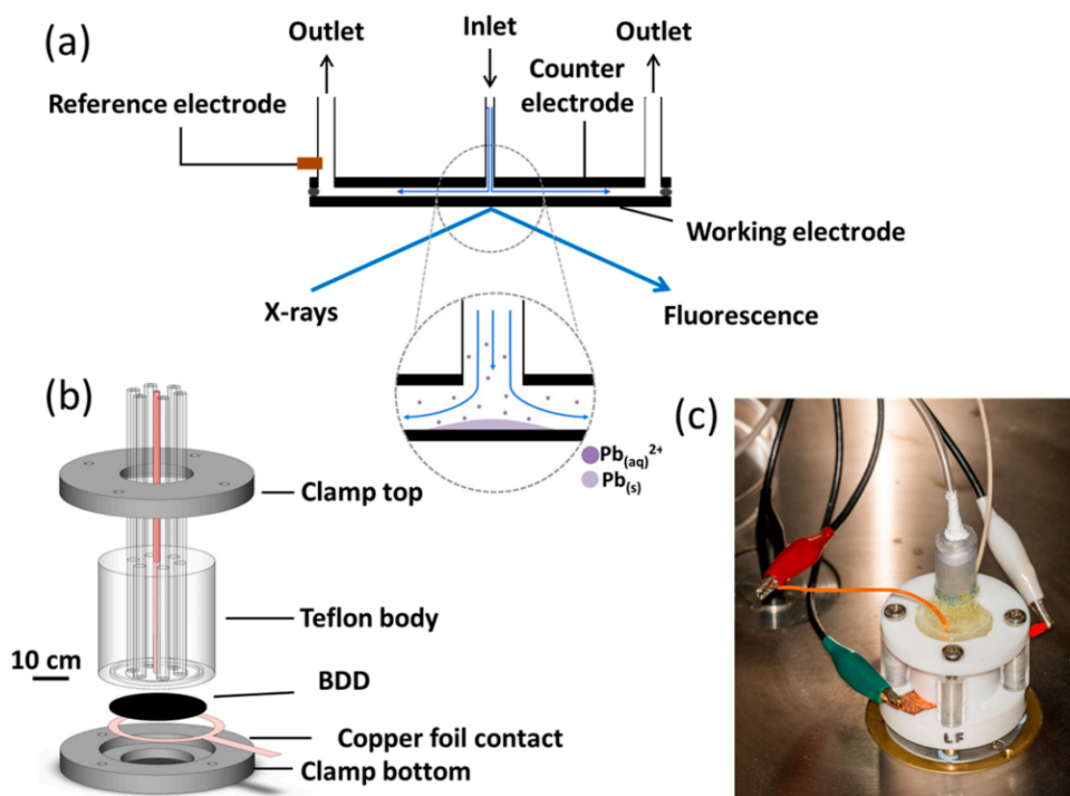


Figure 31 Schematic of wall-jet flow cell a) XRF analysis b) overall cell assembly c) photograph of cell.⁴⁰

Figure 32 shows the characterisation of this system by CV with $\text{Ru}(\text{NH}_3)_6^{3+}$, it can be seen that unlike the other mass transport systems this doesn't reach a steady state regime, which would be expected for a flow cell. The oscillations in current that can be seen are due to the HPLC pump pulses. The peak separations suggest that there were resistance effects, this sort of effect is often seen due to ohmic drop, it appears that the working electrode is not experiencing the potential that has been applied.^{1,50} The reference electrode is not in an ideal position, being in an outlet it is relatively far from the working electrode, also the counter electrode is approximately the same size as the working. The working electrode is connected by a pressure contact between the Ti/Au sputter contact and the Cu foil, all of these factors could contribute to resistance effects.

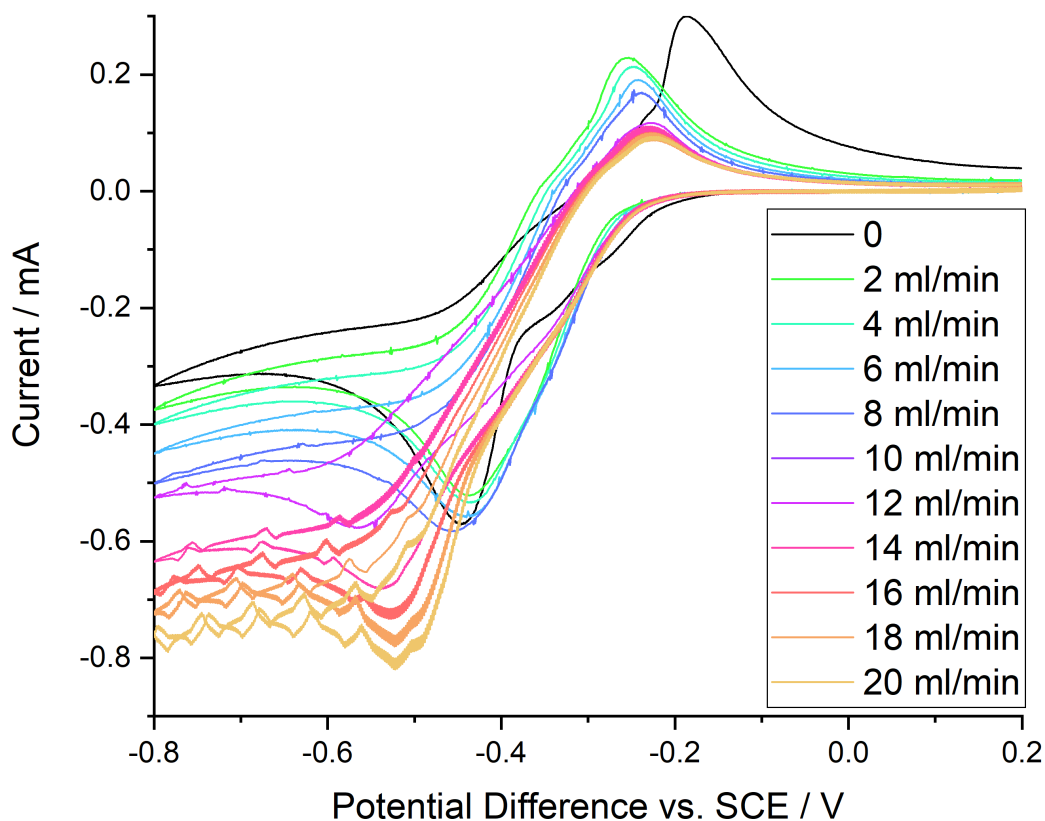


Figure 32 CVs of 1 mM $\text{Ru}(\text{NH}_3)_6^{3+/2+}$ in the O'Neil wall-jet cell, 0.1 Vs^{-1} , 0.1 M KNO_3 at flow rates from 0 to 20 ml min^{-1} .

The theoretical stationary current (calculated using Randles-Sevcik) was -0.79 mA , the experimental peak current of the stationary CV was -0.58 mA . The Randles-Sevcik

equation doesn't hold in this situation as the solution is confined, but it gives an estimate, the experimental value was much lower probably partly due to depletion of the analyte in the small volume of the channel and the resistive effects that are clear even in this stationary experiment. These CVs are far from ideal and this system did not fit well to wall-jet theory, see Figure 33. The theoretical limiting current for this were calculated using the wall-jet Equation 30. The electrode radius = 1.0 cm, kinematic viscosity = $8.8 \times 10^{-3} \text{ cm}^2 \text{ s}^{-1}$, diffusion coefficient = $8.8 \times 10^{-6} \text{ cm}^2 \text{ s}^{-1}$, the diameter of the inlet = 0.05 cm, bulk concentration = 1 mM for this experiment.

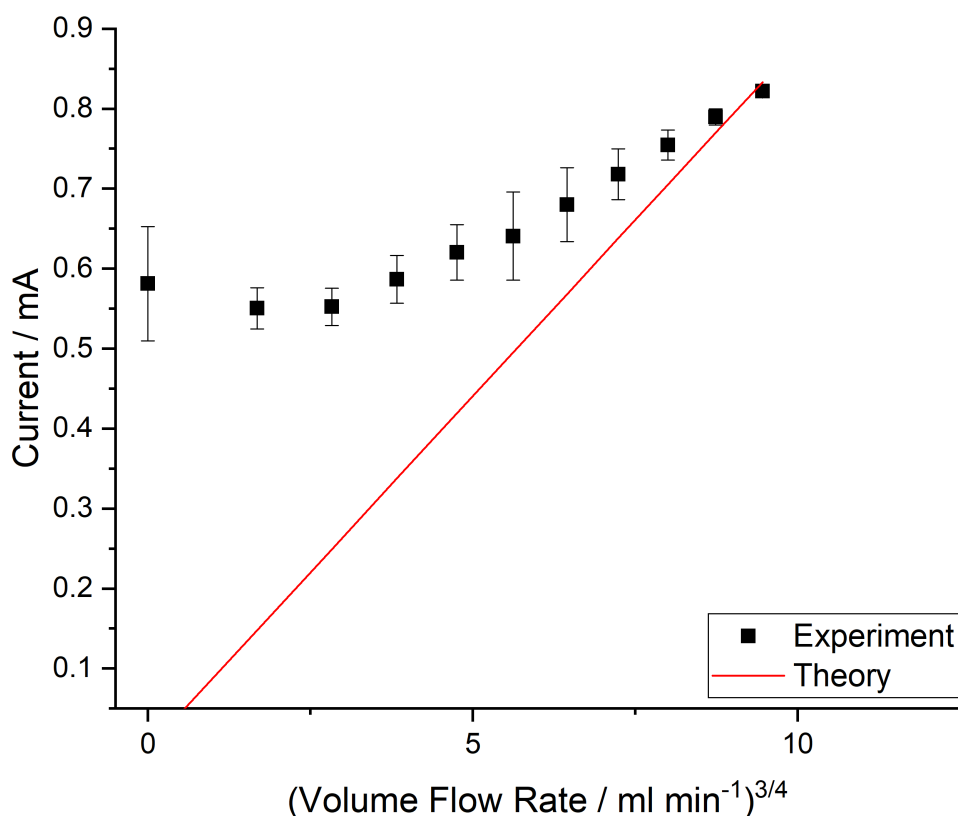


Figure 33 Modulus of maximum current from CVs of 1 mM $\text{Ru}(\text{NH}_3)_6^{3+/2+}$ in the O'Neil wall-jet cell, 0.1 Vs⁻¹, 0.1 M KNO_3 at flow rates from 0 to 14 ml min⁻¹, compared to wall-jet theory.

The deviations from theory at low flow rates are due to the combined effect of diffusion and convection, as previously stated the current value for the stationary system is -0.58 mA (Figure 33 is modulus of current) so even at low flow rates the current would not be expected to drop below this. This explains why most of the data points are higher than the theory, and explains why steady state CVs were not reached, even at the higher flow rates, diffusion was still a sizeable component of mass transport. Mass transport rates from convection and diffusion must have

similar magnitudes under these conditions. At increasing flow rates, the max current adheres closer to theory, but the gradient of the linear region for the experimental values appears to be lower than the theory. This could be due to resistance or other factors such as a change in electrode area, the working area is defined by the O-ring, which could have deformed over time.

This cell saw a 1.4-fold increase in peak current and did unfortunately disintegrate before any XRF experiments could be attempted, the materials had become brittle with age and several parts failed making it prone to leakage and unsafe for analysis by XRF. Araldite had been used to attach tubes to the Teflon coating, and this was not a robust fixing. With refinement a wall-jet flow cell system has the potential for improved results (O'Neil et al saw improvements of approx. 2.5 fold with this system) and the added benefit of its suitability for *in situ* EC-XRF, which has significant potential advantages over *ex situ* analysis, however it remains challenging to use for an inexperienced user in this form. Flow cell systems for EC-XRF are optimised and discussed further in Chapter 4.

3.4.4. EC-XRF RDE

Four different designs of EC-XRF RDE set-ups were explored, all based on a BDD working electrode. The first was based closely on the original EC-XRF RDE.³⁸ The BDD disk, front face for solution contact, back face containing a sputtered Ti/Au contact was placed in a PEEK cap inset with a rubber O-ring. Then a metal rod was screwed into the cap to make a contact with the Ti/Au contact of the BDD disk, this could then be attached to the motor, this assembly is shown in Figure 34. The cap reduced the effective electrode diameter from 25 mm to 14 mm. The O-ring combined with the pressure from the screwed in metal rod created a watertight seal preventing solution from reaching the back contact.

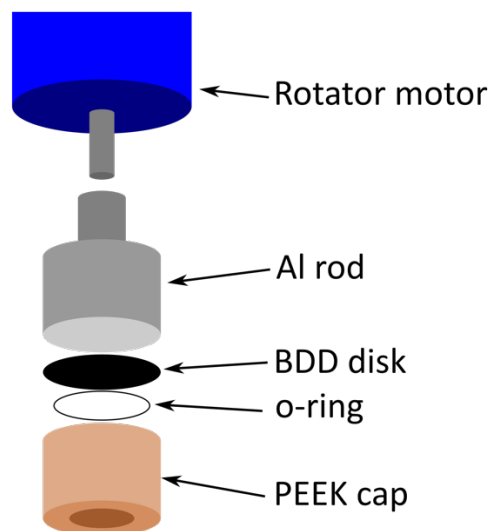


Figure 34 Schematic of original cap design EC-XRF RDE showing an exploded view of components.

The differences between this system and the system used in the paper was (i) the use of a slightly lower grade of BDD i.e. one that contains slightly more sp^2 bonded carbon (MR12 electrochemical processing grade). (ii) A homemade rotator was employed and (iii) the Teflon cap, which was very fragile was replaced with a more robust cap made from PEEK with a slightly increased thickness to increase durability. The resulted in a larger recess – BDD sat 2 mm below the top surface of the PEEK cap. This system will be referred to as the original cap design.

Figure 35 shows the characterisation CVs of this RDE, they show that a limiting current is reached by about 10 Hz. Theoretical stationary peak current as calculated with Randles-Sevcik (Chapter 1, Equation 18) is -0.19 mA, so the experimentally obtained value of -0.17 mA is very similar.

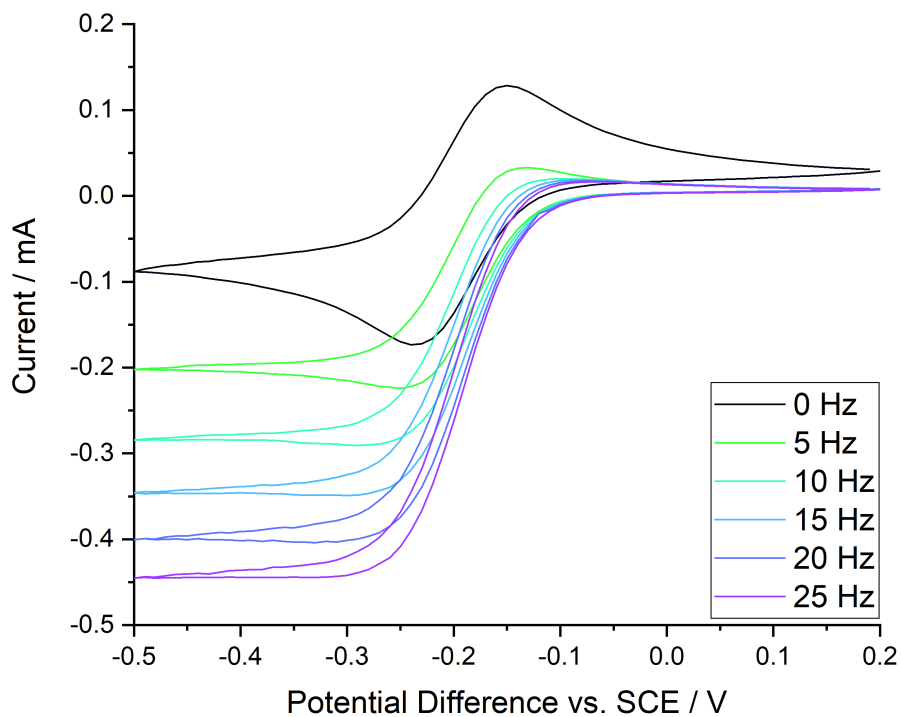


Figure 35 CVs of 0.5 mM $\text{Ru}(\text{NH}_3)_6^{3+/2+}$ with the original cap EC-XRF RDE design, stationary and with varying rotation rate, 0.1 Vs^{-1} , 0.1 M KNO_3 .

For the calculation of the theoretical current for these RDE systems, the Levich Equation 31 is employed, see Figure 36.

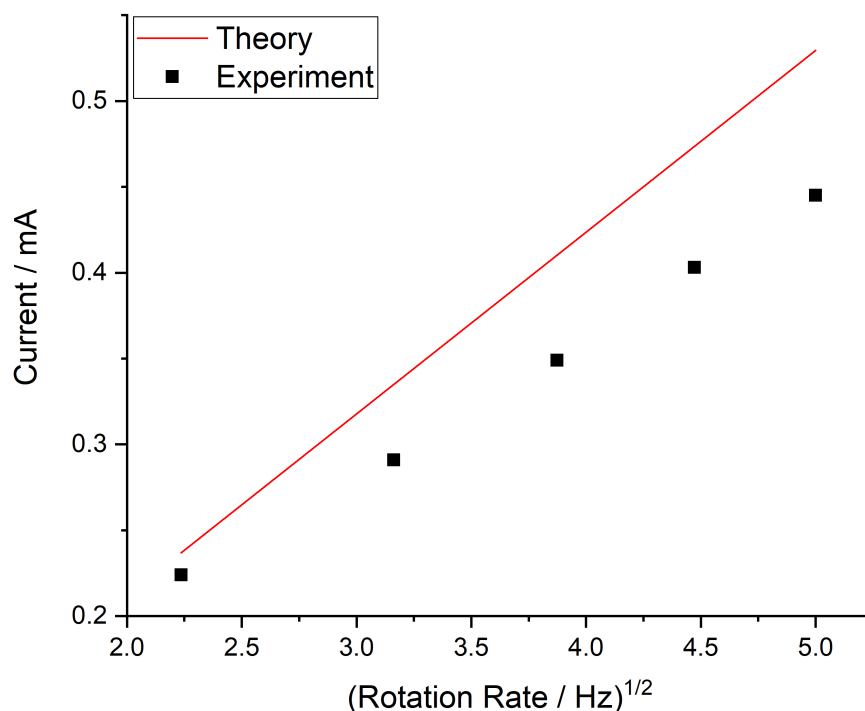


Figure 36 Modulus of maximum current from CVs of 0.5 mM $\text{Ru}(\text{NH}_3)_6^{3+/2+}$ with the original cap EC-XRF RDE design, with varying rotation rates of 5 to 25 Hz, 0.1 Vs^{-1} , 0.1 M KNO_3 , ($n=1$).

The data appears to be linear but with a lower gradient than theory, deviation from theory is greater at faster rotation rates. This lower gradient could be due to the recessed electrode altering the flow, it is possible that stagnant regions are created in the corners of the cap, or some resistance effects. As the peak separation here is approx. 80 mV some resistance is present.

Compared with the stirring, vibrating diaphragm and flow cell systems, the RDE system shows several advantages. (i) Compared to the stationary current, the original RDE system gives the highest relative current increase of 2.6 fold, therefore the highest rate of mass transport. (ii) The CVs are smoothest for the RDE and reach a limiting current, the hydrodynamics are well defined and there are no current fluctuations that could cause variability between experiments. However, for ease of use in an EC-XRF RDE application the system has flaws. In the current design, the BDD electrode must be removed from the housing for placement in the XRF, standalone, for measurement. Cleaning of the surface after measurement (mechanical polishing

with alumina slurry) is also required to remove deposited metal. The BDD must then be reassembled into the EC-XRF system. Removal and more particularly reassembly, involve compressing the O-ring between the BDD disk and the cap, meaning the disk is prone to cracking, it is only 250 μm thick. As the BDD is not meant to be a disposable item due to cost, this causes problems for the user. This led to design modifications to the system in order to improve the usability and lifetime of the EC-XRF RDE system, whilst compromising only minimally on increasing backgrounds.

3.4.5. EC-XRF RDE Prototype 1

The first priority was to design an electrode where the BDD is fixed to a support, to prevent breakage whilst having a temporary contact. The design concept and photo are shown in Figure 37.

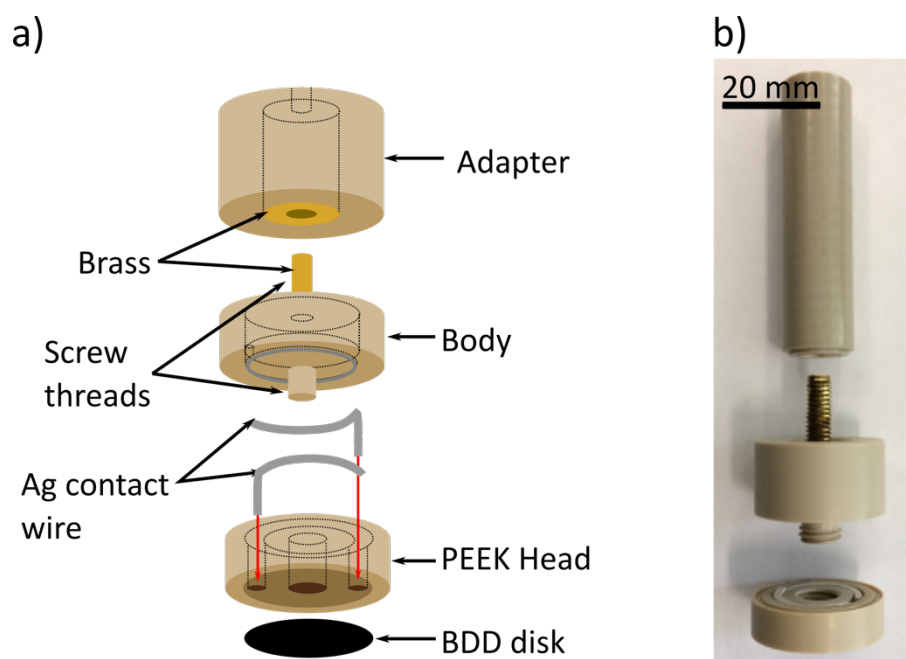


Figure 37 Prototype 1, a) schematic, b) photo, BDD disk sealed in PEEK head with Ag wire contacts screw fit to adapter which screws into RDE body which in turn screws into the rotator motor, electrocal contact kept through brass interiors of adapter and body, scale bar is 25 mm.

Here the BDD is sealed in place into a PEEK head. The head can be simply removed for XRF analysis by unscrewing it from the adapter unit. The Ag wire is contacted to the Pt/Ti sputter on the back of the BDD disk by silver epoxy. The silver wire comes out the back of the head and is inset into the PEEK on that side. This can then make a contact with a complementary inset wire in the adapter unit section that attaches

to the RDE body which screws onto the motor thread. The BDD was easy to handle and clean by mechanically polishing, the electrochemical characterisation is just passable (as defined in Chapter 2) but the XRF backgrounds are greatly increased due to the extra material present behind the BDD, the Ag peak is easily identified but as this is approx. 10 keV higher than the region of interest this is not problematic (Figure 38). Some Fe (6.4 keV), Cu (8.05 keV), Zn (8.64 keV), Pt (9.44 keV) and Au (9.71 keV) can be seen in the backgrounds, Fe, Cu, Zn are found in the XRF instrument chamber and Pt and Au are from the sputter contacts on the BDD, Cu is also present due to small amounts of Cu wire in the systems.

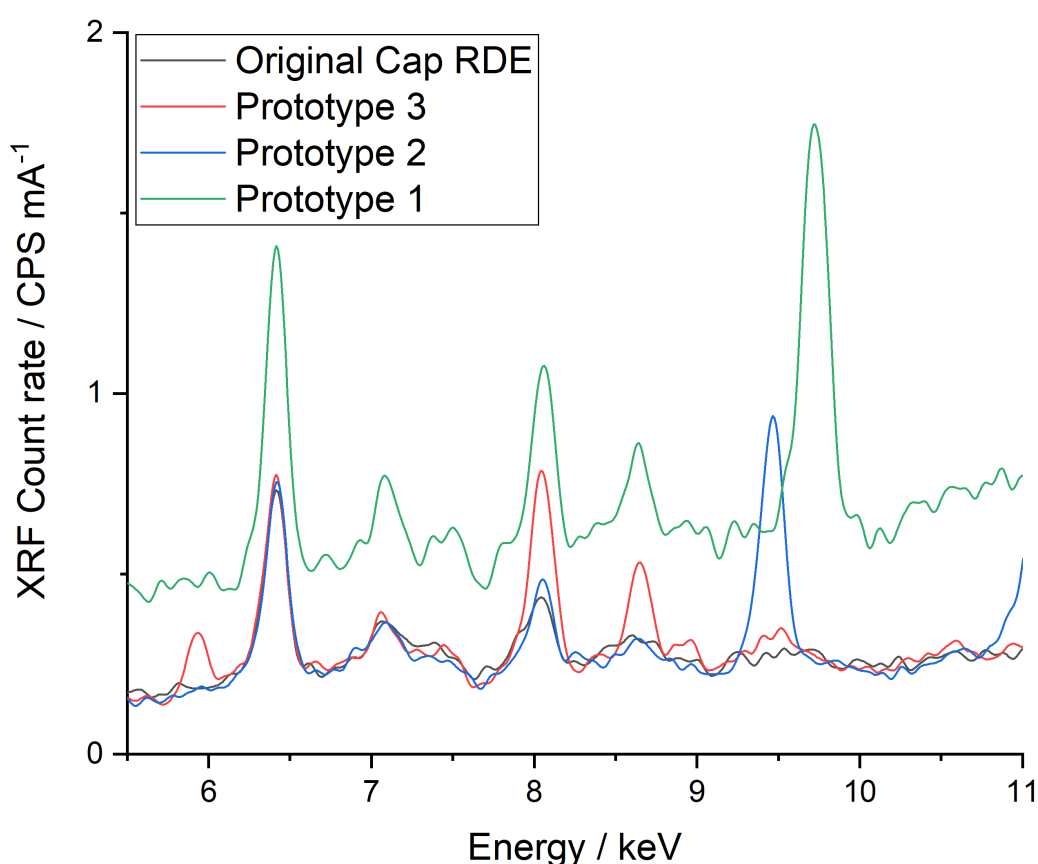


Figure 38 XRF backgrounds of the original design and prototypes 1 to 3 in the region of interest showing peaks corresponding to Fe (6.4 keV), Cu (8.05 keV), Zn (8.64 keV), Pt (9.44 keV) and Au (9.71 keV).

As with the original cap design, limiting currents are reached and the experimental stationary current of -0.76 mA is very close to the theoretical current of -0.79 mA, but the peak separation is still around 80 mV, Figure 39. The rotator motor used for this prototype is a homemade system and there is a small wobble visible on it when running at high rates, which is exacerbated by the length of the electrode, this

probably disrupts the laminar flow to the electrode face and could be the reason for the current fluctuations in the CVs at higher rates.

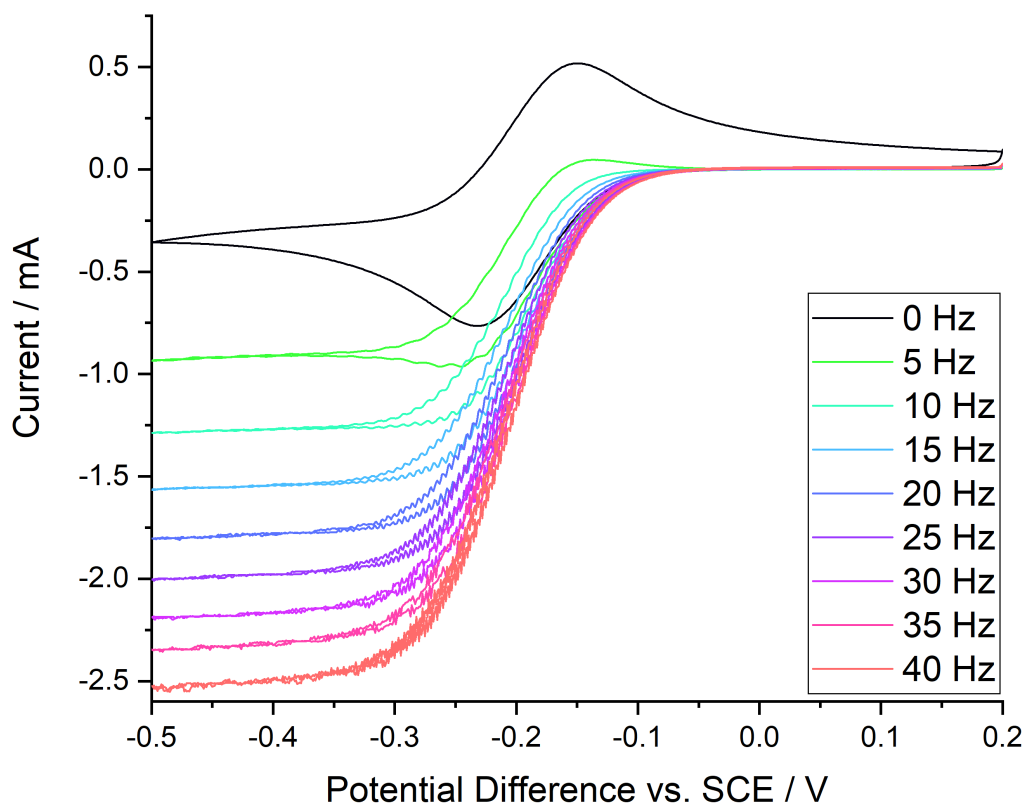


Figure 39 CVs of 1 mM $\text{Ru}(\text{NH}_3)_6^{3+/2+}$ and 0.1 M KNO_3 with Prototype 1 at 0.1 V s^{-1} at varying rotation rates from 0 to 40 Hz.

This prototype follows Levich theory in a similar manner to the original RDE, Figure 35, it appears linear and deviates slightly at higher rotation rates. At 25 Hz a 2.6 fold increase in maximum current is seen which is comparable with the original RDE system. The variation in limiting current increased at higher rotation rates, when running the experiment, the surface of the solution became increasingly turbulent at higher rotation rates and there was some solution loss at 30 Hz and above, so it was decided that the running rate should be below this. The mass transport must also be becoming less laminar at higher rates as current fluctuations can be seen in Figure 39, albeit at a much lower level than for previous system tested. It is probably a combination of this and resistance effects that cause experimental values to be lower than theory.

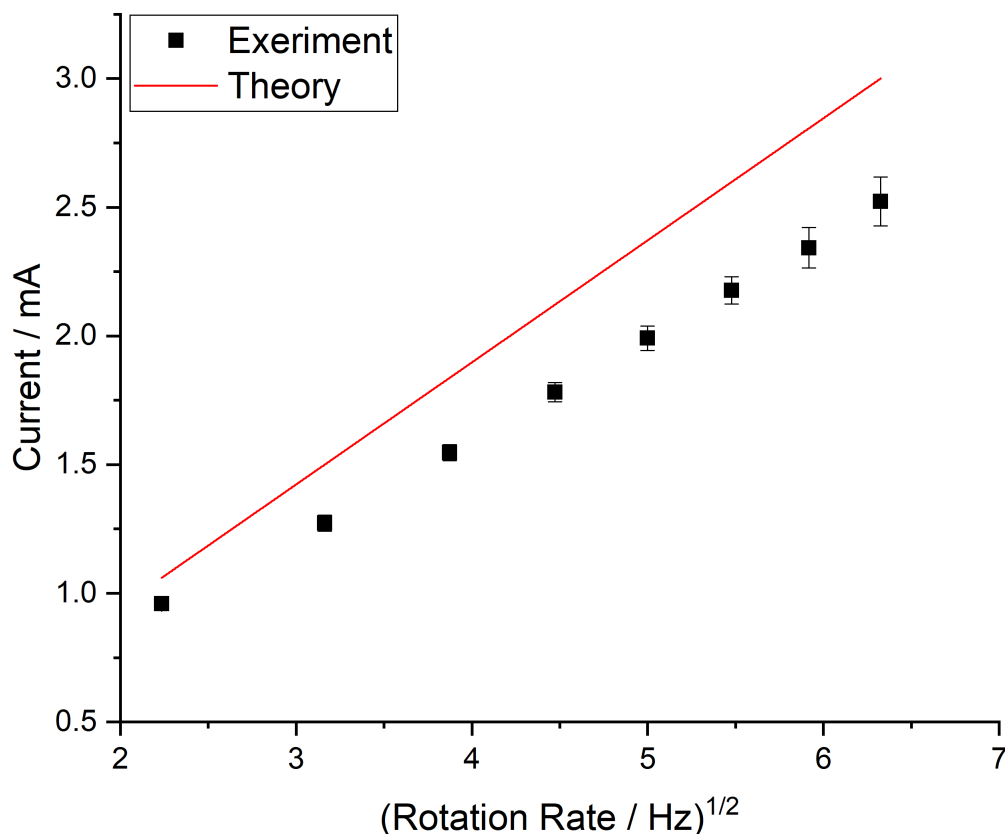


Figure 40 Comparison of Levich theory with experimental peak currents from CVs of 1 mM $\text{Ru}(\text{NH}_3)_6^{3+/2+}$ and 0.1 M KNO_3 with Prototype 1 at 0.1 V s^{-1} at varying rotation rates from 0 to 40 Hz.

In the next prototype the main improvement points were i) to decrease the XRF backgrounds and ii) use a commercial rotator motor and shorter electrode length to see if improvements in the current fluctuations could be obtained, this means a modification to the electrode dimensions and fittings as the fittings are different for the homemade and commercial rotator motors.

3.4.6. EC-XRF RDE Prototype 2

The main objective of this prototype is to reduce the XRF background by returning to the separable contact being between the Pt/Ti sputtered contact on the BDD and the main electrode body as this has always given excellent XRF backgrounds. The sputtered contacts are susceptible to mechanical wear so gold coated brass spring pins were used to contact the BDD and the electrode body as shown in Figure 41. The head and body are attached by means of a push fit with O-rings, this was chosen instead of a screw fit as a screw fit would result in the scraping of the pin heads

around the electrode when assembled, a push fit would only result in the pins touching and pushing against the contacts, thereby reducing mechanical wear to pins and contacts. However, this was not watertight and had to be supplemented with kapton tape, which was also not failure proof and therefore not a viable solution.

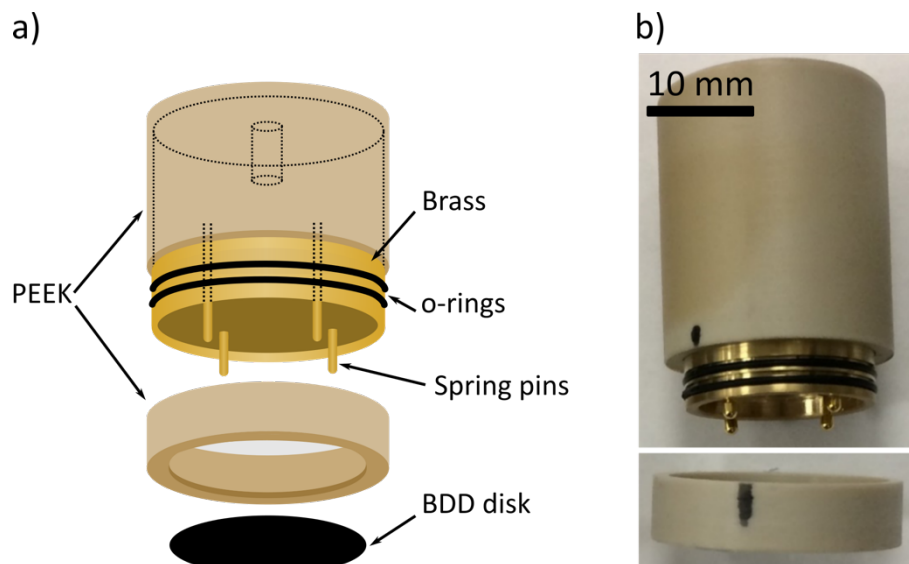


Figure 41 a) schematic b) photo of prototype 2. Dashed lines in a) show the internal brass cylinder connecting the spring pins and screw fitting at the top to enable electrocal conduction.

It was extremely difficult to get any electrochemical data from this system because of solution leakage inside the electrode so it was abandoned. The main points to work on for the next iteration are ensuring a water-tight seal whilst maintaining good contacts and low XRF backgrounds (Figure 38).

3.4.7. EC-XRF RDE Prototype 3

This final prototype retains the same sputtered contact/gold coated spring pin design but used a screw fitting and an O-ring to ensure a watertight seal instead of a push fit. The electrochemical characterisation was passable (as defined in Chapter 2) and the contact reliable as proven by the extended use of this version.

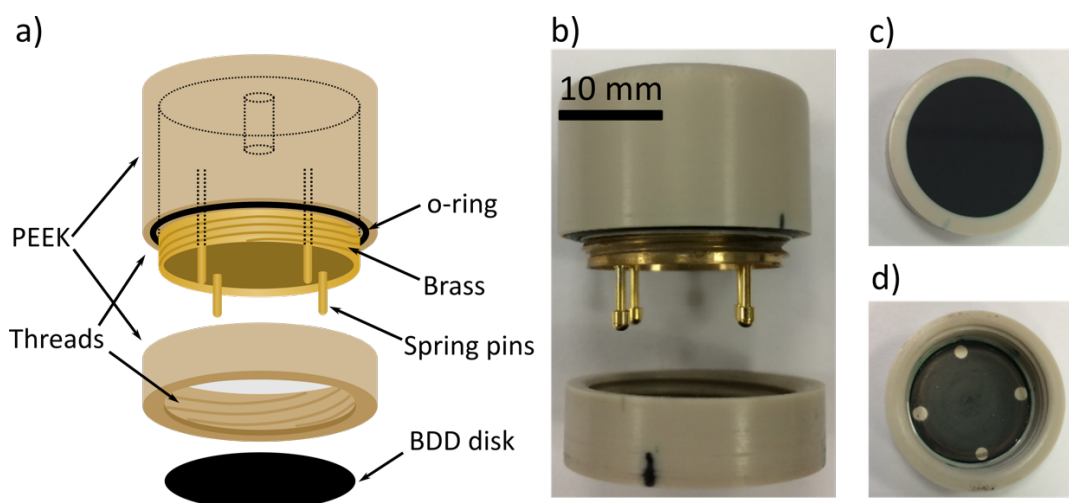


Figure 42 a) schematic b) photo of prototype 3. Dashed lines in a) show the internal brass cylinder connecting the spring pins and screw fitting at the top to enable electrocal conduction, c) is the face of the electrode inset in PEEK head and d) is the back face showing the 4 sputtered areas for the pins to make contact.

The backgrounds were low and comparable to the original system, Figure 38. Note that the slightly higher Cu and Zn signals appeared after extensive use of this prototype. This was caused by the scraping of the pins on the back face of the electrode, which removed the Au plating exposing the brass material underneath. Through repeated use, small amounts of brass were scraped onto the back of the BDD in a ring increasing the background signals, this can be seen in Figure 42 d). This unfortunately meant that backgrounds had to be taken before each experiment as there was not a reliable way of removing this without damaging the sputter contacts. Pins of alternate material in the appropriate dimensions were not available, but with the help of mechanical workshops Ag pins were successfully made with some thick Ag wire and small springs extracted from the Au pins (Ag XRF peak is out of window of interest). Another prototype 3 was made with the Ag pins and showed equivalent electrochemical properties but was not tested further.

The theoretical stationary current for this system was -0.79 mA and the experimental current value was -0.75 mA, with an 80 mV peak separation, limiting currents were reached for 25 Hz and above. The rotator motor used for this prototype was a commercial rotator system (MSR rotator, Pine Research Instrumentation, USA) and appeared to run extremely smoothly (no electrode wobble) but large current variations are seen in the CV at 42 Hz without marked increase in maximum current

from 33 Hz, Figure 43. Turbulence on the surface of the solution and some solution losses were noted for 42 Hz as well as bubbles in the solution, from air being drawn into the solution by the turbulence. This extreme turbulence and air bubble effect are probably the cause of the lack of maximum current increase from 33 to 42 Hz.

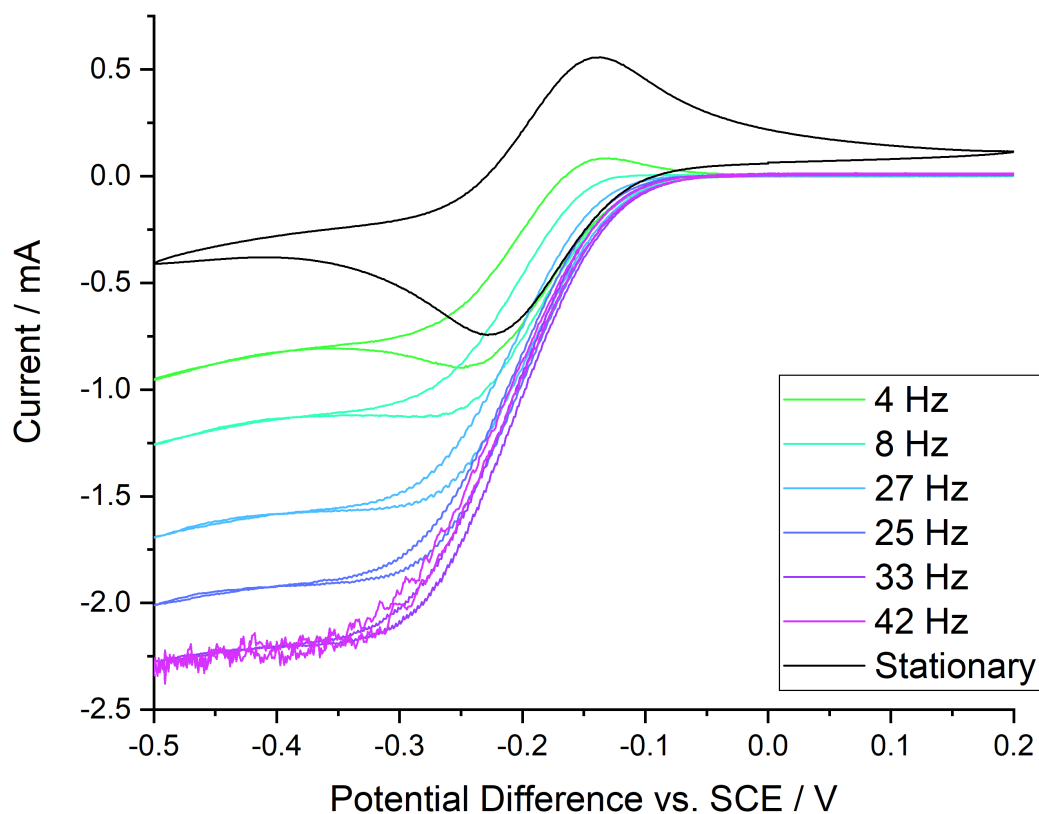


Figure 43 CVs of 1 mM $\text{Ru}(\text{NH}_3)_6^{3+/2+}$ and 0.1 M KNO_3 with Prototype 3 at 0.1 V s^{-1} at varying rotation rates from 0 to 42 Hz.

This prototype fit Levich well at lower rotation rates, but varied more at higher rates, appearing less linear than other RDE versions. The limiting current variation, however, was extremely reproducible between runs, Figure 44.

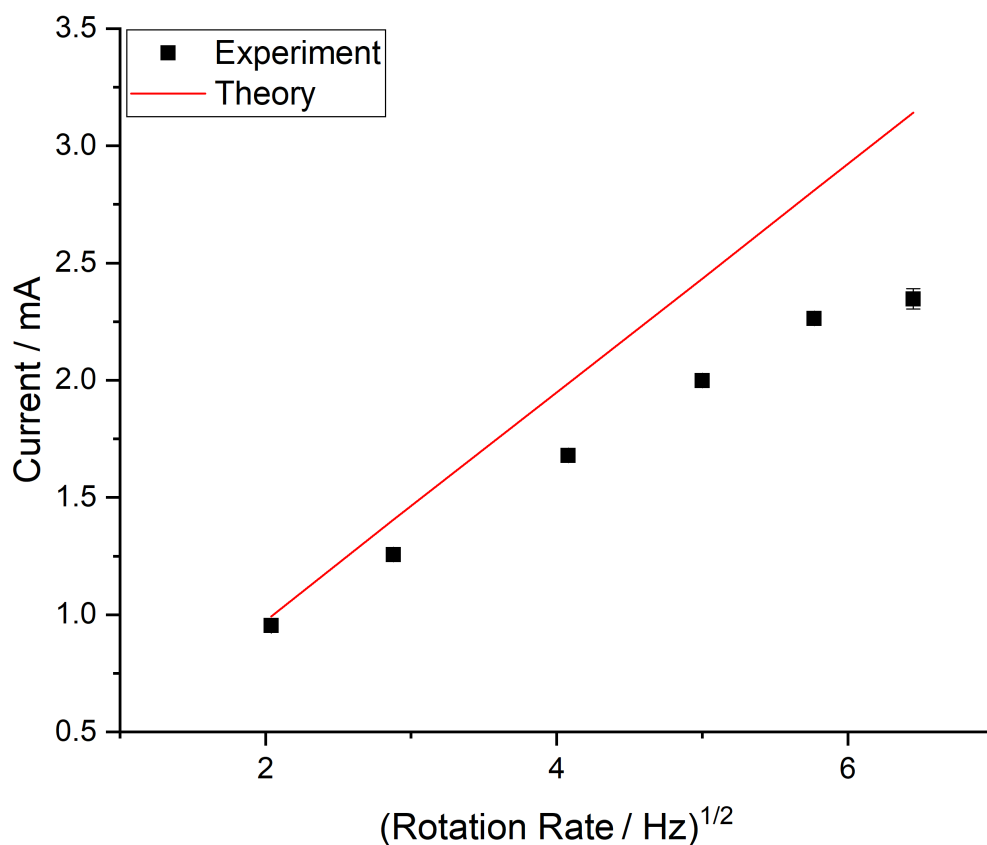


Figure 44 Comparison of Levich theory with experiment peak currents for CVs of 1 mM $\text{Ru}(\text{NH}_3)_6^{3+/2+}$ and 0.1 M KNO_3 with Prototype 3.

This system gave a 2.7 fold increase at 25 Hz, improving slightly on the previous versions. Due to the good XRF backgrounds, mass transport increase and usability, the system was used for EC-XRF experiments with Cu.

3.4.8. EC-XRF of Cu with Prototype 3

Firstly CVs of $\text{Cu}(\text{NO}_3)_2$ (100 ppm = 1.6 mM with 0.1 M KNO_3) were run to gain some understanding of the system, four different conditions were selected to see the effects of dissolved oxygen and pH on copper electrodeposition and stripping, Figure 45.

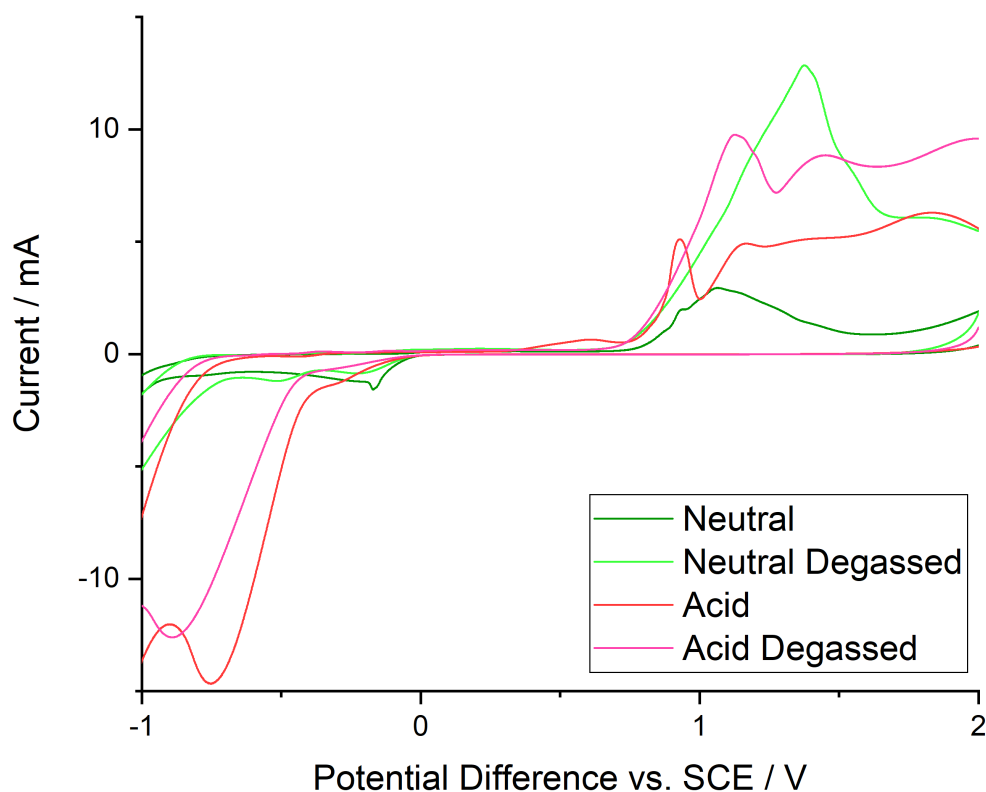


Figure 45 CVs of 100 ppm (1.6 mM) $\text{Cu}(\text{NO}_3)_2$ and 0.1 M KNO_3 on EC-XRF RDE prototype 3, at 0.1 V s^{-1} in neutral (approx. pH 5.5-7) and acidic (pH 2) solutions with and without dissolved oxygen (degassed).

Figure 45 shows that both pH and the presence of dissolved oxygen have an effect on the electrodeposition of Cu. For the neutral solutions (unadjusted, approx. pH 5.5-7) there appeared to be a deposition peak around -0.2 V, for the acidic (pH 2, adjusted with HNO_3) CVs there is not a clear deposition peak, there is a shoulder at -0.3 V on the large peak appearing at -0.7 V and -0.9 V on the aerated and degassed respectively. The shoulder could be the oxygen reduction reaction (ORR) on Cu, the large peak around -0.8 V is probably connected to the nitrate reduction reaction (NRR) on Cu, it is more pronounced at low pH.⁵¹ There is no clear stripping peak, but as several cathodic peaks are visible and the CV window large (out to -2 V), it is likely that a layer of a Cu oxide or some other non-metallic form of Cu has been formed, preventing the classic stripping peak. The electrodeposition and stripping characteristics of Cu are explored in more detail in Chapter 5, exact assignments are not important here as XRF is sensitive to all speciations of Cu.

To decide on the best parameters for EC-XRF deposition potential tests were conducted, Figure 46. For the neutral solution (only $\text{Cu}(\text{NO}_3)_2$ and 0.1 M KNO_3) -0.2 V was the potential that gave the greatest Cu signal in XRF and -0.7 V for acidic. However, when a similar experiment was run at a lower concentration (10 ppb = 1.6 μM , neutral aerated) a different effect was seen with deposition potential. A deposition potential of -0.2 V gave the lowest XRF signal whilst -1 V gave the highest with potentials between producing almost identical signals to the higher concentration. This change in onset potential is explained by the change in the reaction quotient in the Nernst equation, pushing deposition potentials more positive for higher concentrations. It was decided that an intermediate potential of -0.5 V was suitable as the deposition potential in neutral solutions, as although it did not produce the highest signal in either, it did not perform poorly in either concentration.

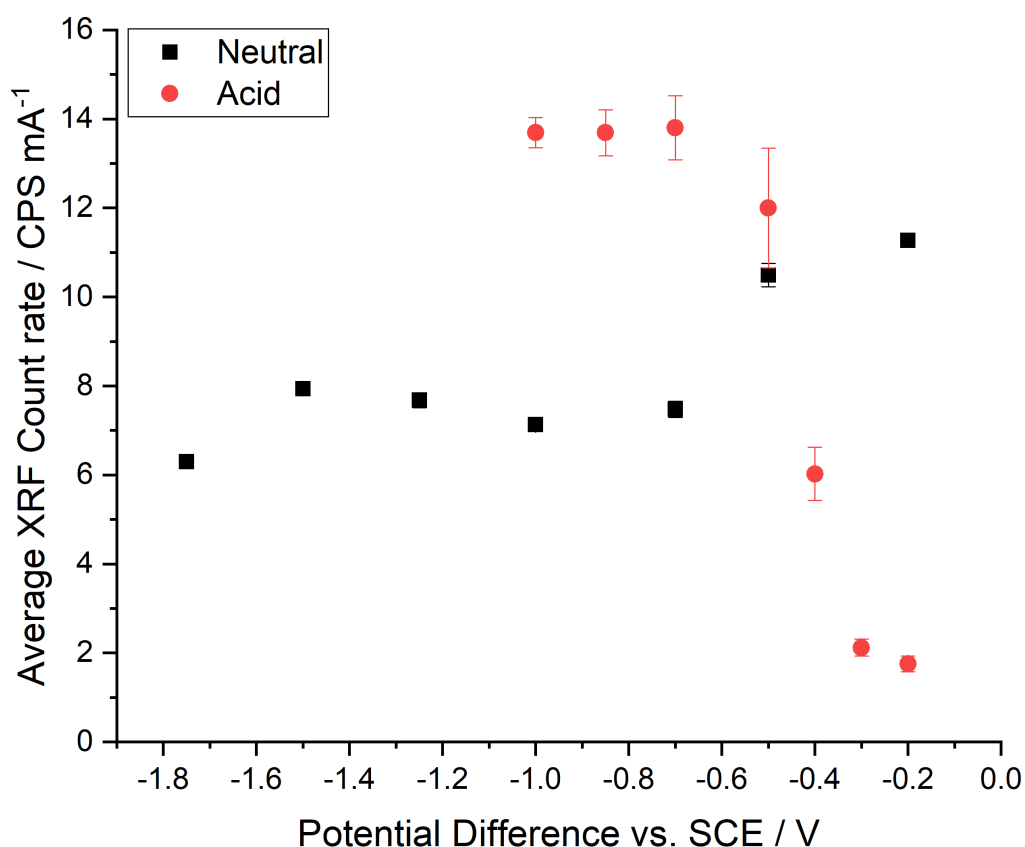


Figure 46 Experiment to find optimal deposition potential for Cu EC-XRF experiments in 100 ppm $\text{Cu}(\text{NO}_3)_2$ and 0.1 M KNO_3 on EC-XRF RDE prototype 3. For a neutral solution (pH 5.5-7) and a pH 2 solution, 25 Hz.

Despite the increasing over-potential for the neutral solution, the Cu XRF signal decreases, this could be due to several other processes occurring such a solvent

spitting on Cu, which is much more active than BDD, or reactions such as the NRR, or the ORR, which can cause an increase in pH at the electrode surface. This increase in pH has the potential to make Cu unavailable by precipitation or complexation. The neutral solution has noticeably lower variability than the acidic solution, especially at higher deposition potentials, this could be due to bubble formation from HER in acidic solution or variability in the NRR that could be making Cu inaccessible. The advantage of acidic solution seems to be improvement in sensitivity, but the disadvantage is higher variability, because of this, concentration calibrations were run for both solutions, Figure 47.

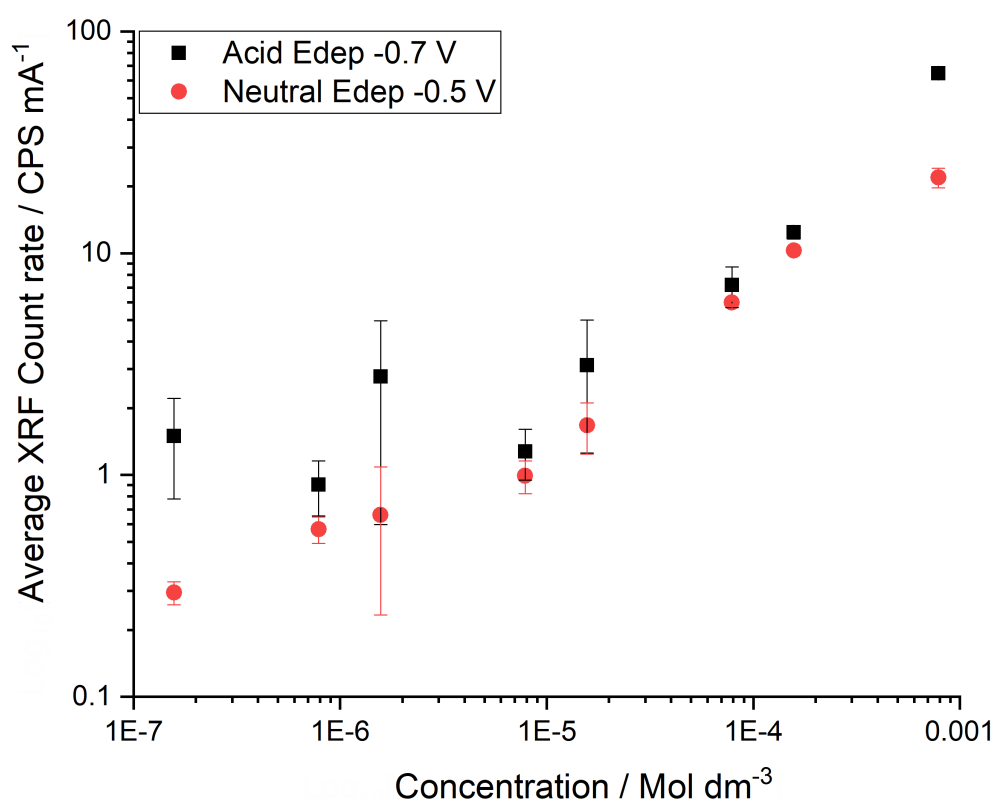


Figure 47 EC-XRF data, collected on Prototype 3. Concentration vs XRF signal graph, 25 Hz, two different deposition potentials in pH 6 and pH 2 solutions, aerated.

As with Figure 46, the acidic provides higher XRF intensity but larger variation. The \log_{10} of the XRF count rate and \log_{10} of the concentration are fairly linear for both solutions until about 10 μM . LODs based on XRF were calculated as 3 x the standard deviation of the background (8.05 keV, Cu ka) which gives 0.014 CPS mA⁻¹, but the lines of best fit are both negative in the concentration axis when XRF count rate is equal to 0.014 CPS mA⁻¹, meaning LODs cannot be calculated. Results obtained below

about 10 μM did not fit well with the rest of the data, the variability of the XRF background is not the limiting factor for LOD of this technique, it seems that the variability of some other aspect of the method is greater.

The presence of dissolved oxygen and the use of sulfate electrolyte (to eliminate NRR) appeared to make negligible difference to these experiments, so the earlier postulation that the ORR and NRR are increasing variability appears to be incorrect.

An interesting result was the visual appearance of the electrode after a deposition in neutral solution (100 ppm), Figure 48. The pattern in the deposit matches the theoretical flow profile seen in the literature,⁵² adding credibility to the claim of well-defined hydrodynamics for this system. The deposit is blue in colour, suggesting that the deposit is actually $\text{Cu}(\text{OH})_2$ precipitate, not metallic Cu for these conditions, speciation for electrodeposited Cu is investigated further in Chapter 4.

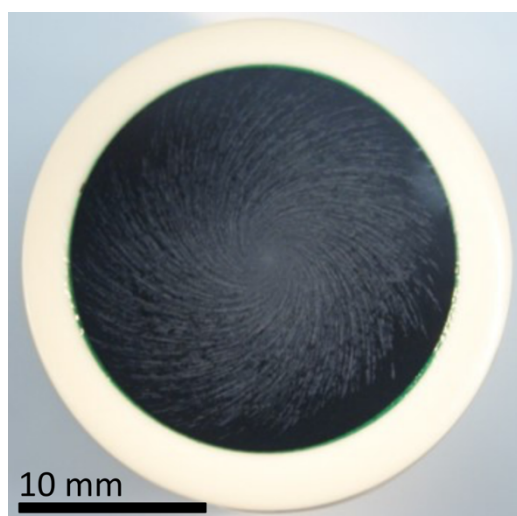


Figure 48 photograph of the electrode surface after a deposition in 100 ppm $(\text{NO}_3)_2$ solution at -0.5 V and 25 Hz , showing the flow profile of solution by a blueish coloured deposit. Scale bar is 10 mm.

An observation that was made during the EC-XRF experiments could explain some of the variability seen in the results. As the RDE was lifted from solution it would retain a droplet on the surface, as this droplet fell off, it sometimes took some of the deposit from the surface. It is likely that it is not the electrodeposition that is variable, but instead how intact the deposit remains on the surface during transfer from solution to XRF. This disruption to the surface is unfortunately inevitable in the current set up, the sheering force of solution moving over the electrode face cannot be avoided

without perhaps an extremely long drying step avoiding inverting the electrode which would make the method unviable. It is possible that Hutton *et al.* achieved a lower LOD (around 1 nM) because the electrode surface may have received some protective effect by being recessed, however as the experimental protocol mentions rinsing of the electrode face between deposition and XRF analysis, so similar losses would be expected. It is not fully understood what the limit to a better LOD is but is suspected to be at least partly related to post electrodeposition losses. It is also plausible that any deposits lost during rotation would be collected in the corner of the recess, an area which would be within the XRF beam.

3.5. Conclusion

A new EC-XRF RDE electrode has been developed which displays low XRF backgrounds, good electrochemistry and is easy for a user to handle. Magnetic stirring and vibrating diaphragm systems were assessed to be unsuitable for analytical applications due to their irreproducibility, low mass transport increases and practical difficulties. Table 3 lists the increases in currents of each system relative to their corresponding stationary CV. RDE systems clearly provided the best mass transport increases and were also found to be the most suitable for application to EC-XRF. Prototype 3 achieved the same increase as the original RDE EC-XRF system with excellent reproducibility.

System	Magnetic Stirrer	Vibrating Diaphragm	O'Neil Wall-jet	Original EC-XRF RDE	Prototype 1	Prototype 3
Relative current increase	1.8	2.4	1.4	2.6	2.6	2.7

Table 3 Current increase possible relative to no induced mass transport in each system.

The RDE was found to be the best compromise of well understood and easy to use due to the availability of high-quality commercial systems, well understood flow theory, good reproducibility and simplicity of instrumentation. The flow cell is more

challenging but offers the possibility of *in situ* analysis and is worth further investigation in this respect, see Chapter 4.

It was found that having a backing support for the BDD disk increased XRF backgrounds by an undesirable amount and that a ring of PEEK to support the electrode around the circumference of the BDD was sufficient to maintain low backgrounds while making the disks much easier to handle. Threaded attachments with O-rings proved to be the only reliable connections and PEEK to brass threads stood up extremely well to repeated use. The XRF backgrounds for the RDE prototype electrodes are shown in Figure 38. The backgrounds of all except Prototype 1 are very comparable to the old system of a standalone XRF disk, the notable differences are that a Pt contact was used for prototypes 2 and 3 and the Cu peaks are a little higher for Prototype 3 due to the scraping of the pins on the back of the disk.

Cu experiments showed linearity down to about 10 μM . The variability and sensitivity were not influenced by dissolved oxygen or background electrolyte. The comparison of the estimated LOD of this new system with the LOD from Hutton *et al.* (1 nM) was not favourable. It is likely that the loss of deposit due to the removal of the electrode from solution, perhaps connected to the planar geometry of the electrode, has negatively affected LODs. However, the experiments were sufficient to meet the aims of the project. The new electrode design (prototype 3) is durable, easy to handle, with low backgrounds, good electrochemistry and acceptable EC-XRF results with an LOD around 10 μM . The guidance for acceptable concentrations of Cu in drinking water is 2 ppm or 31 μM meaning that the LOD achieved here is sufficient for drinking water standards. No BDD disks broke in this system proving its suitability as a reusable system.

3.6. Bibliography

- 1 N. Elgrishi, K. Hammon, B. McCarthy, T. Eisenhart and J. Dempsey, *J. Chem. Educ.*, 2018, **95**, 197–206.
- 2 F. Scholz, *Electroanalytical Methods*, 2nd edn., 2010.
- 3 C. M. A. Brett, A. M. C. F. Oliveira Brett, A. C. Fisher and R. G. Compton, *J. Electroanal. Chem.*, 1992, **334**, 57–64.
- 4 F. Opekar, *Anal. Chem.*, 1962, **34**, 164–166.
- 5 L. Meng, J. G. Iacobini, M. B. Joseph, J. V. Macpherson and M. E. Newton, *Faraday Discuss.*, 2014, **172**, 421–438.
- 6 M. Hersey, S. N. Berger, J. Holmes, A. West and P. Hashemi, *Anal. Chem.*, 2019, **91**, 27–43.
- 7 T. R. Copeland and R. K. Skogerboe, *Anal. Chem.*, 1974, **46**, 1257A-1268a.
- 8 J. Wang, *Stripping analysis : principles, instrumentation, and applications*, VCH, 1985.
- 9 E. Alonso, A. Santos, M. Callejón and J. C. Jiménez, *Chemosphere*, 2004, **56**, 561–570.
- 10 M. Kazemipour, M. Ansari, A. Mohammadi, H. Beitollahi and R. Ahmadi, *J. Anal. Chem.*, 2009, **64**, 65–70.
- 11 S. M. Rosolina, J. Q. Chambers and Z. L. Xue, *Anal. Chim. Acta*, 2016, **914**, 47–52.
- 12 S. M. Rosolina, J. Q. Chambers, C. W. Lee and Z. L. Xue, *Anal. Chim. Acta*, 2015, **893**, 25–33.
- 13 P. M. Chapmann, H. E. Allen, K. Godtfredsen and M. N. Z'Graggen, *Environ. Sci. Technol.*, 1996, **30**, 448A-452A.
- 14 A. Martelli, E. Rousselet, C. Dycke, A. Bouron and J. M. Moulis, *Biochimie*, 2006, **88**, 1807–1814.
- 15 H. Needleman, *Annu. Re. Med.*, 2004, **55**, 209–222.
- 16 M. Olivares and R. Uauy, *Am. J. Clin. Nutr.*, 1996, **63**, 791–796.
- 17 H. A. Schroeder, A. P. Nason, I. H. Tipton and J. J. Balassa, *J. Chronic Dis.*, 1967, **20**, 179–210.
- 18 A. Helaluddin, R. S. Khalid, M. Alaama and S. A. Abbas, *Pharm Res Trop. J.*

- Pharm. Res. J. Cit. ReportsScience Ed.*, 2016, **15**, 427–427.
- 19 J. W. Olesik, *Anal. Chem.*, 1991, **63**, 12A-21A.
 - 20 C. Reimann, U. Siewers, H. Skarphagen and D. Banks, *Sci. Total Environ.*, 1999, **239**, 111–130.
 - 21 G. Gillain, G. Duyckaerts and A. Disteche, *Anal. Chim. Acta*, 1979, **106**, 23–37.
 - 22 J. Wang, *Electroanalysis*, 2005, **17**, 1341–1346.
 - 23 J. Wang, J. Lu, Ü. A. Kirgöz, S. B. Hocevar and B. Ogorevc, *Anal. Chim. Acta*, 2001, **434**, 29–34.
 - 24 J. F. Van Staden and M. C. Matoetoe, *Anal. Chim. Acta*, 2000, **411**, 201–207.
 - 25 R. W. Gerlach and B. R. Kowalski, 1982, **134**, 119–127.
 - 26 T. R. Copeland, R. A. Osteryoung and R. K. Skogerboe, *Anal. Chem.*, 1974, **46**, 2093–2097.
 - 27 G. E. Batley and T. M. Florence, *J. Electroanal. Chem.*, 1974, **55**, 23–43.
 - 28 P. M. Bersier, J. Howell and C. Bruntlett, *Analyst*, 1994, **119**, 219–232.
 - 29 R. Jenkins, *Quantitative X-Ray Spectrometry, Second Edition*, CRC Press, 1995.
 - 30 A. M. T. Pereira and P. R. G. Brandao, *Miner. Eng.*, 2001, **14**, 1659–1670.
 - 31 F. L. Melquiades and C. R. Appoloni, *J. Radioanal. Nucl. Chem.*, 2004, **262**, 533–541.
 - 32 L. P. Eksperiandova, A. B. Blank and Y. N. Makarovskaya, *X-Ray Spectrom.*, 2002, **31**, 259–263.
 - 33 E. Marguá, B. Zawisza and R. Sitko, *TrAC - Trends Anal. Chem.*, 2014, **53**, 73–83.
 - 34 <https://www.addspex.com/rigaku-ultracarry.html>,
<https://www.addspex.com/rigaku-ultracarry.html>, (accessed 27 April 2020).
 - 35 B. Beckhoff, habil. B. Kanngießer, N. Langhoff, R. Wedell and H. Wolff, *Handbook of Practical X-Ray Fluorescence Analysis*, Springer Berlin Heidelberg, Berlin, Heidelberg, 1st edn., 2006.
 - 36 J. V. Macpherson, *Phys. Chem. Chem. Phys.*, 2015, **17**, 2935–2949.
 - 37 M. K. Tiwari and K. J. S. Sawhney, *J. Phys. Condens. Matter*, 2010, **22**, 175003.
 - 38 L. A. Hutton, G. D. O’Neil, T. L. Read, Z. J. Ayres, M. E. Newton and J. V. Macpherson, *Anal. Chem.*, 2014, **86**, 4566–4572.
 - 39 Z. J. Ayres, M. E. Newton and J. V. Macpherson, *Analyst*, 2016, **141**, 3349–3357.

- 40 G. D. O’Neil, M. E. Newton and J. V. Macpherson, *Anal. Chem.*, 2015, **87**, 4933–4940.
- 41 L. A. Hutton, G. D. O’Neil, T. L. Read, Z. J. Ayres, M. E. Newton and J. V. Macpherson, *Anal. Chem.*, 2014, **86**, 4566–4572.
- 42 L. Landau and B. Levich, *Acta Physicochim. URSS*, 1942, **17**, 141–153.
- 43 H. W. Webb, *Analyst*, 1945, **70**, 301–304.
- 44 G. C. Richard, C. E. John and M. Frank, *Electroanalysis*, 1997, **9**, 509–522.
- 45 C. R. S. Hagan and L. A. Coury, *Anal. Chem.*, 1994, **66**, 399–405.
- 46 Z. Bi, C. S. Chapman, P. Salaün and C. M. G. Van Den Berg, *Electroanalysis*, 2010, **22**, 2897–2907.
- 47 C. S. Chapman and C. M. G. Van Den Berg, *Electroanalysis*, 2007, **19**, 1347–1355.
- 48 D. E. Williams, K. Ellis, A. Colville, S. J. Dennison, G. Laguillo and J. Larsen, *J. Electroanal. Chem.*, 1997, **432**, 159–169.
- 49 B. C. Towe, *IEEE Trans. Biomed. circuits Syst.*, 1987, **34**, 657–663.
- 50 J. C. Myland and K. B. Oldham, *Anal. Chem.*, 2000, **72**, 3972–3980.
- 51 C. M. Welch, M. E. Hyde, C. E. Banks and R. G. Compton, *Anal. Sci.*, 2005, **21**, 1421–1430.
- 52 M. M. Jaksic, *J. Electroanal. Chem.*, 1988, **249**, 63–68.

4. Flow cell EC-XRF

4.1. Overview

The electrochemical x-ray fluorescence spectroscopy (EC-XRF) wall-jet flow cell design from Chapter 3 is improved upon by increasing the durability and usability, and then tested on a Cu deposition XRF detection system to demonstrate the potential of EC-XRF as an *in situ* analytical method. It is shown that several factors must be carefully considered for flow cell design for this application. Cu was successfully detected down to low μM concentrations and deposition patterns are in agreement with theory.

4.2. Introduction

The importance of analytical methods for the fast and accurate detection of heavy metals has already been addressed in Chapter 1, however this focused on *ex situ* methods of analysis. This chapter aims to explore developments made towards *in situ* analysis of metals by means of a confined wall-jet cell. Flow cells are extremely convenient when it comes to *in situ* or 'in the field' analysis as they are generally a self-contained unit. For electrochemical applications, fixed cell systems such as this are easier to transport and are less prone to set up variation.^{1,2} They can also offer other advantages such as high, well defined mass transport and the requirement of smaller reagent or sample volumes. Continuous, simultaneous and high throughput analysis are possible depending on the circumstances.^{3,4} For example, flow cells have been used in literature to aid the anodic stripping voltammetry (ASV) analysis of multi-element samples of Cu, Pb, Cd and Zn and provide useful limits of detection (LODs).^{3,5,6} *In situ* or 'in the field' methods can also greatly reduce the time from taking the sample to getting a result if transport to a centralised lab facility is not required. This can also reduce costs and risks of contamination or sample degradation due to transport.⁷ A plethora of different types of flow cells exist but amongst electrochemical applications the most popular are the wall-jet and the channel flow (Figure 49) electrodes.⁸

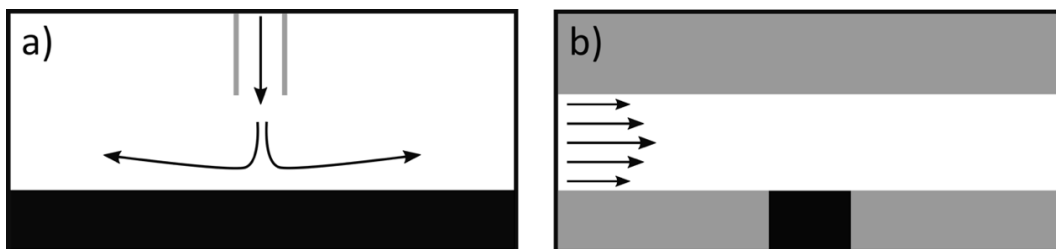


Figure 49 schematic of two examples of electrochemical flow cells a) a wall-jet and b) a channel flow electrode, black surface denotes electrode surface and arrows show fluid flow profile.

These two systems have also found use in hybrid spectroscopy-electrochemistry methods for heavy metal detection.^{9,10} For *in situ* EC-XRF the wall-jet is a preferred option as metal deposition (excluding the stagnant region) is highest around the centre of the electrode due to the current distribution.¹¹ The centre of the disk electrode is aligned with the centre of the x-ray irradiated area and matches well with the geometry of the irradiated area. This provides greater sensitivity than a channel flow cell that has essentially uniform distribution and generally uses thin rectangular electrodes.¹

There are several different versions of the wall-jet, varying in electrode and nozzle geometry which can result in different levels of confinement of the flow,¹² see Figure 50, which in turn lead to modifications in the current response at the electrode. This is often referred to as an impinging jet electrode.¹¹

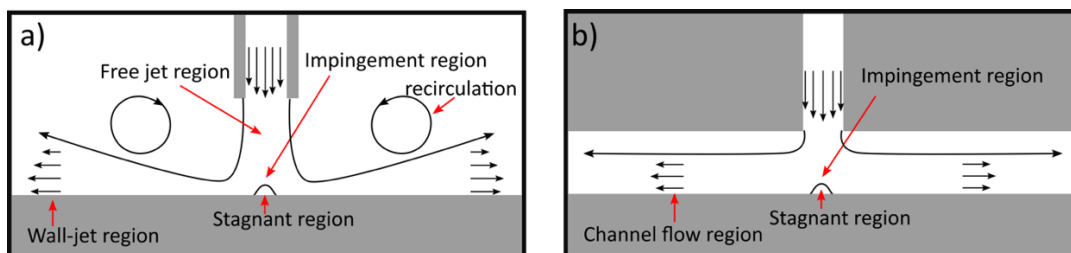


Figure 50 schematics of two different wall-jet systems demonstrating a) a free wall-jet, adapted from ¹³ and b) confined microjet displaying channel flow.¹⁴

The equation for calculating the theoretical limiting current, i_{lim} , for a free wall-jet electrode, Figure 50 a) is given by Equation 32,¹⁵

$$i_{lim} = 1.597nFk_cR^{3/4}\nu^{-5/12}D^{2/3}a^{-1/2}V_f^{3/4}c \quad \text{Equation 32}$$

where n is the number of electrons, F Faradays constant, k_c is 0.9, R is electrode radius (cm), ν is kinematic viscosity ($\text{cm}^2 \text{s}^{-1}$), D is diffusion coefficient ($\text{cm}^2 \text{s}^{-1}$), a is

inlet nozzle diameter (cm), V_f is volume flow rate (ml s^{-1}) and c is concentration (mol cm^{-3}).² The assumptions of this equation are that there is laminar flow and that the system is not confined.¹⁶ Note if the size of the electrode is smaller than that of the jet the system is described as a wall tube configuration and the electrode is uniformly accessible.^{17,18}

This equation does not have a term for nozzle-electrode separation although this does affect limiting currents. Yamada and Matsuda¹⁹ found that in their system ($R = 1.5 \text{ mm}$, $a = 0.3\text{-}1.5 \text{ mm}$) if the nozzle-electrode separation was between 2-4 mm there was a negligible difference in current and so this was not considered further. It has been documented in literature that not all wall-jet configurations can be described by this equation. Gunasingham *et al.* found that if the nozzle-electrode separation was below 0.5 mm (for $R = 1.5 \text{ mm}$, $a = 0.3\text{-}1.5 \text{ mm}$) the gradient of a $\log i_{lim}$ vs $\log V_f$ plot was less than 0.5 at low flow rates, moving to 0.75 at high flow rates. At nozzle-electrode separations greater than 0.5 mm, the plots matched theory. Their explanation was that if the nozzle is within the hydrodynamic boundary layer of the electrode then large flow gradients will result in significant friction, lowering the radial flow solution momentum, resulting in lower currents on the electrode surface. At high flow rates, the hydrodynamic boundary layer is smaller, and so the nozzle may no longer be interfering with it at the same separation and will follow theory.⁴

The hydrodynamics of the wall-jet electrode can be complex, as the electrode is not uniformly accessible. There are several regions that can occur to different extents based on the flow rate, Reynolds number, separation (and other dimensions) and the presence of confinement. The free jet region has been shown to remain intact even at large nozzle-electrode separations but interestingly wall-jets often display a stagnant region at the point of impingement, also called the wall-tube zone (Figure 50)¹⁷ The flow velocity in the wall-jet region varies radially, it is generally highest just outside the stagnant region and then falls as the hydrodynamic boundary layer increases, there is an effect of the flow bouncing back off the wall in the free jet

system (Figure 50 a). Recirculation rings can also occur under certain conditions (flow rates, separations) and act to disrupt the linear wall-jet region.^{12,13,16}

Confinement often results in a departure from the ideal case. The nature of the resulting flow profile depends on the nozzle-electrode separation and the size of the insulating sheath surrounding the capillary. In extreme cases, small separation distances, large insulator sheath, the wall-jet flow can transition to channel flow (Figure 50 b).¹⁴ Equation 33 describes the theoretical limiting current for a confined wall-jet.²⁰

$$i_{lim} = 3.15nFV_f^{1/3}d^{-2/3}D^{2/3}R^{4/3}C \quad \text{Equation 33}$$

Where d is nozzle-electrode separation (m), note that the other variables are in SI units, unlike in Equation 32. O'Neil *et al.* demonstrated the use of a confined wall-jet flow cell for the EC-XRF analysis of metal electrodeposition using a boron doped diamond (BDD) electrode.⁹ BDD, as previously discussed has several properties making it ideal for such an application, it is an inert, low background current electrode material that is also x-ray transparent and non-metallic meaning it is an ideal substrate for XRF samples. This cell design allowed the direct irradiation of the back of the working electrode (WE) for XRF analysis whilst minimising metallic components, a BDD counter electrode (CE) was used and a small chloridised Ag wire as the reference (RE). It provided high, reproducible solution flow, allowing simultaneous and time resolved analysis of the electrodeposition of Ni, Cu, Zn, Hg and Pb, Figure 51. Pb could be detected down to 100 nM after 1 hour of electrochemical preconcentration.

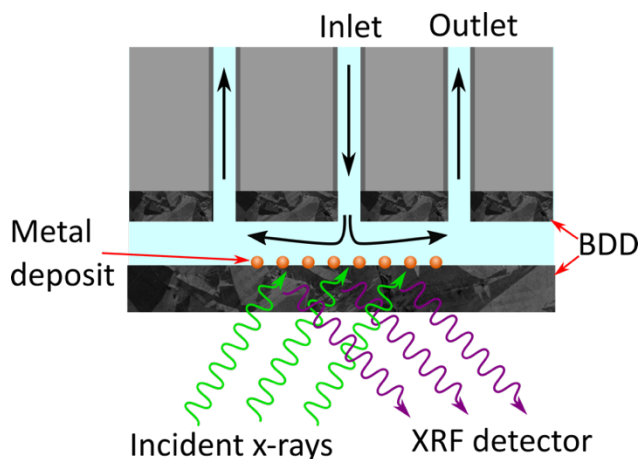


Figure 51 Schematic of an in situ EC-XRF flow cell.

In this chapter a confined wall-jet flow cell is developed for further use in EC-XRF analysis, with Cu chosen as an illustrative system. A bespoke system has been designed and built based on the original design by O'Neil *et al.* but here with the aim of improving usability and robustness whilst maintaining good LODs for the detection of aqueous Cu. There were several issues with the original O'Neil cell, most importantly the materials used were not robust enough and ultimately lead to failure of the integrity of the cell, Teflon and Araldite were replaced with PEEK and machined fittings, the changes are discussed in detail in 4.4.1. For these studies in contrast to the work of O'Neil *et al.* the cell is operated *ex situ* due to difficulty in safely plumbing the system into the XRF instrument. The electrodeposition was run on the bench then the cell transferred to the XRF chamber for analysis. This work aims to comment on both the theoretical and practical aspects of flow cell design to aid future bespoke flow cell development and to test the extent of theoretical agreement with this system.

4.3. Experimental

4.3.1. Solutions

All solutions were prepared using Milli-Q water (18.2 MΩ cm at 25 °C). The flow cell was characterised using either a 0.1 mM or 1 mM solution of hexamine-ruthenium (III) chloride, $\text{Ru}(\text{NH}_3)_6^{3+/2+}$ (98%, Aldrich), in 0.2 M potassium nitrate (KNO_3) (99% Aldrich), as described in Chapter 2, unless otherwise stated. EC-XRF experiments used copper (II) nitrate (99.99% Aldrich). All experiments were done with solution recirculation to avoid excessive use of $\text{Ru}(\text{NH}_3)_6^{3+/2+}$ or $\text{Cu}(\text{NO}_3)_2$.

4.3.2. Materials and equipment

The BDD is electrochemical processing grade and was supplied and processed as described in Chapter 2, ohmic contacts are Ti/Au as previously described. The flow cell body was fabricated from PEEK (Ensinger, UK) by Lee Butcher and Marcus Grant in the mechanical workshops (Department of Chemistry), from the author's designs,

Figure 52. Choices behind the cell and electrode dimensions employed are described in further detail in the Results section.

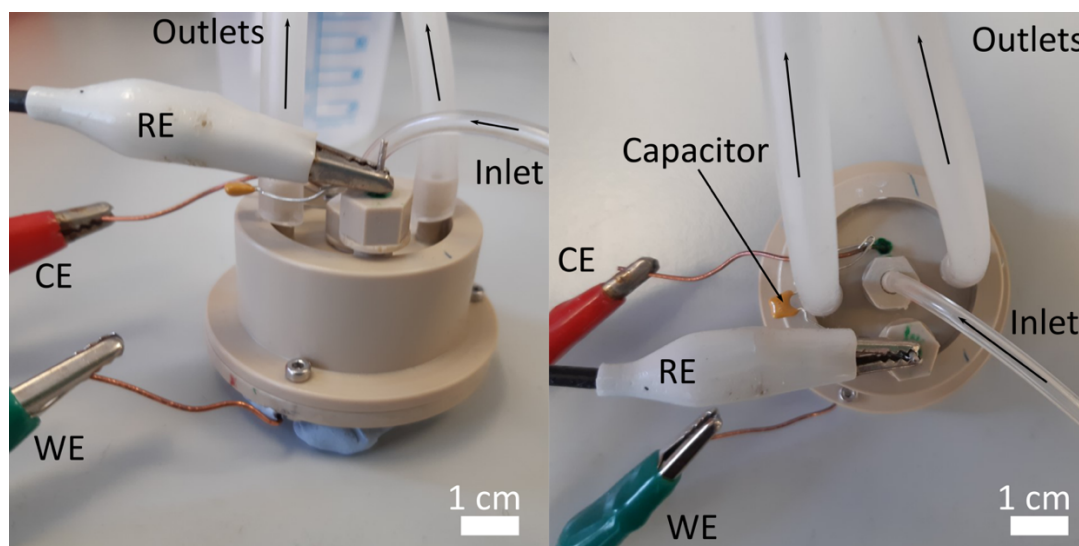


Figure 52 Photographs of flow cell assembled showing position of the wires for the WE, CE and RE, and the positions of the capacitor, outlets and inlet.

The WE is a 2.1 cm diameter disk and is contacted using Cu wire and silver epoxy as described for other electrode designs previously. The CE is a 1.6 cm diameter disk of 350 μM thick BDD with 6 hexagonal (3 mm diameter) arrays of 817 60 μm diameter holes (to increase surface area). The RE is a chloridised Ag wire. Figure 53 shows the inside of the flow cell; the electrodes, inlet and an outlet.

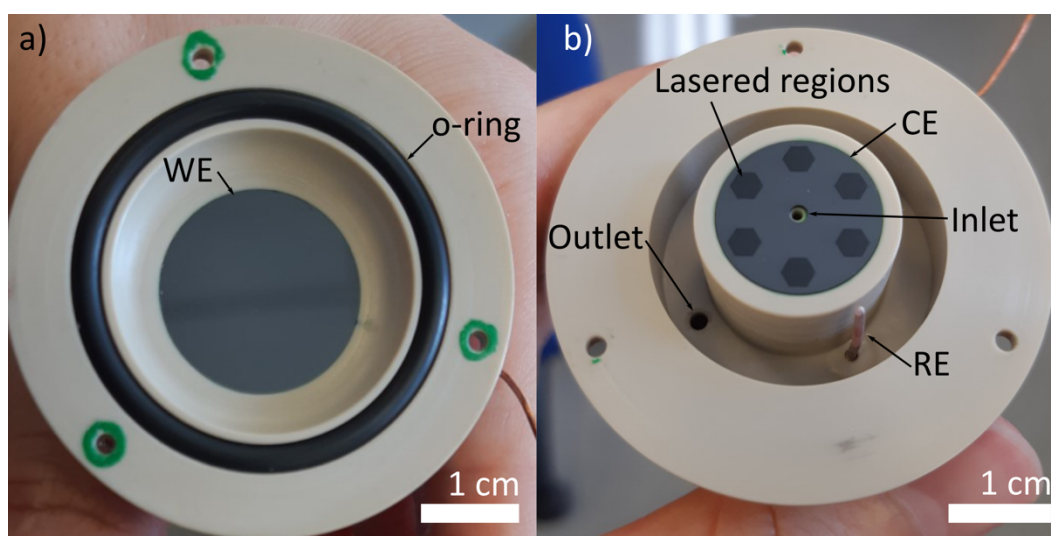


Figure 53 Photographs of the inside of the flow cell showing a) the WE and b) the CE, RE, inlet and an outlet.

The inlet nozzle diameter is 1 mm and the nozzle-electrode separation, d , was designed to be 0.5 mm, however due to tolerances during the fabrication there is

expected to be significant error on this, which will be addressed in the discussion.

Figure 54 is a schematic of the cell with dimensions.

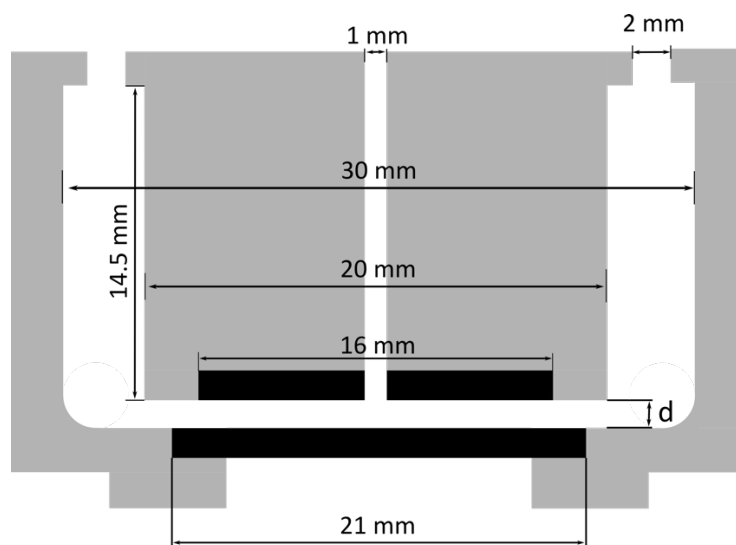


Figure 54 Schematic cross section of the flow cell showing critical dimensions.

The flow cell pump was a bespoke system designed and made by Rod Wesson (Warwick electrical workshops), with four, two bearing peristaltic pumps sequenced to remove the dead flow points that cause pulsing in single and multi-bearing designs. The drive motor is a 12 V, 350 mA, 1.8°, 200 step stepper driven in half step mode to reduce pulsing, giving 400 steps per revolution and enabling consistent flow. The motor is force air cooled to limit heat transfer to the fluid via the rotor. The 3D printed parts are a mixture of high impact polystyrene and acrylonitrile butadiene styrene, the printer is a CEL Robox dual material printer and the materials are all sourced from CEL. The tubes are 3.2 mm Tygon (RS components, 4194373). The manifold block is machined from a piece of PEEK. The control box is based on the Microchip PIC16F1519 controller and MTS2916A stepper motor driver. The control firmware monitors button presses, drives a simple display and sends the drive signals to the MTS2916A motor drive IC. Integer steps from 1 ml min⁻¹ to 20 ml min⁻¹ can be selected as well as controlling the flow direction and start/stop function.

4.3.3. X-ray Fluorescence Spectroscopy

4.3.3.1. ED-XRF

A Rigaku NEX-CG: 50 kV Pd x-ray tube secondary target carousel system with Cu, Mo, Al and RX9 targets (RX9 is a polarising target) was used with an irradiated spot size of

24 x 22 mm (ellipse), and a Zr collimator. Unless otherwise stated the following measurement parameters were used for all XRF analysis: air atmosphere, Mo target, 300 s live time, automatic current, 1.6 μ s shaping time. The molybdenum secondary target was used as this was most appropriate as it caused the most efficient excitation of Cu α out of the available targets, thereby giving the best signal to noise ratio.

4.3.3.2. Mapping XRF

A Bruker M4 Tornado mapping XRF spectrometer (Rh tube) was used for the Cu mapping experiment. It was run at vacuum, 50 kV, no filter, 600 μ A to take a 14.9 x 11.2 mm image over 3700 s. The signal is collected by 2 detectors at different positions and their signals combined to build the map.

4.4. Results and Discussion

4.4.1. Wall-Jet design

In Chapter 3 the confined wall-jet flow cell from O'Neil *et al.* was used as an example flow system, however there were structural issues with the cell and significant pump noise that needed to be improved upon. The new confined wall-jet flow cell was designed in order to provide a simple and robust flow cell suitable for *in situ* analysis of metals in solution, (Figure 55).

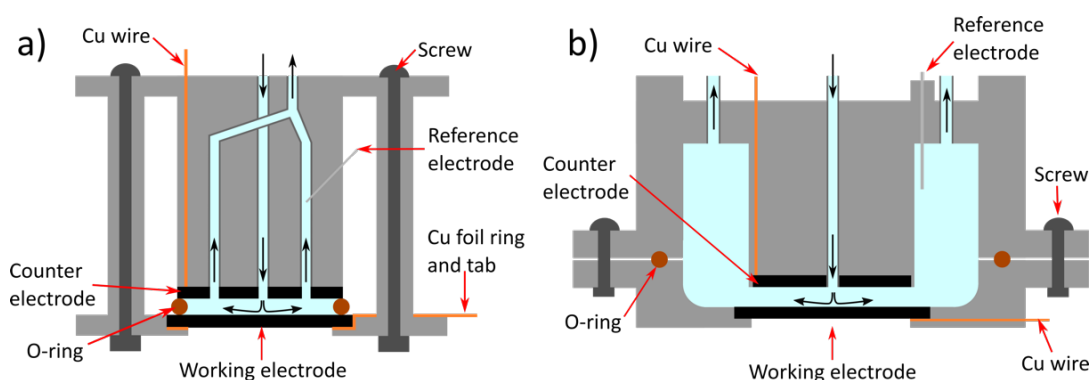


Figure 55 Schematics of a) original O'Neil cell⁹ and b) the new cell design.

Figure 55 shows schematics of the two confined wall-jet designs, so that the relative internal differences can be displayed, note that the original cell had 6 outflows which cannot be seen in these figures, whereas the new cell had only 2. Figure 56 shows photos of the cells assembled.

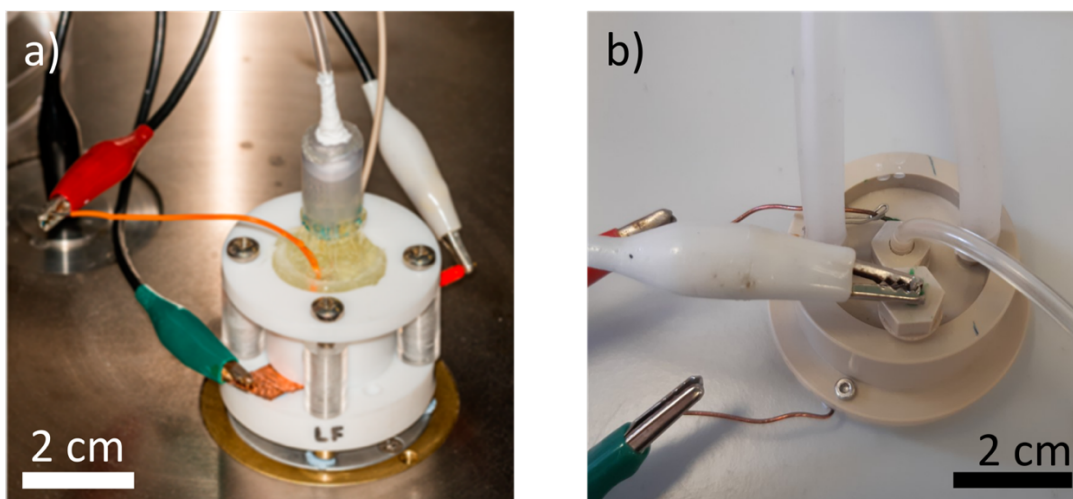


Figure 56 Photos of a) the original O'Neil flow cell and b) the new flow cell. WE wire is clipped to the green, RE white and red CE.

Several features have stayed the same, such as the RE, a chloridised Ag wire and the WE-CE arrangement but others such as outlet number were altered (discussed later). The position of the CE was considered carefully, ideally in electrochemistry it is placed far enough away that any species turned over on it do not influence the WE redox process. It must also be large enough such that current flow through the WE is not compromised. It was located in the position indicated in Figure 55 b. However, due to the close placement it is likely that the reactions occurring on the CE are affecting the WE environment, this will be further discussed later. The BDD disk CE from the old design was reused in the new design, but instead of contacting a wire by Ag paint to a graphitised area, a small Ti/Au sputter contact was made on the back to ensure an ohmic contact, non-carbide forming contacts have been shown to be less effective.²¹ As mentioned in experimental section 4.3.2 the CE has 6 hexagonal arrays of lasered holes to increase the surface area. The lasered areas are also more active due to an increased amount of sp^2 bonded carbon on the surface.^{22,23} A larger WE (21 mm diameter instead of < 2 cm) was used in the new design, so the Ti/Au contact and Cu wire could be kept further away from the XRF irradiated area, which is a 24 mm x 22 mm ellipse with an ideal sample spot in the centre, 20 mm in diameter.

The outlet number was reduced. It has been shown previously that one outlet only creates an area of higher solution velocity directly between the inlet and outlet, and

therefore not displaying uniform radial flow. Unpublished work by M. E. Snowdon showed that 4 outlets, spaced evenly around the nozzle displayed uniform radial flow, unfortunately there was no information on the effect of 2 or 3 outlets.²⁴ Unbiased flow can be achieved with well-designed cells but has been overlooked in many commercial systems which have only one outlet.⁸ In the old EC-XRF design 6 outlets were incorporated, the connections for the outlet tubing proved to be a point of failure resulting in significant leakage, possibly due to the fact that epoxy was used to attach them. The decision was made to reduce to 2 outlets (instead of 4 or 6) as this greatly simplified the design and usability.

Preliminary experiments showed that maintaining equal solution flow from each of the 2 outlet tubes is challenging. Any effect that can change the resistance or pressure in tubing can result in uneven flow from each outlet, which could result in non-uniform radial flow in the channel. Different tube lengths, different heights of parts of tubing or the extent to which a tube was bent could all result in different rates of flow from each outlet. Maintaining even flow in only 2 outlets was manageable due to the symmetry (see Figure 56 b, both tubes can be arranged in identical ways to deposit solution into the same beaker, and allowed sufficient space for access to electrode wires. It was not known at the time of design if 2 outlets would result in uniform flow or not, but it was considered an acceptable compromise. If there was increased flow along one axis, this axis could be aligned with the long dimension of the XRF irradiated ellipse and potentially be advantageous due to the expected increase in deposition in the higher velocity areas. To reduce the possible disruption to uniform radial flow, the outlets were placed opposite each other, were larger in diameter than the original cell (2 mm instead of 1.6 mm) and placed further away from the channel. It was expected that if the pressure (and therefore flow velocity) was kept equal across both of the outlets in this way, that it would sufficiently reduce pressure gradients that could cause disruption to uniform radial flow. This is aided by the design of the channel up the sides of the cell leading to the outlet, the expansion in channel cross section at this point causes an increase in pressure due to the Bernoulli principle, diminishing relative effects of gradients caused by outlet pressure or positioning upon flow within the electrode channel.

The O-rings were also moved further away from the electrodes as experience using O-rings previously had resulted in a detectable amount of Zn being leached from the polymer into the EC-XRF system. The O-ring was designed to be in the outflow, where any leaching should not affect the measurement. The HPLC pump was replaced by a bespoke pump system comprised of 4 tandem peristaltic pumps with a 3D printed pressure release (Figure 57). This system was expected to produce smoother flow than the HPLC and provide a safety feature if a pressure build-up (e.g. blockage) occurred. The pressure release mechanism would trigger before flow cell failure, avoiding potential leaks over the XRF optics, which would be disastrous, given the cost of replacement.

The mounting of the cell in the XRF required refinement, in the original design it was placed over the optics and held in place with a removable adhesive. However, this could result in variations in position and height which can both effect the efficiency of excitation of the sample by the x-rays potentially leading to more variable results. Sample holders are designed specifically to put the sample at the optimal height for the XRF optics, so this needs to be replicated for this system to ensure optimal performance and reproducibility. A new component was therefore designed and made; a ring, that could screw into the XRF chamber around the optics. The new flow cell could then be located precisely as there was a close fit between the cell and the ring, ensuring reproducible position and height after removal and replacement of the cell.

Figure 57 shows the full new flow cell and pump system in use. In these experiments the solution was recirculated to avoid excessive solution use, the inlet and outlets all feed into the same reservoir beaker.

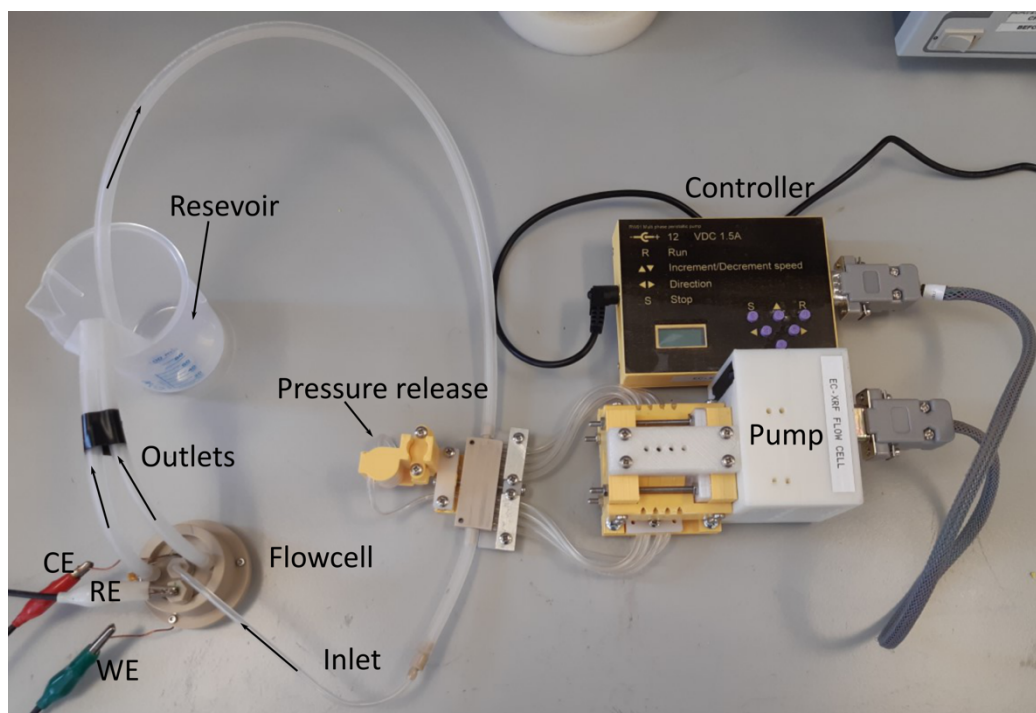


Figure 57 Picture of the flow cell system running, the pump system pulls solution from the reservoir beaker and into the manifold where it splits into 4 smaller tubes, these tubes are compressed using the 4 peristaltic bearings inside the 3D printed pump and passed back into the second chamber of the manifold to be combined into one tube that flows into the centre of the flow cell, the outlets are two thick tubes returning solution to the reservoir.

Initially there was great difficulty in generating a reproducible noise free CV. Current magnitude for the reduction of $\text{Ru}(\text{NH}_3)_6^{3+}$ varied wildly between reassembly of the cell and a high amplitude and high frequency noise was seen consistently in the CVs. It was assumed that some electrical noise, low conductivity or solution leakage was the cause. Attempts at grounding, changing $\text{Ru}(\text{NH}_3)_6^{3+}$ and KNO_3 concentration (conductivity concerns), faraday cage alteration, O-ring modification and screw insulating (in case of leakage) were all ineffective. Eventually it was found that putting a 100 nF capacitor between the CE and the RE removed the noise. The feedback loop of the potentiostat was unable to properly function due to a large RC component causing system instability by critically reducing the loop phase margin. Large oscillations in the CVs were seen but the capacitor helped to damp the oscillations, stabilising the feedback circuit, but this was believed to be at the expense of the dynamic response. The size of the resistance-capacitance (RC) component was thought to be due to a small WE-CE electrode separation that contained only a thin layer of solution and large electrode sizes. Although this dimension is not precisely known it is expected to be on the order of ≈ 0.5 mm. The capacitor was used for all

experiments. For future experiments it may be even better to place the capacitor in series with the CE lead; this arrangement would not affect the dynamic response of the system as it would be inside the feedback loop.

On the issue of the WE-CE separation, the cell was made with the intention of having a 0.5 mm separation (comparable to the original design), however several factors could have caused this to not be the case in the final system. (1) The accuracy of machining bespoke equipment; (2) the extent of the fastening of the 3 screws on the flange altering the extent of compression of the O-ring (done by hand/eye) and; (3) the thickness of the epoxy layers used to contact and seal the electrodes will have all resulted in some error contributing to the difference between design specification and actual system. Due to the irregular shape of the cell attempts at measurements with callipers of the inner and outer dimensions to try to infer separation resulted in a larger error than the expected cell separation. The exact separation is not critical for this application, as long as it can be kept consistent. It was found after repetition that an experienced operator could achieve a consistent result and the cell was characterised with $\text{Ru}(\text{NH}_3)_6^{3+}$ upon assembly each time to ensure consistency between experiments. Obviously, this could lead to inter-operator variability which is a great disadvantage to the usability of the system, improvements on this method will be discussed later in Section 4.4.3.

4.4.2. Characterisation

To characterise the new flow cell 0.1 mM $\text{Ru}(\text{NH}_3)_6^{3+}$ (0.2 M KNO_3 , 0.1 V s⁻¹) was used to run CVs at different flow rates, Figure 58, this shows how the shape of the CV changes from the classic stationary peaked CV shape to a limiting current at flow rates above 10 ml min⁻¹. The CVs obtained here are a significant improvement on those in Chapter 3, the peaks are the classic CV shape and the peak separation is now 45 mV for the stationary CV. This is sub Nernstian and indicates thin-layer effects,²⁵ which are expected from solution thicknesses less than a few 100 μm .²⁶ This is strong evidence that the WE-CE separation is smaller than 500 μm . The fluctuations in current are due to fluctuations in the flow from the pump (turbulent flow is not

expected due to a Reynolds number of approximately 470 within the inlet which expected to be the most narrow point of restriction), this is not as smooth as anticipated from the peristaltic pump system, but the system still functions well. Overall the electrochemistry is much better with the new cell design as it displays reproducible behaviour and after several continuous hours of experiments on the bench no leaks had occurred.

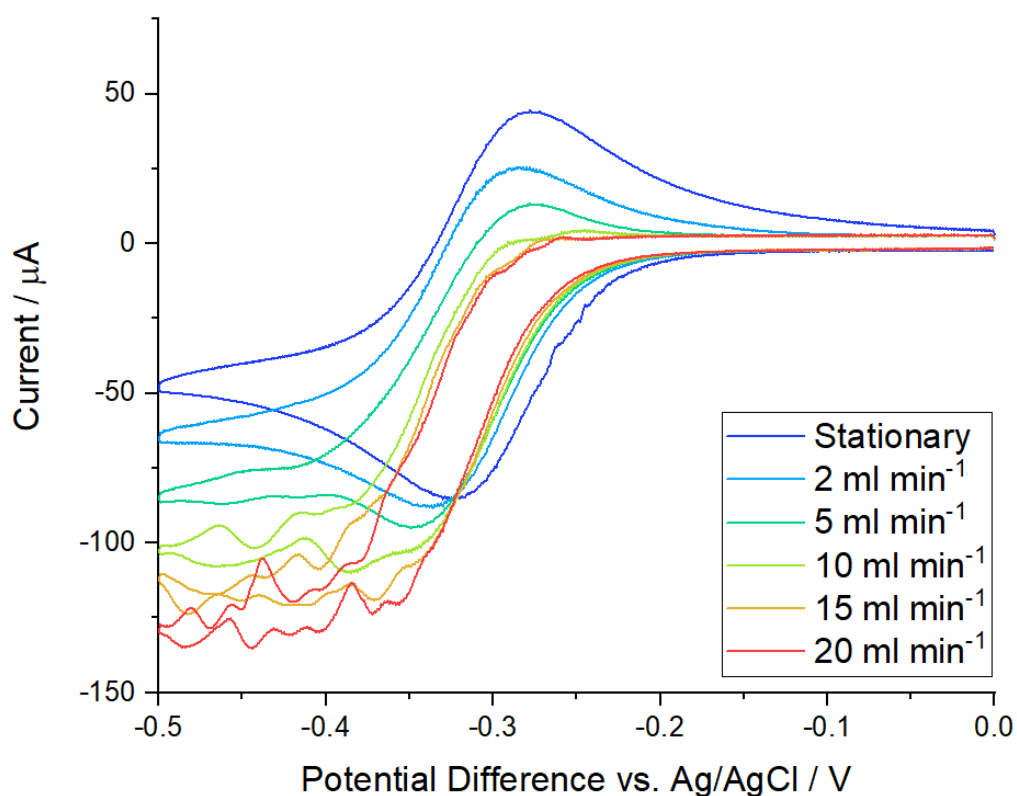


Figure 58 CV of $0.1 \text{ mM Ru(NH}_3)_6^{3+}$ 0.2 M KNO_3 run at 0.1 V s^{-1} at different flow rates from stationary to 20 ml min^{-1} .

Limiting current increases with increasing flow rate (Figure 58). The intended nozzle-electrode separation is suspected to be different to the real separation, as discussed, therefore Equation 33 was used to estimate actual separation from the data in Figure 59.

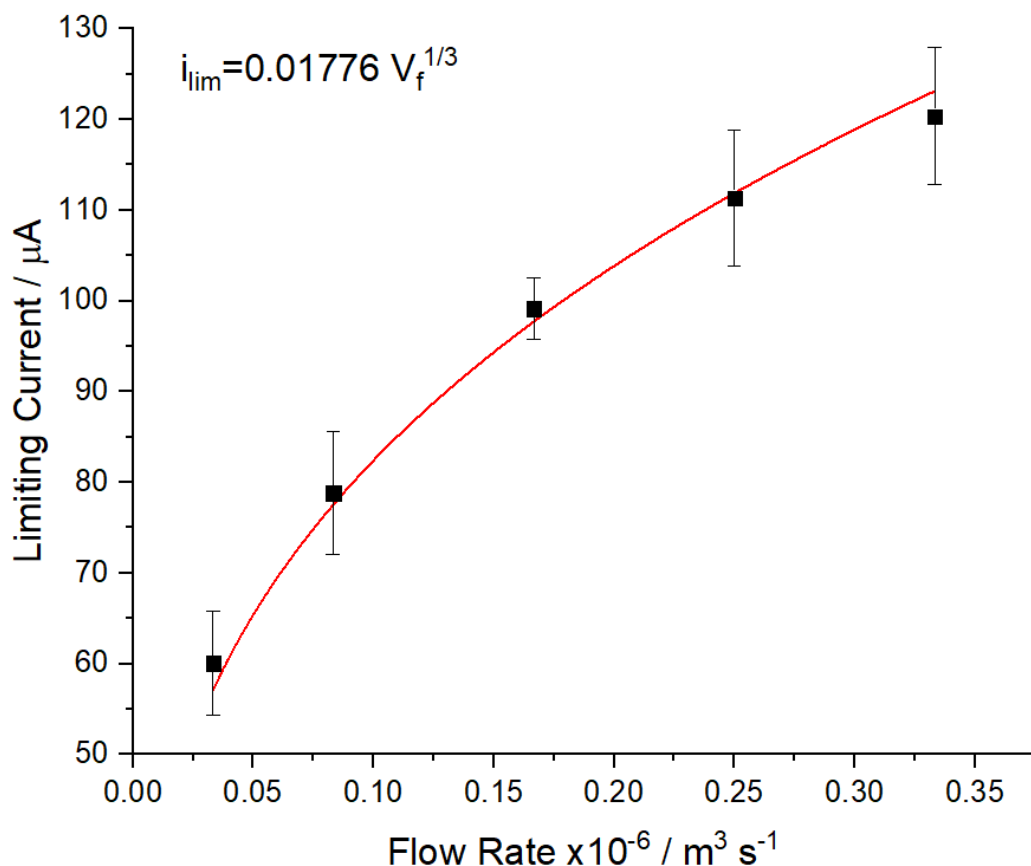


Figure 59 Limiting current vs flow rate of 0.1 mM $\text{Ru}(\text{NH}_3)_6^{3+}$ 0.2 M KNO_3 at 0.1 V s^{-1} . Error bars are standard deviation, $n=3$, line resulting from fitting Equation 33 is shown in red, $R^2 = 0.990$.

From the fit coefficient determined in Figure 59, the experimental parameters were used to calculate a separation of 217 μm . This assumes a homogeneous channel height which may not be entirely appropriate for this cell due to the CE pits, therefore the minimum separation may be slightly smaller as indicated by the sub-Nernstian electrochemistry. However, this does not negatively affect cell performance and it is considered to be working well with reproducible electrochemistry and hydrodynamics, therefore experiments with Cu were conducted next.

4.4.3. Copper Experiments

Firstly, a CV of 100 μM Cu^{2+} ($\text{Cu}(\text{NO}_3)_2$) was run in the flow cell under stationary conditions, Figure 60, in an aerated pH 5 solution containing 0.2 M KNO_3 . The CV shows Cu deposition and the oxygen reduction reaction (ORR) onset around -0.25 V and the broad anodic peak around 0 V is associated with Cu, this is expected to the

oxidation of a mixture of Cu^0 and Cu_2O , as discussed in Chapter 5. Note that the nitrate reduction reaction (NRR) is expected to occur at potentials negative of -1 V. All this is discussed in detail in Chapter 5 for the pH 5 aerated $\text{Cu}(\text{NO}_3)_2$ condition.

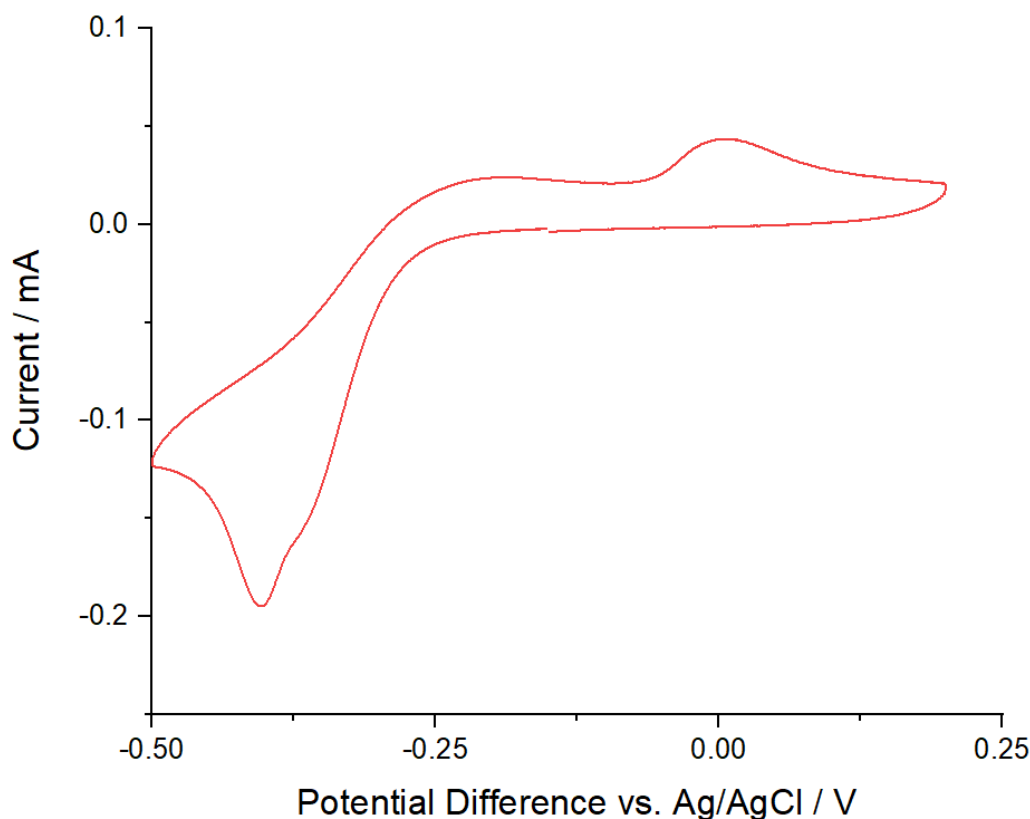


Figure 60 Cu CV in 100 μM $\text{Cu}(\text{NO}_3)_2$ and 0.2 M KNO_3 solution at 0.1 V s^{-1} , initial negative sweep direction.

It is hoped that the right combination of Cu concentration and flow rate will result in a visible deposit, allowing inference of the flow dynamics. From discussions in the introduction, electrodeposition of Cu is expected to vary radially, it is expected to be greater closer to the centre (excluding stagnant zone), as this will mirror solution velocity and the Cu concentration gradient set up. If the flow is not even over the electrode this may be visible in the distribution of the deposit.

A practical issue with the use of the flow cell is maintaining cell geometry, especially WE-CE separation. It was found that during reassembly, reproducibly tightening the three screws around the flange was extremely challenging and could result in different peak currents for what were otherwise the same conditions. To ensure the same WE-CE separation after cleaning and reassembly, a CV in $\text{Ru}(\text{NH}_3)_6^{3+}$ was run before each Cu^{2+} experiment and screws adjusted until a limiting current of 1.2 mA

(1 mM $\text{Ru}(\text{NH}_3)_6^{3+}$ in 0.2 M KNO_3 at 0.1 V s^{-1} , 20 ml min^{-1}) was reached. The cell was then flushed with water to remove $\text{Ru}(\text{NH}_3)_6^{3+}$ before commencing deposition experiments. Figure 61 shows the difference in XRF signal for Cu, electrodeposited under the same deposition conditions (described in detail below), that can occur when different $\text{Ru}(\text{NH}_3)_6^{3+}$ limiting currents (proxy for WE-CE separation) are obtained. A higher limiting current is equivalent to a closer WE-CE electrode separation. The trend of increasing count rate up to a limiting current of 1.5 mA then the decrease in count rate could be due to the constriction of the channel. As separation decreases, the flow velocity and therefore mass transport will increase, initially resulting in more deposition. However, as the separation decreases further, the shearing forces generated may become sufficient to remove some of the deposited material, reducing the observed count rates. Despite running a $\text{Ru}(\text{NH}_3)_6^{3+}$ CV test before each Cu^{2+} experiment separation still remained a source of error as the precision that could be achieved was limited by the fluctuations in limiting current, see for example Figure 58, 20 ml min^{-1} where current fluctuations of around 25% occur.

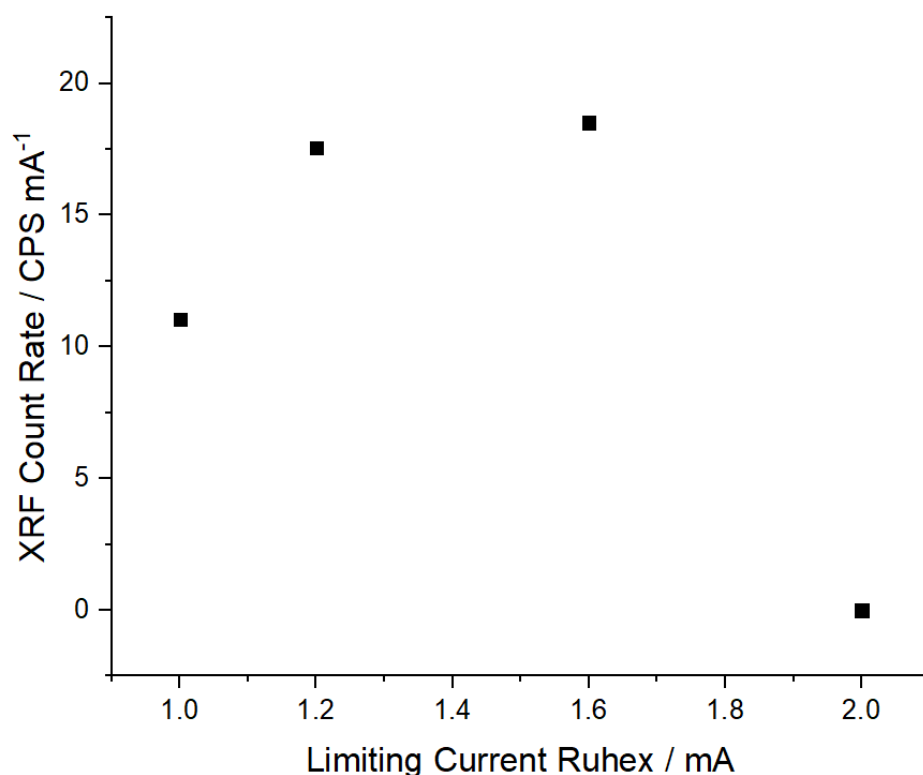


Figure 61 XRF analysis of Cu electrodeposition from $100 \mu\text{M Cu}(\text{NO}_3)_2$ and 0.2 M KNO_3 solution at a deposition potential of -0.5 V , flow rate of 20 ml min^{-1} for 900s where the test CV of $0.1 \text{ mM Ru}(\text{NH}_3)_6^{3+}$ in 0.2 M KNO_3 , 0.1 V

s⁻¹ prior to electrodeposition was adjusted to give different limiting currents as a proxy for electrode separation, higher limiting currents are equivalent to a closer separation.

Between each Cu²⁺ experiment the cell has to be disassembled and cleaned due to Cu being deposited on the electrode. Several cleaning procedures were trialled; the cell was considered clean when the XRF count rate for Cu α was ≤ 2.1 CPS mA⁻¹. This figure was obtained from repeated cleaning, backgrounds plateaued around 2 CPS mA⁻¹. Whilst alumina polishing was found useful for the 1 mm diameter BDD macroelectrodes employed in other chapters, it was not sufficient here. The physical difficulty in polishing the electrode, as it is inset into the PEEK and harder to access than a macroelectrode surface, as well as the lighter pressure used (to avoid breakage) for a large BDD disk with only edge support are probably the reasons for the failure of alumina polishing to achieve a clean surface. Two acid cleaning procedures were tested, these included holding at a constant positive potential of 1.5 V and cycling between ± 1.5 V potentials for at least 50 cycles at 0.5 s intervals in H₂SO₄, HNO₃. The latter was found to be the best method and there was no difference in cleaning ability between acid solutions. Alumina polishing was still required as a final cleaning step as acid cleaning was also not sufficient on its own. The average background (cleaned) XRF signal during the following experiments was 2.05 ± 0.09 CPS mA⁻¹.

Cu electrodeposition was carried out at different deposition potentials at a flow rate of 20 ml min⁻¹ for 900 s (Figure 62) from a solution containing 100 μ M Cu²⁺ (Cu(NO₃)₂) in 0.2 M KNO₃ at 0.1 V s⁻¹, 20 ml min⁻¹. After deposition the flow cell was placed in the XRF and analysed to obtain a Cu count rate which is directly related to the amount of material present on the electrode. XRF does not distinguish between the oxidation states of Cu and provides a count irrespective if the Cu is in the Cu(0), Cu(I) or Cu(II) forms.

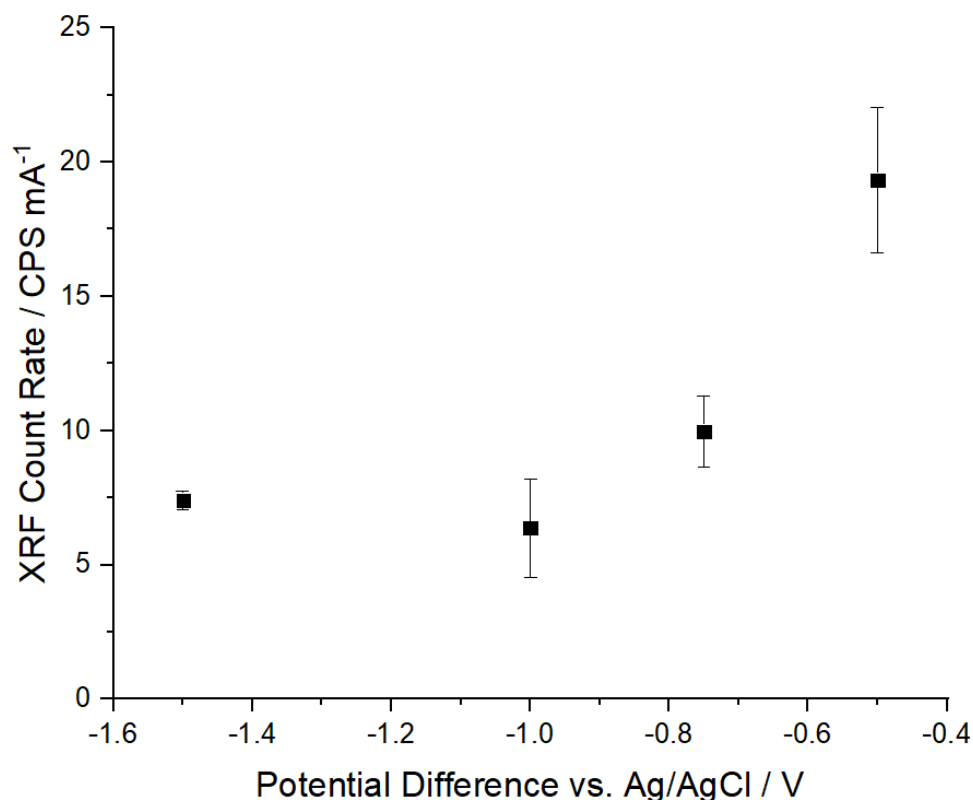


Figure 62 Cu electrodeposition from 100 μM $\text{Cu}(\text{NO}_3)_2$ and 0.2 M KNO_3 solution at deposition potentials of, -0.5, -0.75, -1.0, -1.5 V at a flow rate of 20 ml min^{-1} for 900 s, error bars are standard deviation, $n=3$.

Figure 62 shows that a deposition potential of -0.5 V vs SCE provides the largest XRF signal. At higher potentials (-1.0 and -1.5 V) significant bubbling occurred which produced noticeable bubble formation in the outlet tubing, this is likely due to gas evolution reactions occurring such as the hydrogen evolution reaction (HER) or NRR. This bubbling could be the reason for lower XRF count rates as they could cause surface blockage or detachment of deposits. Along with HER and NRR, ORR is also occurring, all of which will cause a local decrease in pH, possibly resulting in precipitated forms of Cu, such as Cu_2O or Cu hydroxides, that may not adhere as well to the electrode surface under flow. A deposition potential of -0.5 V was used for all subsequent experiments.

A concern of previous work is that higher solution velocities (rotation rate in Chapter 3 of higher flow rates here) may also result in detachment of the Cu deposits from the electrode surface. Hence a test of Cu deposition at different flow rates was

conducted (Figure 63) for a fixed deposition potential of -0.5 V in a solution containing 100 μM Cu^{2+} ($\text{Cu}(\text{NO}_3)_2$) in 0.2 M KNO_3 at 0.1 V s^{-1} , 20 ml min^{-1} .

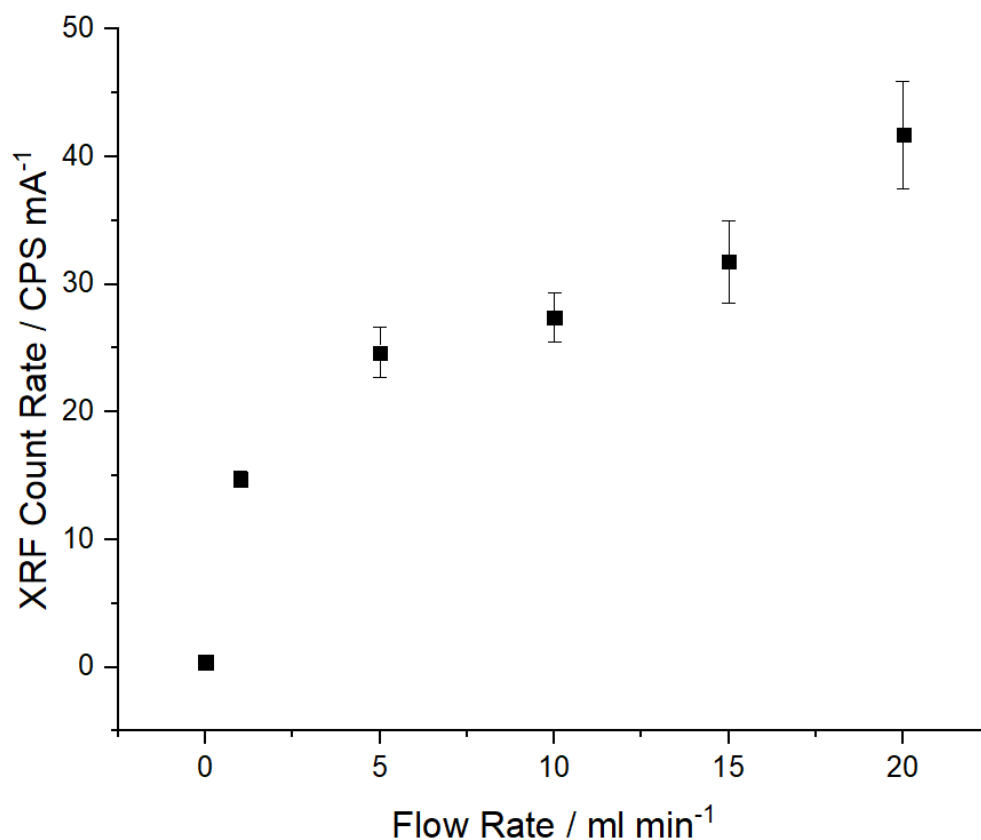


Figure 63 XRF analysis of Cu electrodeposition from 100 μM $\text{Cu}(\text{NO}_3)_2$ and 0.2 M KNO_3 solution at a deposition potential of -0.5 V at varying flow rates from stationary to 20 ml min^{-1} for 900 s, error bars are standard deviation, $n=3$.

Figure 63 shows that in this flow cell configuration, faster flow rates gave higher XRF signals and so a flow rate of 20 ml min^{-1} was used for all subsequent experiments. As this does not correlate with the $V_f^{1/3}$ dependency seen for limiting currents, another effect must be present. It is possible that side reactions could be a factor here, for example the ORR may be altering the Cu^{2+} concentration near the electrode surface by increasing the local pH due to the production of hydroxide ions. This could result in some precipitation of Cu hydroxides that would be removed by the flow and unlikely to be reduced on the electrode at this potential. This could cause a suppression in count rates at lower flow rates. At higher flow rates, the diffusion layer is compressed, and hydroxide ions would be removed more quickly, reducing this effect. However, this does not take into account the effect of reactions on the CE.

Finally, a series of electrodepositions for a range of Cu^{2+} concentrations (2.5 to 100 μM) with subsequent XRF analysis was run to determine a LOD for Cu EC-XRF, for 3600 s, -0.5 V, 20 ml min^{-1} (Figure 64).

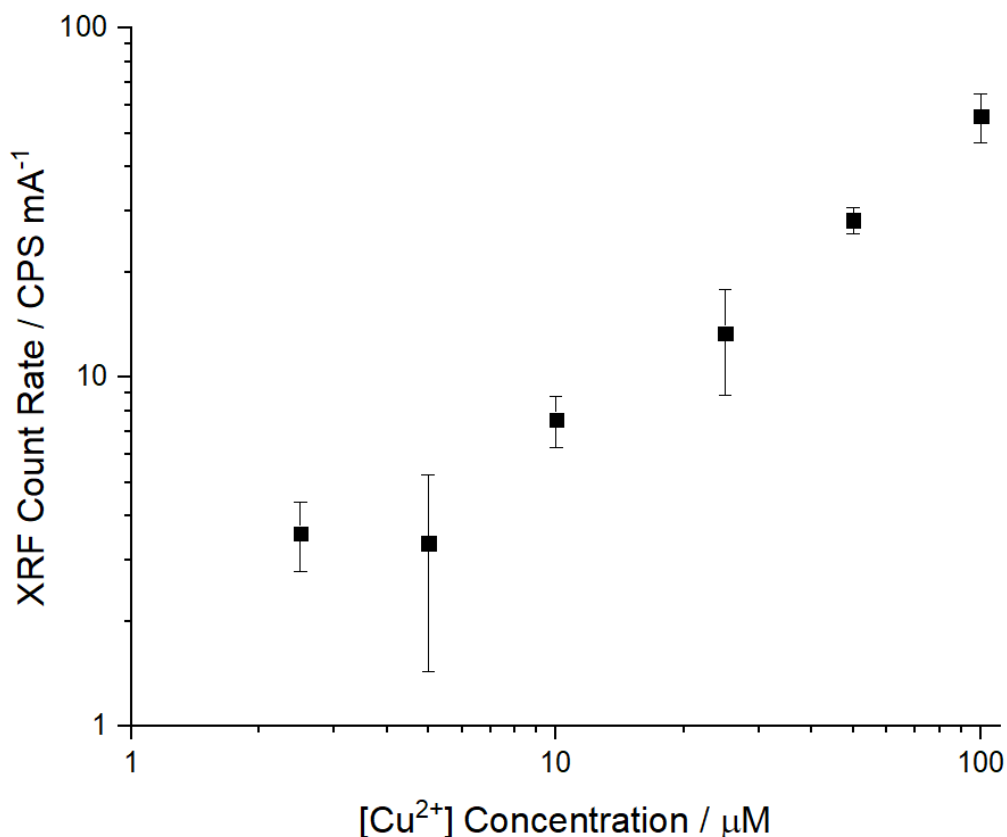


Figure 64 XRF analysis of Cu electrodeposition from 2.5 to 100 μM $\text{Cu}(\text{NO}_3)_2$ and 0.2 M KNO_3 solution at a deposition potential of -0.5 V at a flow rate of 20 ml min^{-1} for 3600 s, error bars are standard deviation, $n=3$.

This data shows that in the flow cell Cu^{2+} concentrations could be linearly analysed down to around 5 μM . The LOD is not as low as would be expected from the background signal. The background variation (σ) of 0.09 CPS mA^{-1} gives a theoretical lowest detectable signal, 3σ ,²⁷ of 0.27 CPS mA^{-1} . As the line of best fit crosses zero concentration at 0.99 CPS mA^{-1} , there must be another factor affecting the LOD of the system, confirming the conclusions of chapter one. Although this is an area for future work, one possibility stems from the fact this flow cell was not used as a true *in situ* system. This was due to the potential dangers of solution leak over the XRF optics during operation and the difficulty in safely plumbing the tubing and potentiostat wires into the XRF chamber (through X-ray shielding). This system was run on the bench, detached from the pump, tubing plugged with syringes and transferred to the XRF chamber for analysis. The detaching and blocking of the tubing

resulted in some flow/agitation of the solution due to compressing the tubing, which could generate forces inside the cell that could be responsible in helping to detach deposits from the surface. The forces generated in this way cannot be quantified but in order to test this theory the flow cell was not directly cleaned after XRF analysis, it was plugged back into the flow cell and flow resumed for 5 minutes (no applied potential), at the same flow rate, before analysing again with XRF. This experiment showed that between 1 and 14 CPS mA^{-1} of signal was lost due to this flushing, the amount lost did not appear to correlate with Cu concentration (or original XRF count rate). This was only done for 1 run of each concentration and so it is not possible to determine the statistical significance, however this does show that post deposition flow could be adversely affecting the reproducibility of the calibration. It is believed that this could be solved by truly running *in situ* but this has unfortunately not been possible to test due to time and safety concerns.

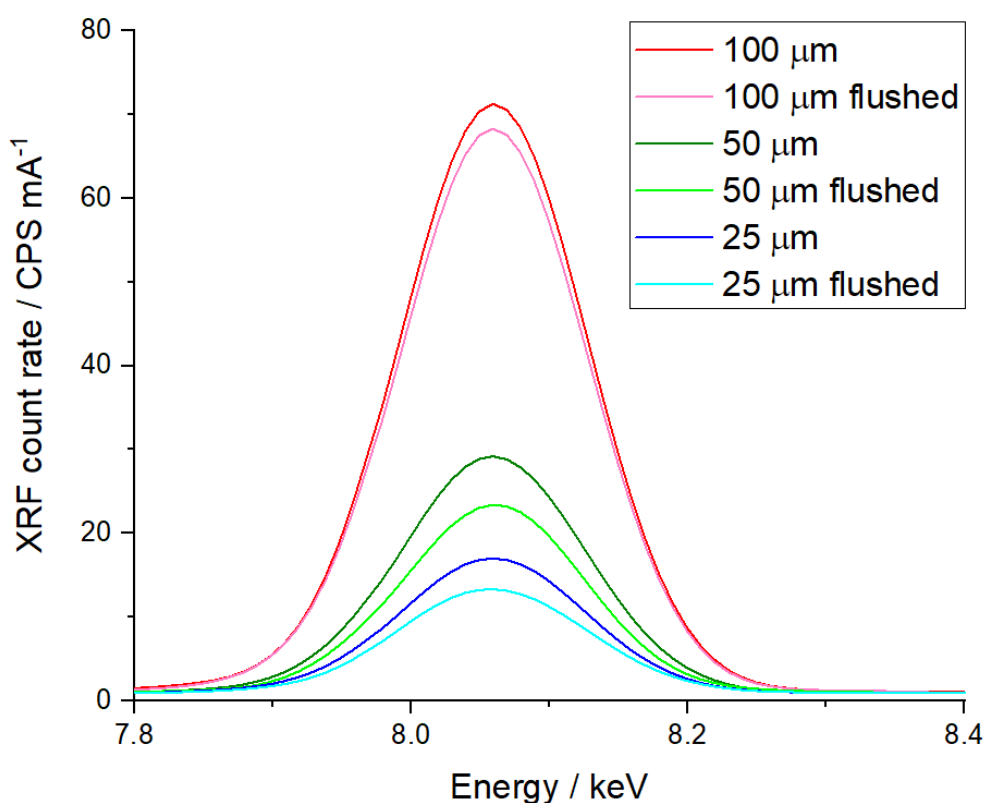


Figure 65 XRF spectra of the Cu $K\alpha$ line after deposition in 25 to 100 μM $\text{Cu}(\text{NO}_3)_2$ and 0.2 M KNO_3 solution at a deposition potential of -0.5 V at a flow rate of 20 ml min^{-1} for 3600 s, and then subsequently flushed with solution for 300 s at 20 ml min^{-1} with no applied potential.

4.4.4. Mapping XRF

After electrodeposition, visual inspection of the electrode surface revealed clear differences in the deposit morphology dependant on the deposition / flow conditions utilised. At very low flow rates and short times barely anything was visible on the surface by eye, however, at longer times, faster flow rates and higher potentials clear deposits could be observed. Figure 66 shows examples of different deposits produced during the previous experiments.

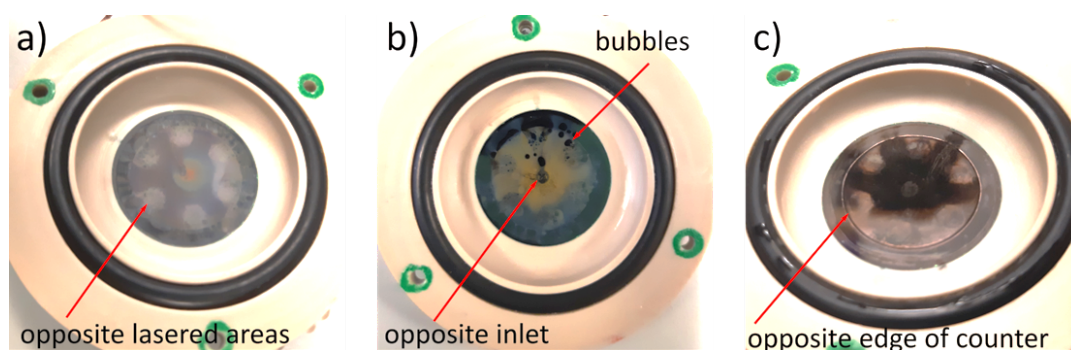


Figure 66 Photographs of a) 20 ml min^{-1} and b) 5 ml min^{-1} at -0.5 V , c) -1.5 V deposition potential, 20 ml min^{-1} , all in $100 \text{ } \mu\text{M Cu(NO}_3)_2$ and 0.2 M KNO_3 for 900 s . Photographs have been brightened to improve visibility of deposits, a) the areas of the WE opposite the lasered hexagonal areas on the CE are highlighted, b) the area opposite the inlet on the CE and some bubbles that have disrupted deposition have been highlighted, c) the ring of deposit that is on the WE is highlighted and where the CE edge is relative to the WE.

In almost all cases of visible deposits, the positions of the 6 hexagonal lasered areas of the CE and the area directly below the inlet, resulted in a visual difference in the deposit. These hexagonal lasered regions, designed to increase surface area are almost certainly more active than the unlasered BDD areas and so more likely to cause a local change in pH or concentration of other species. In this case they would have been causing a decrease in pH, assuming that water splitting (and oxygen evolution) in the anodic region is the most likely reaction. This difference in pH could have caused the Cu speciation produced locally to be slightly different, giving a visibly different deposit, note that Cu compounds can be several different colours the oxides can be pinkish or black and hydroxides can appear blue or green. A few blank (black) areas can also be seen from the photos (annotated in b), these appear to be where bubbles have blocked the surface and prevented deposition on the BDD. Another interesting feature is the area directly below the nozzle in the centre, this is also visible in all deposits. The hydrodynamics of wall-jets results in a stagnant region in

the centre of the jet where it impinges on the wall (electrode), as discussed in the introduction, due to this it was expected that very little electrodeposition would occur directly under the nozzle. It was predicted that the largest concentration of deposit would be just outside the stagnant region and would then decrease towards the outer circumference of the electrode. To test this hypothesis a deposit formed at -0.5 V , 20 ml min^{-1} , in $100\text{ }\mu\text{M Cu(NO}_3)_2$ and 0.2 M KNO_3 run for 1800 s was analysed in a Bruker Tornado mapping XRF spectrometer. Figure 67 compares the photograph and the XRF map of the result of this deposition for comparison.

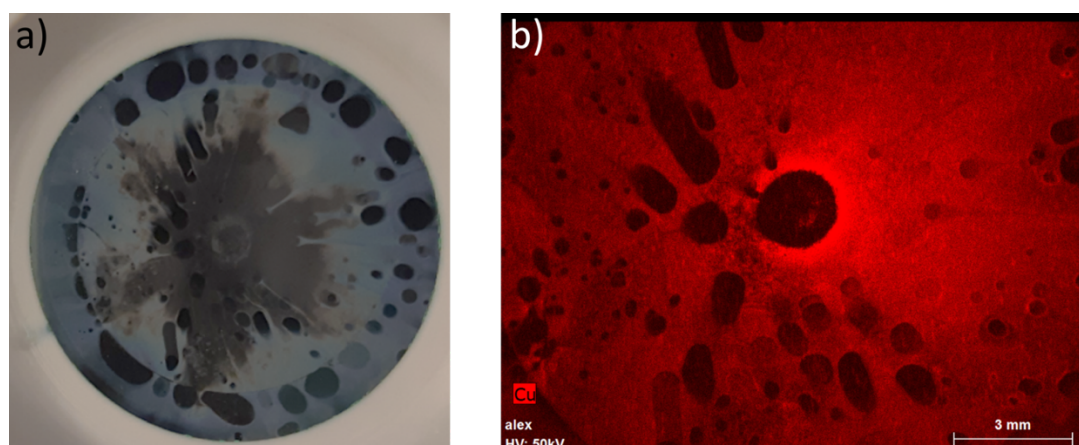


Figure 67 a) photo of electrode surface b) XRF map for Cu, after deposition at -0.5 V , 1800 s , $100\text{ }\mu\text{M Cu(NO}_3)_2$ and 0.2 M KNO_3 . In b) areas exhibiting a Cu signal are coloured red.

Figure 67 a) shows that visible Cu deposits have been created, in a), they appear light grey. There is visible variation in the deposit varying from light grey to dark grey/underlying BDD. A central ring around the inlet region can be seen, similar to Figure 67. Darker areas can be seen where bubbles formed and disrupted deposition and more centrally the deposit appears darker, the area outside the area confined by the CE can also be seen. It is unclear from the photograph if the darker areas correspond to less deposit or another form of Cu. The XRF map in b) shows areas containing more Cu as more intense red, this shows that the area opposite the inlet and the areas with bubbles have very little Cu present. The other visible differences in the photograph appear to not be directly correlated with the amount of Cu present. It is therefore postulated that more than one species of Cu, with different appearances are present here (different apparent colours etc. expected to be different species). XRF is sensitive to all species of Cu, which is one of its major advantages. The distribution of Cu shows that the hexagonal lasered areas are not

having an effect on the amount of Cu deposited and there also does not appear to be a preferred flow path due to the outlet configuration, however this is not definitive as bubbles have obviously influences the deposition and flow. It is likely that (the extent of) bubble formation/location is different for different repeats and could be a reason for the LODs not being as low as expected in the Cu concentration experiment.

The predictions of deposit concentration with respect to the wall-jet hydrodynamics were correct, very little deposition occurred where the jet impinged but the maximum was just outside this area, this has been quantified in Figure 68.

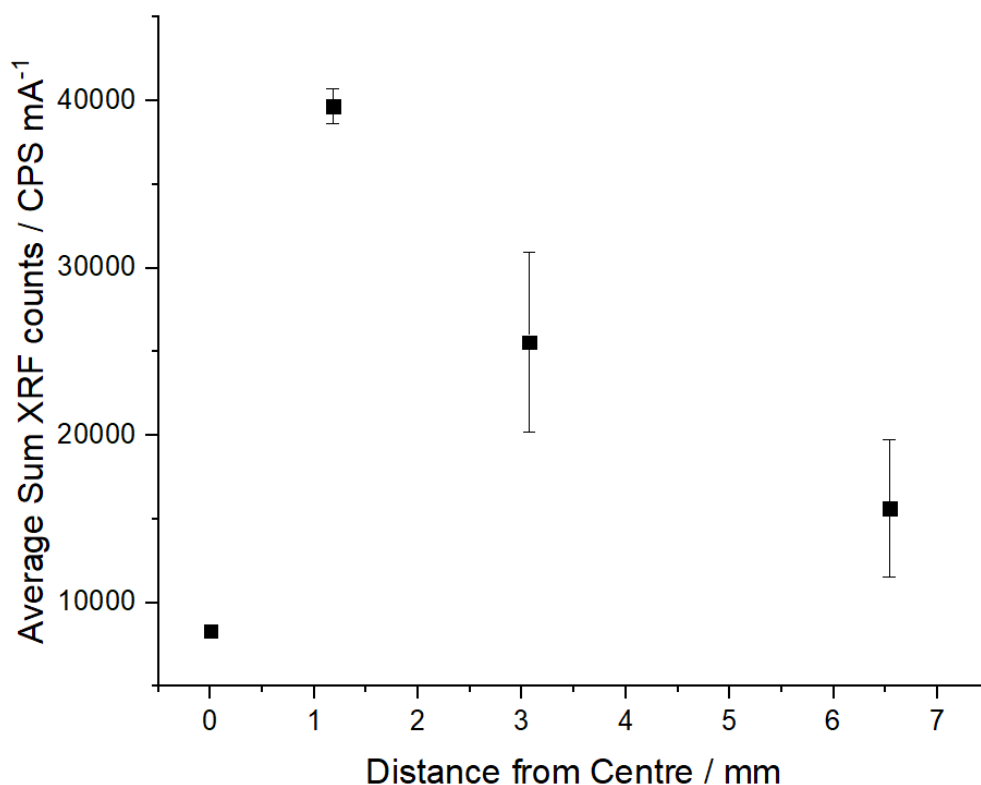


Figure 68 Summed XRF counts from 200 μm radius areas ($n=3$) at 4 different locations on the electrode surface from mapping data.

This is in agreement with the predictions of wall-jet electrodeposition discussed previously and is an excellent result for EC-XRF. The deposits (although low in a small central area) are concentrated in the middle, which would provide better access by x-rays (irradiated ellipse) for XRF analysis, potentially making it more sensitive than a method that produced a uniform layer of Cu over the electrode surface.

4.5. Conclusions

The new design was an improvement on the original O'Neil design,⁹ the cell is a simpler and more robust design, successfully running all experiments without leakage whilst attaining comparable LODs for individual metal analysis. The change in pump system, although little was gained in smoothness of solution flow, was smaller and more flexible than the HPLC pump used previously and would be a practical solution for a portable system.

The system fit to the theory of a confined wall-jet with $\text{Ru}(\text{NH}_3)_6^{3+}$, displaying I_{lim} vs $V_f^{1/3}$. From this it was estimated that the WE-CE separation is around 217 μm . Operating in such a small gap resulted in a large RC component causing system instability and a capacitor was required to help the feedback system stabilise in the potentiostat. However, the small separation does compress the diffusion layer in a way which may further increase mass transport to the WE. There was not a clear dependency of XRF count rate to flow rate and it is expected that additional effects are at play, potentially effects of the ORR changing local pH suppressing the XRF count at lower flow rates.

The mapping experiment showed that the distribution of Cu deposit on the surface agrees with models of flow cells in literature with regards to the stagnant region and the high concentration around it. This experiment also showed that bubble formation is blocking the surface of the electrodes, preventing Cu deposition in those areas. Stochastic formation of these bubbles could be causing the poorer than expected LODs, as well as potential deposit detachment from moving the flow cell from bench to XRF. It is possible that these two factors could be improved by increasing the WE-CE separation and running as a true *in situ* system respectively. Increasing the WE-CE separation could encourage the detachment of bubbles, as once they have spanned the gap between the electrodes, they would be harder to move because of surface tension. Degassing may be of some use if the oxygen evolution reaction is significant

and lowering of the electrolyte concentration would lead to an increase in oxygen solubility, but this could cause increased resistance within the cell.²⁸

Investigation into the effects of varied WE-CE separation (with respect to CE reactions), pH, and even the investigation of multiple metal solutions would be interesting areas for future research with this system. Ultimately the use of this cell in a truly *in situ* system would be an important aim as this would allow time resolved experiments.

In summary a new robust wall-jet flow cell has been developed for *in situ* EC-XRF analysis of aqueous metals has been developed that is a step closer to a useable portable EC-XRF system. This flow cell has also experimentally confirmed the hydrodynamic models of confined wall-jet systems in literature by the analysis of the Cu deposit distribution.

4.6. Bibliography

- 1 M. E. Snowden, P. H. King, J. A. Covington, J. V. MacPherson and P. R. Unwin, *Anal. Chem.*, 2010, **82**, 3124–3131.
- 2 C. M. A. Brett, A. M. C. F. Oliveira Brett, A. C. Fisher and R. G. Compton, *J. Electroanal. Chem.*, 1992, **334**, 57–64.
- 3 J. F. Van Staden and M. C. Matoetoe, *Anal. Chim. Acta*, 2000, **411**, 201–207.
- 4 H. Gunasingham and B. Fleet, *Anal. Chem.*, 1983, **55**, 1409–1414.
- 5 M. G. Tamba and N. Vantini, *Electroanal. Chem. Interfacial Electrochem.*, 1970, **25**, 235–244.
- 6 T. M. Florence, *Analyst*, 1986, **111**, 489–505.
- 7 A. J. Borrill, N. E. Reily and J. V. Macpherson, *Analyst*, 2019, **144**, 6834–6849.
- 8 R. B. Channon, M. B. Joseph and J. V. Macpherson, *Electrochem. Soc. Interface*, 2016, **25**, 63–68.
- 9 G. D. O’Neil, M. E. Newton and J. V. Macpherson, *Anal. Chem.*, 2015, **87**, 4933–4940.
- 10 T. M. Chinowsky, S. B. Saban and S. S. Yee, *Sensors Actuators, B Chem.*, 1996, **35**, 37–43.
- 11 J. V. MacPherson, M. A. Beeston and P. R. Unwin, *J. Chem. Soc. Faraday Trans.*, 1995, **91**, 899–904.
- 12 E. Bitziou, N. C. Rudd, M. A. Edwards and P. R. Unwin, *Anal. Chem.*, 2006, **78**, 1435–1443.
- 13 T. Guo, M. J. Rau, P. P. Vlachos and S. V. Garimella, *Phys. Fluids*, , DOI:10.1063/1.4975394.
- 14 J. V. Macpherson, C. E. Jones and P. R. Unwin, *J. Phys. Chem. B*, 1998, **102**, 9891–9897.
- 15 W. J. Albery and C. M. A. Brett, *J. Electroanal. Chem.*, 1983, **148**, 201–210.
- 16 M. B. Glauert, , DOI:10.1017/S002211205600041X.
- 17 N. V. Rees, O. V. Klymenko, B. A. Coles and R. G. Compton, *J. Phys. Chem. B*, 2003, **107**, 13649–13660.
- 18 W. J. Albery and S. Bruckenstein, *J. Electroanal. Chem.*, 1983, **144**, 105–112.
- 19 J. Yamada and H. Matsuda, *J. Electroanal. Chem.*, 1971, **30**, 271–278.

- 20 A. J. Dalhuijsen, T. H. Van Der Meer, C. J. Hoogendoorn, J. C. Hoogvliet and W. P. Van Bennekom, *J. Electroanal. Chem.*, 1985, **182**, 295–313.
- 21 T. Tachibana, B. E. Williams and J. T. Glass, *Phys. Rev. B*, 1992, **45**, 11968–11974.
- 22 Z. J. Z. J. Ayres, A. J. Borrill, J. C. Newland, M. E. Newton and J. V. Macpherson, *Anal. Chem.*, 2016, **88**, 974–980.
- 23 J. Li, C. L. Bentley, S. Y. Tan, V. S. S. Mosali, M. A. Rahman, S. J. Cobb, S. X. Guo, J. V. Macpherson, P. R. Unwin, A. M. Bond and J. Zhang, *J. Phys. Chem. C*, 2019, **123**, 17397–17406.
- 24 M. E. Snowden, *PhD Thesis, University of Warwick*, 2010.
- 25 G. M. Tom and A. T. Hubbard, *Anal. Chem.*, 1971, **43**, 671–674.
- 26 J. M. Davis, F. R. F. Fan and A. J. Bard, *J. Electroanal. Chem.*, 1987, 238, 9–31.
- 27 J. Holler, D. A. Skoog and S. Crouch, *Principles of Instrumental Analysis*, Cengage Learning, 7th edn., 2007.
- 28 D. Tromans, *Proc. 2nd Int. Conf. Intell. Process. Manuf. Mater. IPMM 1999*, 1999, **1**, 411–416.

5. Copper Electrodeposition and Stripping investigations

5.1. Overview

Copper (Cu) is extremely relevant, both environmentally and technologically. In this chapter we explore how electrolyte conditions influence the electrochemical deposition and subsequent dissolution characteristics of Cu. In particular, we explore buffered versus unbuffered systems, solution pH, electrolyte composition, electrode potential and dissolved oxygen presence. This work also demonstrates why quantification of Cu^{2+} in solution with anodic stripping voltammetry (ASV) in real world '*in situ*' samples is challenging. Our understanding also provides routes for the electrochemical fabrication of a wide range of Cu morphologies (and $\text{Cu}_x\text{O}/\text{CuO}$ materials) without the need for long synthetic procedures, surfactants or extreme conditions. Such structures could be exploited for electrocatalysis, sensing and electronics applications.

5.2. Introduction

Copper is frequently found in environmental and biological systems and is widely used in technological products and processes such as consumer electronics (as metallic Cu, Cu^0 , or its oxides) and photovoltaics.^{1,2} Two reasons for understanding the electrochemistry of Cu^{2+} are: (1) so that cheap, fast and sensitive electrochemical based methods for Cu^{2+} detection in solution can be developed; Cu^{2+} is often found in unnaturally high levels (potentially dangerous to the environment) due to anthropogenic activities;³ (2) to improve electrochemical synthesis methods for Cu^0 , Cu_2O and CuO nanostructures for use in advancing technological applications e.g. improving electrocatalyst product ratios or the efficiency of solar cells.

The electrochemical deposition and subsequent stripping (ASV) characteristics of a metal, such as Cu^{2+} , can vary drastically as it depends on a wide range of factors

including potential applied, pH, temperature, electrode surface, solution composition and dissolved oxygen presence. The ideal electrode for ASV electrochemical studies was the Hg electrode, which due to its toxicity is now rarely used (Chapter 1). At low concentrations, dissolved metals do not significantly perturb the electrochemical characteristics of the Hg electrode; very narrow peaks typically result for stripping analysis. In contrast, at solid electrodes, metal-electrode and metal-metal interactions result in varying overall electrode properties and deposit morphologies. This can lead to a broadening or shifting of stripping peak signals, sometimes causing peak overlap or multiple peaks, making analysis much more challenging. This is further complicated by the response being affected by electrode material and solution properties.⁴ Understanding the electrodeposition of metals is helpful in deciphering the stripping data.

For electrodeposition and electrochemical studies in general, boron doped diamond (BDD) is a useful material as described by Macpherson.⁵ BDD has a large solvent window and is very inactive to background reactions such as the oxygen reduction reaction (ORR).⁵ However, all solid electrodes, including BDD, suffer from the fact that as soon as a metallic species has been deposited, the surface properties and even the surface area of the electrode has changed. For example, for BDD, depositing metal will make an electrocatalytically inert electrode, electrocatalytically active, an effect often overlooked in literature.⁴

Electrolyte conditions are also an important consideration in metal deposition and stripping. The pH of the solution will affect the speciation profile of metal ions in solution.⁶ The chemical identity of the electrolyte ions can also influence the resulting electrochemical process through (i) reduction of the anion e.g. in the case of nitrate to produce hydroxide ions;⁷ (ii) anion adsorption on the deposited metal;⁸ (iii) metal-electrolyte interactions in solution e.g. in the case of chloride.⁹ Oxygen presence can also result in unwanted electrochemical side reactions due to ORR on metals which in turn impacts the local pH.¹⁰

When conducting electrodeposition studies, it is also important to understand the characteristics of the metal of interest and the forms in which it is likely to be found. Cu is a very reactive element and due to the ease of transitions between its oxidation states is a powerful catalyst.¹¹ Cu is most often found in the 0, +1 or +2 states, enabling a wide range of potential species. For example, several hydroxide compounds are possible as are several Cu-chloride-oxide/hydroxide compounds with different stoichiometries.¹² The range of possible compounds combined with the ease of transition between oxidation states means that any analysis of Cu is extremely complex.

Cu, like many other reactive metals easily forms oxides, its two major oxides are Cu₂O and CuO (both are semiconductors).¹³ A third oxide (of Cu³⁺) has been suggested, Cu₂O₃, but this is currently a topic of dispute in literature.¹⁴ Additionally an oxide that is a combination of Cu₂O and CuO is often referred to in literature as Cu₄O₃ as it seems to have distinct electrochemical properties from Cu₂O and CuO.^{15,16} On fresh Cu⁰ surfaces, a layer of Cu₂O is formed in air.¹⁷ However, this process is limited to only a few atomic layers before strains result in cracking of the film due to the difference in lattice parameter of the metallic and oxide layers. This means the film is never fully passivating and can be considered porous; O species and Cu ions can move through this layer to react at different interfaces.¹⁷ When the oxide layer becomes more developed a “duplex” effect is seen where several different Cu species are present in porous layers, for example Cu⁰/Cu₂O/CuO/Cu-OH_(ads).¹⁸ However, the composition of the layers is not generally agreed upon and appears to be condition dependent.^{15,19}

Cu is reported to have catalytic effects on ORR,¹⁸ oxygen evolution,¹⁴ H₂O₂ reduction,²⁰ nitrate reduction reaction (NRR)⁷ and carbon dioxide reduction.²¹ However, it is not always clear exactly which form of Cu, and hence redox state, is involved in the reaction. Furthermore, there is some contention surrounding the mechanisms of many Cu mediated processes, such as carbon dioxide reduction.²²

In the field of ASV, many papers have successfully developed analytical methods for the detection of Cu but most have found issues due to: (i) complexing agents (naturally occurring organic ligands);²³ (ii) Cu interfering with the analysis of other

elements;²⁴ (iii) difficulties with pH control and; (iv) the presence of chloride ions.²⁵ This means that of the methods developed most only work in a narrow range of conditions and so their applicability is severely limited. Theoretical assessments of the electrodeposition and stripping of Cu often present results that do not fit well to progressive/instantaneous nucleation theory,²⁶ unlike those obtained with other elements, such as Ag.²⁷ Whilst there is also much literature on the electrodeposition of Cu,^{26,28–31} few studies have related the electrochemical response to the deposit morphology^{13,15,32–34} and even fewer related the ASV response to the deposit morphology.³⁵

The aim of this chapter is thus to explore the effects of different electrolyte systems (acetate, sulfate, nitrate and chloride), buffered versus unbuffered, pH, deposition potential and dissolved oxygen on the deposit morphology and ASV characteristics of Cu. This will then be applied to Cu₂O electrochemical synthesis for technological applications in Chapter 6.

5.3. Experimental

5.3.1. Solutions

All solutions were prepared using Milli-Q water (Millipore, deionised), with resistivity of 18.2 MΩ cm at 25 °C. All chemicals used as received without further purification. The supporting electrolytes used were K₂SO₄, KNO₃ and KCl (0.1 M) and the corresponding Cu salt was used in each case (CuSO₄, Cu(NO₃)₂, CuCl₂) at a concentration of 100 μM. The corresponding acids (H₂SO₄, HNO₃, HCl) were used for pH adjustment and acetate buffer (0.1 M, 0.04 g sodium acetate, 0.572 g glacial acetic acid in 100 ml for pH 3.6 and 0.57 g and 0.17 g for pH 5) and CuSO₄ was the Cu salt used in acetate solution. pH measurements were made using a commercial pH probe (Mettler Toledo). Deoxygenation was carried out by bubbling Ar_(g) through the solution for 1 minute per ml of solution then moving to a light flow of Ar_(g) over the surface of the solution during electrochemistry to avoid solution agitation.

5.3.2. Electrochemistry

A three-electrode set up was used for all experiments, a 1 mm diameter BDD (see Chapter 2) glass sealed electrode was used as the working electrode, a saturated calomel electrode (SCE) as the reference and a Pt wire as the counter. In all cases a scan rate of 0.1 V s^{-1} was employed. A CHI 760 C potentiostat was used for the experiments. For ASV experiments, the potential was held at the desired potential for 300 s, for deposition, in quiescent solution then turned off for 60 s before the linear sweep voltammogram, the strip, was started. The working electrode was cleaned on a polishing pad in alumina slurry then rinsed, polished on a wet polishing pad and then rinsed between each experiment.

5.3.3. Speciation modelling

The thermodynamic models to calculate the Pourbaix diagrams were done using Hydra Medusa databases and software for $100 \text{ }\mu\text{M Cu}^{2+}$ in water and in 0.1 M KCl , at $25 \text{ }^{\circ}\text{C}$. MINTEQA2 was used to calculate equilibrium speciation and to model the composition of solutions. Interactions and precipitation can be estimated from the results. A simple MINTEQA2 calculation was run to understand the effect of pH on possible Cu species in each solution at $25 \text{ }^{\circ}\text{C}$. These calculations are made based on the inputted species and concentrations, and their constants (stored in the MINTEQA2 database). All concentrations were the same as experiment, 0.1 M electrolyte (H_2SO_4 , KNO_3 and KCl) and $100 \text{ }\mu\text{M Cu}^{2+}$.

5.3.4. Electron Microscopy

After deposition, electrodes were gently rinsed with DI water by dipping in a full beaker and immediately stored in a vacuum desiccator until imaging took place (always within 24 hours of deposition). This greatly minimised the exposure of the samples to atmospheric oxygen and was considered sufficient to prevent oxidation of the material. A Zeiss Gemini FE-SEM, Warwick Microscopy Research Technology Platform, was used to collect data with the In Lens mode, accelerating voltages of $1.5 - 3 \text{ kV}$ and working distances of $1.4 - 2 \text{ mm}$. Electrodes were contacted to the stage by Cu tape connected to Cu wire, attached to the electrode.

5.4. Results and Discussion

5.4.1. Model Speciation of Copper

The composition of real solutions containing several different ions and neutral species can be complicated, especially when metals are involved. Here four different electrolyte anion systems are investigated whilst the cation is always K^+ these include; acetate acting as a buffer (CH_3COOH/CH_3COO^-), sulfate (SO_4^{2-}) i.e. dibasic complex anion, nitrate (NO_3^-) and chloride (Cl^-). Sulfate is a commonly used electrolyte that is often found in acid mine water in concentrations of around 0.06 M³⁶ and in environmental waters,³⁷ so it is important to understand its role and effects with respect to Cu electrodeposition. It is relatively electrochemically inert in the potential window of interest for Cu deposition and stripping, however, it can be oxidised before water electrolysis on BDD.³⁸ Some electrolytes such as nitrate and chloride are more reactive and are also frequently found in environmental³⁷ samples so understanding their effects is also important.

To understand the possible Cu species formed for Cu in acetate, sulfate and nitrate solutions, a Pourbaix diagram for 100 μM Cu^{2+} in water only was made using Hydra Medusa chemical equilibrium modelling software, see Figure 69 a). This is a good approximation for the acetate, sulfate and nitrate electrolyte systems which do not interact strongly with Cu^{2+} in solution.^{39–41} Figure 69 a) shows the most thermodynamically stable form of Cu for a given pH and potential. Figure 69 b) is a Pourbaix diagram for 100 μM Cu^{2+} in 0.1 M KCl. However, care must be taken when using Pourbaix diagrams to inform on dynamic electrochemical experiments, as they do not take into account mechanisms and reaction rates which drive chemical kinetics. Nevertheless, Figure 69 is a useful starting point and gives information about the possible states of Cu in the system, at different pHs and electrode potentials. Note, Figure 69 has been adjusted to the SCE reference electrode scale (used herein) and the green dotted lines indicate the solvent electrolysis reactions. The pink and green bands denote the pHs of interest (pH = 2 and 5) used in the following experiments.

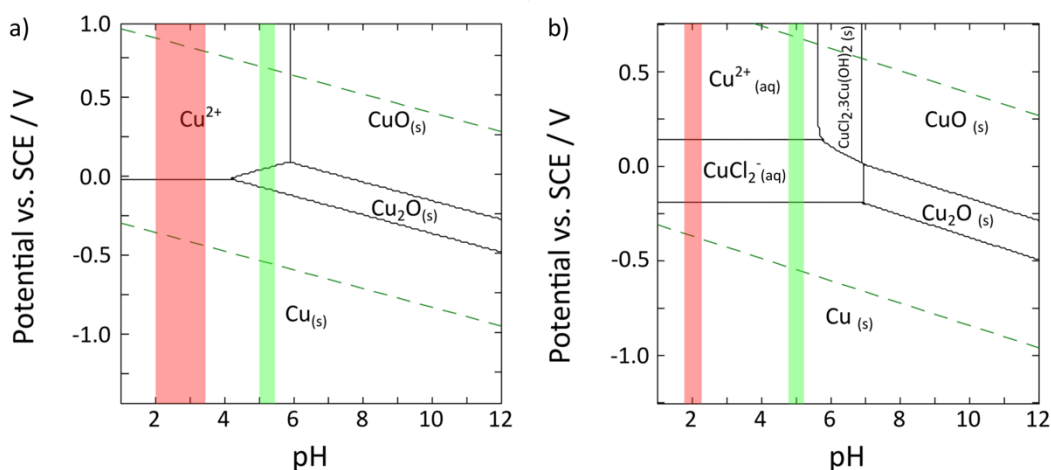


Figure 69 Pourbaix diagram of 100 μM Cu a) only in water b) in 0.1 M KCl, at 25 $^{\circ}\text{C}$ made using Hydra Medusa. The pink shaded area indicates the acidic pHs of interest in this experiment, and the green the higher pH of interest. The green dashed lines indicate where the solvent electrolysis reactions occur in this system.

Figure 69 a) shows, that below approximately pH 4.5, only Cu^0 and Cu^{2+} are expected to be present in the system. In this pH range, potentials above 0 vs SCE V, Cu^{2+} species (solvated by water and/or anions) are expected to be the species in solution. Upon initiation of deposition via application of a reductive potential sweep (from positive to negative) and for any pH value below 4.5, the direct reduction of Cu^{2+} to Cu^0 (Cu metal) would be expected (Equation 34) when only thermodynamics are considered. Upon reversing the potential, the reverse reaction is expected, i.e. the direct stripping of Cu^0 to Cu^{2+} , reflecting a simple electrodeposition (and the reverse, stripping reaction). E^0 values are vs SHE unless otherwise stated.



According to Figure 69 a), above approximately pH 4.5 there is the possibility of forming both Cu_2O and Cu^0 , however the proportions depend upon the applied potential, kinetic rates and solvation energies. At pH 6 and above, all forms of Cu are predicted to be solid (CuO , Cu_2O or Cu^0), and at intermediate pHs (4.5 to 6), Cu_2O is expected to form at potentials around 0 V.

Figure 69 b) for the chloride electrolyte, the diagram is more complicated, the simple reaction of Cu^{2+} ions reduction to metallic Cu as shown in Equation 34 does not occur for any pH or potential, instead Cu can form a Cu-chloride complex in solution. Between pH 6 and 7 a Cu-Cl-OH complex can be formed; these chloride complexes

are in addition to the Cu^{2+} , CuO , Cu_2O and Cu^0 formed in a). Chloride, unlike the other electrolyte systems explored herein has the ability to stabilise Cu^+ in solution, creating a more complex scheme of possible reactions and species. In general, in sulfate and nitrate solution, mostly hydrated Cu^{2+} species exist whilst in chloride solution Cu^{+2+} ions are complexed with chloride.

To understand solution composition better, speciation simulations were also run using MINTEQ, Figure 70, for the electrolyte systems under investigation herein in a) acetate, b) sulfate c) nitrate and d) chloride. These show the thermodynamically stable composition of a $100\ \mu\text{M}\ \text{Cu}^{2+}$ solution in $0.1\ \text{M}$ respective electrolyte solution over the pH range 1-12. In general, these agree with the Pourbaix diagrams in Figure 69, but now show the presence of electrolyte-Cu interactions (ligand type) i.e. Cu^{2+} as Cu_xL_y .

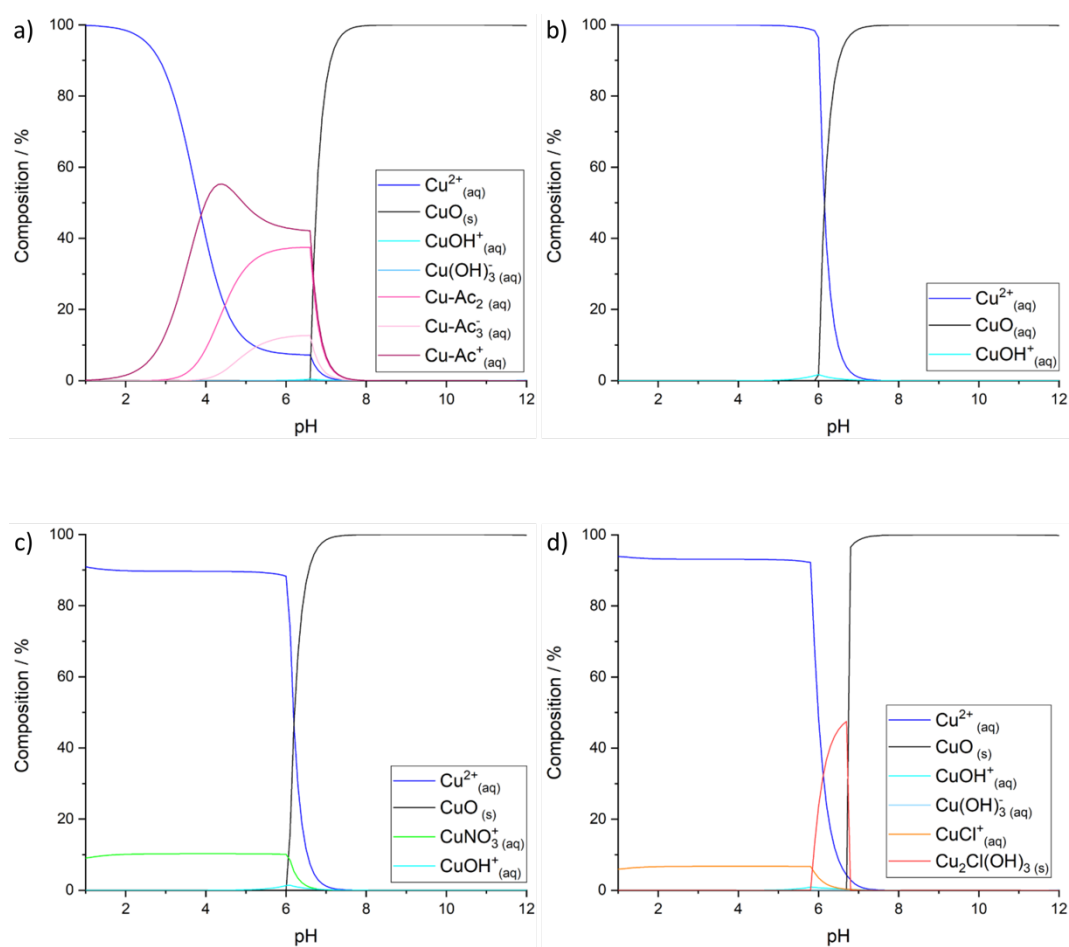


Figure 70 Speciation composition diagrams made using MINTEQ of $100\ \mu\text{M}\ \text{Cu}^{2+}$ in $0.1\ \text{M}$ a) acetate, b) sulfate c) nitrate and d) chloride at $25\ ^\circ\text{C}$ for pH 1 to 12.

MINEQ predicts formation of the thermodynamically most stable solid CuO species is expected to occur at $\text{pH} \geq 6-8$, with a slightly different onset pH for each electrolyte system. This solution precipitation process results in loss of available aqueous Cu^{2+} in the solution. Below this pH Cu^{2+} can exist in a variety of environments, depending on the extent of interaction with the anion of each electrolyte. Figure 70 a) indicates that acetate can complex with the Cu^{2+} to form three different species, it weakly interacts with the ion and is easily removed from the Cu^{2+} as pH decreases.^{40,42} Note that acetate is also a buffer, this is discussed further in the next section.

Sulfate is the simplest system with only 2 major constituents, Cu^{2+} free in solution (only H_2O solvation) or a Cu solid. There is a minor CuOH^+ contribution around neutral pH, but the important result is that the sulfate ion does not interact appreciably with Cu^{2+} in solution. In the nitrate system c) the nitrate ion interacts with a small proportion of the Cu^{2+} in solution forming CuNO_3^+ from pH 1-7, again, with only a small contribution of CuOH^+ . For chloride, d), the speciation of Cu^{2+} in solution looks similar to nitrate, there is a small proportion of Cu^{2+} associated with chloride at all pHs where precipitation is not occurring, and a negligible hydroxide complex contribution. In terms of possible solids, these models predict $\text{Cu}_2\text{Cl}(\text{OH})_3$ in addition to CuO which is different to other electrolyte systems investigated so far. Note that this does not estimate that any CuCl_2^- will exist, this agrees with the Pourbaix only if a potential more positive than 0.2 V is applied. Note also that only the Pourbaix predicts a Cu^+ species in solution. This shows that neither model can give a full description of the system.

These Pourbaix and speciation composition models aid in the understanding of the systems, but they do not fully explain them. The use of dynamic electrochemistry in real experiments means that the conditions can change rapidly and alter equilibria. Therefore, kinetic effects become more prevalent and real results can vary drastically from these models.

It is also important to appreciate that the most thermodynamically stable species may not be the species that is (initially) formed. For example, literature shows that

electrodeposition and solution precipitation of non-metallic Cu, typically initiated by working in alkaline solutions, rarely results in initial formation of CuO. Typically Cu₂O forms first, which is then converted into CuO over time.³⁴ Some research claims that it is actually Cu(OH)₂ that forms first, which is quickly converted into Cu₂O and then further oxidised over time to CuO.²⁸

Finally the reaction in Equation 34 does not provide information on whether two electrons are transferred at once, or if it is two successive, one electron transfer reactions, Equation 35 and Equation 36.^{43,44}

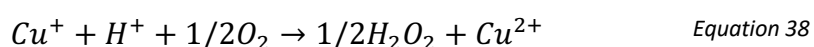


Research has suggested that Cu⁰ electrodeposition occurs in two steps,^{45–47} however they can be difficult to resolve, unless using appropriate conditions, such as chloride containing solutions.^{26,48} Also, there is the possibility of mixed electrochemical and chemical reactions, as discussed below.

When investigating Cu electrodeposition, it is important to not only consider electrochemical and chemical reaction pathways involving the species identified in the above models but also the role electrolysis of the electrolyte or dissolved oxygen plays. Reactions of interest, in addition to Equation 34, Equation 35 and Equation 36, are discussed below, written as reductions (for electron transfer processes) as per convention. Thermodynamic E^0 values are provided (quoted with respect to SHE, unless otherwise stated) where the information is known. The reactions in Equation 35 and Equation 36 are further complicated by a possible disproportionation reaction.^{49,50}

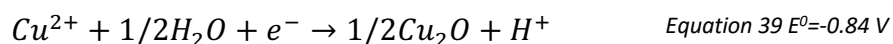


A chemical pathway for removal of Cu⁺ also exists in the presence of oxygen, Equation 38.

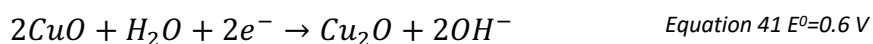
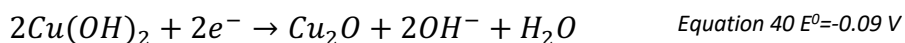


Under alkaline conditions, as discussed above, Cu is likely to directly electrodeposit in the form Cu₂O or Cu(OH)₂⁵¹ which could transition into the thermodynamically

more stable CuO.⁵² Cu₂O can also be formed via electrodeposition provided only one electron transfer takes place, Equation 39, this is expected to be the main pathway for the formation of Cu₂O.^{2,53}



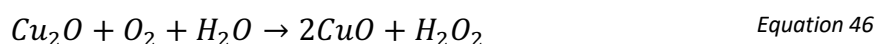
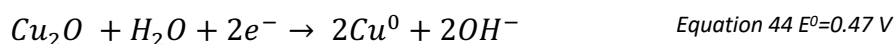
Note, Equation 39, is a combination of the one electron reduction of Cu²⁺ to Cu⁺ (Equation 35) and the subsequent reaction of Cu⁺ with H₂O (2Cu⁺ + 2H₂O → Cu₂O + 4H⁺).⁴⁷ Using the Nernst equation applied to Equation 39 E⁰ = -0.84 V, for a pH 5 solution and [Cu²⁺] = 1 × 10⁻⁴ M, the formal potential is -0.018 V (vs SCE).⁵⁴ As Cu₂O electrodeposition proceeds, the local pH decreases as H⁺ are produced (which will impact the formal potential), stabilising the Cu⁺ ion in solution.² Decreasing the pH increases the reversibility of the chemical reaction, allowing stable morphologies to form because of a dissolution and reprecipitation process.² Even in low pH solutions it has been reported that Cu₂O can electrodeposit simultaneously with Cu⁰ and that the proportion of Cu₂O is larger at lower overpotentials (low driving force).⁵⁵ The other electrochemical mechanisms for the formation of Cu₂O are Equation 40 and Equation 41 and require the presence of Cu(OH)₂ and/or CuO.^{53,56–58}

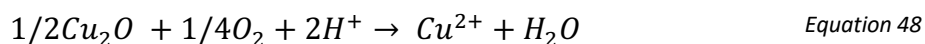


Cu₂O can also be formed chemically by dehydration of Cu hydroxide and oxidation of Cu⁰ in air, Equation 42 and Equation 43 respectively.^{34,59}

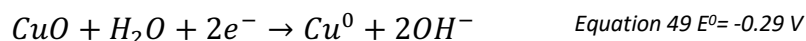


Reactions that result in loss of Cu₂O are also important to consider, such as its electrochemical reduction, Equation 44, its chemical oxidation (Equation 45 to Equation 47) and dissolution (Equation 48) in the presence of oxygen (chemical). Dissolution is facilitated in more acidic solutions.⁵³

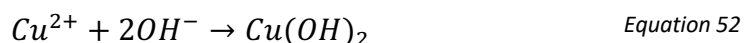




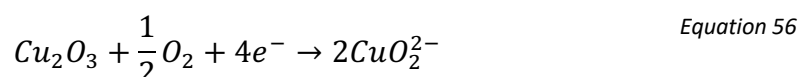
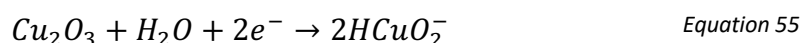
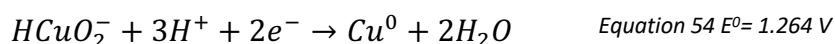
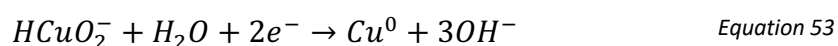
According to the Pourbaix diagram, there is also a possibility of forming CuO. Potential pathways for this are electrochemical oxidations of Cu⁰/Cu₂O in alkaline solutions, such as the reverse of Equation 41 and Equation 49, and chemical oxidations (Equation 45) and dehydration (Equation 50).



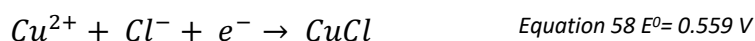
Cu hydroxides can be chemically formed via reactions with hydroxide ions, Equation 51 and Equation 52.



Other Cu oxides that appear in the literature are Cu₄O₃, CuO₂²⁻ and Cu₂O₃. Cu₄O₃ is a mixed oxide so can form with a combination of the aforementioned oxide formation reactions.¹⁵ CuO₂²⁻ can be formed by electrochemical oxidation from Cu⁰, (reverse of) Equation 53 and Equation 54. Cu₂O₃, whose existence is contentious, has several proposed reactions in the literature, Equation 55 and Equation 56.^{15,57}



Cu-chloride species are also expected to form. Electrochemical pathways include Equation 57 and Equation 58, and chemical ones are Equation 59 and Equation 60.⁹



Other important reactions to consider do not directly involve Cu, but other species in solution such as dissolved oxygen and electrolyte reactions. ORR can occur via a two

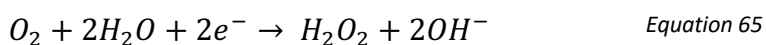
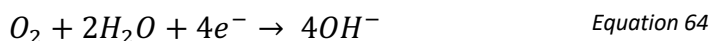
or four electron transfer mechanism. Under acidic conditions Equation 61 and Equation 62 apply.^{58,60}



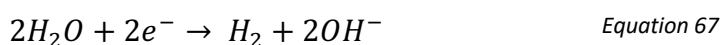
If the two electron transfer route is prominent, electrogenerated hydrogen peroxide (Equation 62) can react further to result in hydroxide ions (Equation 63), a process catalysed by the presence of Cu₂O/CuO.¹⁸ Interestingly ORR is thought to be inhibited by CuO whilst hydrogen peroxide reduction is inhibited by Cu⁰.^{18,20}



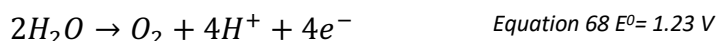
Literature on the ORR on Cu⁰ in acidic (0.5 M, pH 0) sulfate electrolyte found that it follows a 2e⁻ pathway at -0.05 to -0.2 V, a mixed pathway -0.2 to -0.4 V and a 4e⁻ pathway -0.4 to -0.5 V (vs SCE).⁶⁰ Both processes result in a local depletion of H⁺. The reactions are slightly different in neutral pH, Equation 64 and Equation 65, but are still 2e⁻ or 4e⁻ pathways.



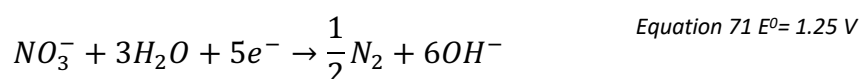
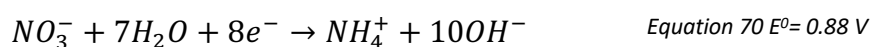
The hydrogen evolution reaction (HER) occurs at the negative extremes of the solvent/electrolyte window and also contributes to pH change, the reaction is pH dependent, Equation 66 occurs in acidic solutions and Equation 67 in neutral solutions.⁶¹



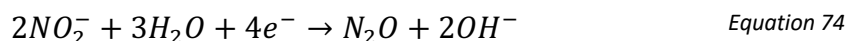
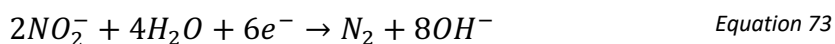
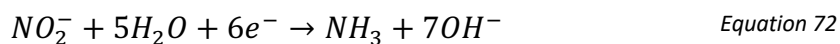
At the positive end of the solvent window water oxidation occurs, via Equation 68.



Nitrate undergoes NRR. Several equations are proposed, all resulting in the production of hydroxide ions, Equation 69, Equation 70 and Equation 71.^{7,62}

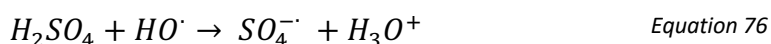
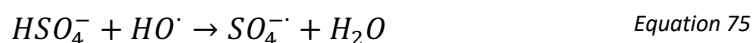


Equation 69 shows nitrite is also a possible product of NRR, which itself can undergo electrochemical reduction (Equation 72, Equation 73 and Equation 74) again forming hydroxide ions.^{63,64}



Several other further reactions of NRR products are also possible such as the conversion of nitrite to NO in acidic media,⁷ hence the complexity of the NRR process should not be underestimated. NRR is also catalysed by Cu⁰ and is surface and pH dependent.⁷ Note, the Cu⁰ surface can be deactivated towards NRR via an adsorbed layer of H atoms from HER,^{7,63} or by NRR products such as nitrite.⁶³ Of importance to this work is the production of hydroxides via electrolysis of the electrolyte anion (nitrate), a process not present in sulfate or chloride media. Also there have been reports of nitrates in solution oxidising deposited Cu⁰, which could result in less Cu⁰ being present on the electrode surface in nitrate electrolyte.⁴⁹

Sulfate can be oxidised at potentials below that for water oxidation on BDD,³⁸ Equation 75 to Equation 77.



5.4.2. Electrochemistry of Cu in acetate buffer solution

For techniques such as ASV, pH adjustment and/or buffers are often added to solutions to improve the stripping response. This works in two ways; firstly, buffers such as acetate have a weak binding interaction with metal ions and are thus labile complexes.^{40,65} This can improve the homogeneity of deposits, thereby improving the stripping response, as varying Cu⁰ deposit morphologies can result in a range of energies (electrode potentials) for stripping and broader or multiple peaks in ASV.⁶⁶ Secondly, the buffer prevents local pH changes resulting from possible interfering

electrochemical reactions (such as ORR, water reduction, anion reduction or HER as discussed in 5.4.1, Equation 61, Equation 62, Equation 64 to Equation 67, Equation 69 to Equation 71). In this way, buffers mitigate (up to a point) a local change in pH that could result in precipitation of $\text{Cu}_x\text{O}/\text{CuO}$ or hydroxide compounds (Equation 51 and Equation 52). Keeping the pH low also encourages free metal ions in solution, the proportion of free Cu^{2+} in solution generally increases with decreasing pH as shown in Figure 69 and Figure 70. Low pH also reduces the effects of the hydroxide generating electrochemical reactions, Equation 63 to Equation 65, Equation 67, Equation 69 to Equation 74. The addition of buffer or acid does however inherently alter the solution pH and composition/equilibria. This is problematic when the concentration of free aqueous Cu^{2+} in the real environmental system is desired. It is thus desirable to choose buffer systems as close to the real pH as possible.⁴

For buffered solution studies, firstly, the electrochemistry of 100 μM CuSO_4 in 0.1 M acetate buffer was considered. Figure 71 shows cyclic voltammograms (CVs) in two acetate buffer solutions pH 3.6 (pink) and 5 (green) from 0 V to -2.5 V and then out to +2.5 V, at a scan rate of 0.1 V s^{-1} , in aerated and deoxygenated (by bubbling with nitrogen gas) solutions. The concentration of oxygen in quiescent solutions is around 0.2 mM.⁶⁷ The pH at 3.6 is such that Cu is in mostly the Cu^{2+} (or Cu-Acetate⁺) form making deposition unlikely to go through an oxide state according to the Pourbaix and speciation composition models. In real world applications, the pH of the sample water source is often not as acidic as pH 3.6. To investigate the behaviour in more realistic conditions, experiments were also carried out in pH 5, as it is the highest pH possible without significant risk of chemical precipitation according to the thermodynamic models (Figure 69 and Figure 70). Cu^{2+} is mostly expected to be in one of the acetate complexes in the conditions used for Figure 70.

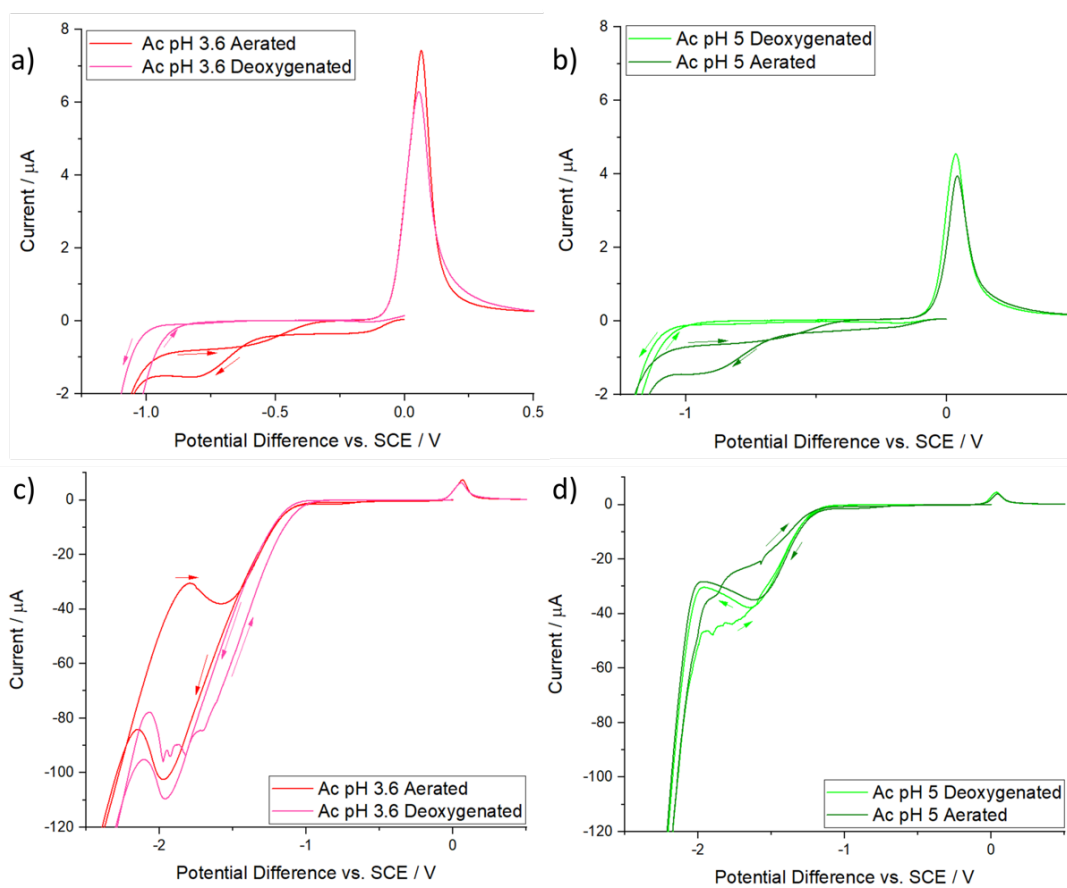


Figure 71 CV of $100\ \mu\text{M}\ \text{Cu}^{2+}$ in $0.1\ \text{M}$ acetate buffer, a) pH 3.6, b) pH 5 with c) extended window of a), and d) extended window of b), on a $1\ \text{mm}$ BDD macrodisk electrode, $0.1\ \text{V s}^{-1}$ starting at $0\ \text{V}$ in the negative direction to $-2.5\ \text{V}$ where the scan direction was reversed. All scans shown are the first scan.

A well-defined anodic $\text{Cu}^0 \rightarrow \text{Cu}^{2+}$ stripping peak was observed at $+0.1\ \text{V}$ for both pH 3.6, pH 5, aerated and deoxygenated solutions (Figure 71). The stripping peak current for pH 3.6, Figure 71 c), is larger than for pH 5, Figure 71 d), indicating that more Cu^0 was electrodeposited at the lower pH. At this concentration ($100\ \mu\text{M}$) the cathodic response associated with Cu^0 deposition is not obvious. From the Pourbaix diagram, it is expected to occur at potentials between 0 to $-0.2\ \text{V}$ vs SCE for Cu^{2+} on Cu^0 . Cu^{2+} reduction on BDD is expected to be kinetically retarded compared to Cu^{2+} on Cu^0 ,⁶⁸ and so is likely to occur at more negative potentials.

In the presence of oxygen there are clear waves associated with ORR on Cu deposits. The ORR onset occurs between -0.05 and $-0.5\ \text{V}$ vs SCE on Cu^0 in acidic solutions according to literature.⁶⁰ There are two waves associated with oxygen in these CVs, indicating a possible change in mechanism from the 2e^- to the 4e^- pathway as a function of potential (Equation 61, Equation 62 and Equation 64, Equation 65).

Furthermore, the crossover observed in the CV is indicative of a nucleation and growth mechanism.⁶⁹ By showing the CV response over the full potential range (Figure 71 c) and d)), the peak at -2 V in Figure 71 a) is most likely the HER reaction, from proton reduction. This peak has reduced significantly in d) compared to c) as expected for an increase in solution pH.

The buffer used here is 0.1 M acetate, the buffer capacity of the pH 3.6 and pH 5 solutions are slightly different, see Figure 72, where the buffer capacity has been calculated across the pH range 1-12.⁷⁰ This shows that at pH 5 approximately 0.055 moles of acid (or base) can be added per litre of buffer before a pH change of 1 unit will occur, whilst for pH 3.6 it is 0.015 moles. However, during the CV especially when pushing out into HER and water reduction, which results in proton depletion and hydroxide formation respectively (Equation 66 and Equation 67), it is possible that the buffer capacity could be exceeded. For example, in unbuffered solutions, it was shown that the interfacial pH increased from 7 to 10 in NaClO₄ due to ORR, during a CV of Cu⁰ reduction on a rotating ring disk electrode.⁷¹ Furthermore, for pH 5 the buffer capacity drops rapidly with increasing pH. This may explain why slightly less Cu⁰ is electrodeposited at pH 5 than at pH 3.5 (from the Cu⁰ stripping peak).

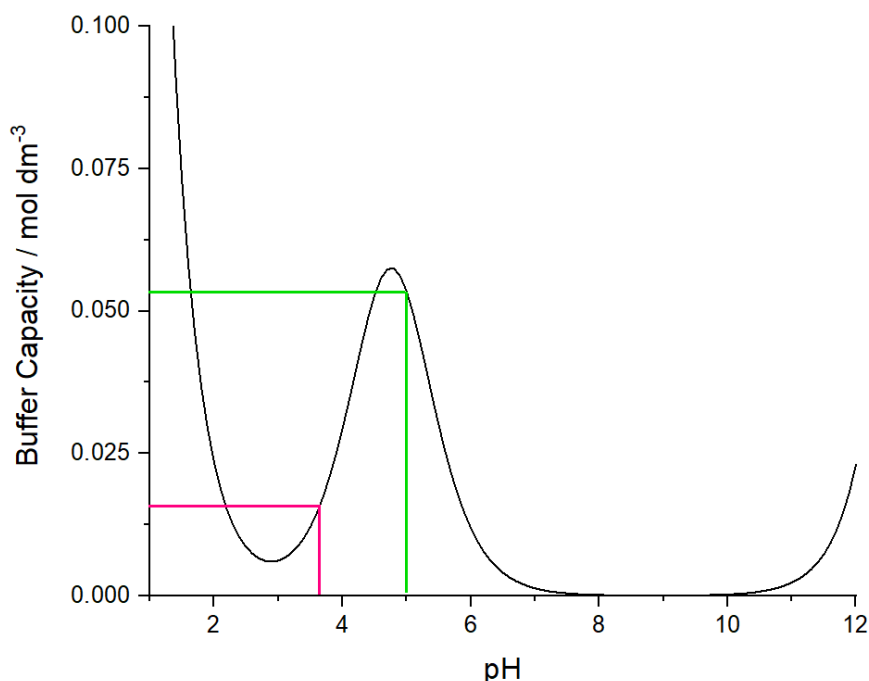


Figure 72 Change in buffer capacity with respect to pH of a 0.1 M acetate buffer solution ($pK_a=4.76$), pink line denotes pH 3.6 and the green line denotes pH 5.

5.4.3. Electrochemistry of Cu in low pH electrolyte solutions

Figure 73 shows CVs highlighting the background electrolyte response of the three electrolytes, sulfate, nitrate and chloride at 0.1 M concentration at a scan rate of 0.1 V s^{-1} , at a BDD electrode. This enables background electrolyte peaks on BDD to be excluded from the Cu responses detailed below.

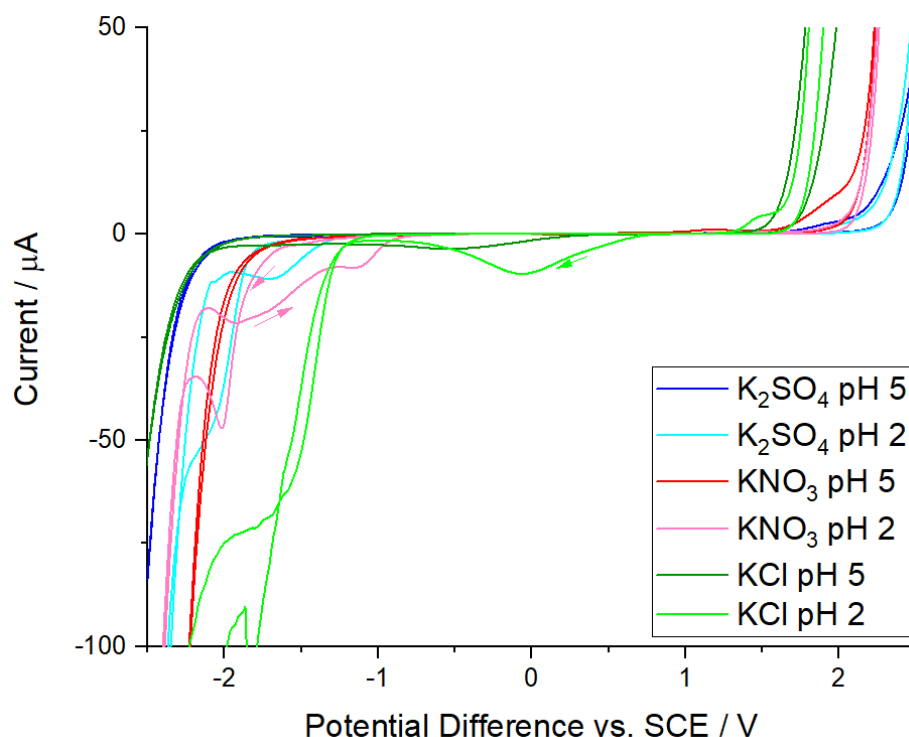


Figure 73 Background CVs of pH 2 and pH 5 in 0.1 M, K_2SO_4 , KNO_3 and KCl , using a 1 mm BDD macrodisk electrode, 0.1 V s^{-1} starting at 0 V in the negative direction to -2.5 V where the scan direction was reversed.

Figure 74 shows the CV characteristics for Cu deposition and stripping in unbuffered pH 2 a) sulfate, b) nitrate and c) chloride solutions under both aerated and deoxygenated conditions. The potential was scanned from 0 V to -2.5 V and returned. The top row of figures shows the regions of interest for deposition/stripping and the bottom shows the extended windows to show the side reactions/deposition, such as HER. pH 2 was chosen as Cu is predominantly in the free Cu^{2+} form for these electrolytes and is a common pH for acidified ASV methods.⁶⁵

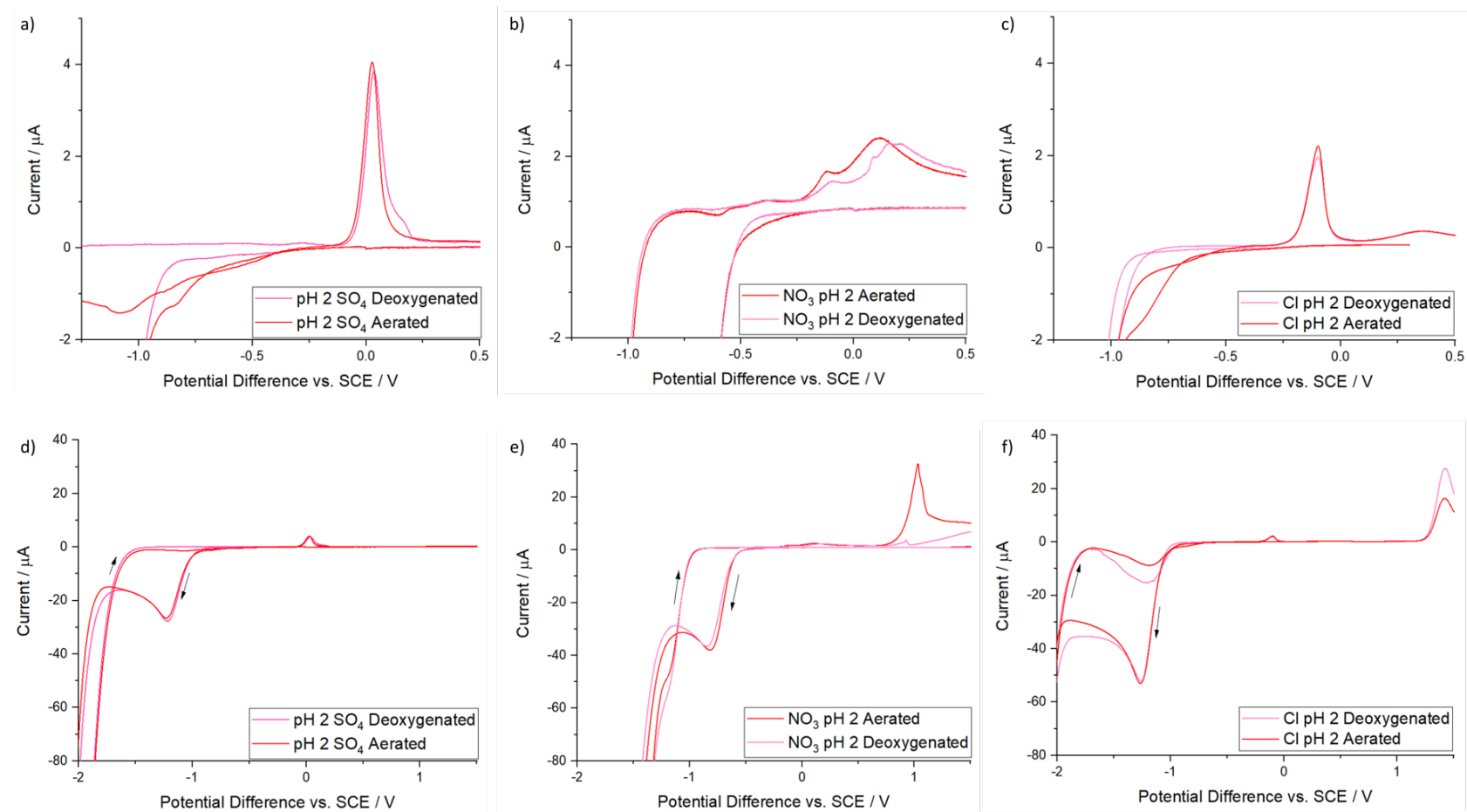


Figure 74 CVs of $100 \mu\text{M Cu}^{2+}$ in pH 2 with background electrolyte consisting of 0.1 M a) K_2SO_4 , b) KNO_3 , c) KCl , using 1 mm BDD macrodisk electrode, 0.1 V s^{-1} starting at 0 V in the negative direction to -2.5 V where the scan direction was reversed. The respective regions of interest are shown for each CV; d) K_2SO_4 , e) KNO_3 and f) KCl .

For individual electrolytes, the stripping peaks show similar currents, when comparing deoxygenated and aerated solutions for the same electrolyte, indicating comparable amounts of Cu are being stripped from the surface irrespective of dissolved oxygen. Comparing electrolytes against each other, sulfate media shows the largest stripping peak current but is only about half that obtained in the acetate buffer. Chloride and nitrate have similar current magnitudes, but more charge is passed under the broader ASV signal in nitrate media.

Unlike acetate and sulfate, for nitrate there is a much smaller, less well-defined stripping peak, for both aerated and deoxygenated solutions; the peak is a combination of a peak at ≈ -0.1 V, which appears as a shoulder on a broader peak on the more positive side. This broad peak is shifted slightly negative and is higher in current in deoxygenated compared to aerated. The broadness of the peak could indicate a wider range of Cu morphologies on the surface of the electrode, than for sulfate, and even the presence of non-metallic Cu species. There is also a large anodic peak in aerated nitrate solution, at much more positive stripping potentials, here around +1 V, in Figure 74 e) that is not present in the sulfate. We speculate this is due to oxidation of a non-metallic Cu species in Cu^+ form such as Cu_2O , CuOH or $\text{Cu}(\text{OH})_2$. A stripping-like feature at high positive potentials is also observed in chloride media at 1.4 V which could be due to a Cu-chloride species, or another oxidation/reaction of non-metallic Cu.

Overall, the process of Cu^{2+} to Cu electrodeposition is less efficient in these three solutions compared to acetate, governed by the magnitude of the stripping peak, attributed to the contribution of other chemical and electrochemical pathways becoming prominent and resulting in the formation of non-metallic Cu. The situation is most pronounced in nitrate solutions, suggesting the contribution played by NRR in generating a local alkaline environment and locally increasing pH to promote formation of Cu^+ and Cu^{2+} oxides/hydroxides is highly significant, even in this acidic environment.

CVs can be complex to interpret as the electrode surface and deposits are exposed to varying potentials. Whilst deoxygenation can help assess the impact ORR has on the electrodeposition and stripping mechanism, it is also important to investigate the impact of deposition potential. Figure 75 shows the stripping ASV characteristics only, in pH 2 aerated a) sulfate b) nitrate and c) chloride solution (and their respective deoxygenated runs d), e) and f)), where deposition ($100\text{ }\mu\text{M Cu}^{2+}$) was undertaken at fixed deposition potentials of 0, -0.2, -0.4, -0.6, -0.8, -1 and -2 V for a time period of 300 s in quiescent solution.

Figure 75 a) shows the ASV for sulfate in aerated pH 2 solution. For all deposition potentials more negative than 0 V a well-defined single peak is seen at approximately 0.05 V. The peak current magnitude (and charge under the peak) is generally increasing with an increasing negative deposition potential (increasing overpotential) as expected. The exception to the trend being deposition potentials of -0.8 V and -1 V (-0.8 V gave a higher peak than -1 V). For nitrate and chloride electrolytes conditions (b-f) and sulfate deoxygenated, whilst this peak is still evident, other features are present at higher oxidative potentials.

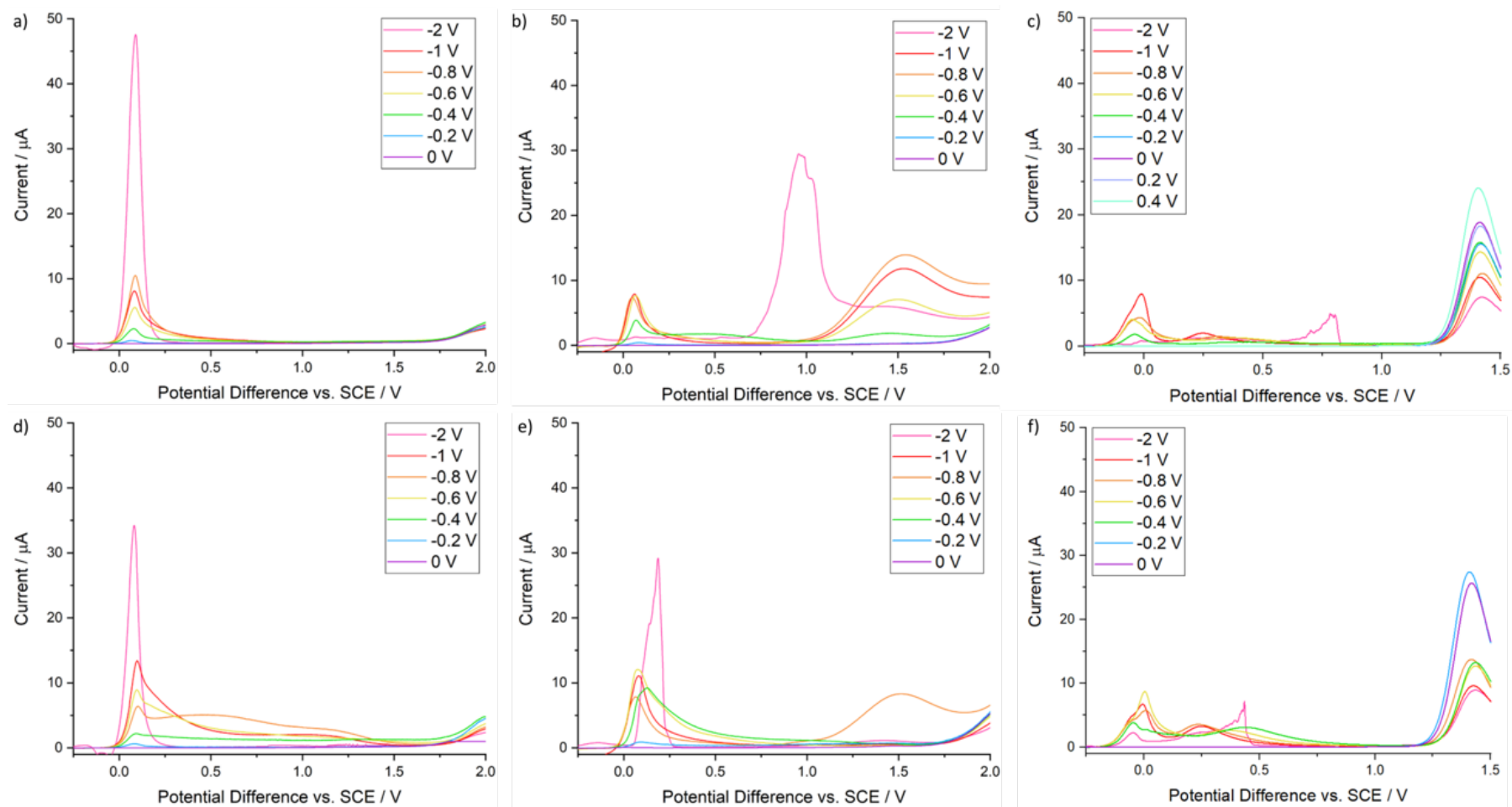


Figure 75 ASV stripping voltammograms of $100\ \mu\text{M}\ \text{Cu}^{2+}$ in pH 2, 0.1 M respective background electrolyte aerated a) K_2SO_4 , b) KNO_3 , c) KCl , and deoxygenated d) K_2SO_4 , e) KNO_3 , f) KCl , 1 mm BDD macrodisk electrode, $0.1\ \text{V s}^{-1}$, after 300 s deposition in quiescent solution.

In sulfate, there will be a competition between the driving potential for Cu^0 and Cu_2O electrodeposition (the larger the overpotential the more Cu^0 is likely to be deposited on the surface) and additional effects from local pH increases due to either ORR or HER. The latter resulting preferentially in the formation of Cu_2O , CuO or Cu hydroxide on the surface,⁷² depending on the starting pH of the solution. From Figure 74 it can be seen that HER commences at around -0.8 V vs SCE. At -2 V, given the huge increase in electron transfer kinetics for Cu^0 electrodeposition (dependence on overpotential⁷³), Cu^0 electrodeposition is seen to be winning out over formation of other non-metallic Cu species. Furthermore, Equation 44 suggests that thermodynamically Cu_2O can be converted to Cu^0 on the electrode surface if the potential is sufficiently negative. Cu_2O reduction to Cu^0 is utilised in the CO_2 reduction reaction literature to create active catalytic surfaces.^{74,75}

Interestingly under deoxygenated sulfate conditions, Figure 75 d), whilst the peak height is still generally scaling with electrode potential (exception of -0.6 V and -0.8 V, probably also due to HER pH changes), it is a deposition potential of -2 V that provides the most well-defined Cu^0 stripping peak. All others in d) show a large tail over a large positive potential range. The peak currents are also lower than in the aerated solutions. One possibility is that oxygen leads to the formation of Cu^{2+} from Cu_2O due to a chemical dissolution pathway (Equation 48)^{17,53} and promotes formation of CuO (Equation 45 to Equation 47) which can itself be electrochemically reduced to Cu (Equation 49). The tails at more positive potentials for the deoxygenated experiment are likely caused by the incomplete stripping of Cu^0 that instead electrochemically oxidises in a non-stripping mechanism,⁷⁶ resulting in several oxidative processes and broad stripping peaks.

For the nitrate experiments, focusing on the Cu stripping peak (+0.05 V), in aerated solution, b), the peak current increases with increasingly negative deposition potentials until -0.6 V, -0.8 V and -1 V where it appears to plateau, then at -2 V no stripping peak is seen. This is in stark contrast to the aerated sulfate data in Figure 75 a) and highlights the role NRR (Equation 69 to Equation 71) must be playing in increasing the local pH, above that from ORR and HER, such that there is no metallic

Cu^0 on the surface to oxidatively remove. The slight shifting in potential is likely due to different morphologies being present. Other notable features at 1 V and 1.5 V are likely oxidations of the non-metallic Cu species on the surface, perhaps Cu_2O to $\text{Cu}(\text{OH})_2$ (Equation 40) Cu_2O to CuO (Equation 41) for 1 V or duplex layer formation for 1.5 V.^{15,17}

The deoxygenated nitrate experiment, e), shows stripping peaks at 0.05 V for deposition potentials -0.2 to -1 V as for the aerated but the peak height does not increase with increasing negative deposition potential. Generally, these peaks were higher in deoxygenated than in aerated, possibly as a result of no ORR induced local pH changes. Interestingly, in contrast to the aerated data, a stripping peak is now present for a -2 V deposition potential for deoxygenated but shifted slightly positive. The peak also does not take the form of a typical stripping peak seen in other experiments. It is unclear whether this indicates Cu^0 or a non-metallic Cu species.

ASV data for the chloride system for aerated, c), and deoxygenated, f), solutions are more similar to nitrate than may have been expected from the CVs in Figure 74. Experiments showed that the results for both aerated and deoxygenated solutions were also very similar, demonstrating that again ORR had little effect, except at the higher deposition potentials. This could mean that the interfacial pH did not get high enough to cause significant effects until the HER onset, or the chloride ion could compete with oxygen for available surface sites on the deposited Cu, reducing the effect of the ORR.

In the aerated chloride experiment, c) $\text{Cu}^0 \rightarrow \text{Cu}^+$ stripping peaks⁴⁸ are seen for deposition potentials in the range -0.4 to -1 V, as chloride stabilises the Cu^+ ion. The peaks generally increase in size with increasing negative deposition potential and are broad. No peaks are observed for -0.2 V which suggests this is not a sufficient potential for deposition in chloride media. All negative deposition potentials have some small features around 0.2 to 0.5 V, which possibly indicates $\text{Cu}^+ \rightarrow \text{Cu}^{2+}$.⁴⁸ However, the -2 V deposition potential also has a peak at 0.75 V indicating possibly Cu_2O or Cu-chloride-hydroxide, if the interfacial pH has increased sufficiently enough.

A large oxidative peak, which appears stripping-like exists at 1.4 V which interestingly decreases in size as the deposition potential is made more negative. It appears in a similar position to that obtained for Cu^{2+} deposition and stripping in nitrate media but is less broad.

In the deoxygenated experiment, f), $\text{Cu}^0 \rightarrow \text{Cu}^+$ stripping peaks are seen for all potentials more negative than -0.2 V; these appear to have shoulders and may be indicative of different morphology deposits on the surface. Again, features can be seen around 0.2-0.5 V which are associated with $\text{Cu}^+ \rightarrow \text{Cu}^{2+}$. The 1.4 V feature is also present and decreases in size as deposition potential is made more negative.

5.4.4. SEM of Cu deposits formed in pH 2 sulfate, nitrate and chloride solutions

SEM was employed to examine the morphology of the deposits formed on the surface under the same deposition conditions in Figure 75 for potentials of -0.4, -1 and -2 V, in aerated and deoxygenated sulfate, nitrate and chloride solutions. These potentials were chosen because at -0.4 V this signifies the onset of ORR, -1 V relates to high overpotential ORR and the onset of HER whilst - 2 V is high overpotential ORR and HER. Attempts were made to confirm the chemical identity of the Cu species electrodeposited on the BDD electrode in this work, none except TEM (Chapter 6) were successful. The SEM was equipped with an EDX system, spot resolution approximately 1 μm . Maps, point spectra and several different accelerating voltages were investigated but as the amount of deposited material was so small and O is present on the surface of the oxygen terminated BDD the spectra were not conclusive in differentiating between Cu, CuO and Cu_2O etc. X-ray photoelectron spectroscopy (XPS) was also attempted, but again due to the spot size (1 μm), small amount of material and background of oxygen-terminated BDD, results were inconclusive. X-ray diffraction (XRD) was also investigated, both regular and grazing angle but this suffered the same result as EDX and XPS, the BDD background was complicated as it is a polycrystalline solid and so extraction of the sample signal from this was not possible.

Raman spectroscopy had limited success, as the spot size (circa. 600 nm) was too large to interrogate individual particles, longer deposition times (900 s) were therefore required to increase coverage but in many cases the signals were still too small. Raman peaks for Cu_2O (at 150, 220, 415, 520 and 630 cm^{-1} ⁷⁷) were seen for electrodepositions in sulfate and nitrate media, including in deoxygenated conditions. Figure 76 is an example of one of the more successful spectra, collected from a deoxygenated sulfate deposition (100 μM Cu^{2+} , 0.1 M K_2SO_4 pH 5). For this a Horiba LabRam HR Evolution was used with a 488 nm laser and SWIFT XS, EMCCD (400 nm \rightarrow 1100 nm) detector.

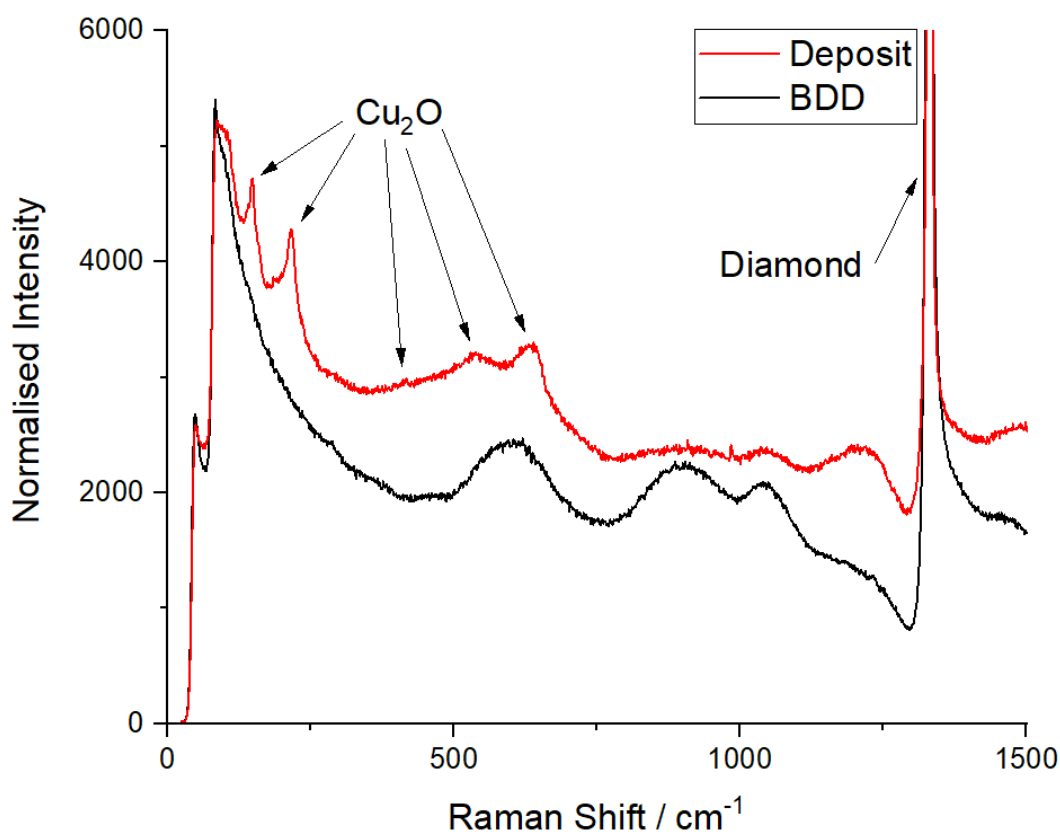


Figure 76 Raman spectra of bare BDD (background) and of deposits on BDD surface after electrodeposition at -0.4 V for 900s in 100 μM Cu^{2+} , 0.1 M K_2SO_4 pH 5 deoxygenated. Cu_2O peaks and the diamond Fano peak are seen. 100x objective lens, 488 nm laser at 10% power, 10 s acquisition time, 5 accumulations.

Raman however cannot detect Cu^0 and backgrounds on different BDD grains varied, making appropriate background subtractions difficult. Results from these experiments were neither quantitative nor conclusive. However, they were enough

to suggest that Cu_2O is formed in several conditions and does not require the presence of dissolved oxygen.⁵⁵

Figure 77 shows the SEM results for the sulfate system, a) aerated and b) deoxygenated at different deposition potentials for a time of 300 s, which is the same time as the ASVs in Figure 75. These are representative images of deposits formed on the BDD surface. The shape of an electrodeposited material is controlled by many factors including deposition overpotential, time, electrolyte and solvent adsorption, mass transport. Adsorption events will also influence the surface energies of different crystal faces which in turn will determine their respective rates of growth, as well as blocking potential catalytic sites for ORR and HER. It is thus not surprising Cu deposition morphology has been found to be pH and solvent dependent.^{2,78}

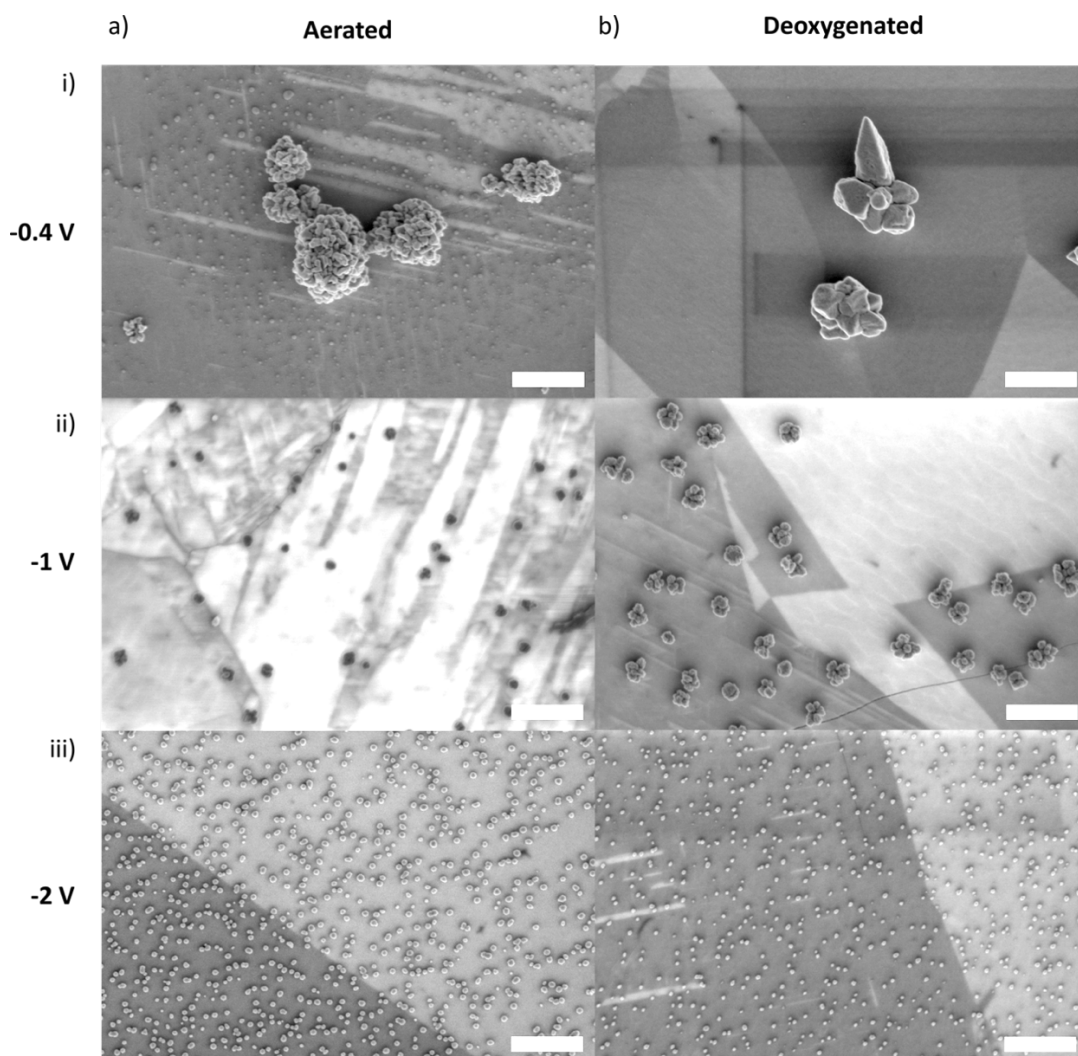


Figure 77 FE-SEM images of BDD electrode surfaces after deposition for 300 s in $100\ \mu\text{M}\ \text{Cu}^{2+}$, pH 2 ($0.1\ \text{M}\ \text{K}_2\text{SO}_4$), aerated solution a) and deoxygenated b) at i) $-0.4\ \text{V}$, ii) $-1\ \text{V}$ and iii) $-2\ \text{V}$. Scale bar 400 nm.

For the aerated sulfate -0.4 V image a) i), two different morphology deposits are distinct, large (low density) amorphous type deposits hundreds of nm in size and smaller nanoparticles (NPs) tens of nm in size (higher density). Increasing deposition potential results in the formation of small NPs (tens of nm in size) at low density, whilst at -2 V the particle density has increased resulting in a fairly uniform coverage of NPs, approx. 50 nm in size. Under deoxygenated conditions a similar pattern is seen except at -0.4 V the deposits appear more crystalline in morphology and much larger in size (100-200 nm). NP sizes of around 100 nm and 40 nm are observed for the -1 V and -2 V deposition conditions respectively. An increasing number density is expected as the overpotential is increased.²

Figure 78 shows SEM images of the deposits from nitrate pH 2 solutions, a) aerated and b) deoxygenated.

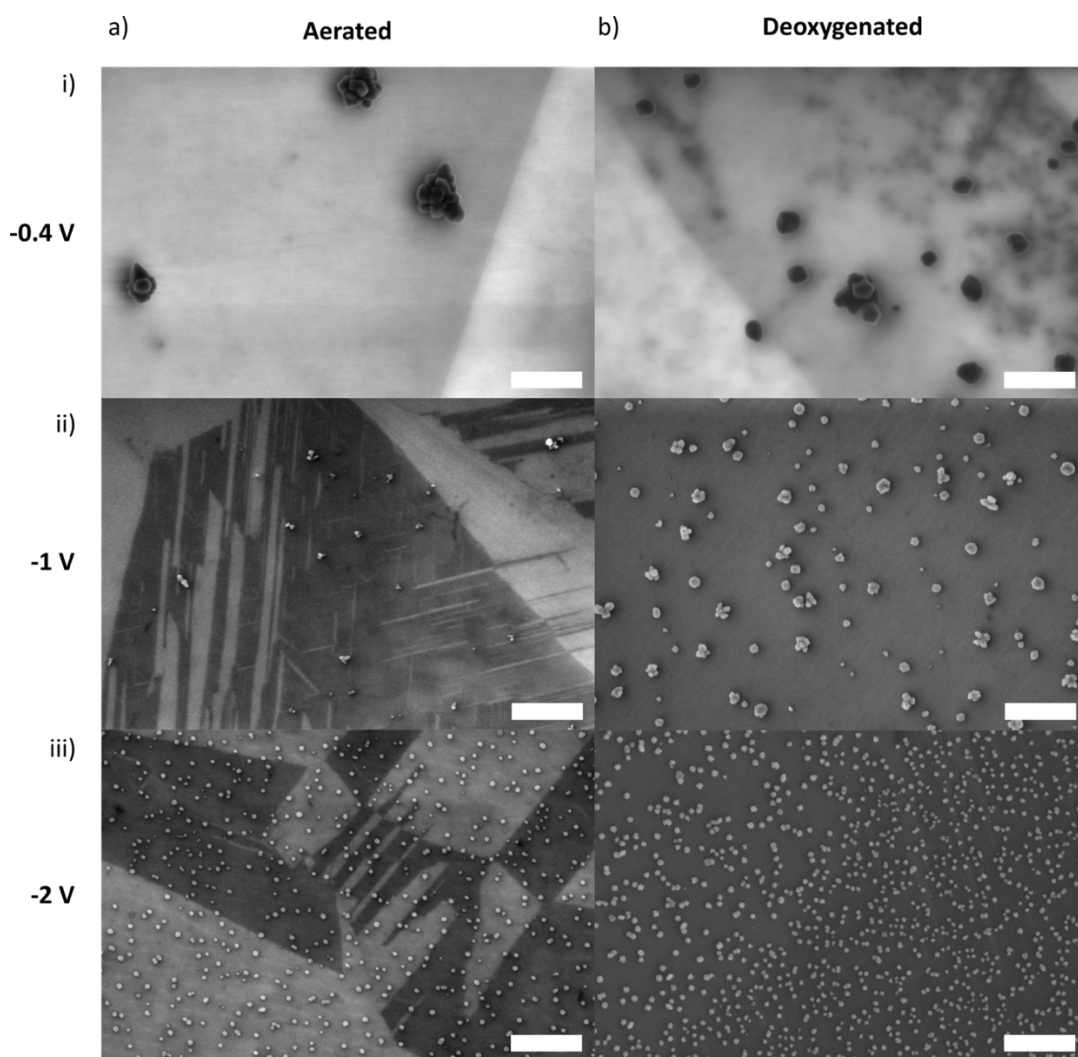


Figure 78 FE-SEM images of BDD electrode surfaces after deposition for 300 s in 100 μM Cu^{2+} (pH 2, 0.1 M KNO_3) aerated solution a) and deoxygenated b) at i) -0.4 V, ii) -1 V and iii) -2 V. Scale bar is 400 nm.

At -0.4 V aerated, a) i), NPs approx. 200 nm in size are obtained, whilst at -1 V the particle size has decreased to approx. 20-30 nm. With an increased overpotential, deposition potential of -2 V, the number density is visibly increased, and NPs of size approx. 30 nm are produced. Note that there was no Cu stripping peak for nitrate aerated at a deposition potential -2 V, so these deposits must be predominantly non-metallic Cu species. In the deoxygenated experiments, NPs of approx. 100-200 nm, 50-100 nm and 20-40 nm are found, for -0.4, -1 and -2 V respectively, the size decreasing and number density increasing with overpotential.

Figure 79 shows SEM images of the deposits from chloride pH 2 solutions, a) aerated and b) deoxygenated.

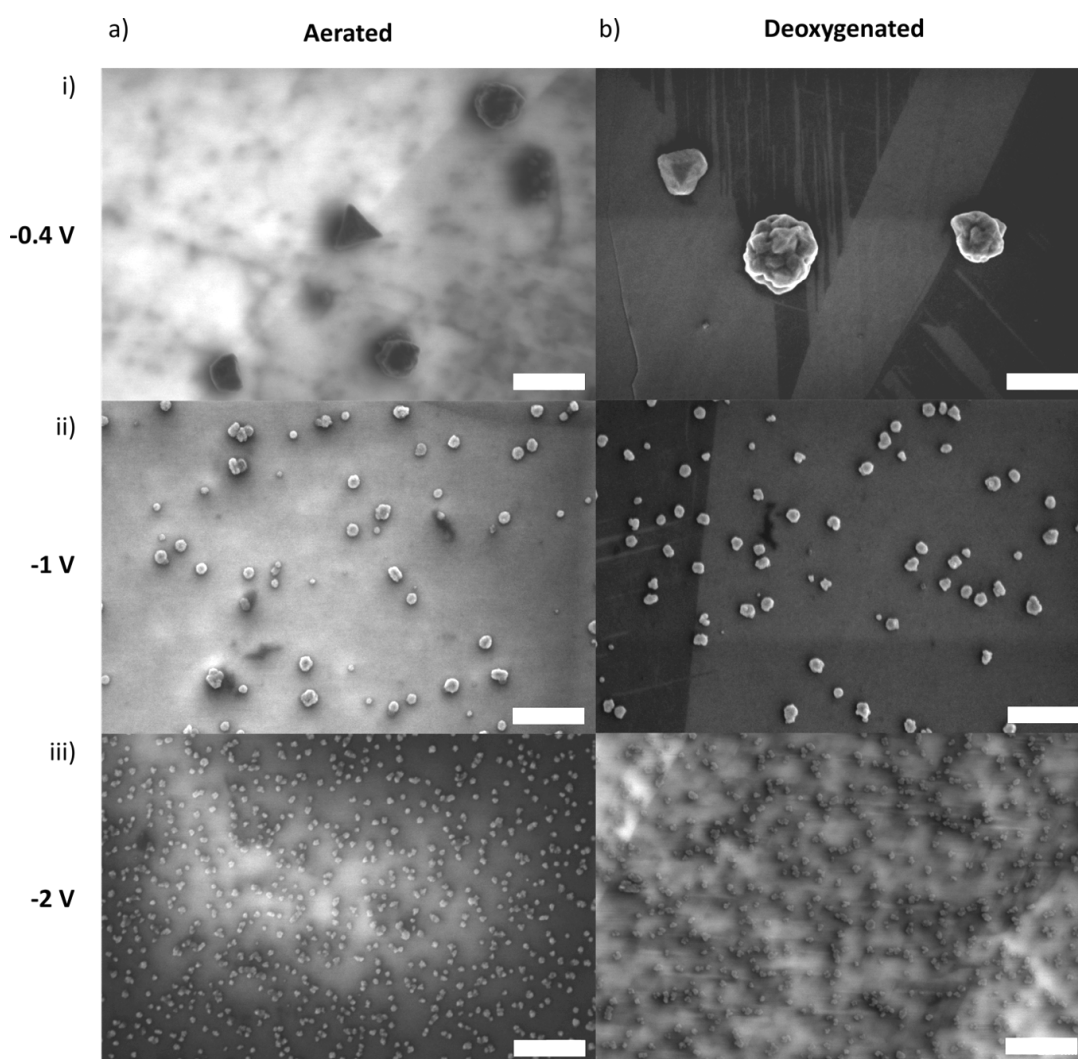


Figure 79 FE-SEM images of BDD electrode surfaces after deposition for 300 s in 100 μM Cu^{2+} (pH 2, 0.1 M KCl) aerated solution a) and deoxygenated b) at i) -0.4 V, ii) -1 V and iii) -2 V. Scale bar is 400 nm.

NPs formed under -0.4 V conditions, a) i) and b) i), are of two morphologies, one amorphous and one triangular based with particle sizes around 200-400 nm. -1 V for both aerated and deoxygenated gives NPs around 50-100 nm in size and -2 V produced NPs around 20-40 nm with a high number density.

For some of these experiments, especially at lower overpotential a grain dependence in the deposits was observed, for example preferential deposition on darker grains, or deposits being smaller and more numerous on darker grains than lighter ones. As the BDD is grown, different crystal faces take up different amounts of boron leading to a variation in conductivity of different grains on the electrode. Darker, more highly doped grains are more conducting and so will have a lower resistance, meaning the effective potential on these grains will be higher than on light, lower conductivity grains. This matches observations, as higher potentials (negative in this case) have been shown to result in more nucleation and a higher number density and smaller particles.^{79,80}

5.4.5. Electrochemistry of Cu in pH 5 electrolyte solutions

In real world applications, the pH of the sample water source is not often as acidic as pH 2. To investigate the deposition and stripping behaviour in electrolyte solutions, more realistic experiments were carried out in pH 5 (unbuffered), as it is the highest pH possible without significant risk of chemical precipitation according to the Pourbaix diagram (Figure 69). Under these conditions, ORR, HER and NRR induced local pH changes are all expected to play a much greater role than at lower pH, due to the reduced concentration of protons initially present. Figure 80 shows 100 μM Cu^{2+} CVs in a) sulfate, b) nitrate and c) chloride solutions at pH 5 using a scan rate of 0.1 V s^{-1} . Figure 80 will be contrasted with Figure 71 (acetate buffered) and low pH data (Figure 74) to highlight the differences between buffered and unbuffered CVs and pH.

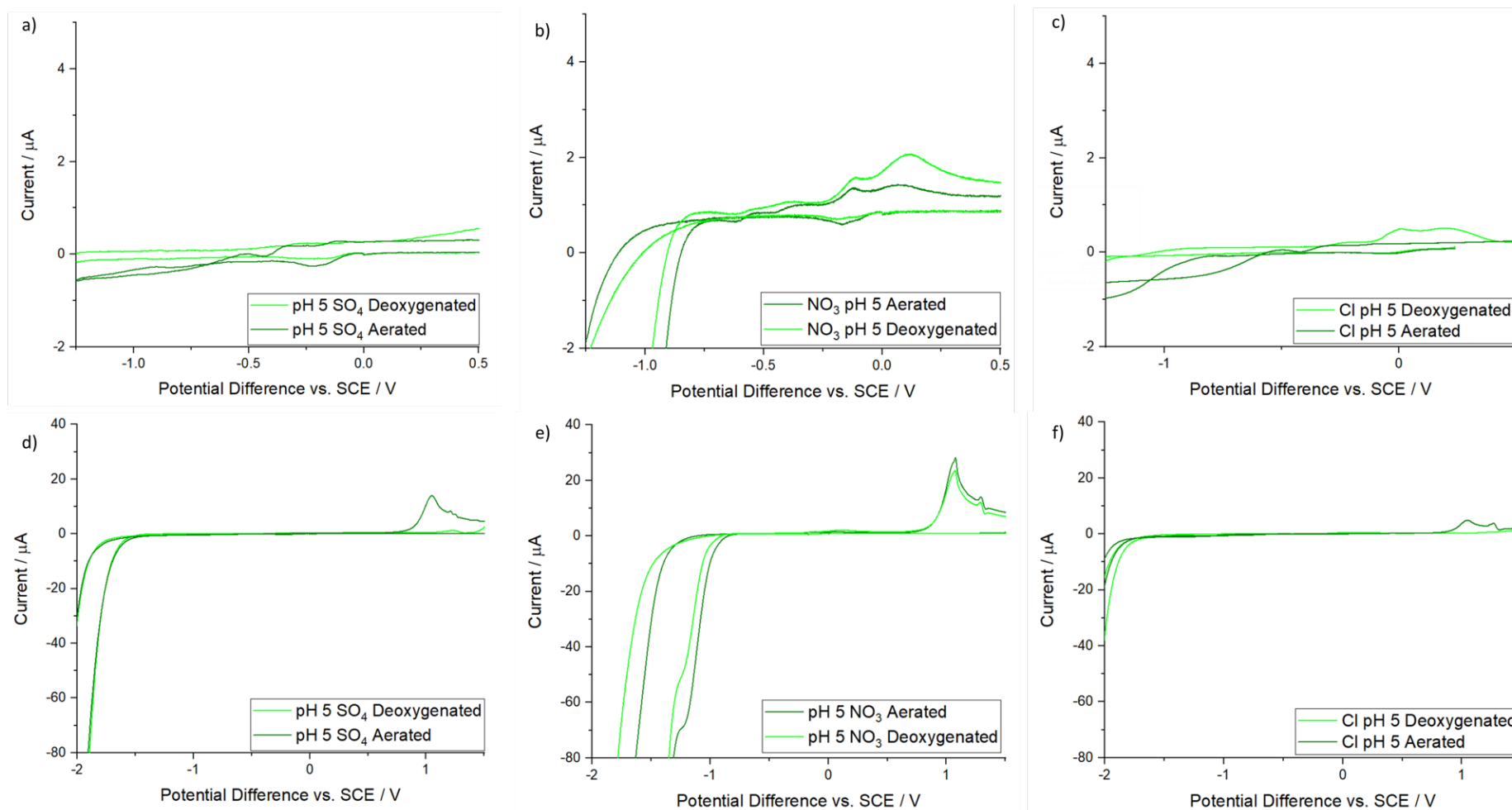


Figure 80 CVs of $100 \mu\text{M Cu}^{2+}$ in pH 5 with background electrolyte consisting of 0.1 M a) K_2SO_4 , b) KNO_3 , c) KCl , using 1 mm BDD macrodisk electrode, 0.1 V s^{-1} starting at 0 V in the negative direction to -2.5 V where the scan direction was reversed. The respective extended window scans are shown for each CV; d) K_2SO_4 , e) KNO_3 and f) KCl .

Looking at the CV experiments in Figure 80, there is a clear difference in response compared to the pH 2 data (Figure 74), and buffered pH 5 data (Figure 71). In particular, almost no Cu^0 stripping peak is visible, even in deoxygenated solutions. However, there are clear anodic signatures about 1 V in all aerated electrolytes (plus nitrate deoxygenated). As stated above, we attribute these signatures to non-metallic Cu species in the Cu^+ state, which are being oxidised e.g. Equation 40 and Equation 41. A cathodic feature at -0.2 V in aerated solution is also visible, which is likely to be ORR. In the pH 5 nitrate solution, an additional anodic feature at -0.1 to -0.2 V appears. The solvent window occurs at less negative values in nitrate media due to the NRR; there is almost a peak shaped response in this region. On the reverse sweep a cathodic peak around -0.4 V is observed, attributed to possible Cu_4O_3 formation.¹⁵

Figure 81 shows the ASV results for deposition in $100\ \mu\text{M}\ \text{Cu}^{2+}$, pH 5 solution including 0.1 M sulfate, nitrate and chloride for 300 s and then stripping at $0.1\ \text{V}\ \text{s}^{-1}$. These results are again very different to the previous experiments in pH 2 or in the pH 5 buffer.

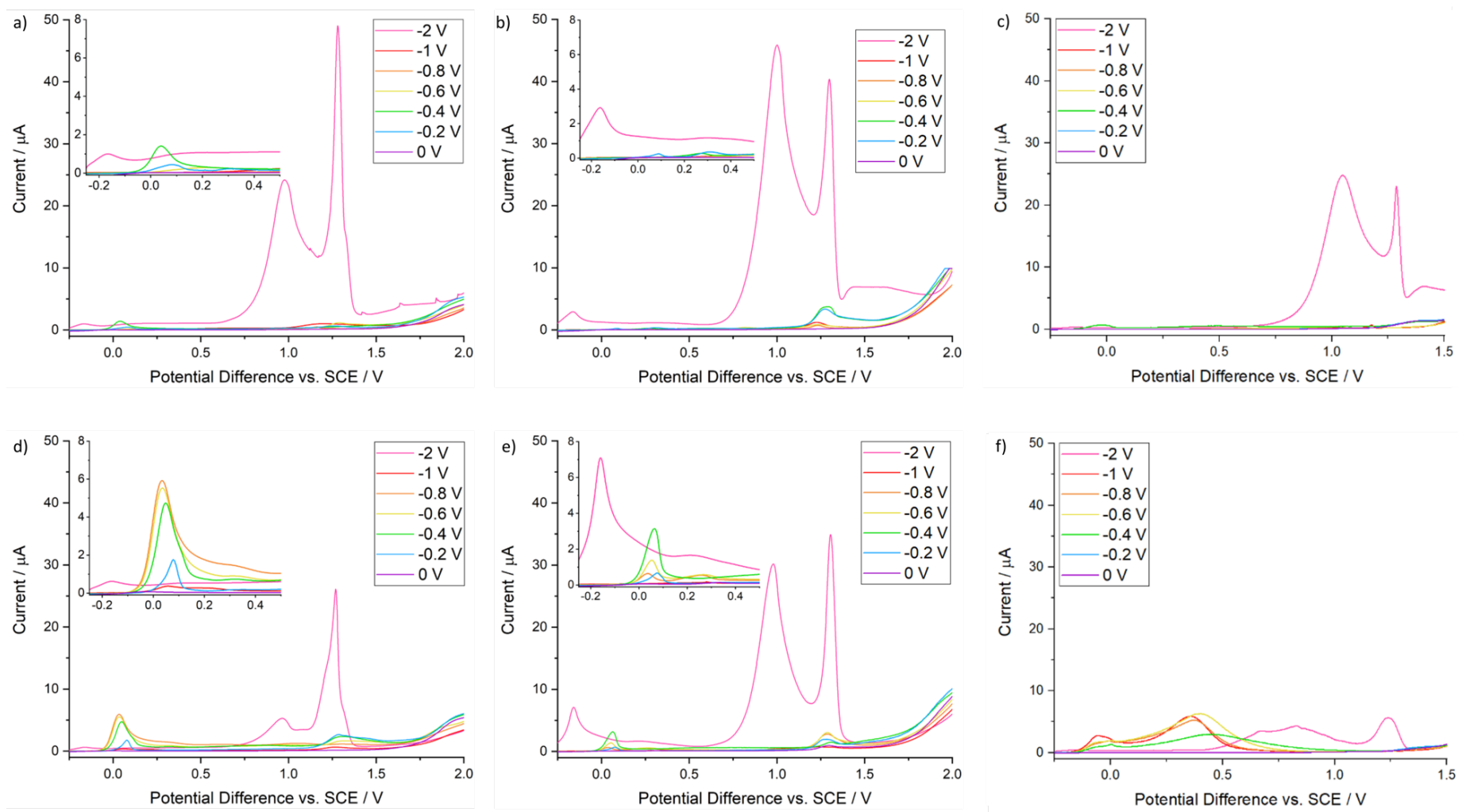


Figure 81 ASV stripping voltammograms of $100 \mu\text{M Cu}^{2+}$ in pH 5, 0.1 M respective background electrolyte aerated a) K_2SO_4 , b) KNO_3 , c) KCl , and deoxygenated d) K_2SO_4 , e) KNO_3 , f) KCl , 1 mm BDD macrodisk electrode, 0.1 V s^{-1} , after 300 s deposition in quiescent solution.

For the aerated experiments, a), b) and c), virtually no Cu stripping was seen, except for sulfate at deposition potentials of -0.2 and -0.4 V (contrast with pH 2 data, Figure 75). At potentials more negative than -0.4 V, the overpotential for ORR is likely to be causing a high rate of dissolved oxygen turnover, resulting in an increase in interfacial pH (Equation 64 and Equation 65). At these potentials, Cu^0 is being deposited in an alkaline environment resulting in hydroxide or oxide deposition and no Cu^0 stripping. In contrast, in the deoxygenated sulfate solution, d), a Cu^0 stripping peak was seen for the deposition potentials, -0.2 to -0.8 V, the peak current increases with increasingly negative potential until a deposition potential of -1 V where the current drops to nearly zero.

In the deoxygenated nitrate experiment, e), small stripping peaks are seen for all potentials except -1 V and -2 V, with peak height increasing from -0.2 V to -0.4 V, but then decreasing with increasingly negative deposition potentials. This must be due to an increasing rate of NRR, acting to increase the local pH even further. For the deoxygenated chloride experiment, f), for all deposition potentials except for -2 V, $\text{Cu}^0 \rightarrow \text{Cu}^+$ and $\text{Cu}^+ \rightarrow \text{Cu}^{2+}$ is seen (0.05 and 0.25 V respectively). Again the clear difference between aerated and deoxygenated shows that ORR had a large effect at pH 5 in chloride media. This data suggests that the pH change has shifted enough to produce the Cu-chloride-hydroxide species. It has been shown that ORR on Cu^0 in neutral chloride solutions goes by the $4e^-$ pathway and is catalysed by a mixture of Cu^0 and Cu^+ sites, the Cu^+ sites being stabilised as Cu_2O or Cu hydroxide around neutral pH.⁸¹ It is therefore quite likely that the ORR is catalysed more at pH 5 than pH 2 which helps to explain why the effect of ORR was larger at pH 5, giving an ASV response more similar to aerated nitrate.

Small broad peaks in the potential region 1 to 1.5 V are observed for all electrolytes and potentials less than -2 V; they are more pronounced in nitrate and deoxygenated sulfate, and as discussed previously are likely to be due to non-metallic Cu oxidations. At -2 V the most striking differences to other voltammograms are seen, here interfacial pH must be extreme, due to solvent splitting and the ORR, resulting in potential hydroxide deposition/formation processes. A deposition potential of -2 V in

nitrate produces a similar CV result to sulfate, features are at -0.1, 1 and 1.25 V, except in the nitrate case the -0.1 V and 1 V peaks are higher than in aerated sulfate. This is further evidence of the possible presence of a hydroxide species which would be more prevalent in nitrate due to ORR and NRR. These peaks are generally larger in the aerated experiments.

Clearly in all cases for this pH 5 experiment some form of reaction is occurring to alter the pH, resulting in multiple species of Cu to be present on the electrode instead of pure Cu⁰. It is more dramatic here than for pH 2 as there are fewer H⁺ ions to counteract a change, the expected interfacial pH will be much higher. These experiments also show that dissolved oxygen had a greater effect on the electrodeposition and stripping CVs in higher pH solutions.

Figure 82 shows the deposits formed in 100 μ M Cu²⁺, pH 5 sulfate solution (0.1 M sulfate) for 300 s a) aerated and b) deoxygenated at the same three different deposition potentials as for the pH 2 experiments.

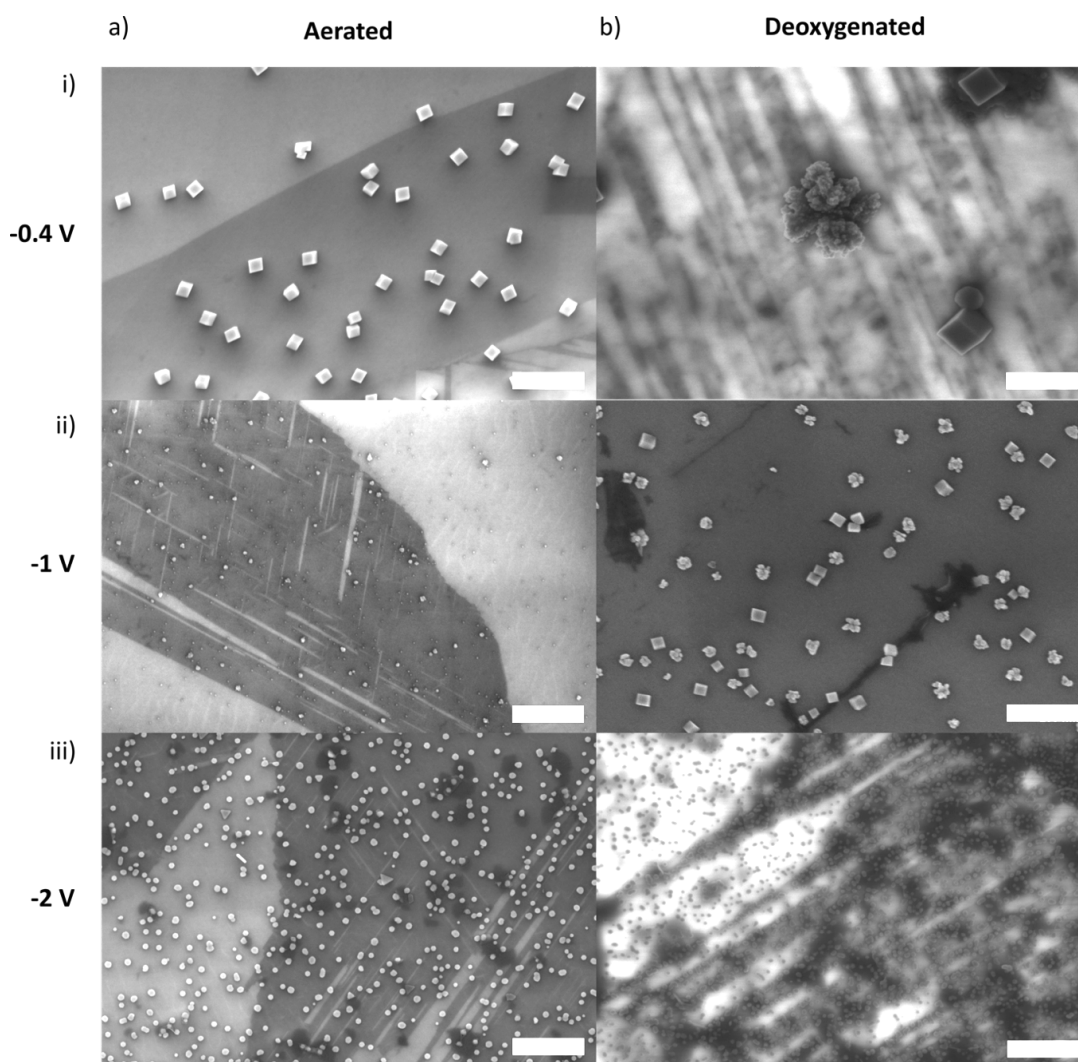


Figure 82 FE-SEM images of BDD electrode surfaces after deposition for 300 s in 100 μM Cu^{2+} , pH 5 (0.1 M K_2SO_4), aerated solution a) and deoxygenated b) at i) -0.4 V, ii) -1 V and iii) -2 V. Scale bar is 400 nm.

At -0.4 V sulfate aerated a) i) cubic NPs of approx. 50 nm were formed. At -1 V aerated a) ii) two morphologies were formed, a smaller approx. 10 nm and a larger approx. 20 nm. At -2 V aerated a) iii) mostly circular NPs of approx. 20 nm were formed, however a few triangular NPs can also be seen. In the deoxygenated solution at -0.4 V b) i) two morphologies exist, cubes, larger than those in a) i) at about 200 nm, and a more dendritic type of NP, approx. 400 nm in size. At a higher overpotential of -1 V these two morphologies are still evident but reduced in size to 50-100 nm. At -2 V very small approx. 10 nm NPs are seen in high number density. Cu^0 stripping was only observed for a) and b) i) out of the samples imaged, and even then with lower currents passed compared to pH 2 sulfate solutions. Hence many of these deposits must be largely non-metallic Cu species.

Figure 83 shows the deposits formed in 100 μM Cu^{2+} , pH 5 nitrate solution including 0.1 M nitrate for 300 s, a) aerated and b) deoxygenated.

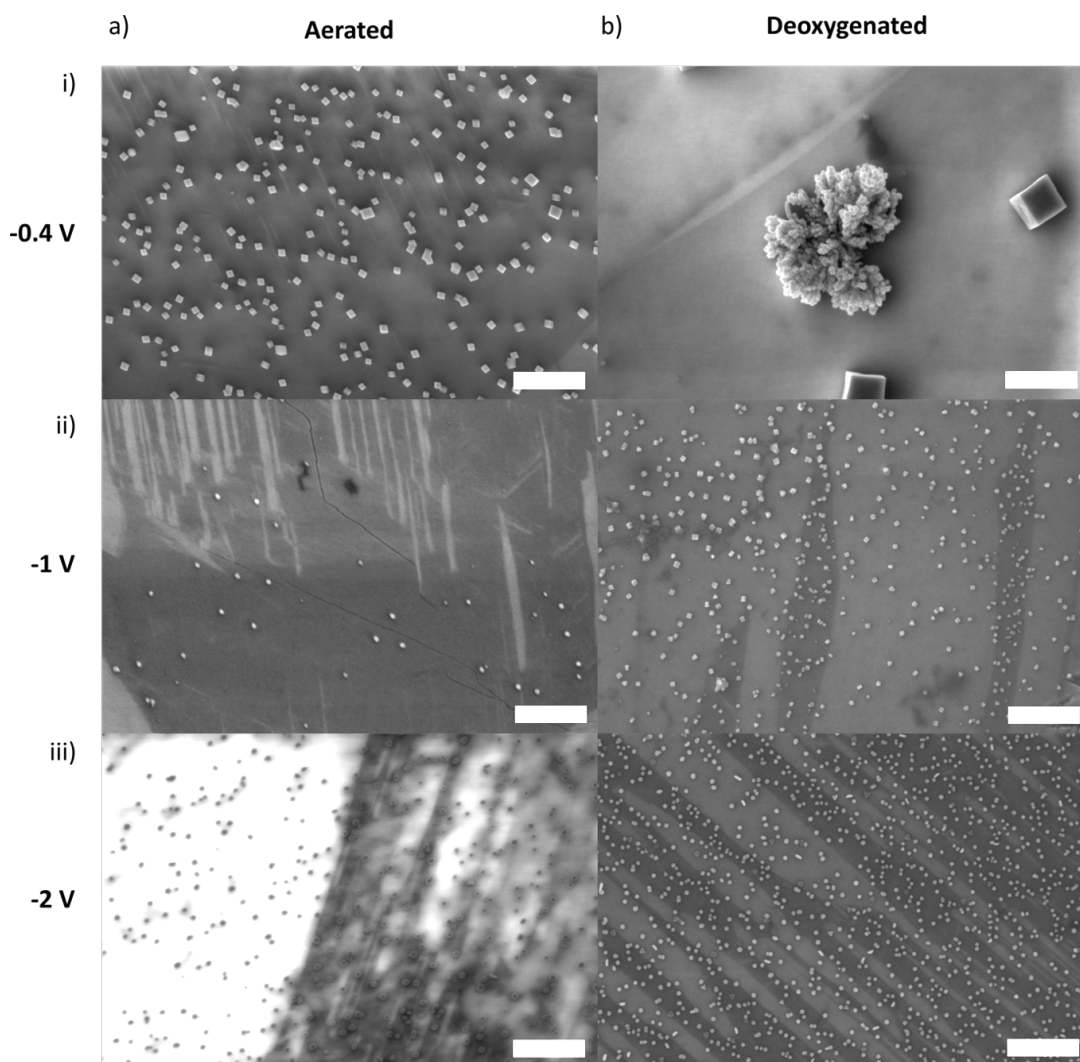


Figure 83 FE-SEM images of BDD electrode surfaces after deposition for 300 s in 100 μM Cu^{2+} , pH 5 (0.1 M KNO_3), aerated solution a) and deoxygenated b) at i) -0.4 V, ii) -1 V and iii) -2 V. Scale bar is 400 nm.

At -0.4 V aerated a) i) cubic NPs are seen, as for the sulfate experiments, but slightly smaller in size (approx. 30-40 nm). At -1 V sparse, small NPs are observed, approx. 20 nm in size. At -2 V NPs are of a similar size but higher in number density. For the deoxygenated experiment -0.4 V b) i) a very similar combination of cubes and dendrite type deposits are formed as in the sulfate experiments, with similarly sized particles. However, at -1 V only one morphology, cubes (10-30 nm) are observed. At -2 V a high number density of approx. 20 nm NPs are formed with a few triangular

NPs visible. As only a) i) showed any sign of stripping, the deposits imaged here are expected to be mostly non-metallic Cu.

The cubic NPs in a) i) were determined to be Cu₂O (confirmed by TEM analysis for a) i), see Chapter 6. Cubic NPs such as those obtained here have appeared frequently in the literature by electrodeposition from a mid-range pH (5-7).^{54,78} They are a promising electrocatalyst for the CO₂ reduction reaction as they reduce the overpotential required for the reaction onset and have a good product distribution.^{82,83} Cu₂O can also exist in other morphologies, such as dendrites and triangular NPs. The full range of morphologies is discussed in detail in an article by Sun et al.⁸² Note Cu⁰ can also exist as a cubic morphology.^{31,84}

Figure 84 shows the deposits formed in 100 μM Cu²⁺, pH 5, 0.1 M chloride solution, a) aerated and b) deoxygenated.

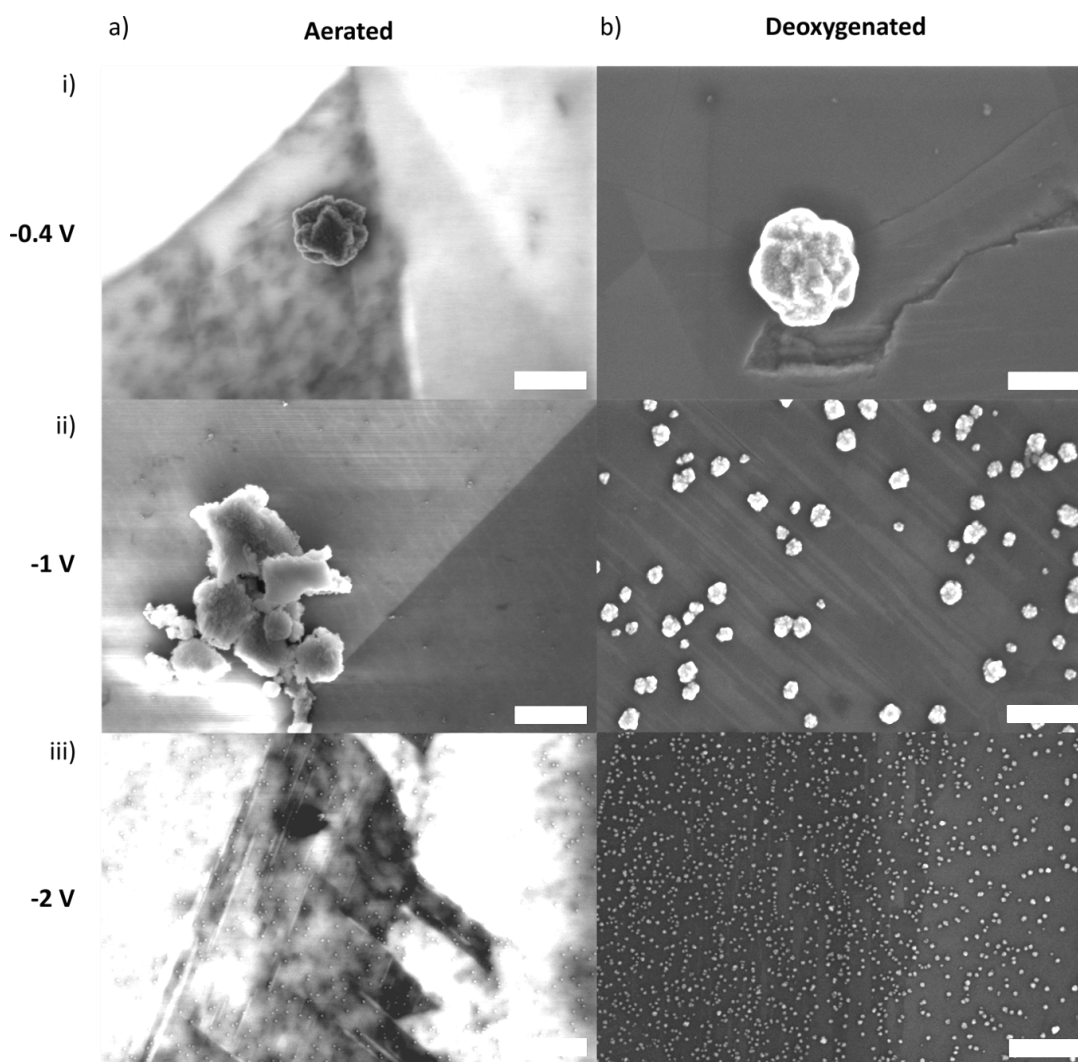


Figure 84 FE-SEM images of BDD electrode surfaces after deposition for 300 s in 100 μM Cu^{2+} , pH 5 (0.1 M KCl), aerated solution a) and deoxygenated b) at i) -0.4 V, ii) -1 V and iii) -2 V. Scale bar is 400 nm.

At -0.4 V aerated a) i) NPs were very few in number and widely distributed, approx. 400 nm in size, the same was observed for the deoxygenated experiment at -0.4 V. In the aerated at -1 V a) ii) very small NPs (a few nm in size) were visible around larger flake like deposit clusters hundreds of nm in size. Again, at -2 V a high number density of small NPs, here approx. 10 nm in size are formed. In deoxygenated solution the NPs formed at -1 V b) ii) are very different to aerated, amorphous NPs around 50-100 nm in size are observed. At -2 V a higher number density of smaller (10-20 nm) NPs are seen. No clear metallic Cu^0 stripping is seen in pH 5 chloride so again these are expected to be non-metallic Cu, possibly Cu-chloride-oxide/hydroxide compounds.

In addition to the NPs shown in b) i) triangular NPs were observed, similar to those in Figure 79 a) i), see Figure 85. However due to the low number density an image of both together at a useful magnification was not possible.

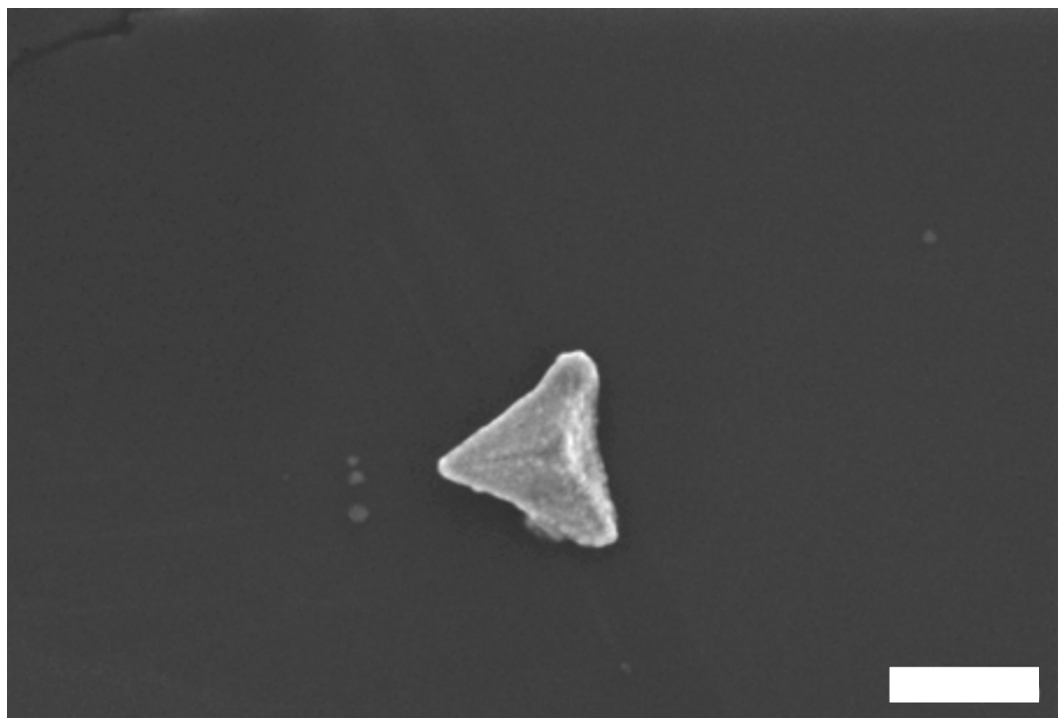


Figure 85 FE-SEM images of BDD electrode surfaces after deposition for 300 s in 100 μM Cu^{2+} , pH 5 (0.1 M KCl), deoxygenated solution -0.4 V. Scale bar is 400 nm.

All these experiments show the complexity of performing stripping analysis in unbuffered solutions, primarily resulting from local pH increases that result from e.g. HER, NRR and ORR. The impact of the local pH increase is exacerbated the less acidic the solution. This is an important factor to consider when designing methodologies for at-the-source ASV.

5.5. Conclusions

These experiments showed that the ASV of Cu^0 is highly dependent on pH, electrolyte, buffering, dissolved oxygen and potential. Dissolved oxygen was found to have a larger effect at more neutral pH, low pH was found to improve Cu stripping peak height and shape but was different for nearly every case. The presence of nitrate and chloride both complicated the analysis in different ways, nitrate weakly interacted with Cu and NRR was catalysed on the Cu nanoparticles, causing further pH shifts. Chloride on the other hand interacted strongly, stabilising the Cu^+ oxidation

state and enabling Cu-chloride complexes to be formed resulting in a potential shift of the stripping peak by around -0.1 V.

The characteristics of the deposits are determined by the interplay of different reactions and factors, e.g. in acidic solutions (pH 2) -2 V gave the highest driving force for Cu^0 and generally outcompeted other, non-metallic Cu species whereas in pH 5 little Cu^0 was formed. The data collected shows that without even having the complication of another metal ion present, a different optimal ASV method to detect Cu would have to be devised for each application, even if the only difference was a small change in one of these factors. This inflexibility in ASV is probably why, despite being a relatively cheap and quick analytical method, it has not been widely adopted commercially.

Future work on this topic would look to quantify the local pH changes taking place at the electrode surface during metal electrodeposition through the use of confocal microscopy with a pH sensitive dye.²⁸ This would help elucidate the extent to which deposition conditions are locally perturbed by the ORR and NRR reactions, enabling a more accurate relation of conditions and products to the Pourbaix diagram. It would also be interesting to investigate the chemical identity of the wide range of particles observed on the BDD surface using TEM to provide more information on relating the peaks in ASV to chemical species.

The observations of the morphologies produced some interesting trends and results, at more negative potentials NPs became smaller and higher in number density. At more positive potentials, larger NPs with more varied morphologies were formed such as the cubic NPs seen for pH 5 sulfate and nitrate solutions. For nitrate, TEM confirmed these NPs to be Cu_2O and are a promising electrocatalyst for the CO_2 reduction reaction. This is the topic of further investigation in Chapter 6. The ability to form these cubic NPs quickly and without the use of synthetic procedures or surfactants at low potentials is an important improvement on the popular synthetic procedures where high temperatures and many additives are required.^{82,85}

5.6. Bibliography

- 1 P. C. Andricacos, C. Uzoh, J. O. Dukovic, J. Horkans and H. Deligianni, *IBM J. Res. Dev.*, 1998, **42**, 567–574.
- 2 C. M. McShane and K. S. Choi, *J. Am. Chem. Soc.*, 2009, **131**, 2561–2569.
- 3 P. M. Bersier, J. Howell and C. Bruntlett, *Analyst*, 1994, **119**, 219–232.
- 4 A. J. Borrill, N. E. Reily and J. V. Macpherson, *Analyst*, 2019, **144**, 6834–6849.
- 5 J. V. Macpherson, *Phys. Chem. Chem. Phys.*, 2015, **17**, 2935–2949.
- 6 J. Huang, F. Yuan, G. Zeng, X. Li, Y. Gu, L. Shi, W. Liu and Y. Shi, *Chemosphere*, 2017, **173**, 199–206.
- 7 E. Pérez-Gallent, M. C. Figueiredo, I. Katsounaros and M. T. M. M. Koper, *Electrochim. Acta*, 2017, **227**, 77–84.
- 8 G. M. Brown and G. A. Hope, *J. Electroanal. Chem.*, 1996, **405**, 211–216.
- 9 W. Shao, G. Pattanaik and G. Zangari, *J. Electrochem. Soc.*, 2007, **154**, 201–207.
- 10 C. Deslouis, I. Frateur, G. Maurin and B. Tribollet, *J. Appl. Electrochem.*, 1997, **27**, 482–492.
- 11 J. Zhao, S. Xue, J. Barber, Y. Zhou, J. Meng and X. Ke, *J. Mater. Chem. A*, 2020, **8**, 4700–4734.
- 12 W. Shao and G. Zangari, *J. Phys. Chem. C*, 2009, **113**, 10097–10102.
- 13 C. Kartal, Y. Hanedar, T. Öznülüer and Ü. Demir, *Langmuir*, 2017, **33**, 3960–3967.
- 14 Y. Deng, A. D. Handoko, Y. Du, S. Xi and B. S. Yeo, *ACS Catal.*, 2016, **6**, 2473–2481.
- 15 Z. Mezine, A. Kadri, L. Hamadou, N. Benbrahim and A. Chaouchi, *J. Electroanal. Chem.*, 2018, **817**, 36–47.
- 16 Y. Wang, S. Lany, J. Ghanbaja, Y. Fagot-Revurat, Y. P. Chen, F. Soldera, D. Horwat, F. Mücklich and J. F. Pierson, *Phys. Rev. B*, 2016, **94**, 1–10.
- 17 D. J. G. Ives and A. E. Rawson, *J. Electrochem. Soc.*, 1962, **109**, 458–462.
- 18 M. V. Vazquez, S. R. de Sanchez, E. J. Calvo and D. J. Schiffrin, *J. Electroanal. Chem.*, 1994, **374**, 189–197.
- 19 M. Scherzer, F. Girgsdies, E. Stotz, M. G. Willinger, E. Frei, R. Schlögl, U. Pietsch and T. Lunkenbein, *J. Phys. Chem. C*, 2019, **123**, 13253–13262.

- 20 M. V. Vazquez, S. R. de Sanchez, E. J. Calvo and D. J. Schiffrin, *J. Electroanal. Chem.*, 1994, **374**, 179–187.
- 21 D. Ren, J. Fong and B. S. Yeo, *Nat. Commun.*, , DOI:10.1038/s41467-018-03286-w.
- 22 T. C. Chou, C. C. Chang, H. L. Yu, W. Y. Yu, C. L. Dong, J. J. Velasco-Vélez, C. H. Chuang, L. C. Chen, J. F. Lee, J. M. Chen and H. L. Wu, *J. Am. Chem. Soc.*, 2020, **142**, 2857–2867.
- 23 T. M. Florence and G. E. Batley, *Princet. Univ. Press*, 1977, **75**, 791–798.
- 24 E. Y. Neiman, L. G. Petrova, V. I. Ignatov and G. M. Dolgoplova, *Anal. Chim. Acta*, 1980, **113**, 277–285.
- 25 G. Gillain, G. Duyckaerts and A. Disteche, *Anal. Chim. Acta*, 1979, **106**, 23–37.
- 26 T. Zapryanova, A. Hrussanova and A. Milchev, *J. Electroanal. Chem.*, 2007, **600**, 311–317.
- 27 M. M. Nicholson, *J. Am. Chem. Soc.*, 1957, **79**, 7–12.
- 28 F. Texier, L. Servant, J. L. Bruneel and F. Argoul, *J. Electroanal. Chem.*, 1998, **446**, 189–203.
- 29 S. Song, C. M. Ortega, Z. Liu, J. Du, X. Wu, Z. Cai and L. Sun, *J. Electroanal. Chem.*, 2013, **690**, 53–59.
- 30 M. R. Majidi, K. Asadpour-Zeynali and B. Hafezi, *Electrochim. Acta*, 2009, **54**, 1119–1126.
- 31 W. Y. Ko, W. H. Chen, C. Y. Cheng and K. J. Lin, *Nanoscale Res. Lett.*, 2009, **4**, 1481–1485.
- 32 D. Grujicic and B. Pesic, *Electrochim. Acta*, 2002, **47**, 2901–2912.
- 33 A. B. Couto, M. C. E. Ribeiro, F. L. Migliorini, N. G. Ferreira and M. R. Baldan, *Diam. Relat. Mater.*, 2013, **38**, 104–108.
- 34 M. A. Hossain, R. Al-Gaashani, H. Hamoudi, M. J. Al Marri, I. A. Hussein, A. Belaidi, B. A. Merzougui, F. H. Alharbi and N. Tabet, *Mater. Sci. Semicond. Process.*, 2017, **63**, 203–211.
- 35 C. Prado, S. J. Wilkins, F. Marken and R. G. Compton, *Electroanalysis*, 2002, **14**, 262–272.
- 36 D. Feng, C. Aldrich and H. Tan, *Miner. Eng.*, 2000, **13**, 623–642.
- 37 R. Down and J. Lehr, *Environmental Instrumentation and Analysis Handbook*,

2005, vol. 2005.

- 38 J. Davis, J. C. Baygents and J. Farrell, *Electrochim. Acta*, 2014, **150**, 68–74.
- 39 J. M. Casas, J. P. Etchart and L. Cifuentes, *AIChE J.*, 2003, **49**, 2199–2210.
- 40 Y. K. Chau and K. Lum-Shue-Chan, *Water Res.*, 1974, **8**, 383–388.
- 41 J. L. Anderson and I. Shain, *Anal. Chem.*, 1978, **50**, 163–171.
- 42 I. Sinko and J. A. N. Dolezal, *Electroanal. Chem. Interfacial Electrochem.*, 1970, **25**, 299–306.
- 43 A. J. Bard, R. Parsons and J. Jordan, *Standard Potentials in Aqueous Solution*, Routledge, 2017.
- 44 R. Drissi-Daoudi, A. Irhzo and A. Darchen, *J. Appl. Electrochem.*, 2003, **33**, 339–343.
- 45 A. Milchev and T. Zapryanova, *Electrochim. Acta*, 2006, **51**, 4916–4921.
- 46 J. Y. Zheng, A. P. Jadhav, G. Song, C. W. Kim and Y. S. Kang, *Thin Solid Films*, 2012, **524**, 50–56.
- 47 S. Y. Ng and A. H. W. Ngan, *J. Electrochem. Soc.*, 2015, **162**, D124–D128.
- 48 M. P.-P. M. G. Montes de Oca, J. Mostany, M. T. Ramírez-Silva, M. Romero-Romo, B. R. Scharifker, *ECS Trans.*, 2007, **3**, 25–34.
- 49 A. Ramos, M. Miranda-Hernández and I. González, *J. Electrochem. Soc.*, 2001, **4**, C315–C321.
- 50 J. L. Anderson and I. Shain, *Anal. Chem.*, 1976, **48**, 1274–1282.
- 51 I. G. Casella and M. Gatta, *J. Electroanal. Chem.*, 2000, **494**, 12–20.
- 52 Y. Cudennec and A. Lecerf, *Solid State Sci.*, 2003, **5**, 1471–1474.
- 53 I. S. Brandt, M. A. Tumelero, S. Pelegrini, G. Zangari and A. A. Pasa, *J. Solid State Electrochem.*, 2017, **21**, 1999–2020.
- 54 X. Guo, W. Lv and X.-Y. Li, *J. Phys. Chem. C*, 2014, **118**, 11062–11077.
- 55 D.-L. Lu and K. Tanaka, *J. Electrochem. Soc.*, 1996, **143**, 2105–2109.
- 56 S. T. Mayer and R. H. Muller, *J. Electrochem. Soc.*, 1992, **139**, 426–434.
- 57 H. P. Leckie, *J. Electrochem. Soc.*, 1970, **117**, 1478.
- 58 a J. deBethune, T. S. Licht and N. Swendeman, *J. Electrochem. Soc.*, 1959, **106**, 616–625.
- 59 M. Lenglet, K. Kartouni, J. Machefert, J. M. Claude, P. Steinmetz, E. Beauprez, J. Heinrich and N. Celati, *Mater. Res. Bull.*, 1995, **30**, 393–403.

- 60 Y. Lu, H. Xu, J. Wang and X. Kong, *Electrochim. Acta*, 2009, **54**, 3972–3978.
- 61 A. Paracchino, V. Laporte, K. Sivula, M. Grätzel and E. Thimsen, *Nat. Mater.*, 2011, **10**, 456–461.
- 62 K. Bouzek, M. Paidar, A. Sadílková and H. Bergmann, *J. Appl. Electrochem.*, 2001, **31**, 1185–1193.
- 63 D. Reyter and L. Roú, *Electrochim. Acta*, 2008, **53**, 5977–5984.
- 64 T. Öznülüer, B. Özdurak and H. Öztürk Doğan, *J. Electroanal. Chem.*, 2013, **699**, 1–5.
- 65 T. M. Florence, G. E. Batley and P. Benes, *C R C Crit. Rev. Anal. Chem.*, 1980, **9**, 219–296.
- 66 D. Menshykau and R. G. Compton, *J. Phys. Chem. C*, 2009, **113**, 15602–15620.
- 67 R. O. D. Clark, K. Ngamchuea, C. Batchelor-McAuley and R. G. Compton, *Electroanalysis*, 2017, **29**, 1418–1425.
- 68 T. A. Ivandini and Y. Einaga, in *Reference Module in Chemistry, Molecular Sciences and Chemical Engineering*, 2017.
- 69 B. D. T. Electrodes, M. Awada, J. W. Strojek and G. M. Swain, 1995, 3–7.
- 70 E. T. Urbansky and M. R. Schock, *J. Chem. Educ.*, 2000, **77**, 1640–1644.
- 71 F. King, C. D. Litke and Y. Tang, *J. Electroanal. Chem.*, 1995, **384**, 105–113.
- 72 G. H. A. Therese and P. V. Kamath, *Chem. Mater.*, 2000, **12**, 1195–1204.
- 73 M. Schlesinger and M. Paunovic, *Fundamentals of Electrochemical Deposition*, 2006.
- 74 C. W. Li and M. W. Kanan, *J. Am. Chem. Soc.*, 2012, **134**, 7231–7234.
- 75 A. A. Permyakova, J. Herranz, M. El Kazzi, J. S. Diercks, M. Povia, L. R. Mangani, M. Horisberger, A. Pătru and T. J. Schmidt, *ChemPhysChem*, 2019, 1–9.
- 76 C. M. Welch, A. O. Simm and R. G. Compton, *Electroanalysis*, 2006, **18**, 965–970.
- 77 A. Singhal, M. R. Pai, R. Rao, K. T. Pillai, I. Lieberwirth and A. K. Tyagi, *Eur. J. Inorg. Chem.*, 2013, 2640–2651.
- 78 M. J. Siegfried and K. S. Choi, *Adv. Mater.*, 2004, **16**, 1743–1746.
- 79 H. V. Patten, K. E. Meadows, L. A. Hutton, J. G. Iacobini, D. Battistel, K. McKelvey, A. W. Colburn, M. E. Newton, J. V. MacPherson and P. R. Unwin, *Angew. Chemie - Int. Ed.*, 2012, **51**, 7002–7006.

- 80 A. L. Colley, C. G. Williams, U. D. H. Johansson, M. E. Newton, P. R. Unwin, N. R. Wilson and J. V. Macpherson, *Anal. Chem.*, 2006, **78**, 2539–2548.
- 81 F. King, M. J. Quinn and C. D. Litke, *J. Electroanal. Chem.*, 1995, **385**, 45–55.
- 82 S. Sun, X. Zhang, Q. Yang, S. Liang, X. Zhang and Z. Yang, *Prog. Mater. Sci.*, 2018, **96**, 111–173.
- 83 H. Jung, S. Y. Lee, C. W. Lee, M. K. Cho, D. H. Won, C. Kim, H. S. Oh, B. K. Min and Y. J. Hwang, *J. Am. Chem. Soc.*, 2019, **141**, 4624–4633.
- 84 A. Loiudice, P. Lobaccaro, E. A. Kamali, T. Thao, B. H. Huang, J. W. Ager and R. Buonsanti, *Angew. Chemie - Int. Ed.*, 2016, **55**, 5789–5792.
- 85 Y. Q. Wang, W. S. Liang, A. Satti and K. Nikitin, *J. Cryst. Growth*, 2010, **312**, 1605–1609.

6. Transmission Electron Microscopy

Investigation of Copper (I) Oxide

Electrodeposition and Carbon

Dioxide Electrocatalysis

6.1. Overview

Cu based materials have shown great potential as CO₂ reduction catalysts due to their enhanced ability to produce multi-carbon products. Electrochemistry can be used to synthesise and analyse catalyst materials enabling advancements in our understanding and aid in the development of future catalysts. In this work the morphology and speciation of nanocubes electrodeposited from copper nitrate solution is investigated during growth, before and after electrocatalysis using Transmission Electron Microscopy (TEM). The nanocubes were found to be copper (I) oxide (Cu₂O), they were reproducibly synthesised electrochemically without the need for surfactants or other additives, providing a simple route to these important catalytic structures. During growth Cu and Cu₂O were both formed but Cu particles were unstable at the applied potential (-0.4 V) while Cu₂O persisted. After electrolysis the speciation had changed to predominantly Cu and significant morphological change had occurred. Boron doped diamond (BDD) was chosen as the electrode substrate due to its exceptional electrode properties and the ability to use it as an electron transparent TEM substrate. A BDD TEM electrode enabled the investigation of the Cu₂O formation mechanism by Identical location (IL) and resulting degradation during CO₂ electrocatalysis at multiple time points due to its robustness as a substrate.

6.2. Introduction

Copper (Cu) is an element widely used in electronics, (electro)catalysis and sensing. As well as being significantly cheaper and more available than platinum group metals such as gold and platinum, it has relatively low toxicity.¹ It is also possible to synthesise metallic Cu, or various copper oxides and copper hydroxides nanostructures and films.^{2–4} Cu and its oxide derivatives have shown a lot of promise as a catalyst for green chemistry, for example the electrochemical reduction of carbon dioxide (CO₂) to fuels and other chemical feedstocks using renewable energy.^{5–8} This has the advantages of using an unwanted resource, the greenhouse gas CO₂ and turning it into useful products that would otherwise be made from fossil fuels. This can be classed as a form of carbon recycling.^{9,10} It is thus not surprising that efforts are in place to examine the possible modes of activity and deactivation of Cu based materials during CO₂ electrocatalysis.

Many metal electrodes such as Ag and Au,⁹ and BDD electrodes have also been reported as catalysts for CO₂ reduction.¹¹ However, Cu is thought to be particularly useful for the CO₂ electrochemical reduction reaction (CO₂RR) as it has a negative adsorption energy for the intermediate CO* (adsorbed CO). This intermediate is relatively stable on the surface and therefore likely to persist long enough to react further.⁵ This is thought to be critical to C-C formation for C₂ products and also results in inhibition of the hydrogen evolution reaction (HER).¹² Polycrystalline Cu has been shown to produce up to 16 different CO₂RR products, highlighting the need for increased selectivity.¹³ It is generally accepted that for the CO₂RR, the surface structure of Cu nanoparticles or films play a major role during the conversion reaction. For example, Cu[100] preferentially produces ethylene, whilst Cu[111] predominantly results in methane¹⁴ and Cu[110] produces a range of C₂ products such as acetaldehyde, ethanol and ethanoic acid.⁹ However, there are still ongoing discussions in the literature about the exact mechanism(s) and active site(s) involved in CO₂RR.^{12,15}

To date, the literature in the Cu / CO₂RR area is still contradictory. The main species suspected to act as electrocatalysts during the CO₂RR are Cu(0) (metallic Cu) and Cu(I) (as Cu₂O).^{16–18} In addition, there are reports that address the possibility of using Cu(II)O, Cu hydroxides and Cu(I)-Cl compounds, but these are less prevalent.^{3,19–21} Some literature also claims that Cu(0) has no activity towards CO₂RR,¹⁵ while others claim that it is Cu₂O that has no activity towards CO₂RR.²¹ In general, there are a wide range of Cu-based electrocatalysts in the literature where the influence of oxidation state, oxygen content and crystal facets have all been investigated. Cu catalysts appear in many forms, some examples are; Cu₂O films grown on Cu plates,^{17,22} Cu/Cu₂O core nanoparticles, Cu nanoparticles grown on Cu₂O films,²³ Cu films derived from Cu₂O films^{7,24} and Cu₂O nanoparticles on various supports.²⁵

The difficulty with understanding the behaviour of Cu catalysts is that they are reactive and can react in many different ways. This was often not acknowledged in the literature until relatively recently but is now a focal point in Cu electrocatalyst research.^{6,15,16} The terms “derived” or “based” are often used to describe these catalysts as this inherently acknowledges the changes/mixtures of species that can occur during electrocatalysis that contribute to the activity or product ratios. It has been suggested that Cu₂O catalysts are electrochemically reduced to Cu(0) but retain their Cu₂O structure at potentials before the onset of CO₂RR.^{9,12} These have been found to have improved C-C coupling, resulting in increased C₂ products than bulk Cu.^{7,22,26} Although the driving force for Cu(0) is strong the conversion may not be complete. There are ongoing discussions in literature about the existence and effect of subsurface oxygen and its role in the apparent increased stability for the CO* intermediate on these catalysts (suggested by DFT studies).^{9,16,27,28} Similarly, many Cu(0) catalysts are suspected to have a thin layer of surface oxide or some subsurface oxygen, from air exposure or contact to aqueous solution which contributes to activity.^{12,29}

The mechanism of CO₂ electrochemical reduction is still largely unknown but there are proposed mechanisms (Figure 86). Many steps are predicted using computational techniques,³⁰ but some steps or intermediates are supported by experimental

evidence (such as infrared spectroscopy³¹) such as the formation CO* intermediate and dimerization.^{5,15}

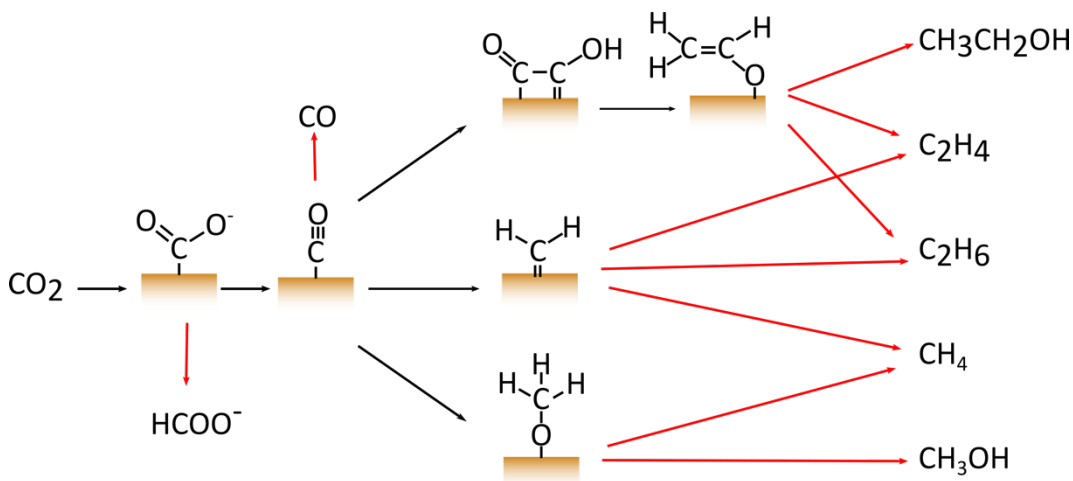


Figure 86 Proposed mechanism for CO₂ reduction on Cu surfaces, adapted from ⁵.

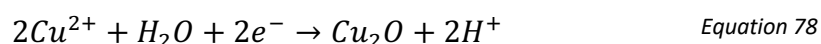
There are several possible pathways from adsorbed CO* to a range of products, some are shown in Figure 86. Note, other research efforts have different proposed mechanisms, pathways and products.^{6,9,12,13,17,20,32} In addition to catalyst properties, solution composition can affect activity and product ratio by changing the solubility of CO₂, stabilising the intermediates and by reducing the extent of HER, leading to different product ratios.⁹ Overpotential also changes the product ratios but has to be balanced carefully with the onset of HER. The exact effect of pH (both bulk and local), and applied potential depend on the specific system (catalyst properties) and they are often interdependent.^{12,33} In terms of the electrolyte, it has been found that a larger cation will increase selectivity for multi carbon (C₂₊) products but the explanation behind this has still not been agreed upon.³⁴

Cu₂O based catalysts, especially in the nanocube form, appear to yield improved faradaic efficiencies and C₂/C₃ product ratios compared to other materials due to their improved ability to form C-C bonds.^{7,22,26} The ability to form multi carbon compounds is linked to the ability of the catalyst sites to stabilise and couple the CO* intermediate (to itself).^{8,9}

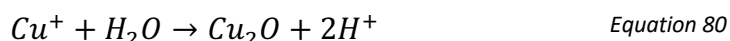
Synthesis of Cu₂O nanocubes has been demonstrated chemically,³⁵ physically³⁶ (sputtering and annealing) and electrochemically³⁷ previously. Chemical synthesis of

the Cu₂O cubes, or sizes in the nm to µm range appears a popular literature route and can result in very good size control.^{35,36,38} Despite this, to control the morphology during chemical growth often involves several additives, wet chemistry processes and extreme pH and in some cases annealing steps are required, making these methods resource and time intensive.^{36,38}

Electrochemical synthesis has the advantage that the electrode is directly modified as well involving fewer processing steps and a reduction in the number of chemicals/additives that need to be added to solution. Electrochemically and thermodynamically Cu₂O is predicted to form via Equation 78.^{36,39,40}



This is a combination of two steps, a reduction, Equation 79 and a precipitation, Equation 80, the latter occurring because of the instability of Cu⁺. The viability of this (contrary to the Pourbaix prediction for many experimental conditions used in literature) is due to the kinetic preference of Equation 80.⁴¹



The potential of this reaction (Equation 78) can be calculated using Equation 81, vs the standard hydrogen electrode.

$$E = 0.203 + 0.0591 \text{ pH} + 0.0591 \log[Cu^{2+}] \quad \text{Equation 81}$$

There are a number of electrochemical methods which have been shown to result in Cu₂O and the specific conditions (electrolytes, potentials, electrode materials and pHs) vary from study to study.^{25,36,40–43} There does not appear to be any single consensus on the preferred conditions. Work from Chapter 5 found that Cu₂O cubes could be electroformed using an aerated nitrate electrolyte (pH 5) on BDD electrodes at a deposition potential of -0.4 V vs SCE.

Despite the number of electrodeposition methods published for synthesising Cu₂O cubes, relatively few investigate the nucleation or evolution of the cubic morphology and so there is only a rudimentary understanding of the formation of these electrocatalysts. Studies have attempted to follow the growth and evolution of Cu

catalysts *in situ*, but these experiments are practically challenging. They tend to use electrodes in confined set ups (possible resistance issues) which are not representative of electrocatalysis conditions and suffer from poor resolution as a result of the beam having to pass through liquid.^{17,19,20,39,44,45}

The long-term stability of Cu electrocatalysts is currently an issue for scale-up and commercialisation as many catalysts display progressive deactivation during CO₂RR.^{16,27} Often within minutes of CO₂RR commencing.²⁵ Deactivation can occur by detachment of active material, reshaping (fragmentation, agglomeration and facet changes), dissolution and transformation of the active species.¹⁶ Activity can also be lost by poisoning of the catalyst by the presence of other transition metals, organic species and even intermediates of the CO₂RR.⁴⁶ Understanding these processes will help inform on better catalyst design and condition selection to improve reaction yields. Deactivation studies of note are detailed below.

Arán-Ais *et al.* investigated both the growth and anodic dissolution of Cu₂O cubes by cyclic voltammetry, using *in situ* electrochemical TEM in a CuSO₄ and KCl solution. They found that the main Cu₂O loss effects were Cu₂O detachment and dissolution along with redeposition of Cu as dendritic structures. This loss of the cubic morphology (predominantly [100]) resulted in an increase in H₂ production and decrease in ethylene formation.¹⁹ *In situ* TEM has the benefits of dynamic reaction imaging but suffers from reduced spatial resolution (compared to *ex situ* TEM studies) due to the presence of the electrolyte solution. Electron beam effects can also result in changing solution conditions due to changes in temperature and solution electrolysis.⁴⁷

'Before and after' (*ex situ*) studies have also been conducted. For example, Grosse *et al.* found using SEM and Atomic Force Microscopy (AFM), that smaller Cu₂O cubes were less stable, leading to a greater loss of material by detachment, as well as reduction to Cu⁰ (measured by x-ray Photoelectron Spectroscopy), which decreased the ethylene yield.²⁵ For the cubes remaining on the surface, the shape was completely lost after 3 hours of electrolysis and mostly transformed to Cu⁰. TEM has

the advantage over SEM and AFM of higher resolution imaging (atom-level when *ex situ*) and the ability to precisely define the chemical identity of the nanostructure via electron beam diffraction and spectroscopy. Huang *et al.* found using TEM that a combination of potential induced shape deterioration, nanoclustering and coalescence resulted in a loss of CO₂RR activity.⁴⁸ These studies are exceptionally important for understanding the activity of these catalysts. More in depth understanding of the synthesis and deactivation could allow better catalyst control and design, leading to more efficient catalysts.

For the ultimate in high resolution dynamic imaging of electrochemically driven processes identical location (IL) – TEM⁴⁷ is useful. In IL-TEM the electrode (and supported nanostructure) are subject to a defined electrochemical treatment e.g. applied potential/current. The process is stopped, the electrode removed from solution, imaged at high resolution in the TEM, then replaced in solution and the electrochemical reaction continued. The process is again stopped and TEM imaging carried out in the same location. This process is repeated as many times as the experiment requires to provide temporal information on the reaction of interest, without the loss of resolution associated with *in situ* techniques.⁴⁷

As a support electrode, BDD is proving useful. BDD has a large solvent window, is chemically inert to species such as oxygen and has low background currents making it an attractive material for electrochemical studies. BDD also has many useful physical and mechanical properties making it useful as a TEM electrode substrate. It is robust to radiation (i.e. the TEM beam), is electron transparent when thin enough and has extremely high thermal conductivity. BDD is thus ideal for both electrocatalyst and electrodeposition TEM studies. The initial proof of concept work using BDD TEM electrodes was carried out by Hussein *et al.* to follow the nucleation and growth of Au, from single atoms to nanoparticles.⁴⁷

The aim of this work is to investigate the nucleation and growth of Cu₂O nanocubes by electrodeposition using an IL-TEM method in combination with BDD TEM electrodes. The electrodeposition is carried out in a nitrate solution, free of additives,

allowing a quick and simple route to Cu₂O catalyst production. The CO₂RR activity is investigated using on-line electrochemical mass spectrometry (OLEMS) and the deactivation investigated using a time dependent *ex situ* TEM procedure. This will help inform on the synthesis and deactivation routes of this catalyst allowing better understanding for the design of improved CO₂RR catalysts and demonstrates the versatility of BDD TEM electrodes for this type of study.

6.3. Experimental

6.3.1. Solutions

All solutions were prepared using Milli-Q water (Millipore, deionised), with resistivity of 18.2 MΩ cm at 25 °C. All chemicals used as received without further purification. Deposition solutions consisted of 100 μM Cu(NO₃)₂ and 0.1 M KNO₃. Electrocatalysis of CO₂ (99.8%, BOC) was carried out in 0.1 M K₂CO₃ (pH 11) saturated with CO₂ gas by bubbling through solution for 30 mins, after an initial degassing by Ar bubbling for 1 minute per ml of solution. CO₂ bubbling was stopped and moved to flow over the surface of solution during electrochemistry to prevent solution agitation and maintain the concentration of CO₂ in solution during the experiment.

6.3.2. Electrochemistry

A three-electrode set up was used for all experiments. An SCE as the reference (RE) and a Pt wire as the counter (CE) for all except the OLEMS experiments where a high surface area Au electrode was used. In all cases the scan rate was 0.1 V s⁻¹. The working electrode (WE) used depended on the experiment and are detailed below. For CVs a 1 mm diameter BDD glass sealed electrode was employed. An Ivium compactstat potentiostat was used for these experiments. In the electrocatalysis experiments the potential difference is converted to the NHE to be comparable with literature.

6.3.3. OLEMS

The electrode used for OLEMS was a 10 x 30 mm rectangle of BDD polished on both sides. A 2x2 mm area at one edge was laser roughened then a Ti/Au contact sputtered on the roughened area. The contact was annealed for 5 hours in a 400 °C oven as for the glass sealed electrodes (see Chapter 2). The electrode was then contacted to a wire using silver epoxy. The wire was put through a hole in a subbaseal and the contact and wire sealed in 5-minute Araldite to fix to the subbaseal and protect the contact from solution. The subbaseal was then placed in a 3D printed lid that fits a glass dish. The subbaseal allowed the needle from the OLEMS system to be placed next to the electrode to collect the gasses evolved from the electrocatalysis reaction.

Electrochemical measurements were performed with an Autolab PGSTAT12, all solutions were purged with Ar before saturation with CO₂ gas. The pressure of the two chambers in the OLEMS were stabilised for 1 h prior to the experiment. Multi ion mass detection as a function of time was used. This enabled measurements of up to 6 channels in each experiment and a time difference of 50 ms between the detection on each channel. One of the channels was used to follow the changes in the total pressure and the other five channels were used to measure the following fragments: H₂, CH₄, C₂H₂, CO and H₂O. A secondary electron multiplier voltage of 1340 V was used for the samples of H₂O, CO, CO₂, C₂H₄ and CH₄ and 2100 for H₂. Due to the difference in size of the tip and the inlet and the different solubilities of the product species in the solution, a quantitative analysis to determine the faradic efficiency was not possible. It is also important to note that NMR analysis was unsuccessful and liquid products were not detected.

6.3.4. Electron Microscopy

6.3.4.1. SEM

A Zeiss Gemini FE-SEM, Warwick Microscopy RTP, was used to collect images of Cu₂O cubes on glass sealed BDD electrodes and the OLEMS electrode in in-lens mode at 2 kV and 2 mm working distance.

6.3.4.2. TEM

The BDD TEM electrode is a 3 mm disk with a hole in the centre, these were fabricated from freestanding BDD which was polished to $\approx 50\text{ }\mu\text{m}$ thickness using a scaife. To make the disks suitable for TEM they need to be electron transparent, this was achieved by ion milling using a GATAN precision ion polishing system (PIPS) by mounting on a post support using glycolphthalate bonding wax (Agar Scientific). Each side was milled with Ar^+ at a voltage of 6 kV and an angle of incidence of $\approx 4^\circ$ until a small hole (*ca.* 50 - 100 μm in diameter, approx. 2 hours each side) was formed in the centre of the BDD disk. A final low energy ion mill was done for both sides to smooth the surface at an accelerating voltage of 2 kV with a modulated ion beam. An Ohmic contact was made by masking all but approx. 0.5 mm of the outer edge and sputtering and annealing as previously described.

Electrical contact to the Au contact of the electrode was made with a pair of stainless-steel metal tweezers. An O-ring was used to keep the tweezers closed and hold the electrode in place. The tweezers were held by a custom-made fitting to allowed it to be fixed to a manual x,y,z micropositioner (Newport, Oxford, UK). The BDD TEM electrode was then dipped into the electrolyte solution such that the central hole was in the solution, but the Au contact remained dry, above the solution. The setup is shown in Figure 87. The CE is symmetrically placed around the WE to provide uniform current fields at both faces i.e. the front and the back face. The RE is positioned very closely at the side of the WE/CE to minimise ohmic drop.

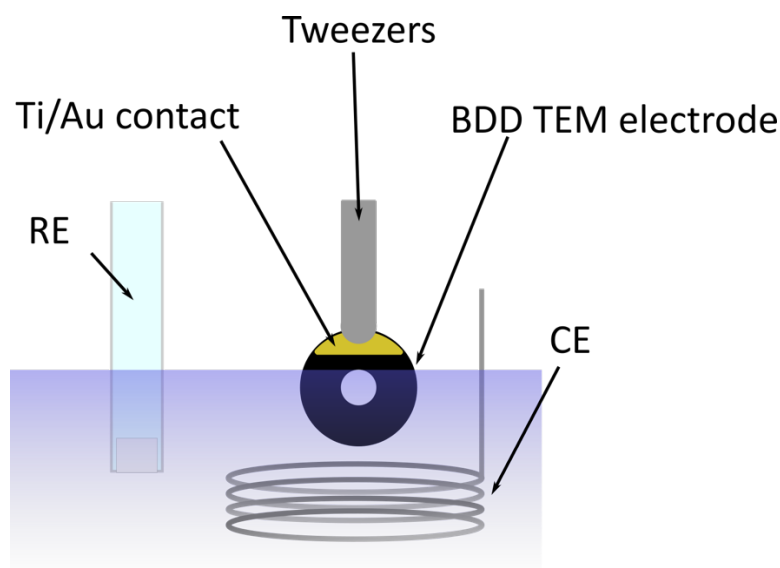


Figure 87 schematic of the electrochemical set up for the TEM samples. An SCE was the reference electrode (RE), a Pt counter electrode (CE), tweezers were used to connect to the Ti/Au contact on the BDD TEM electrode which was the working electrode.

Identical location scanning transmission electron microscopy (IL-STEM) tracking of metallic copper and copper Oxide electrodeposition

Immediately after electrodeposition, the BDD TEM electrode was gently rinsed by dipping it into a beaker of DI water ($18.2 \text{ M}\Omega \text{ cm}^{-1}$) and left to dry in a desiccator before imaging. The BDD TEM electrodes were stored under vacuum at 50°C for 6-8 h before transfer to the TEM instrument (i.e. this process is called bake out and it aims to minimise any hydrocarbon contamination and hence reduces the risk of surface contamination during long periods of imaging).

Surface characterisation using annular dark field - aberration corrected scanning transmission electron microscopy (ADF-ac-STEM)

The mechanism of Cu, Cu_2O nucleation and growth during the electrodeposition was investigated *ex situ* by IL-STEM in a double aberration-corrected JEOL JEM-ARM200F TEM/STEM, equipped with a Gatan Quantum spectrometer, operated at 200 kV. Please note electrodeposition occurred on both sides of the BDD TEM plate, and the ADF-STEM images provide depiction of the structures formed on both sides. ADF-STEM images were recorded with a probe current of 23 pA and a convergence semi-angle of $\sim 16 \text{ mrad}$. The inner collection semi-angle for ADF-STEM imaging was 38

mrاد. To confirm the chemical nature of the Cu, and Cu₂O electron energy loss spectroscopy (EELS) spectra were recorded, at a probe convergence semi-angle of 32 mrad and a spectrometer collection semi-angle of 25 mrad, and a dispersion of 0.1 eV per channel. The energy resolution of the EELS measurements was 1.2 eV, which was estimated from the full-width-half-maximum of the zero-loss peaks.

6.3.5. Data Analysis

ADF-STEM images were analysed using imageJ and Digital Micrograph software. ImageJ software was used to collect statistical information about size, perimeter, and number of nanostructures on the surface. Both imageJ and Digital Micrograph software were used to generate the FFT of high magnification and atomic resolution images for analysis. Digital Micrograph software equipped with EELS analysis package was used to analyse the EELS spectra.

6.4. Results and Discussion

6.4.1. Electrodeposition of Cu Cubes

The synthesis of Cu₂O cubes was carried out using electrodeposition by holding at a potential of -0.4 V vs SCE for 300 s in 100 μ M Cu(NO₃)₂ with 0.1 M KNO₃ (pH 5) aerated solution (Chapter 5), initially at a 1 mm glass sealed BDD electrode. Figure 88 (a) shows the resulting current time transient where the current drops quickly. After approximately 50 s the current reaches -0.8 μ A after which a gradual increase of the current is observed that may indicate growth of Cu materials on the surface. It is also important to note that since we are working in oxygen containing solution, once the Cu nanostructures are deposited, the oxygen reduction reaction (ORR) is also likely to be occurring, as discussed in Chapter 5.

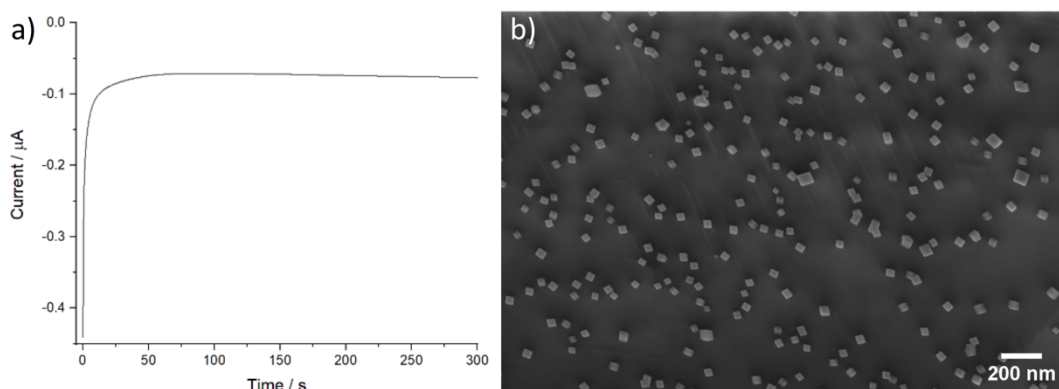


Figure 88 a) chronoamperogram of electrodeposition on a 1 mm diameter BDD glass sealed electrode from 100 μM $\text{Cu}(\text{NO}_3)_2$ in 0.1 M KNO_3 for 300 s at -0.4 V b) example SEM image of the deposit formed on the BDD electrode electrodeposited by the method described above.

By examining the surface after electrodeposition using SEM, the resultant deposits are shown to be cubic in shape, Figure 88 (b). Image analysis was conducted in 7 different areas (multiple electrodes and depositions) created with the same conditions, 3788 particles were analysed in total and the cubes had a median side length of 45 nm. A histogram of particle area is shown in Figure 89.

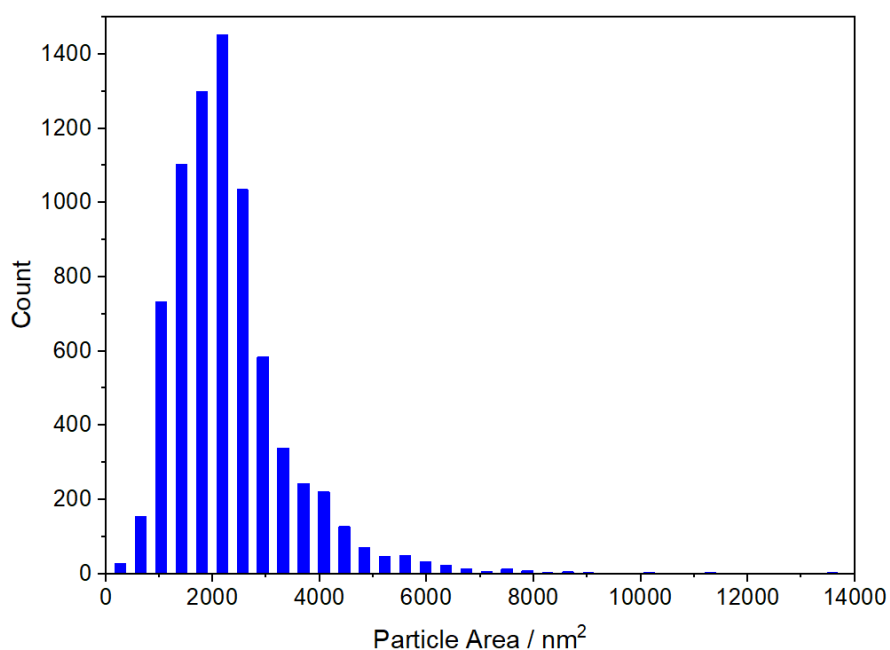


Figure 89 Histogram of particle area from samples made by electrodeposition on a 1 mm diameter BDD glass sealed electrode from 100 μM $\text{Cu}(\text{NO}_3)_2$ in 0.1 M KNO_3 for 300s at -0.4 V.

An interesting observation made during imaging was that there was a clear effect of BDD boron dopant density on particle size (Figure 90). Grains that appear darker in

the SEM image are more conductive as they contain more B from the BDD growth process. Lighter grains are less highly doped and are slightly more resistive as a consequence. For the fixed deposition potential of -0.4 V, the surfaces of the different grains will thus experience slightly different overpotentials for the electrodeposition reaction, resulting in more (dark) or less (light) facile electron transfer.

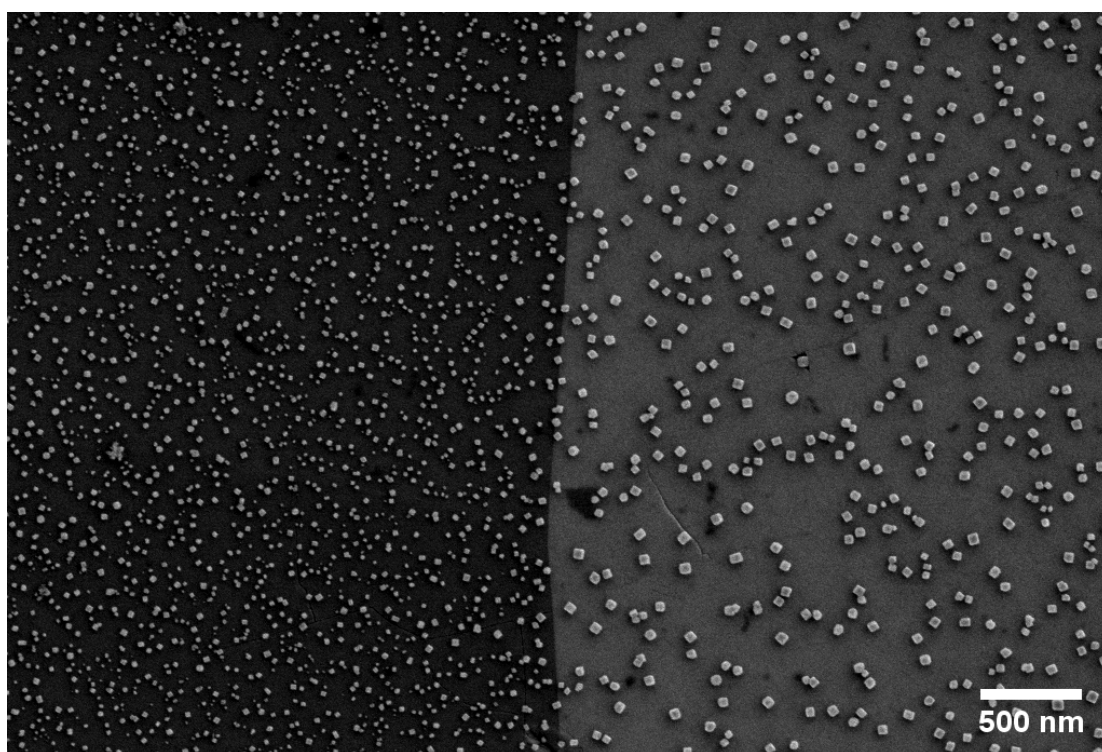


Figure 90 SEM image over two grains from a sample made by electrodeposition on a 10 x 30 mm rectangle of double sided polished BDD electrode (OLEMS electrode) from 100 μM $\text{Cu}(\text{NO}_3)_2$ in 0.1 M KNO_3 for 3 depositions of 300 s at -0.4 V.

An increased nucleation density is observed for the darker grains resulting in smaller size cubes, whilst the opposite is true for the lighter grains. The two different distributions are shown in Figure 91. The surface of the BDD is polished prior to use and the resulting surface is [110] textured.^{47,49} In catalysis narrow size distributions are often preferred as different size particles can exhibit different product ratios.⁵⁰ Polycrystalline BDD does provide an opportunity to study different sized nanostructures within one electrode, especially useful in TEM morphological and chemical studies. The data also shows that subtle changes in overpotential (caused by the different dopant densities on different grains in this scenario) may be useful for controlling cube size.

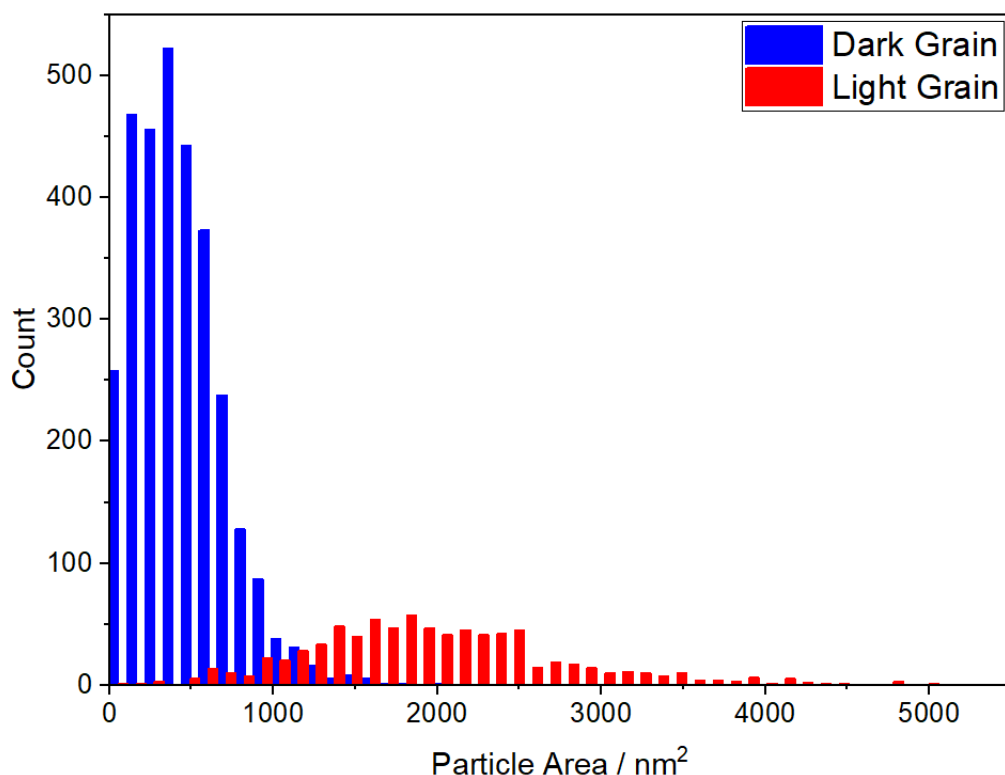


Figure 91 Histogram of particle area from SEM images from samples made by electrodeposition on a 1 mm diameter BDD glass sealed electrode from 100 μM $\text{Cu}(\text{NO}_3)_2$ in 0.1 M KNO_3 for 300s at -0.4 V. Blue shows particles from dark grains, red light grains.

Table 4 shows the nanocube statistics for the two different boron dopant density zones investigated on the electrode. Both the median area and size distribution are larger on the lower doped grains. Assuming cubic shape, the average side length on higher doped grains is 21 nm and 44 nm for lower doped grains. The data was taken from 2 images, in total 793 particles were analysed from the lighter grains and 3079 from the darker grain.

Table 4 Particle statistics summary from data in Figure 91. Median side length calculated assuming cubic particles

	Median Area / nm^2	Quartile 1 / nm^2	Quartile 3 / nm^2	Median side length / nm
Dark grain	382.4	226.0	593.4	19.6
Light grain	1893.1	1469.3	2401.7	43.5

the finger print for Cu in the +1 oxidation state, thus proving that the nanocube is Cu₂O.^{52–54}

Cu₂O is simple cubic (space group *pn3m*) with 4 Cu and 2 O atoms forming its basis, and a lattice parameter of 4.269 Å. The Cu atoms in Cu₂O form a face-centred cubic (fcc) lattice and the O atoms form a body-centred cubic (bcc) lattice, where each O atom is surrounded by a tetrahedron of Cu atoms. This is further confirmed by indexing the experimentally obtained rectangular diffraction patterns FFT (see Figure 92 (c)) to the diffraction planes of the single crystal structure of cubic Cu₂O, which matches the simulated FFT along the [100] axis.⁴² The atomic-resolution STEM images of a small nanocube (7 × 7 nm) is viewed from one of its {100} faces. At the corner of this nanocube, visible lattice fringes with d-spacings of 2.45 Å was determined and correspond to the (111) lattice planes of Cu₂O. Over the central region of this nanocube face, two perpendicular sets of lattice planes with the same d-spacings of 3.00 Å were obtained. These planes correspond to the (110) lattice planes of cubic Cu₂O, and point to the edges of this truncated nanocube. These data provide information about the chemical bonding of these nanocubes and confirm that the particles are single crystalline Cu₂O. By examining multiple nanocubes, we also confirm no sign of metallic Cu or other Cu species such as CuO or CuOH. For comparison the FFTs of Cu⁰ and Cu₂O is shown in Figure 93 along the [100], [110] and [111] directions.

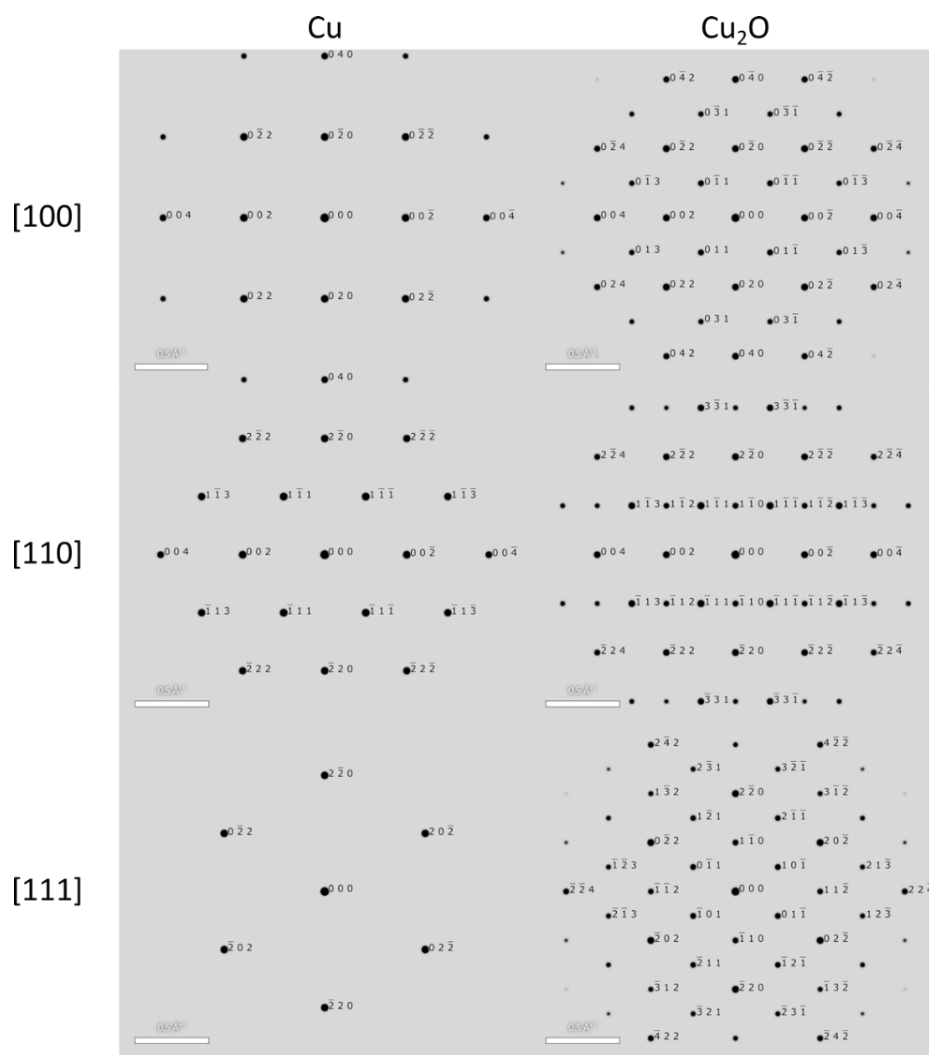


Figure 93 FFT simulations of Cu^0 and Cu_2O along the $[100]$, $[110]$ and $[111]$ directions.

Previous studies have investigated the electrodeposition of Cu_2O nanocubes. Lu and Tanaka³⁹ conducted an *in situ* TEM study on the electrodeposition of Cu_2O nanocubes on amorphous carbon from sulfate and perchlorate solutions (pH 2). They found that Cu_2O exclusively formed at potentials positive of -0.55 V (vs SCE) and deduced that the potential was not sufficient to form $\text{Cu}(0)$. They found that as they increased the overpotential, both Cu and Cu_2O were formed. They also investigated the effects of different anions and found that the addition of chloride ions and sulfate ions affects the crystal shape by stabilising Cu^+ and interacting with the Cu_2O surface, respectively, in this case resulting in the loss of the cube morphology. They determined that the oxygen in the Cu_2O came from H_2O , rather than dissolved oxygen as even in deoxygenated solutions Cu_2O was formed. The spatial resolution in this

study was poor and no surface detail or lattice images of the particles could be obtained.

Very recently in 2020 Arán-Ais *et al.* performed an *in situ* investigation of the nucleation and growth of Cu₂O nanocubes in sulfate electrolyte with the addition of chloride.¹⁹ They showed that during cyclic voltammetry, cubes began to grow before other morphologies were seen. On the positive scan other morphologies dissolved, while cubes were stable over a wider potential range. They found that at low pH and in the absence of chloride, no cubes were formed. These results are in contrast to Lu and Tanaka,³⁹ but a direct comparison is difficult due to the number of differences between studies. The resolution through liquid is poor and as such little information could be gathered about the early stages of cube nucleation and growth. These studies show how easily different morphologies can be obtained in similar conditions and that several conditions may lead to cubic Cu₂O, demonstrating the need for further investigation to gain better understanding of Cu₂O cube electrodeposition. The expected potential for Cu₂O deposition (Equation 78) according to Equation 81, for a pH 5 and [Cu²⁺] = 1 x 10⁻⁴ M is -0.018 V (vs SCE). This means that a deposition potential of -0.4 V is a 0.382 V overpotential for this reaction.

6.4.2. Identical location STEM study of growth

IL-STEM is used here to track the particle growth and speciation of specific particles through the electrodeposition process during the first 20 s of growth. This is only possible due to the robust nature of the BDD TEM electrode, which enables the repeated switching between electrochemistry and ac-ADF-STEM imaging and allowing tracking of individual particles.⁴⁷ Using the same substrate for electrodeposition and imaging removes the need to disturb or transfer the particles from one substrate to another in order to image them which could cause damage or unforeseen changes to the particles. Electrodeposition was stopped after 1 s, the electrode removed from solution and imaged by ac-ADF-STEM, then returned and the electrodeposition continued. The experiment was stopped twice more, at 10 s (9 s of extra deposition time) and 20 s (10 s of extra deposition) and the same area

imaged. Figure 94 shows the three chronoamperograms and Figure 95 the three ac-ADF-STEM images recorded in the same area at times of 1 s, 10 s and 20 s growth, which depict the identical location tracking of the electrodeposition process.

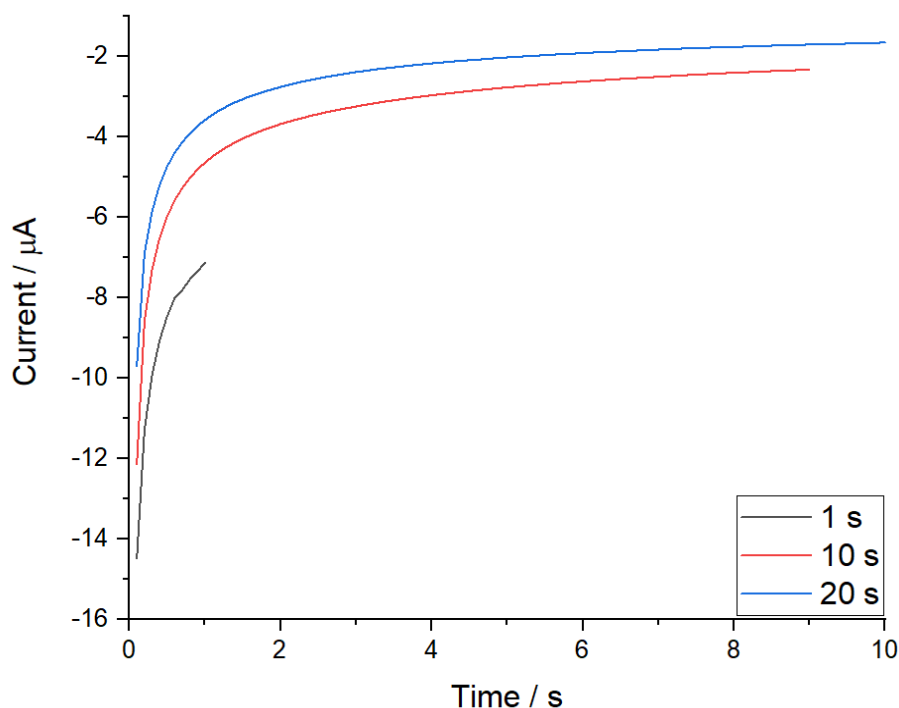


Figure 94 Chronoamperograms of the 1, 10 and 20 s steps of electrodeposition for the IL STEM growth study on the BDD TEM electrode, deposited from $100 \mu\text{M Cu}(\text{NO}_3)_2$ in 0.1 M KNO_3 at -0.4 V .

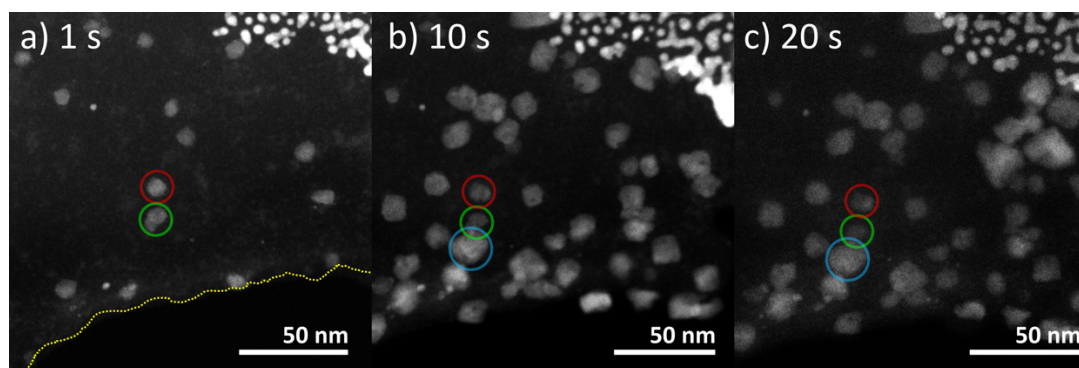


Figure 95 ac-ADF-STEM image of the BDD TEM electrode after a) 1 s, b) 10 s, c) 20 s of electrodeposition of Cu_2O from $100 \mu\text{M Cu}(\text{NO}_3)_2$ in 0.1 M KNO_3 at -0.4 V . Red circle denotes particle 1, green, particle 2 and blue, particle 3. The yellow dotted line shows the edge of the hole (vacuum) in the BDD TEM electrode. The bright particles in the top right corner are Au nanoparticles that were used to help locate the area.

Figure 95 presents low magnification ac-ADF-STEM images, which demonstrate imaging the same location after each deposition experiment. The distinct shape of the edge of the hole in the BDD (see the yellow demarcation line between the BDD and the vacuum in Figure 95 a) and the Au nanostructures at the top right of the

images act as identical location markers. In ADF-STEM mode, the images are Z-contrast dependent images hence Au particles appear brighter than Cu particles. The Au is likely to be there due to the ion milling process also redepositing some of the Au on the surface. However, will not affect the results observed. After 1 s of electrodeposition there are only a few particles visible, of around 2-10 nm in length. In each of the 10 s and 20 s images more particles have formed. Table 5 shows the average particle area and the first and third quartiles of the size distribution.

Table 5 particle size statistics for the electrodeposition IL STEM growth study. Median side length calculated assuming cubic particles.

Time / s	Median Area / nm²	Quartile 1 / nm²	Quartile 3 / nm²	Median side length / nm
1	12.0	0.7	33.0	3.5
10	51.9	11.7	93.1	7.2
20	36.2	2.8	100.7	6.0

Table 5 shows that the average size of the particles increases from 1 s to 10 s but decreases after 20 s. The interquartile range of the particle size distribution is increasing as the deposition time progresses. Figure 96 shows this data as a histogram.

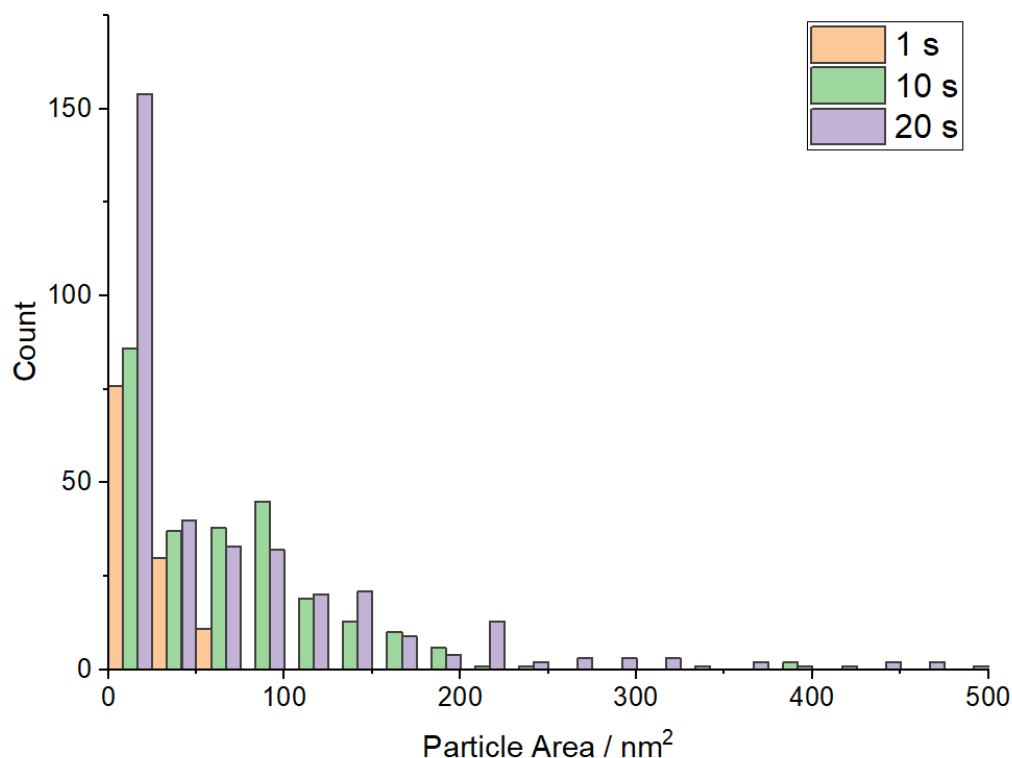


Figure 96 Histogram of particle area of the particles in the IL STEM growth study.

For the 1 s data 5 images and 117 particles were analysed, for 10 s, 5 images and 259 particles and for 20 s, 6 images and 346 particles. This shows that some particles grew throughout the experiment and as new particles were nucleated there remained a considerable number of small particles, this contributed to the increasing spread of the distribution.

A more in-depth analysis of the fate of these particles over the experiment is shown in Figure 97, Figure 98 and Figure 99. Figure 97 (top) shows a high magnification ac-ADF-STEM image and (below) the FFT analysis of the same particle, particle 1, at 1 s, 10 s and 20 s; red circle in Figure 95.

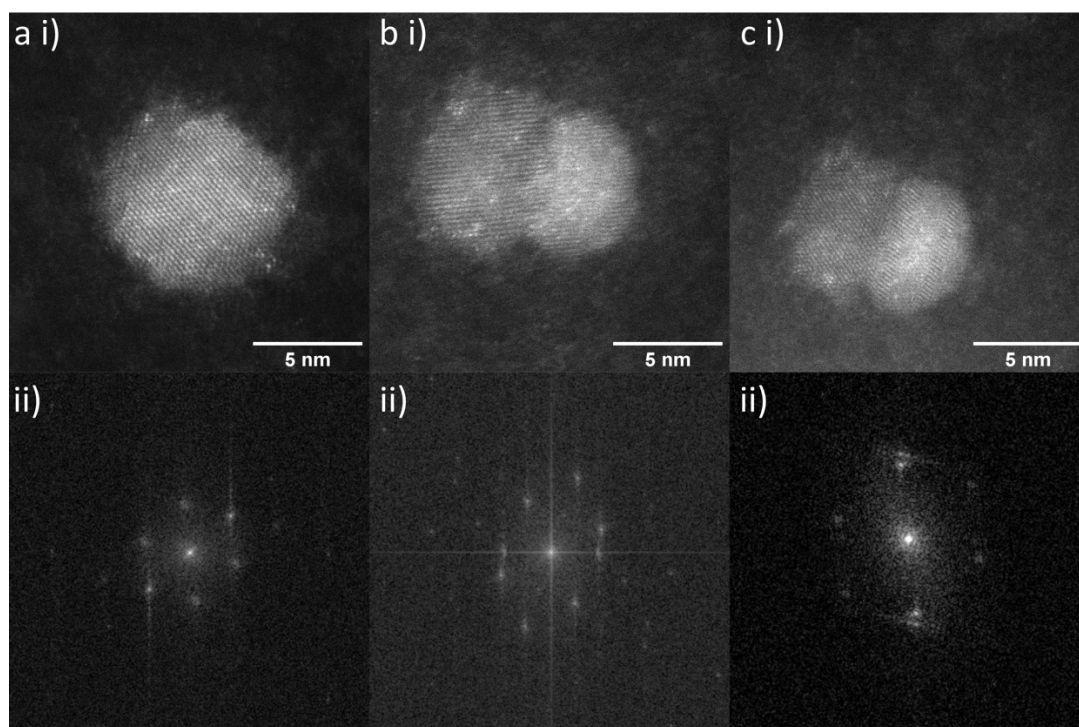


Figure 97 High magnification ac-ADF-STEM image of particle 1 after a i) 1 s, b i) 10 s and c i) 20 s ii) respective FFTs of particle 1, deposited from $100 \mu\text{M Cu(NO}_3)_2$ in 0.1 M KNO_3 at -0.4 V .

At 1 s, only one particle is present; particle 1. The FFT analysis shows that the particle is metallic Cu, Cu^0 , the experimental data fits well with Figure 93 a). At 10 s, particle 1 is still present but there is now a second particle. The second particle is slightly out of focus compared to particle 1 (the out of focus particles are not numbered). The FFT shows signals from both particles in Figure 97 bii). Such events are not uncommon as the BDD TEM electrode is double sided and as such electrodeposition can occur on either side. For all 3 times, particle 1 is metallic Cu as proved by the FFTs, along the [111] axis.

Figure 98 shows higher magnification images of another particle, particle 2 (see green circle Figure 95) at (a) 1 s (b) 10 s and (c) 20 s. Again, there is the presence of a second particle on the other side of the BDD TEM electrode. At 10 s another particle is present on the in-focus side of the TEM electrode, this is particle 3 (see blue circle Figure 95).

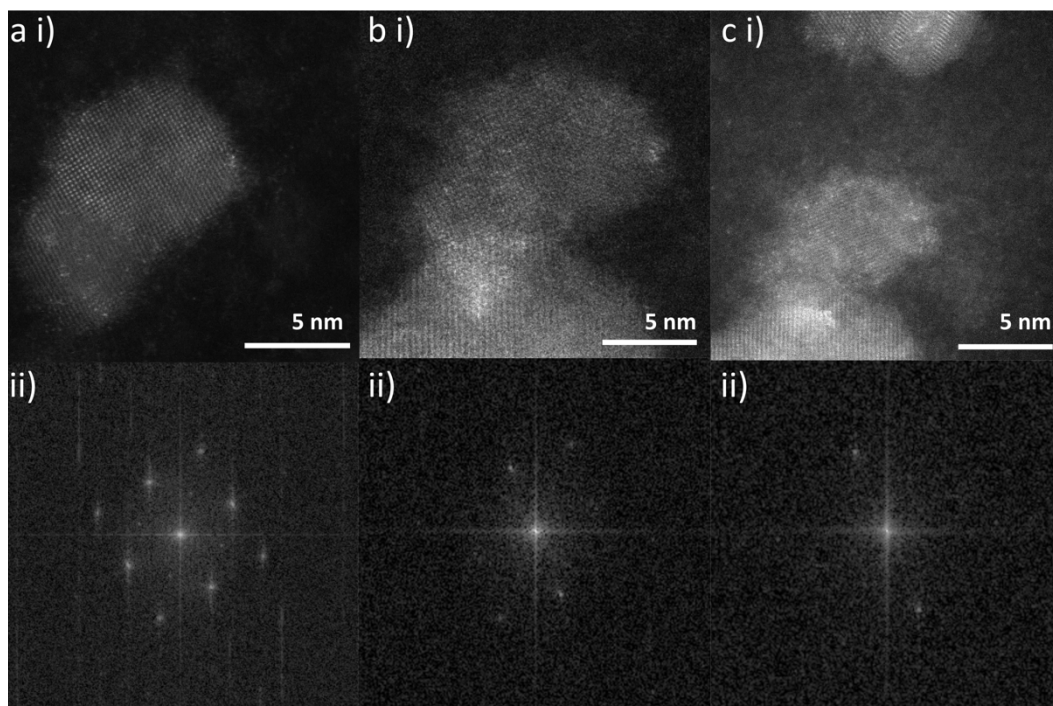


Figure 98 High magnification ac-ADF-STEM image of particle 2 after a i) 1 s, b i) 10 s and c i) 20 s ii) respective FFTs of particle 2, deposited from 100 μM $\text{Cu}(\text{NO}_3)_2$ in 0.1 M KNO_3 at -0.4 V.

Particle 2 grew to during the 1st second of deposition but between 1 s and 10 s decreased in size. FFT a ii) shows a cubic structure, in the [110] orientation. This particle is also metallic Cu in all 3 time points. Particle 3 (Figure 99) was not present at 1 s, its growth was followed after 10 s and 20 s only.

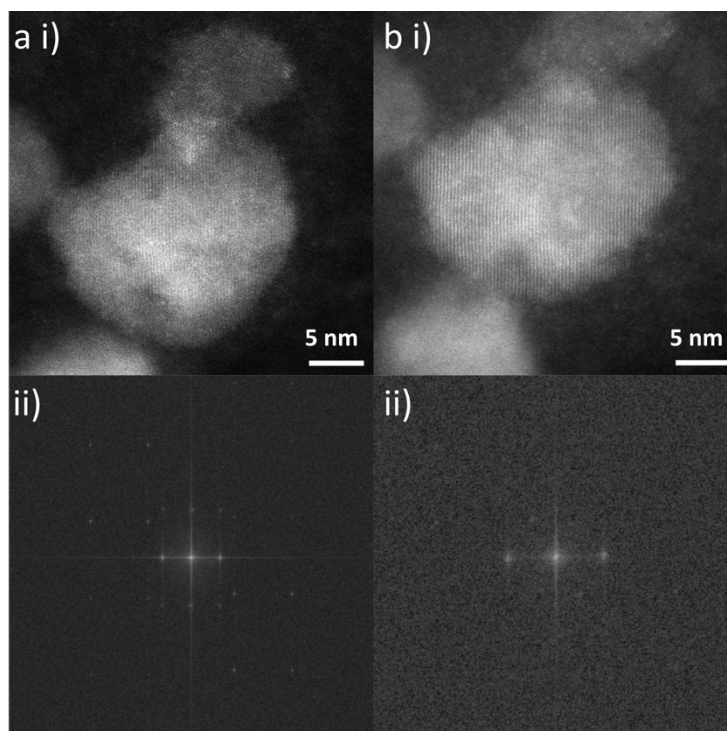


Figure 99 High magnification ac-ADF-STEM image of particle 3 after a i) 10 s and b i) 20 s ii) respective FFTs of particle 3, deposited from 100 μM $\text{Cu}(\text{NO}_3)_2$ in 0.1 M KNO_3 at -0.4 V.

FFT shows that particle 3 is Cu_2O , whilst it grows in size from 10 s to 20 s, particle 2 is decreasing in size over the same time frame.

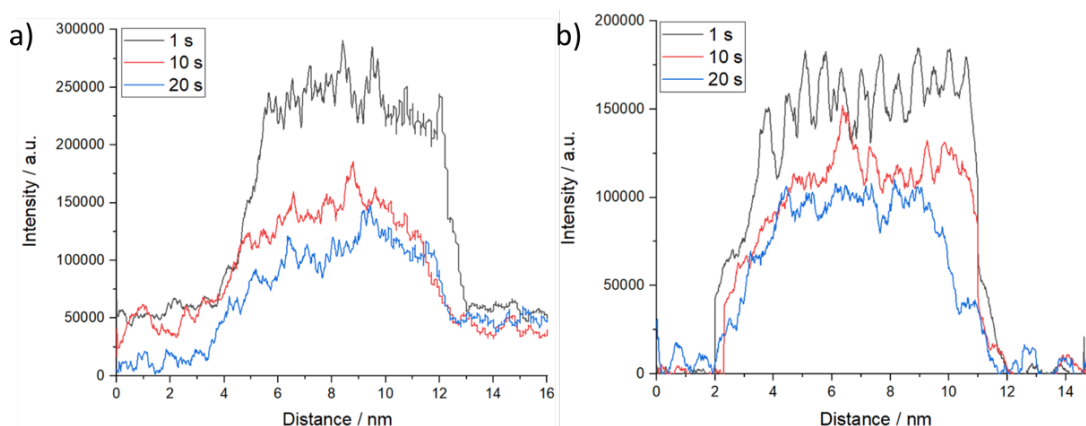


Figure 100 shows intensity vs distance plots for particles 1 and 2 from the ac-ADF-STEM images. Intensity is used as an indicator of particle thickness, the higher the intensity the thicker the particles. Both particles, which are Cu^0 , decrease in size, both by area and thickness over the course of the experiment.

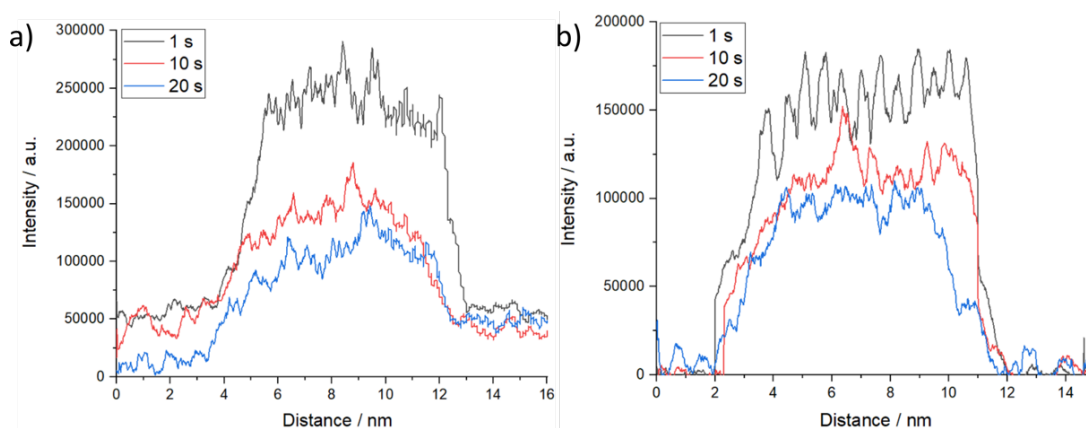


Figure 100 Intensity vs distance plots from the TEM images of a) particle 1 b) particle 2.

From this data it can be seen that some particles nucleated then decreased in size whilst others nucleated and continued to grow. The particles that decreased in size are Cu^0 whereas the particles that grew were Cu_2O . It is proposed that the potential held (in these conditions) was sufficient to nucleate both Cu^0 and Cu_2O , but Cu^0 was

not stable and dissolution of these particles occurred. Cu_2O , however, was stable and was able to continue growing, explaining the observation that only Cu_2O particles are present after the 300 s deposition in section 6.4.1. This is in agreement with other research using different solution conditions containing more than one electrolyte anion.^{19,39} The thermodynamic potentials for Cu_2O formation is -0.018 V and that for Cu^0 is -0.140 V (vs SCE, $[\text{Cu}^{2+}] = 1 \times 10^{-4}$ M). Both do not take into account kinetic factors such as deposition is on BDD rather than on Cu_2O or Cu^0 itself and the occurrence of other potential reactions, as discussed in Chapter 5, that could interfere.

6.4.3. Electrocatalysis

Cu_2O cubes have been shown to be catalytic to the CO_2RR , to test the catalytic activity of these cubes a higher coverage was required. This was achieved by repeating the deposition from section 6.4.1 three times. Figure 101 shows the chronoamperogram of deposition and an SEM image of the deposits produced on the BDD OLEMS electrode (10 x 30 mm double sided polished BDD rectangle).

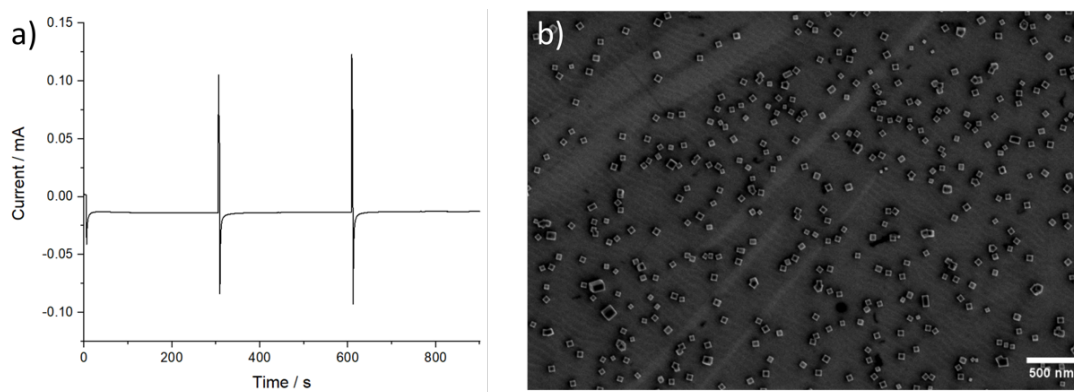


Figure 101 a) chronoamperogram of the electrodeposition of Cu_2O for OLEMS, deposition was 3x -0.4 V for 300 s steps with 5 s intervals (OLEMS method), b) SEM of the Cu_2O modified BDD surface, from 100 μM $\text{Cu}(\text{NO}_3)_2$ in 0.1 M KNO_3 .

Image analysis was conducted to see how the size and size distribution varied between the 1x deposition and the 3x deposition, Figure 102. Differences in grain were not taken into account in this study, but a range of areas were imaged to get representative statistics of the whole surface. This image analysis was collected from 75 images and 53118 particles, the data from Figure 89 is also included for comparison.

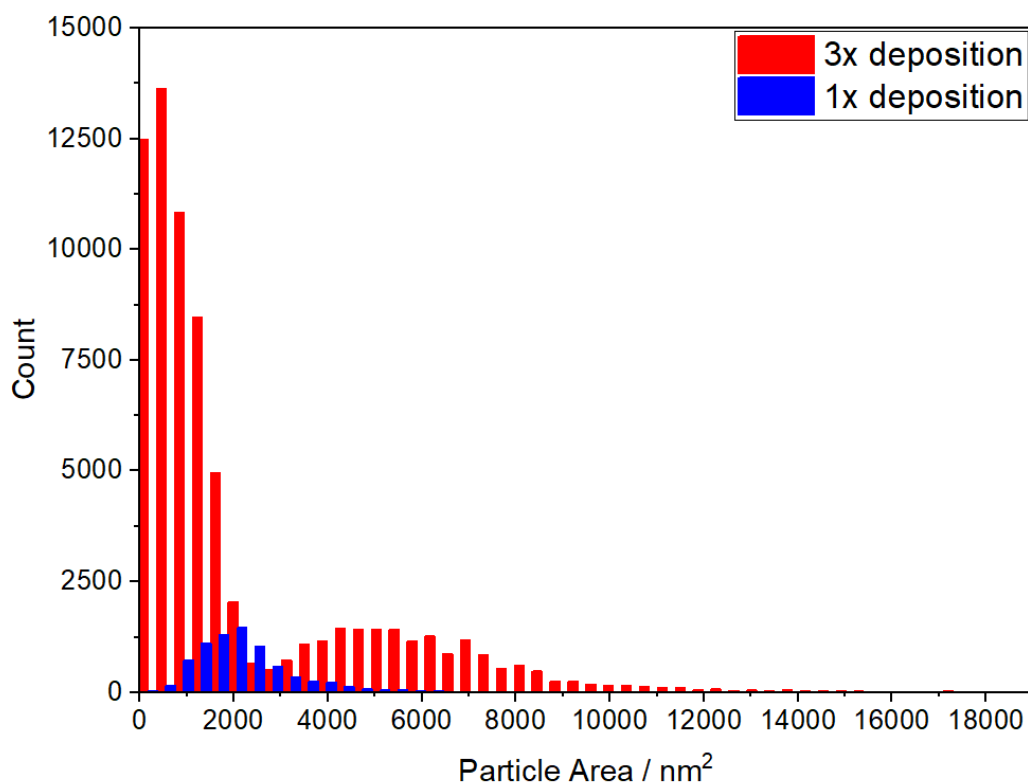


Figure 102 Histogram of particle areas from blue – the 1x method deposition and red – the 3x deposition.

Table 6 Particle size statistics for the 1x and 3x depositions. Median side length calculated assuming cubic particles.

Deposition method	Median Area / nm ²	Quartile 1 / nm ²	Quartile 3 / nm ²	Median side length / nm
1x	2064.166	1501.212	2627.1209	45.4
3x	1071.385	517.268	2722.03	32.7

This shows that the average particle size is smaller for the 3x deposition method, this is possibly due to there being repeated nucleation at the start of each of the 3 depositions. It appears that there are at least 2 particle size distributions present in the 3x deposition size data, which has the effect of significantly broadening the size distribution compared to the 1x method. However, the effect of differently doped grains cannot be discounted as a possible effect on the distributions.

To test the electrocatalytic activity of these cubes CVs were run in a 0.1 M K₂CO₃ solution (pH 9) with a blank BDD 1 mm glass sealed electrode, 3x deposited Cu₂O modified electrode in a degassed solution and 3x deposited Cu₂O modified BDD in a

CO₂ saturated solution at 0.1 V s⁻¹ starting from 0 V and commencing in the negative direction out to -2 V (vs NHE) (Figure 103).

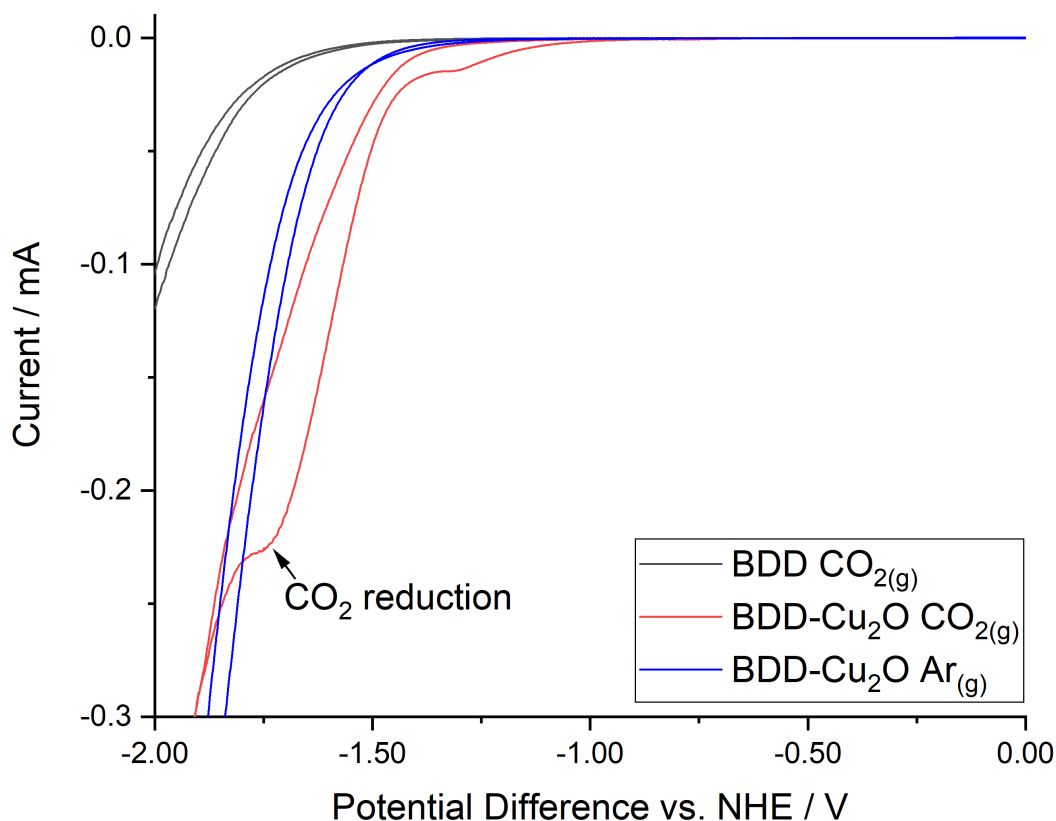


Figure 103 CV in 0.1 M K₂CO₃ solution at 0.1 V s⁻¹ black line) blank BDD in CO₂ saturated solution, red line) Cu₂O modified BDD in CO₂ saturated solution and blue line) Cu₂O modified BDD in degassed solution (with Ar). BDD electrode was 1 mm diameter. All CVs are the first scan.

The Cu₂O modified BDD shows two CO₂ related reduction signals, one at -1.25 V and a second larger one at -1.75 V. The CO₂RR was expected at around -1.75 V. It is currently unclear what the smaller peak is due to. These signals are not present in the argon bubbled solution or on the blank BDD. From this it was decided that the optimal potential for electrocatalysis was -1.9 V vs NHE (-2.3 V vs SCE, pH 9).

To investigate the products of this reaction OLEMS experiments were conducted, which required considerable refining of the set-up. Two configurations were trialled, a tip system and a headspace system. The tip system was attempted first and consisted of a tip in solution covered with a gas permeable membrane that was held close to the electrode surface during electrocatalysis. The tips were prone to failure and the electrodes initially used (1-5 mm diameter BDD rounds) did not produce

sufficient OLEMS signal. The larger rounds were sealed in PEEK with epoxy but were susceptible to rapid degradation due to the solution conditions (pH) and electrodes repeatedly failed by loss of contact.

Electrode size was limited in this set up by the diameter of the neck of the vessel containing the tip equipment and that the electrode must be held perpendicular to the tip. The headspace configuration collected the product gasses above the solution surface by way of a needle. This allowed the use of a significantly larger electrode (more signal) as the glassware set-up and electrode positioning was more flexible and did not rely on a membrane. For this, a rectangle of 30 x 10 mm double sided polished BDD electrode was initially sealed into a 3D printed cap. However, keeping this cap stable and in contact with the solution surface was difficult and so the BDD electrode was sealed into a subbaseal which was placed in a 3D printed lid to hold it in place over the solution, Figure 104. Due to this set up exact electrode area in contact with the solution was difficult to determine.

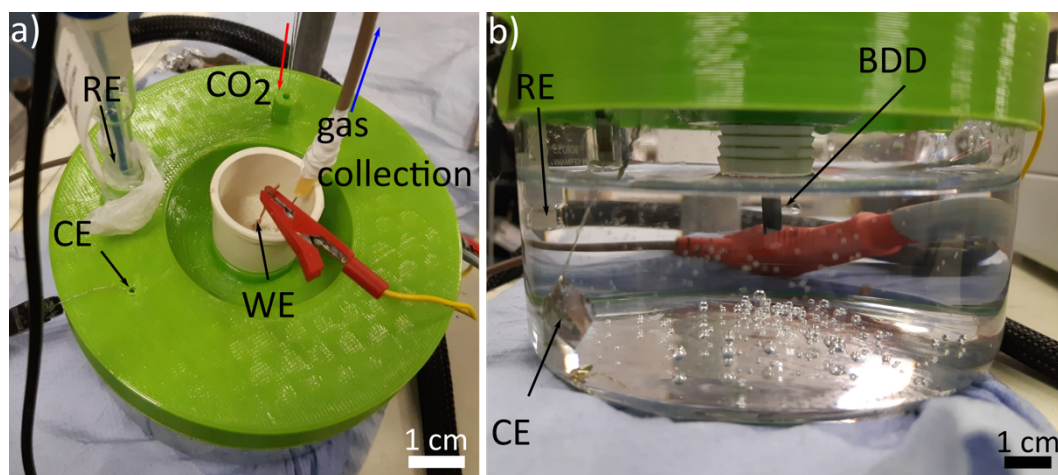


Figure 104 Photograph of the OLEMS headspace set up showing from a) above and b) side on. Showing working electrode (WE, BDD), reference electrode (RE), counter electrode (CE), CO₂ gas line in and product gas collection line out of the cell. The subbaseal is making contact with the surface of solution so that the product gasses collect in the space above the BDD working electrode for collection.

A background run was conducted in the exact same solution and set up but with a clean BDD electrode and 3 repeats on the Cu₂O modified BDD (Figure 105).

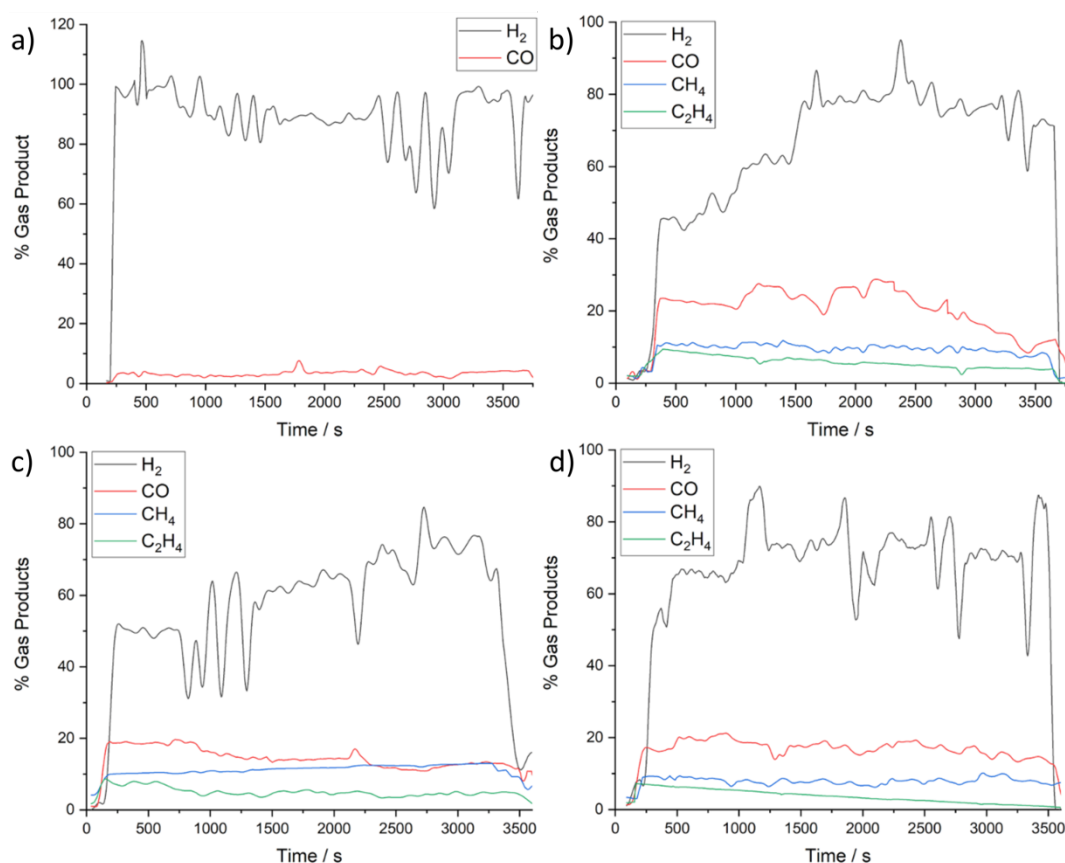


Figure 105 OLEMS product gas composition results in CO_2 saturated $0.1 \text{ M K}_2\text{CO}_3$ solution, $10 \times 30 \text{ mm}$ double sided BDD electrode held at -1.9 V vs NHE for 1 hour a) blank BDD electrode b), c) and d) 3 repeats of OLEMS on a Cu_2O modified BDD electrode.

These experiments show that $\text{H}_2(\text{g})$ and $\text{CO}(\text{g})$ are the main products in both the blank and Cu_2O modified experiments. The Cu_2O experiments also produced $\text{CH}_4(\text{g})$ and $\text{C}_2\text{H}_4(\text{g})$ which are desired products from this reaction. The graphs are presented as % of gas product. This was obtained through the relationship between the partial pressure of each gas and the total pressure of the system. The calibration, baseline correction (water pressure changes correction) and determination of each partial pressure are described in references 55–57. Due to the experimental limitations of the equipment (number of channels/species measured per experiment), not all of the products could be analysed and therefore for the faradaic efficiency for each of the products cannot be calculated. NMR was carried out on solutions after the experiment, but the products were not concentrated enough to be detected and so only gas products could be determined. Hence, as not all products could be analysed, faradaic efficiencies could not be calculated and the OLEMS results are therefore not quantitative. The interesting result here is that over time, the ratios of useful

products decreases over time, suggesting that there is either a loss or a deactivation of the catalyst occurring. This is an effect that has been reported in literature.¹⁶ In order to investigate this result the electrode was imaged in SEM (Figure 106) after 1 hour of electrocatalysis.

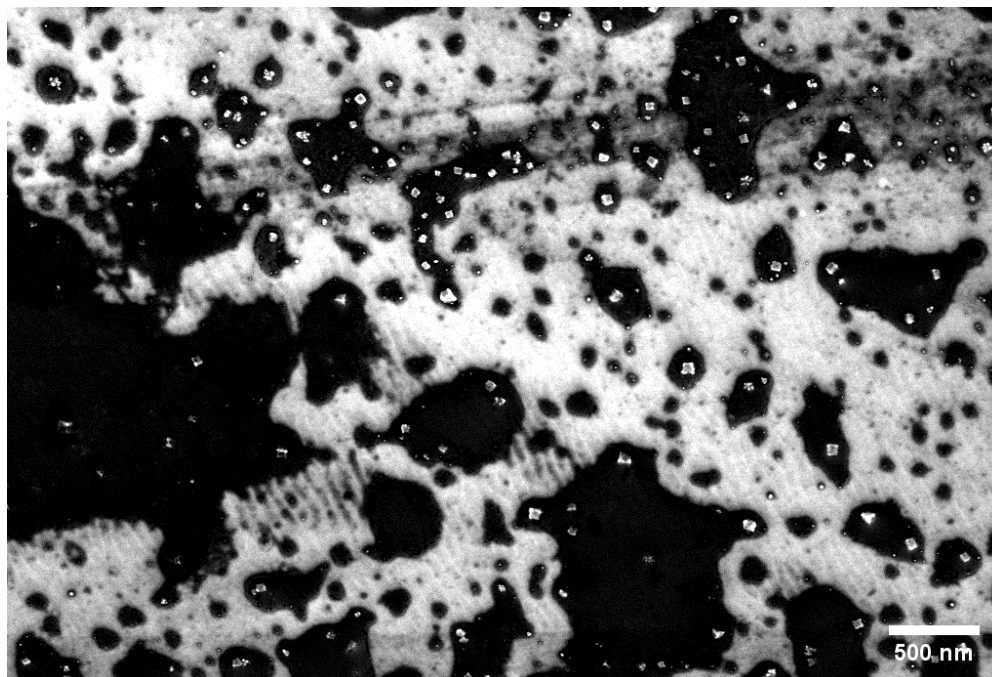


Figure 106 SEM of Cu₂O modified BDD after 1 hour of electrocatalysis in CO₂ saturated 0.1 M K₂CO₃ solution at -1.9 V vs NHE.

SEM shows that number density has decreased, indicating that detachment is a factor in the deactivation of this catalyst, it also appears that there could be a shape change element but due to the organic residues on the surface (presumably from the CO₂RR) this is hard to determine in SEM. To further investigate the mechanism of deactivation of the catalyst an *ex situ* TEM study was conducted.

6.4.4. TEM of dissolution by electrocatalysis

TEM study was conducted on Cu₂O modified BDD TEM electrodes after 10 s and 3600 s of CO₂RR electrocatalysis (Figure 107). It is important to note that this study was not an IL study and images shown are different areas on the electrode, of the same BDD TEM electrode. This study showed that after only 10 s of electrocatalysis agglomeration and fragmentation of the particles has begun but the cubic shape is still generally recognisable. Lots of small particles can be seen on the BDD between the cubic particles.

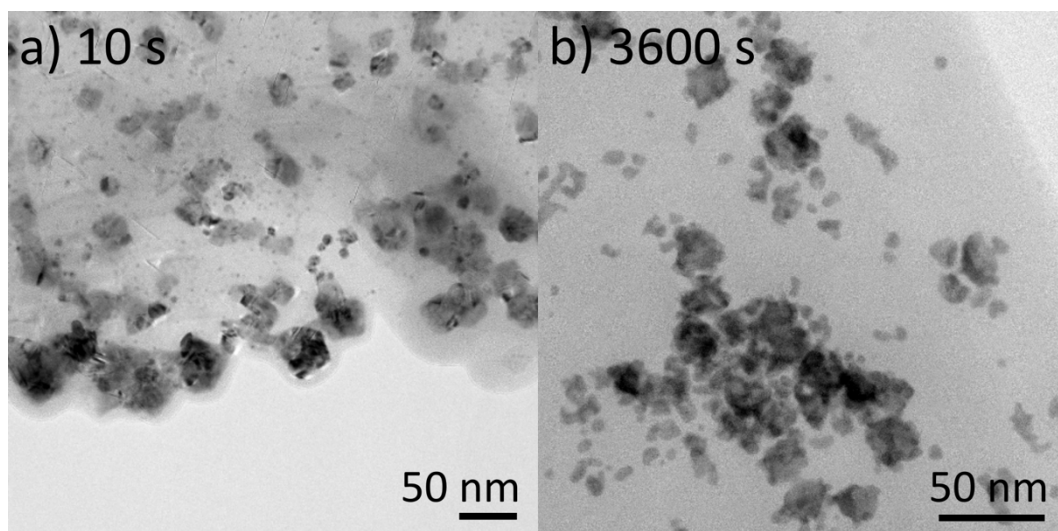


Figure 107 Cu_2O modified BDD TEM electrode after a) 10 s and b) 3600s (1h) of CO_2RR electrocatalysis in CO_2 saturated 0.1 M K_2CO_3 solution at -1.9 V vs NHE.

After 3600 s of electrocatalysis the cube shape has disappeared, there again has been an increase in agglomeration. The large particles have come together and begun to fragment further; the smaller round particles seen at 10 s have decreased in number. There has been a significant loss of material from the electrode surface. Figure 108 shows the high magnification images and FFT of 3 particles from 10 s and from 3600s.

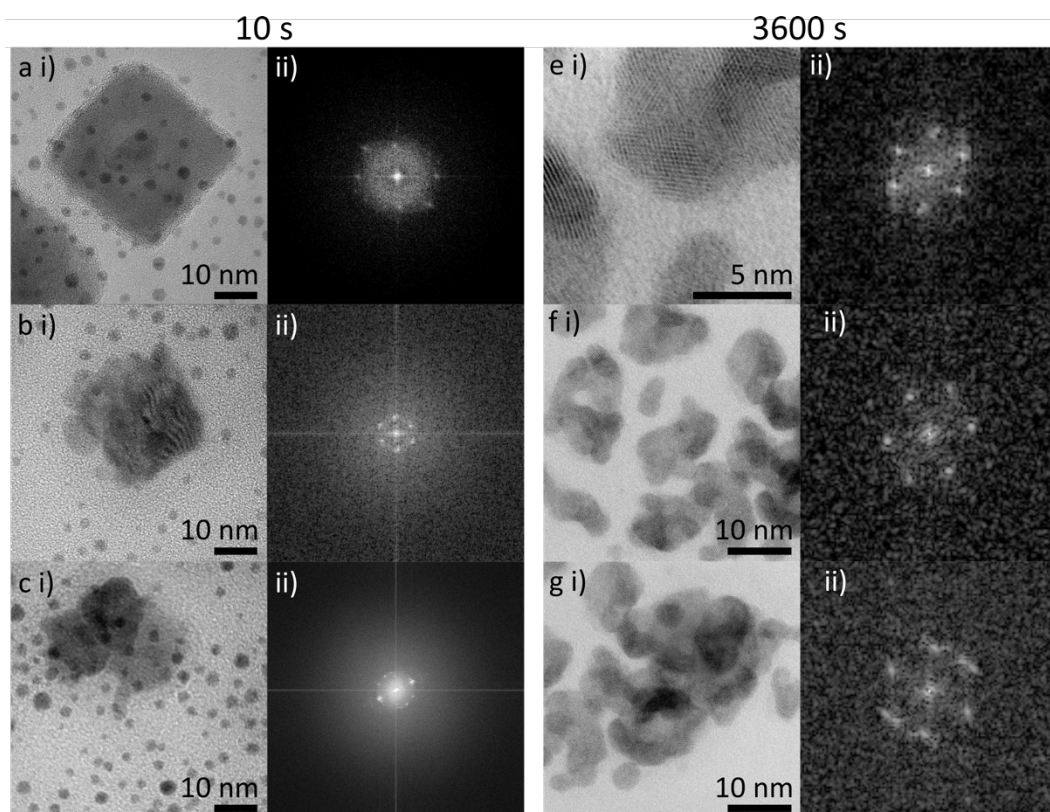


Figure 108 High magnification TEM images of nanoparticles on a Cu_2O modified BDD TEM electrode after a) 10 s and b) 3600 s of CO_2RR electrocatalysis in CO_2 saturated 0.1 M K_2CO_3 solution at -1.9 V vs NHE.

The FFT after 10 s and 3600 s of electrocatalysis show that the speciation of the particles has changed from Cu_2O to Cu^0 , along the [111] axis. This is likely due to the high negative potential held during CO_2RR causing an electrochemical reduction of the nanoparticles.

This study showed that the cubes quickly underwent drastic changes to their shape, speciation and distribution on the surface, it looks as though detachment or loss of material could be a major factor, as well as the changes in morphology and speciation, in the deactivation of this particular system.

6.5. Conclusions

Cu_2O cubes were formed from a 100 μM $\text{Cu}(\text{NO}_3)_2$ and 0.1 M KNO_3 solution at -0.4 V vs SCE for 300 s. SEM Image analysis showed that polycrystalline diamond, due to its range of doping of grains gives a range of cube sizes. It was found that deposition on

a darker, highly doped grains, gave an average particle size 55% smaller than on a light, lower doped grain. The average particle side length (all grains) was 45 nm for the 300 s deposition. The characterisation of the nanocubes by TEM demonstrated that the nanocubes are single crystal Cu_2O with a [100] orientation.

The IL STEM study was used to focus on short times up, to 20 s in the growth process. This showed that nucleation of new particles occurred at all 3 time points investigated, many of the particles continued to grow after nucleation but some decreased in size. It was shown that Cu^0 particles decreased in size and Cu_2O particles continued to grow. The average particle size increased from 3.5 nm side length at 1 s to 7.2 nm at 10 s then decreased to 6 nm at 20 s. The interquartile range of the distribution increased with each time point reflecting the new nucleation and continuous particle growth. It was postulated that Cu^0 particles were not stable at this potential and that Cu_2O was, resulting in the loss of all Cu^0 particles over time leaving exclusively Cu_2O on the surface. This agrees with *in situ* literature and is important for understanding the early stages of Cu_2O nanocube growth as greater spatial resolution has been achieved here than is currently possible *in situ*.

The electrodeposition method for the first section was repeated 3 times for the OLEMS experiments to increase the catalyst loading. Image analysis showed that the average side length of these particles was 32.7 nm. CVs in a 0.1 M K_2CO_3 solution saturated with CO_2 showed that the Cu_2O modified BDD is catalytic to the CO_2RR and an electrolysis potential of -1.9 V (vs NHE) was selected for OLEMS experiments.

OLEMS experiments showed that BDD alone produces mainly H_2 and CO were produced on blank BDD whereas Cu_2O modified BDD also produced CH_4 and C_2H_4 . The OLEMS experiments showed that product ratios became progressively worse over the course of the 1 hour experiment, which prompted investigation into the deactivation of these catalysts.

The deactivation of the Cu_2O nanocubes was studied by TEM using BDD TEM electrodes to provide *ex situ* time resolved information. After 10 s of electrolysis

there was already a significant change to speciation and morphology of the deposits on the surface as well as detachment. The Cu_2O particles had become Cu^0 , most likely through electrochemical reduction on the BDD surface. After 3600 s the cubic morphology was completely lost and fragmentation extensive. This loss of the [100] is correlated with reduced methane production in literature, which is in agreement with our experiments.

Work for the future on this topic includes analysis of the two CO_2RR features to distinguish the reactions occurring, this may help to optimise the electrolysis potential. Growth studies at different potentials may help to improve yields of cubes if Cu^0 nucleation can be avoided. There is some scope for testing the possibility of regenerating the catalyst by the application of a potential which may improve the overall product ratios.

This work shows that Cu_2O nanocube catalysts can be made quickly, without additives by a simple electrodeposition method. BDD TEM electrodes enable the interrogation of the growth and deactivation of catalysts without having the potential issues of sample transfer from electrode to TEM grid. This gives more realistic information on the system and allows time resolved IL experiments to be carried out. Environmental or *in situ* TEM suffers from limited resolution whereas these experiments do not and therefore greatly increase the amount of information that can be accessed about the activity of these structures.

6.6. Bibliography

- 1 J. D. Cuppett, S. E. Duncan and A. M. Dietrich, *Chem. Senses*, 2006, **31**, 689–697.
- 2 H. Y. H. Chan, C. G. Takoudis and M. J. Weaver, *J. Phys. Chem. B*, 1999, **103**, 357–365.
- 3 J. Kim, W. Choi, J. W. Park, C. Kim, M. Kim and H. Song, *J. Am. Chem. Soc.*, 2019, **141**, 6986–6994.
- 4 Y. Deng, A. D. Handoko, Y. Du, S. Xi and B. S. Yeo, *ACS Catal.*, 2016, **6**, 2473–2481.
- 5 B. Khezri, A. C. Fisher and M. Pumera, *J. Mater. Chem. A*, 2017, **5**, 8230–8246.
- 6 J. Zhao, S. Xue, J. Barber, Y. Zhou, J. Meng and X. Ke, *J. Mater. Chem. A*, 2020, **8**, 4700–4734.
- 7 Y. Zheng, A. Vasileff, X. Zhou, Y. Jiao, M. Jaroniec and S. Z. Qiao, *J. Am. Chem. Soc.*, 2019, **141**, 7646–7659.
- 8 D. Raciti and C. Wang, *ACS Energy Lett.*, 2018, **3**, 1545–1556.
- 9 P. Sebastián-Pascual, S. Mezzavilla, I. E. L. Stephens and M. Escudero-Escribano, *ChemCatChem*, 2019, cctc.201900552.
- 10 G. A. Olah, G. K. S. Prakash and A. Goepfert, *J. Am. Chem. Soc.*, 2011, **133**, 12881–12898.
- 11 P. Kuang, K. Natsui and Y. Einaga, *Chemosphere*, 2018, **210**, 524–530.
- 12 S. Nitopi, E. Bertheussen, S. B. Scott, X. Liu, A. K. Engstfeld, S. Horch, B. Seger, I. E. L. Stephens, K. Chan, C. Hahn, J. K. Nørskov, T. F. Jaramillo and I. Chorkendorff, *Chem. Rev.*, 2019, **119**, 7610–7672.
- 13 K. P. Kuhl, E. R. Cave, D. N. Abram and T. F. Jaramillo, *Energy Environ. Sci.*, 2012, **5**, 7050–7059.
- 14 D. Gao, R. M. Arán-Ais, H. S. Jeon and B. Roldan Cuenya, *Nat. Catal.*, 2019, **2**, 198–210.
- 15 T. C. Chou, C. C. Chang, H. L. Yu, W. Y. Yu, C. L. Dong, J. J. Velasco-Vélez, C. H. Chuang, L. C. Chen, J. F. Lee, J. M. Chen and H. L. Wu, *J. Am. Chem. Soc.*, 2020, **142**, 2857–2867.
- 16 S. Popović, M. Smiljanić, P. Jovanović, J. Vavra, R. Buonsanti, N. Hodnik, I.

- Edition, S. Popović, M. Smiljanić, P. Jovanović, J. Vavra, R. Buonsanti and N. Hodnik, *Angew. Chemie Int. Ed.*, 2020, 2–13.
- 17 D. Ren, Y. Deng, A. D. Handoko, C. S. Chen, S. Malkhandi and B. S. Yeo, *ACS Catal.*, 2015, **5**, 2814–2821.
 - 18 P. Yang, Z.-J. Zhao, X. Chang, R. Mu, S. Zha, G. Zhang and J. Gong, *Angew. Chemie Int. Ed.*, 2018, **57**, 7724–7728.
 - 19 R. M. Arán-Ais, R. Rizo, P. Grosse, G. Algara-Siller, K. Dembélé, M. Plodinec, T. Lunkenbein, S. W. Chee and B. R. Cuenya, *Nat. Commun.*, 2020, **11**, 3489.
 - 20 P. De Luna, R. Quintero-Bermudez, C. T. Dinh, M. B. Ross, O. S. Bushuyev, P. Todorović, T. Regier, S. O. Kelley, P. Yang and E. H. Sargent, *Nat. Catal.*, 2018, **1**, 103–110.
 - 21 G. Iijima, T. Inomata, H. Yamaguchi, M. Ito and H. Masuda, *ACS Catal.*, 2019, **9**, 6305–6319.
 - 22 L. Mandal, K. R. Yang, M. R. Motapothula, D. Ren, P. Lobaccaro, A. Patra, M. Sherburne, V. S. Batista, B. S. Yeo, J. W. Ager, J. Martin and T. Venkatesan, *ACS Appl. Mater. Interfaces*, 2018, **10**, 8574–8584.
 - 23 R. Kas, R. Kortlever, A. Milbrat, M. T. M. Koper, G. Mul and J. Baltrusaitis, *Phys. Chem. Chem. Phys.*, 2014, **16**, 12194–12201.
 - 24 F. S. Roberts, K. P. Kuhl and A. Nilsson, *Angew. Chemie - Int. Ed.*, 2015, **54**, 5179–5182.
 - 25 P. Grosse, D. Gao, F. Scholten, I. Sinev, H. Mistry and B. Roldan Cuenya, *Angew. Chemie - Int. Ed.*, 2018, **57**, 6192–6197.
 - 26 Q. Zhu, X. Sun, D. Yang, J. Ma, X. Kang, L. Zheng, J. Zhang, Z. Wu and B. Han, , DOI:10.1038/s41467-019-11599-7.
 - 27 C. W. Li and M. W. Kanan, *J. Am. Chem. Soc.*, 2012, **134**, 7231–7234.
 - 28 A. Eilert, F. Cavalca, F. S. Roberts, J. Osterwalder, C. Liu, M. Favaro, E. J. Crumlin, H. Ogasawara, D. Friebe, L. G. M. Pettersson and A. Nilsson, *J. Phys. Chem. Lett.*, 2017, **8**, 285–290.
 - 29 R. M. Arán-Ais, F. Scholten, S. Kunze, R. Rizo and B. Roldan Cuenya, *Nat. Energy*, 2020, **5**, 317–325.
 - 30 F. Calle-Vallejo and M. T. M. Koper, *Angew. Chemie Int. Ed.*, 2013, **52**, 7282–7285.

- 31 S. Zhu, B. Jiang, W. Bin Cai and M. Shao, *J. Am. Chem. Soc.*, 2017, **139**, 15664–15667.
- 32 B. Zijlstra, X. Zhang, J. X. Liu, I. A. W. Filot, Z. Zhou, S. Sun and E. J. M. Hensen, *Electrochim. Acta*, 2020, **335**, 135665.
- 33 A. S. Varela, M. Kroschel, T. Reier and P. Strasser, *Catal. Today*, 2016, **260**, 8–13.
- 34 A. Murata and Y. Hori, *Bull. Chem. Soc. Jpn.*, 1991, **64**, 123–127.
- 35 I. C. Chang, P. C. Chen, M. C. Tsai, T. T. Chen, M. H. Yang, H. T. Chiu and C. Y. Lee, *CrystEngComm*, 2013, **15**, 2363–2366.
- 36 S. Sun, X. Zhang, Q. Yang, S. Liang, X. Zhang and Z. Yang, *Prog. Mater. Sci.*, 2018, **96**, 111–173.
- 37 M. J. Siegfried and K. S. Choi, *Angew. Chemie - Int. Ed.*, 2005, **44**, 3218–3223.
- 38 L. Gou and C. J. Murphy, *Nano Lett.*, 2003, **3**, 231–234.
- 39 D.-L. Lu and K. Tanaka, *J. Electrochem. Soc.*, 1996, **143**, 2105–2109.
- 40 X. Guo, W. Lv and X.-Y. Li, *J. Phys. Chem. C*, 2014, **118**, 11062–11077.
- 41 I. S. Brandt, M. A. Tumelero, S. Pelegrini, G. Zangari and A. A. Pasa, *J. Solid State Electrochem.*, 2017, **21**, 1999–2020.
- 42 Y. Sui, W. Fu, H. Yang, Y. Zeng, Y. Zhang, Q. Zhao, Y. Li, X. Zhou, Y. Leng, M. Li and G. Zou, *Cryst. Growth Des.*, 2010, **10**, 99–108.
- 43 M. J. Siegfried and K. S. Choi, *J. Am. Chem. Soc.*, 2006, **128**, 10356–10357.
- 44 H. Jung, S. Y. Lee, C. W. Lee, M. K. Cho, D. H. Won, C. Kim, H. S. Oh, B. K. Min and Y. J. Hwang, *J. Am. Chem. Soc.*, 2019, **141**, 4624–4633.
- 45 A. Eilert, F. S. Roberts, D. Friebe and A. Nilsson, *J. Phys. Chem. Lett.*, 2016, **7**, 1466–1470.
- 46 Y. Hori, H. Konishi, T. Futamura, A. Murata, O. Koga, H. Sakurai and K. Oguma, *Electrochim. Acta*, 2005, **50**, 5354–5369.
- 47 H. E. M. Hussein, R. J. Maurer, H. Amari, J. J. P. Peters, L. Meng, R. Beanland, M. E. Newton and J. V. Macpherson, *ACS Nano*, 2018, **12**, 7388–7396.
- 48 J. Huang, N. Hörmann, E. Oveisi, A. Loiudice, G. L. De Gregorio, O. Andreussi, N. Marzari and R. Buonsanti, *Nat. Commun.*, 2018, **9**, 1–9.
- 49 D. Liu, C. Chen, D. Perry, G. West, S. J. Cobb, J. V. Macpherson and P. R. Unwin, *ChemElectroChem*, 2018, **5**, 3028–3035.

- 50 A. D. Handoko, C. W. Ong, Y. Huang, Z. G. Lee, L. Lin, G. B. Panetti and B. S. Yeo, *J. Phys. Chem. C*, 2016, **120**, 20058–20067.
- 51 A. Loiudice, P. Lobaccaro, E. A. Kamali, T. Thao, B. H. Huang, J. W. Ager and R. Buonsanti, *Angew. Chemie - Int. Ed.*, 2016, **55**, 5789–5792.
- 52 A. Singhal, M. R. Pai, R. Rao, K. T. Pillai, I. Lieberwirth and A. K. Tyagi, *Eur. J. Inorg. Chem.*, 2013, 2640–2651.
- 53 Y. Q. Wang, W. S. Liang, A. Satti and K. Nikitin, *J. Cryst. Growth*, 2010, **312**, 1605–1609.
- 54 Y. Wang, S. Lany, J. Ghanbaja, Y. Fagot-Revurat, Y. P. Chen, F. Soldera, D. Horwat, F. Mücklich and J. F. Pierson, *Phys. Rev. B*, 2016, **94**, 1–10.
- 55 E. Sargeant, A. Kolodziej, C. S. Le Duff and P. Rodriguez, *ACS Catal.*, 2020, **10**, 7464–7474.
- 56 C. S. Le Duff, M. J. Lawrence and P. Rodriguez, *Angew. Chemie - Int. Ed.*, 2017, **56**, 12919–12924.
- 57 J. Monzó, Y. Malewski, R. Kortlever, F. J. Vidal-Iglesias, J. Solla-Gullón, M. T. M. Koper and P. Rodriguez, *J. Mater. Chem. A*, 2015, **3**, 23690–23698.

7. Conclusions and Future Directions

Aqueous metal ions are found in the environment, both naturally and at increased levels due to anthropogenic activities, they can be both essential to biological function and toxic to life. Many metals, often nanosize in dimensions, are also vitally important for technological applications such as electrocatalysis where they can be used to catalyse important reactions including the carbon dioxide reduction reaction (CO₂RR). For these reasons, techniques for the analysis of aqueous metals and metal nanodeposits are important to develop.

Electrochemical X-Ray Fluorescence Spectroscopy (EC-XRF) is a technique with the potential to quickly and cheaply analyse the concentration of aqueous metal ions. Electrochemistry is used to electrodeposit and hence, preconcentrate metal ions onto an x-ray transparent electrode, boron doped diamond (BDD). This is then analysed by XRF which produces a characteristic signal for each element present and can be related to concentration by means of intensity with a calibration curve. In Chapter 3 several different methods of mass transport; magnetic stirrer, vibrating electrode, confined wall jet cell and rotating disk electrode (RDE) were investigated as a means of increasing the mass transport rate of analyte to the electrode surface. This was with a view to investigating whether a new design of an EC-XRF electrode could be implemented for more widespread uptake which also accommodates ease of use.

The relative maximum current increases, compared to a stationary solution response, when assessed with Ru(NH₃)₆^{3+/2}, were 1.8, 2.4, 1.4 and 2.7 times respectively. The RDE was found to be the most effective mass transport method and a BDD EC-XRF electrode was developed. Three prototypes were made, with the third being the best combination of maximum current increase, low backgrounds and useability. Prototype 3 consisted of a detachable BDD disk head with a screw fitting to the main body, which formed an electrical contact to the BDD via Au coated spring pins. The detachable aspect allowed it to be placed into the XRF without much material behind

the electrode, reducing the XRF background. With this electrode, Cu deposition and analysis by XRF in a 0.1 M potassium nitrate solution, resulted in a linear relationship between Cu^{2+} concentration and XRF intensity down to 10 μM . This LOD is sufficient to meet the drinking water standard of 31 μM of Cu^{2+} . EC-XRF has the advantages of cost, useability and portability over more traditional techniques such as inductively coupled plasma mass spectrometry, which are limited to being located in labs, operated by expert users. EC-XRF could be transported to sites of interest and therefore could allow results to be obtained quickly after sampling due to the removal of sample transport time. The main source of error was assumed to result from loss of electrodeposited material when moving from solution to the XRF and also possibly as a result of the frictional force force exhibited on the rotating electrode surface by the flowing solution. This was one of the reasons for moving to a form of *in situ* analysis (Chapter 4). Decreasing LODs would be an important consideration for future work, along with exploring the LODs for other metals such as Pb, Cd, and Zn. Lowering LODs may require investigation into the effect of different solution conditions on Cu deposition or a further investigation into the EC-XRF *ex situ* process to see if deposit loss can be avoided. The most useful test for a real-world application would be to look at the LODs of multi metal solutions, as all applications would expect a more complex solution matrix, and to investigate the effect of metal ions on another metal ions deposition in this system.

Chapter 4 built on the work in Chapter 3 by further exploring a flow cell system that could be applied to *in situ* analysis of aqueous metals, in this case the test system was Cu. A flow cell design was designed and fabricated based on the work by O'Neil et al.¹ but adapted to improve durability, usability and reproducibility. A bespoke tandem peristaltic pump system was successfully implemented alongside the flow cell. The flow cell was initially characterised using $\text{Ru}(\text{NH}_3)_6^{3+/2}$ and found to follow theory for a confined wall jet. It was estimated from experiments that the working electrode-counter electrode separation was of the order of 200 μm . Optimal deposition conditions for Cu^{2+} in KNO_3 was found to be at -0.5 V at a volume flow rate of 20 ml min^{-1} . The LOD for Cu in this system was in the low μM range. For these experiments

the Cu was deposited under flow, the flow stopped, the flow cell detached and moved to the XRF for analysis with solution still present in the cell.

Microscopically, the Cu deposit was found to vary radially in deposit concentration on the BDD working electrode surface. Mapping XRF (resolution approx. 20 μm) showed that at the very centre (under the inlet nozzle) very little deposition occurred. Just outside of this stagnant region the highest concentration of deposit was found which then decreased moving radially outwards from the centre of the electrode. This behaviour fits with the hydrodynamics of a wall jet flow system. The system also proved more robust than the previous design,¹ and the bespoke pump was far more practical for an *in situ* style system than the HPLC pump used previously. Although not yet a true *in situ* system this is a significant step towards that goal. Issues with the current design include; the effect of solution flow on deposits and gas bubbles becoming trapped and blocking the electrode area. Solution flow was tested at 20 ml min^{-1} and it was found to have a detrimental effect on the XRF signal through loss of deposit, presumably through friction with the flowing solution. Gas bubbles, which could have been from dissolved gasses or possibly solvent electrolysis (despite low potential the surface could have been more active to Cu), blocked the electrode surface. Where bubbles were present deposition could not occur, this decreased signal and increased variability between runs.

Future work would look to conduct both the *in situ* deposition by electrochemistry and XRF analysis at the same time, with the flow cell in the XRF chamber. Changes in the design would include changing the sealing mechanism from screws in a flange to a thread attaching top and bottom, more akin to commercial designs. This would allow easier assembly/disassembly and less variability, hopefully eliminating the need for an electrochemical test before experiment. Potentially a way of changing the working-counter electrode separation could be included to investigate the effect of separation on EC-XRF signal. A change in separation could have beneficial effects in terms of reducing the amount of bubbles that become trapped and prevent deposition, leading to improved reproducibility and sensitivity.

In Chapter 5 the effects of pH, potential and electrolyte on the electrodeposition and anodic stripping voltammetry (ASV) of Cu^{2+}/Cu and other Cu variants were investigated. ASV is a fast and cheap method of aqueous metal analysis, however the results can be complicated to interpret, and methodology must be optimised for each application. Thermodynamic speciation and Pourbaix models of solutions containing different electrolyte anions and an acetate buffer, sulfate, nitrate and chloride were compared to experimental ASV data at pH 2 and 5, (pH 3.6 and 5 for buffer) with and without dissolved oxygen.

ASV demonstrated that the electrochemistry of Cu is complex and cannot be adequately described using only thermodynamic models. Dissolved oxygen and solvent electrolysis reactions can drastically alter the ASV responses indicating a complex interplay between different species in solution. The surfaces of the electrodes were imaged using scanning electron microscopy (SEM) after deposition in the different conditions and demonstrate a range of particle morphologies. Transmission electron microscopy (TEM) was also carried out on the deposits formed in a pH 5 aerated nitrate solution, which were found to be cubic Cu_2O crystals. Future work would involve TEM (diffraction and electron energy loss spectroscopy analysis) investigation of the deposits formed in the other conditions, to gain a better understanding of the form of the Cu species deposited on the electrode surface.

These experiments show that within a range of common conditions for ASV a multitude of deposit morphologies can be produced causing complex ASV signals. It was found that in general higher overpotentials (more negative potentials) resulted in smaller, higher number density deposits that were more likely to produce Cu stripping features in ASV. The exceptions being when large interfacial pH changes were expected to occur due to e.g. the nitrate reduction reaction, water reduction or dissolved oxygen reduction. Buffered acetate (pH 3.6 and pH 5) produced the largest Cu stripping signals out of all the electrolytes tested (under constant voltammetric conditions), with the acidic sulfate (pH 2) showing the next best. When depositing in pH 5 solution conditions, very little evidence of any Cu electrodeposition was observed; due to the absence of a Cu stripping peak. This data further shows how the

precise control and understanding of solution conditions, including anion, dissolved oxygen, buffer and pH, are essential for quantitative ASV analysis and must be considered carefully for each application. Cu electrodeposition itself is complicated due to viable pathways for Cu^+ formation leading to Cu_2O formation. Large interfacial pH swings also can lead to $\text{Cu}(\text{OH})_2$ formation which also provides a pathway for Cu_2O and CuO formation. It would be interesting for the future to interrogate the interfacial region by means of confocal microscopy and a suitable pH sensitive dye to track the changes in pH during electrodeposition.

In the final chapter, Chapter 6 an investigation into the cubic Cu_2O electrodeposited from a pH 5 aerated nitrate solution was conducted. Image analysis was carried out on SEM images and showed a correlation between the boron content of a BDD grain and the size and number density of cube formed. Future work would be looking to quantify this effect, using techniques such as electron backscatter diffraction and secondary ion mass spectroscopy to identify grains and quantify boron content. This effect is thought to occur due to a slight difference in effective overpotential on each BDD grain and so a study into the change in cube size and distribution characteristics would inform on how effective a purely potential controlled strategy may be for cube size control.

An Identical Location (IL) study on the electronucleation and growth of the Cu_2O cubes was carried out. This showed that at a short time of 1 s, initially the deposits were Cu^0 but as time progressed Cu_2O particles grew as the Cu^0 particles dissolved, this shows that although there is a driving force for Cu^0 deposition they are not stable and that Cu_2O crystals are a more stable form that persist throughout the deposition. This effect was observed for several particles observed at different time points using the IL method.

The electrocatalytic activity of these cubes towards CO_2 reduction was tested with On-Line Electrochemical Mass Spectrometry (OLEMS) and they were found to produce H_2 and CO with CH_4 and C_2H_2 as desirable products. The blank run was found to also produce H_2 and CO , but due to the non-quantitative nature of the experiment

this could not be background subtracted from the Cu₂O runs. The liquid products could not be determined with the system used due to concentrations being too low. If the loading of the cubes could be sufficiently increased, it would be possible to create a concentrated enough liquid sample for NMR to determine other products of the reaction and obtain faradaic efficiencies and is a point of interest for future work. During CO₂ RR a change in the electroactivity of the cubes over time was evident from the decline in production of CH₄ and C₂H₂ relative to H₂ and CO by OLEMS. *Ex situ* BDD TEM was used to observe this effect, with the Cu₂O cubes being observed at various time points in the reaction. Detachment, agglomeration, morphology change and electrochemical reduction of the cubes were all identified as deactivation routes from the TEM imaging.

This chapter studied the entire “life cycle” of an important electrocatalytic material. This work shows how the use of BDD TEM electrodes increases the possibilities for the high-resolution and time resolved investigation of electrocatalyst materials without the disruption of transferring them from an experimental set up to a TEM suitable substrate. The robustness of the BDD TEM electrodes allows IL-TEM studies to be carried out allowing the examination of the fate of individual particles during reactions at a resolution that is not possible by *in situ* TEM methods. Future work would look more closely into the nucleation of these particles at shorter times, e.g. less than 1 s. An IL experiment into the fate of specific particles during deactivation would give useful insights into the deterioration of catalytic activity that *ex situ* time resolved experiments could not. Tracking the fate of individual particles would allow connections to be drawn between the initial characteristics of the particle and the rate of its deactivation, this could aid in future catalyst design.

This thesis demonstrates the importance of understanding metal electrodeposition for a range of applications from environmental analysis, the effect of solution conditions on electrodeposition and stripping and the use of metal catalysts generated by electrodeposition for electrocatalysis applications and their fate therein. Alongside the results found in this thesis, many further questions have been raised giving rise to many interesting angles for future work.

7.1. Bibliography

- 1 G. D. O'Neil, M. E. Newton and J. V. Macpherson, *Anal. Chem.*, 2015, **87**, 4933–4940.